SCUOLA DI DOTTORATO
UNIVERSITÀ DEGLI STUDI DI MILANO-BICOCCA

Department of Biotechnology and Bioscience

PhD program in Molecular and Translational Medicine (DIMET)

Cycle XXXV

Type III Interferons: Running Interference with Mucosal Repair.

Sposito Benedetta

822101

Tutor: Prof. Ivan Zanoni

Coordinator: Prof. Andrea Biondi

Academic Year 2021/2022

“Pain is inevitable. Suffering is optional.”

-an ancient Buddhist saying

Table of Contents.

Chapter 1. Introduction.

Interferons and their receptors.

Interferons (IFNs) were first discovered by Isaacs and Lindenmann in 1957 as soluble factors that interfere with viral infection (Isaacs et al. 1957; Isaacs and Lindenmann 1957). Later on, they have been identified as antiviral proteins that are secreted by cells in response to different stimuli (Pestka and Langer 1987).

As of today, three families of IFNs have been identified in mammals. Type I IFNs are composed of 13 IFN-α subtypes in humans (14 in mice), IFN-β, IFN-δ, IFN-ε, IFN-κ, IFN-τ, IFN-ω, and IFN-ζ (McNab et al. 2015; Pestka, Krause, and Walter 2004). Type I IFNs were the first to be discovered (Isaacs et al. 1957; Isaacs and Lindenmann 1957). They can be produced by almost every cell type upon stimulation of pattern recognition receptors (PRRs). Type I IFNs all signal through the heterodimeric type I IFN receptor (IFNAR) composed of IFNAR1 and IFNAR2 subunits whose expression is ubiquitous.

Type II IFNs consist of IFN-γ. IFN-γ was discovered in 1965 (Wheelock 1965). It is produced mainly by lymphocytes of the immune system namely natural killer (NK) cells, natural killer T (NKT) cells and CD8+ and CD4+ T cells in the context of viral and intracellular bacterial infections and in response to tumors (Schoenborn and Wilson 2007). IFN-γ signals through the ubiquitous IFN-γ receptor (IFNGR) that is composed of two IFNGR1 ligand-binding subunits associated with two IFNGR2 subunits.

In humans type III IFNs consist of IFN-λ1 (IL29), IFN-λ2 (IL28A) and IFN-λ3 (IL28B) that were identified by two independent groups in 2003 (Kotenko et al. 2003) (Sheppard et al. 2003). The latest addition to the family is IFN-λ4 which was initially thought to be a pseudogene. It is now clear that it is a gene whose expression depends on a single nucleotide polymorphism (SNP) (ss469415590, TT/ΔG). The TT allele causes a frameshift that suppresses its production while the ΔG allele allows for it to be encoded (Prokunina-Olsson et al. 2013). Mice only have functional *Ifnl2* and *Ifnl3*, while *Ifnl1* and *Ifnl4* are pseudogenes (Hemann, Gale, and Savan 2017). The heterodimeric IFN-λ receptor IFNLR is composed of the specific subunit IFNLR1 (IFNLRA) and IL10RB (IL10R2), which is shared with other cytokines of the IL-10 family (such as IL-10, IL-22 and IL-26) and is ubiquitously expressed (Durbin, Kotenko, and Durbin 2013). On the contrary, IFNLR1 is preferentially expressed on cells of epithelial origin including cells of the intestinal and respiratory tract (Ye, Schnepf, and Staeheli 2019) and on some immune cells including neutrophils (Broggi et al. 2017), plasmacytoid dendritic cells (pDCs) (Megjugorac, Gallagher, and Gallagher 2009), lung DCs (Hemann et al. 2019; Koltsida et al. 2011) and B cells (de Groen et al. 2015).

Canonical and non-canonical signaling of IFNs.

All IFN receptors activate the Janus kinase (JAK)- signal transducers and activators of transcription (STAT) pathway (**Figure 1**).

IFN-I binding to their receptor activates the kinases TYK2 and JAK1 which are bound to IFNAR1 and IFNAR2 respectively. In the canonical pathway, they phosphorylate cytosolic STAT1 and STAT2 leading to the assembly of STAT1-STAT2 heterodimer that associates with IFN-regulatory factor 9 (IRF9) to form IFN-stimulated gene factor 3 (ISGF3) transcription factor. Other pathways are also activated including STAT1 homodimers, also called gamma interferon-activated factor (GAF), and several combinations of STAT 1/2/3/4/5/6 (Stanifer, Pervolaraki, and Boulant 2019). The multitude of these pathways can induce a broad range of IFN-stimulated genes (ISGs) whose promoters are characterized by the presence of IFN-stimulated response elements (ISRE) and/or γ-activated sequence (GAS) elements that are activated by ISGF3 or STAT1 homodimers respectively (McNab et al. 2015). Different tissue expression, binding affinities for IFNAR1 and IFNAR2, as well as receptor density on target cells, are responsible for the specific action of each type I IFN subtype (Jaks et al. 2007; Moraga et al. 2009).

IFN-γ also activates the JAK-STAT pathway. IFNGR subunits IFNGR1 and IFNGR2 are associated with JAK1 and JAK2 respectively (Schroder et al. 2004). Upon activation they preferentially but not exclusively phosphorylate STAT1 leading to the formation of STAT1 homodimers that translocate to the nucleus, bind the GAS DNA sequence and induce ISG transcription.

The post-receptor events elicited by type I and III IFNs share several similarities as well as significant differences. IFN-λ binding of IFNLR1 and IL10RB activates JAK1 and TYK2. However, only JAK1 is indispensable for type III IFN signaling (Fuchs et al. 2016). Moreover, JAK2 is phosphorylated downstream of IFNLR and contributes to the response induced by IFN-III (S.-J. Lee, Kim, and Moon 2012; Odendall et al. 2014; Broggi et al. 2017). Similarly to IFN-I, the subtypes of IFN-III differ in their affinity for the two receptor subunits and the stability of the ligand-receptor complex that they form (Egli et al. 2014).

The JAK-STAT signaling cascade downstream of IFNLR is very similar to that of IFNAR and it leads to the upregulation of a largely overlapping set of ISGs controlled by both ISRE and GAS motifs (Ank et al. 2008) (Z. Zhou et al. 2007). However, the induction of ISGs in response to IFN-III is delayed compared to IFN-I (Marcello et al. 2006) (Jilg et al. 2014). Additionally, IFN-I have been shown to trigger a more potent inflammatory response compared to IFN-III (Davidson et al. 2016) (Galani et al. 2017). This is due to a higher induction of the proinflammatory transcription factor IRF1, a GAS motif-induced ISG, by IFN-I than IFN-III (Forero et al. 2019). Distinct receptor expression and regulation of receptor cell surface levels by internalization and degradation can also differentially modulate type I and III IFN activity. Moreover, their receptors have different susceptibilities to inhibitory phosphatases and to negative regulators such as ubiquitin-specific protease 18 (USP18) and suppressor of cytokine signaling 1 and 3 (SOCS1 and SOCS3), that are all ISGs. USP18 prevents the interaction of IFNAR2 with JAK1 and inhibits IFN-α signaling but does not bind the

IFNLR (Malakhova et al. 2006) (Blumer et al. 2017). SOCS1 and SOCS3 block type I IFN whereas only SOCS1 blocks type III IFN signaling (Piganis et al. 2011; Blumer et al. 2017; Liu et al. 2015).

Several JAK-STAT independent pathways are activated downstream of IFN receptors including the phosphatidyl-inositol 3-kinase (PI3K) and the mitogen-activated protein kinases (MAPK) and can contribute to the diversity of the responses elicited by the three classes of IFNs (Durbin, Kotenko, and Durbin 2013).

Finally, signaling downstream of IFNLR via JAK2 was shown to have translation-independent effects. In particular, it inhibited the activity of the AKT kinase leading to unique IFN-λ immunomodulatory responses (Broggi et al. 2017).

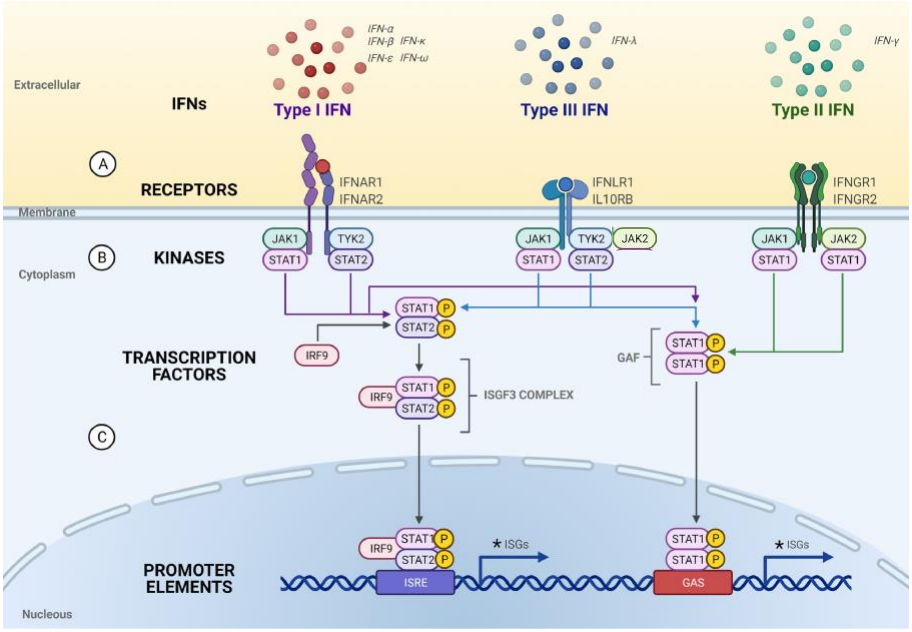

Figure 1. Canonical IFN signaling cascade. IFN-I signal through IFNAR1 and IFNAR2 heterodimers and activate JAK1 and TYK2; IFN-III signal through IFNLR1 and IL10RB heterodimers and activate JAK1, TYK2 and JAK2; IFN-II signals through dimers of heterodimers consisting of IFNGR1 and IFNGR2 and activates JAK1 and JAK2. IFN-I and III lead to the phosphorylation and dimerization of STAT1 and STAT2 and to the recruitment of the IFN-regulatory factor 9 (IRF9) to form the IFN-stimulated gene factor 3 (ISGF3). IFN-II phosphorylates STAT1. Phosphorylated STAT1 homodimers form the gamma IFN-activated factor (GAF). ISGF3 and GAF translocate to the nucleus and induce expression of IFN-stimulated genes (ISGs) regulated by IFN-stimulated response elements (ISRE) and gamma-activated sequence (GAS) promoter elements respectively. Modified from (Akamatsu et al. 2021).

Induction of type I / III IFNs.

My thesis focuses on type I and type III IFNs that constitute a frontline host defense system. They are among the first molecules to be induced upon recognition of a variety of microbial signals called pathogen-associated molecular patterns (PAMPs). PAMPs consist of nucleic acid motifs, lipopolysaccharides, glycoproteins and proteoglycans that are critical for microbial survival and are thus conserved and shared by different microorganisms. They are recognized by germline-encoded pattern recognition receptors (PRRs).

The first major distinction between IFN-I and III is that IFN-I can be produced and sensed by almost every cell type. Thus they can mediate a systemic effect (McNab et al. 2015). Instead, IFN-III act primarily on epithelial and immune cells at barrier surfaces (Galani et al. 2017; Lazear, Schoggins, and Diamond 2019; Ye, Schnepf, and Staeheli 2019). However, IFN-I and III are upregulated downstream of the same subsets of PRRs. In the context of RNA virus infections, they can be induced by RIG-I-like receptors (RLRs) (Loo and Gale 2011) and Toll-like receptors (TLRs) (Uematsu and Akira 2008).

RLRs are a family of cytosolic RNA helicases composed of retinoic acid-inducible gene I (RIG-I), melanoma differentiation-associated factor 5 (MDA5) and laboratory of genetics and physiology 2 (LGP-2). RIG-I and MDA5 are known to recognize viral double-stranded RNA (dsRNA) while LGP-2 is thought to have regulatory functions (Yoneyama et al. 2005). During most viral infections dsRNA is present either as a replicative intermediate or as it constitutes the viral genome of dsRNA viruses (Chen and Hur 2022). RIG-I binds dsRNA with specific

characteristics that are found in viral RNA molecules but not in host cytosolic RNA: 5'ppp-RNA or uncapped 5'ppRNA and with no ribose 2'-O-methylation at the 5' terminal nucleotide. MDA5 recognizes dsRNA filaments whose specific features have not been fully characterized (Rehwinkel and Gack 2020).

RIG-I and MDA-5 form filaments along the fragment of dsRNA and oligomerize via their caspase activation and recruitment domains (CARDs). Their oligomerized CARD domains are then able to interact with the CARD domains on mitochondrial antiviral-signaling protein (MAVS) that is anchored to mitochondria, mitochondrial-associated membranes (MAMs) and peroxisomes that also oligomerize to form filaments. MAVS activates TANK-binding kinase 1 (TBK1) and Iκβ kinase-ε (IKKε) leading to the phosphorylation of IRF3 and IRF7 (Chen and Hur 2022; Rehwinkel and Gack 2020) (**Figure 2**). IRF7 is an ISG and is upregulated upon the initial wave of IFN transcription induced by IRF3. Phosphorylated IRF3 and IRF7 together with nuclear factor kappa B (NF-κB) trigger the expression of type I and III IFNs. Localization of MAVS on the peroxisome or on the mitochondria can favor the production of IFN-λ1 or IFN-β, respectively (Odendall et al. 2014).

TLRs are present on the cell surface or on endosomal compartments. They are formed by an N-terminal PAMP-binding domain and a C-terminal intracellular domain called the Toll/interleukin-1 receptor (IL-1R) (TIR) domain that mediates signaling events. The main TLRs that are involved in RNA virus sensing and IFN-I/III induction are TLR3 and TLR7/8 which recognize dsRNA and single-stranded (ssRNA) respectively. Additionally, TLR4 can recognize proteins present on viral

envelopes (Uematsu and Akira 2008) (Jensen and Thomsen 2012).

Upon binding of dsRNA, TLR3 dimerizes and the two TIR domains recruit TIR domain-containing adaptor protein inducing IFN-β (TRIF) (L. Liu et al. 2008) (Yamamoto et al. 2003). TRIF recruits TNF receptor-associated factor 3 (TRAF3) which activates IKKε and TBK1 that phosphorylate IRF3 and IRF7 and induce type I and III IFNs. TRIF also binds to TRAF6 leading to NF-κB activation and expression of proinflammatory genes (Kawai and Akira 2006) (**Figure 2**).

TLR7 binds ssRNA released by viruses in the endosomes. The adaptor myeloid differentiation primary response gene 88 (MyD88) is recruited to the TIR domain and it associates with interleukin-1 receptor-associated kinase 4 (IRAK4). Ultimately this leads to IRF7 phosphorylation as well as NF-κB and activator protein 1 (AP-1) activation that together trigger IFN-I and proinflammatory gene expression, respectively. This pathway of IFN-I induction has mainly been described in pDCs that constitutively express IRF7 (Uematsu and Akira 2008) (Moynagh 2005).

TLR4 recognition of proteins of the viral envelope leads to its dimerization. Subsequently, it can bind the TIR domain-containing adaptor protein (TIRAP) which recruits MyD88 and induces NF-κB and AP-1-mediated induction of proinflammatory genes. In alternative, it can translocate to the endosomal compartment and bind the TRIF-related adaptor molecule (TRAM) that recruits TRIF allowing for IFN-I and III induction (Kagan and Medzhitov 2006) (Kagan et al. 2008) (Odendall, Voak, and Kagan 2017).

Despite being downstream of the same PRRs there are differences in

the induction of type I and type III IFNs. At the transcriptional level, it has been shown that the promoters of IFN-λ1 and IFN-β are controlled by NF-κB, AP-1 and by either IRF3 or IRF7, whereas IFN-λ2-3 and IFN-α are more dependent on IRF7 (Osterlund et al. 2007) (Onoguchi et al. 2007). Moreover, IRF1 is required for virus-induced IFN-λ1 expression and production but dispensable for IFN-β expression (Odendall et al. 2014; Reis et al. 1994; Siegel, Eskdale, and Gallagher 2011; Ueki et al. 2013). It also appears that IFN-λ1, and not IFN-β, can be induced independently by IRFs or NF-κB and that AP-1 is dispensable for IFN-λ1 expression (Odendall et al. 2014; Thomson et al. 2009). These findings characterize some of the distinctions in the induction of IFN-I and III but additional research will be required to further explain the diversity in cells producing them as well as in the kinetics of their expression.

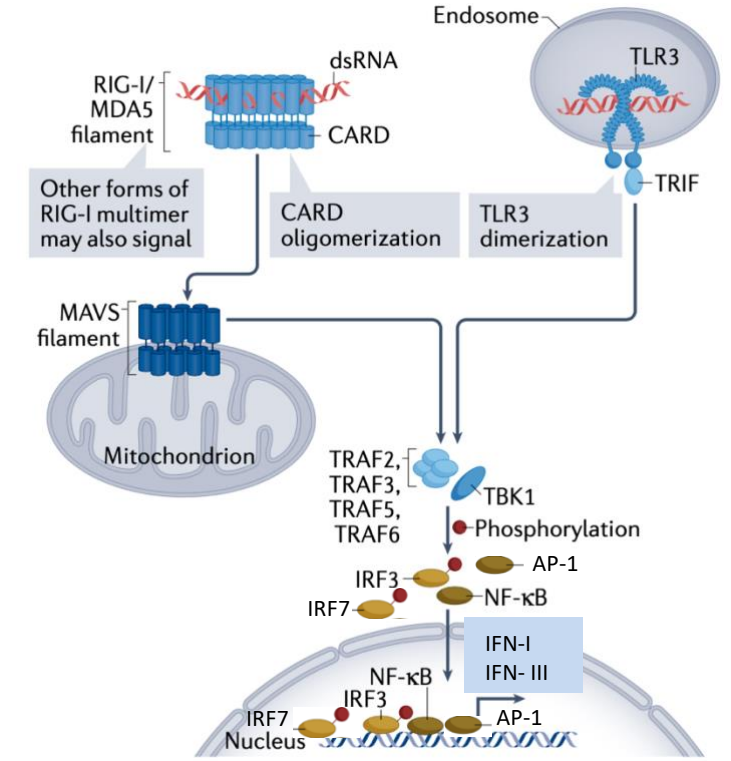

Figure 2. RLR and TLR3 dsRNA sensing and downstream signaling. dsRNA can be detected in the endosome by TLR3 and in the cytosol by the RIG-I and MDA-5. Ligand binding leads to their oligomerization and activation of their adaptors TRIF and MAVS, respectively. Their signaling cascades activate TRAFs and TBK1 that lead to the phosphorylation of IRF3 and IRF7. Phosphorylated IRF3 and IRF7 together with activated NF-κB and AP-1 induce IFN-I and IFN-III expression. Modified from (Chen and Hur 2022).

Type I / III IFNs in IAV and SARS-CoV-2 infections.

Type I and III IFNs are critical effectors of the mucosal innate immune system against infection with respiratory RNA viruses including influenza A virus (IAV) and severe acute respiratory syndrome coronavirus 2 (SARS-CoV-2) (Iwasaki and Pillai 2014; Park and Iwasaki 2020). They trigger an antiviral state in infected and bystander cells via induction of ISGs and activate the adaptive immune response to viruses (Ivashkiv and Donlin 2014). Thus, IAV and SARS-CoV-2 have multiple virulence factors that block IFN responses at every stage from their induction downstream of PRRs, to their signaling, and ultimately to the action of the antiviral effectors encoded by ISGs (García-Sastre 2011; Lei et al. 2020; Park and Iwasaki 2020).

IAV infection in mice deficient in type I and III IFN signaling has shown that only lack of both receptors makes them unable to control the infection, suggesting that their antiviral functions are partially redundant (Crotta et al. 2013; McNab et al. 2015; Mordstein et al. 2010; 2008; Ye, Schnepf, and Staeheli 2019). However, it is increasingly clear that they act in a coordinated manner at different stages of IAV infection progression. The nasal epithelium is the port of entry of IAV. Upon infection, nasal epithelial cells induce IFN-λ more strongly and earlier than IFN-I and are essential to promote a strong and prolonged antiviral response in the upper airways (Galani et al. 2017; Jewell et al. 2010). In models where IAV is selectively administered to the upper airways, IFN-λ are essential to prevent viral spread to the lower

airways and to reduce virus shedding and transmission (Klinkhammer et al. 2018). If the infection progresses, type I IFNs are induced and mediate a strong local and systemic antiviral response (Galani et al. 2017).

In addition to promoting cell-intrinsic antiviral responses, type I IFNs modulate innate and adaptive cell responses to IAV and, according to the experimental model, they enhance or inhibit them (McNab et al. 2015). Also, type III IFNs have immunostimulatory functions during IAV infection. They limit the expression of proinflammatory genes in neutrophils (Galani et al. 2017) and indirectly promote protective adaptive immune responses (Hemann et al. 2019; Koltsida et al. 2011; Ye et al. 2019).

However, type I and III IFNs can also contribute to immunopathology during viral infections. IFN-I can promote uncontrolled lung inflammation and epithelial cell apoptosis (Davidson et al. 2014; Högner et al. 2013a). Prolonged production of type III IFNs also has a detrimental effect during lung repair following IAV infection as they induce apoptosis and reduce the proliferation of epithelial cells (Major et al., 2020). Finally, type I and III IFNs increase susceptibility to post-IAV secondary *Staphylococcus aureus* (*S. aureus*) and *Streptococcus pneumoniae* (*S. pneumoniae*) infections (Kudva et al. 2011; Pires and Parker 2018; Planet et al. 2016; Shahangian et al. 2009).

Exogenous administration of IFN-α and IFN-λ shows that they both restrict IAV replication but only IFN-α cause strong inflammatory side effects that contribute to mouse morbidity (Davidson et al. 2016; Galani et al. 2017).

Critical insight into the role of IFNs in SARS-CoV-2 infections can be obtained from mouse models of two other highly pathogenic coronaviruses: SARS-CoV and Middle East respiratory syndrome coronavirus (MERS-CoV). SARS-CoV mouse-adapted virus causes mild pathology in C57BL/6 and 129 and severe pathology in BALB/c mice. In models of mild pathology, IFN-I and III are necessary for viral control and are thus protective (Frieman et al. 2010; Mahlakõiv et al. 2012). On the contrary, in models with severe SARS IFN-I induction is detrimental because it happens too late to contain the viral spread and it contributes to inflammatory lung damage. Only administration of IFN-β before and not after viral load peak blocks viral replication and is protective (Channappanavar et al. 2016). In MERS-CoV, IFN-I are protective as their induction is sufficiently early in the course of the infection (Channappanavar et al. 2019; Zhao et al. 2014). Similarly to SARS-CoV, also upon infection with MERS-CoV mice benefit only from early treatment with IFN-β while its administration after viral peak aggravates the disease (Channappanavar et al. 2019; Zhao et al. 2014). All these studies show that the timing of IFN responses determines their beneficial or detrimental effect during coronavirus infections (**Figure 3**).

Initially, mice studies on IFN responses to SARS-CoV-2 were limited because SARS-CoV-2 spike (S) protein from viral strains early in the pandemic did not bind mouse angiotensin-converting enzyme 2 (ACE2) that is required to enter host cells (Halfmann et al. 2022). Mice did not support SARS-CoV-2 infection unless the virus was adapted to mouse ACE2 or human ACE2 (hACE2) was expressed in transgenic mice or by

transduction with an adenovirus or adeno-associated virus expressing hACE2 (Muñoz-Fontela et al. 2020). *Irf3*$^{-/-}$*Irf7*$^{-/-}$, *Ifnar1*$^{-/-}$ and *Stat1*$^{-/-}$ mice expressing hACE2 in the lungs via viral vectors all had impaired ISG expression, recruitment of proinflammatory cells into the lungs and in some models viral clearance (Israelow et al. 2020; Sun et al. 2020). Likely IFN-λ also played a protective role as the strongest phenotype of *Stat1*$^{-/-}$ mice couldn't be recapitulated by lack of type I or type II IFN signaling alone (Sun et al. 2020). The lack of IFN-I, IFN-III, and even more both, increased mice susceptibility to infection with mouse-adapted SARS-CoV-2 (Beer et al. 2022). Prophylactic and therapeutic administration of IFN-III protected WT, *Ifnar1*$^{-/-}$ and hACE2-expressing mice from infection with mouse-adapted and original strains of SARS-CoV-2 (Dinnon et al. 2020; Sohn et al. 2021; Beer et al. 2022). When SARS-CoV-2 strains acquired a mouse-adapting mutation in the S protein they could be used to infect mice in the absence of hACE2 (Halfmann et al. 2022). *Ifnlr1*$^{-/-}$ mice had a higher viral burden compared to WT mice when infected with the Beta and Omicron SARS-CoV-2 variants (Chong et al. 2022). Only intranasal delivery of IFN-λ2 (both before and during infection) decreased viral burden and inflammation while its subcutaneous administration did not (Chong et al. 2022). In conclusion, IFN-I and III act in a concerted and nonredundant manner in response to SARS-CoV-2. The use of IFN-λ in the upper airways early in the course of the infection or as prophylaxis are both promising clinical approaches.

Several clinical studies have looked at the induction of IFN-I and III in coronavirus disease 2019 (COVID-19) patients. Autoantibodies against

type I IFNs and inborn defects in TLR3, IRF7, IRF9 and IFNAR1 have been identified in patients with severe COVID-19 indicating that the inhibition of IFN responses can be a driver of disease severity (Bastard et al. 2020; Zhang et al. 2020).

Among the papers that analyzed the peripheral production of IFNs some show that the IFN response in serum and PBMCs of COVID-19 patients is defective (Blanco-Melo et al. 2020; Hadjadj et al. 2020). Others detect robust IFN responses in PBMCs from COVID-19 patients compared to healthy controls (Zhu et al. 2020) and in monocytes from severe compared to mild COVID-19 patients (J. S. Lee et al. 2020). When analyzing serum IFN-α and IFN-λ longitudinally they were sustained at high levels in patients with severe compared to moderate COVID-19 (Lucas et al. 2020) or expressed only in critically ill patients with a delayed kinetic compared to IAV patients (Galani et al. 2021).

Another set of papers looked at IFN responses at the site of infection. The nasal ISG response was correlated with nasal SARS-CoV-2 load and infectivity and with serum IFN-α levels, except in critically ill patients with IFN-I autoantibodies (Lopez et al. 2021). A strong ISGs induction was detected in the nasal mucosa of patients infected with SARS-CoV-2 with mild symptoms compared to other viral infections (Mick et al. 2020; Ng et al. 2021). Finally, a study has shown that in the nasal epithelium severe patients have a defective induction of IFN-responsive and anti-viral genes (Ziegler et al. 2021). These data suggest that when patients mount a strong IFN response at the site of infection disease severity is contained. The impairment of IFN-mediated cell-intrinsic immunity in the nasal mucosa can aggravate pathology, likely

due to the consequent inability to restrict the infection to the upper airways. Moreover, bronchoalveolar lavage fluid (BALF) samples from patients with severe COVID-19 compared to ones with community-acquired pneumonia and healthy controls display higher ISG expression. This indicates that in the lower airways of severe patients IFN responses are indeed induced and are possibly contributing to immunopathology (Zhuo Zhou et al. 2020).

IFN-α and IFN-β have been evaluated for the treatment of COVID-19 in several randomized control trials, often in combination with other antivirals, but their efficacy has not been consistent (Sodeifian et al. 2022). The use of different subtypes, dosage and timing of administration could explain these discrepancies. Even though patients would benefit most from early-stage treatment with IFNs, several trials have assessed their efficacy on severe patients in the later stages of the disease (Jhuti et al. 2022; Park and Iwasaki 2020). Subcutaneous delivery of pegylated IFN-λ1 was also tested in placebo-controlled clinical trials for COVID-19 patients. Despite being administered in the early stages of the infection, it accelerated virus clearance only in one (Feld et al. 2021) of the two trials (Jagannathan et al. 2021).

Timing and location of the IFN response are crucial to promoting an effective antiviral response to SARS-CoV-2 without aggravating disease severity (Channappanavar 2022; Park and Iwasaki 2020). Severe pathology can occur when IFN responses are defective either because of host factors such as autoantibodies against IFN-I and genetic defects in the IFN signaling pathway (Bastard et al. 2020; Zhang et al. 2020) or

due to the ability of SARS-CoV-2 proteins to effectively interfere with PRR sensing, IFN production, IFN signaling and ISG effector functions (Park and Iwasaki 2020). On the other hand, an excess or a delay in them can also be detrimental as they can contribute to immunopathology.

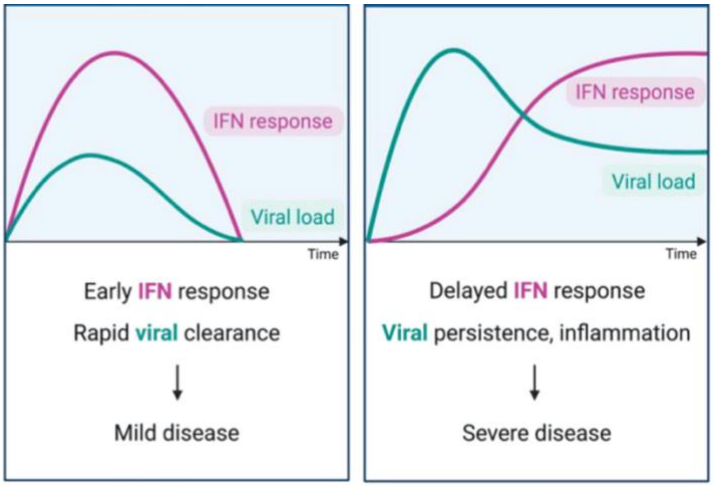

Figure 3. Timing determines the outcome of IFN responses in coronavirus infections. Early induction of IFNs allows for viral clearance and does not contribute to pathology. A delayed IFN response is incapable of containing viral replication, it contributes to inflammation and tissue damage thus aggravating disease severity. Modified from (Park and Iwasaki 2020).

Type I / III IFNs in IBD.

Inflammatory bowel diseases (IBD) are chronic inflammatory disorders of the gastrointestinal tract that include ulcerative colitis (UC) and Crohn's disease (CD). CD is characterized by transmural inflammation that usually affects the ileum but that can extend to any region of the gastrointestinal tract. In UC inflammation is limited to the colon mucosa. Growing evidence indicates that CD and UC are caused by a dysregulation in the interaction between the host's intestinal epithelium, immune system and gut microbiota (Abraham and Cho 2009; Maloy and Powrie 2011; Nell, Suerbaum, and Josenhans 2010).

Mouse studies have investigated the involvement of IFN-I/III in these pathologies. Importantly, the gut mucosa of adult mice has a compartmentalized IFN system in which epithelial cells respond preferentially to IFN-λ and lamina propria lymphocytes mostly respond to IFN-I (Lin et al. 2016; Mahlakõiv et al. 2015; Pott et al. 2011). A widely used mouse model for IBD is dextran sulfate sodium (DSS)-induced colitis. It involves an acute phase in which DSS administration in drinking water causes chemical destruction of the intestinal epithelium, invasion of the lamina propria by commensals and inflammation. It is followed by a repair phase in which the epithelial barrier is reestablished after the removal of DSS (Kiesler, Fuss, and Strober 2015). In this model, IFN-I are protective in the acute phase as they reduce inflammation, but are detrimental because they delay tissue recovery (Katakura et al. 2005; Rauch et al. 2014). Type III IFNs

are beneficial in the acute phase as lack of IFN-III signaling aggravates DSS-induced colitis and administration of exogenous IFN-λ2 ameliorates it (Broggi et al. 2017; Chiriac et al. 2017; Rauch et al. 2015). This phenotype can be explained by their ability to inhibit tissue-damaging functions of neutrophils (Broggi et al. 2017) and to induce a STAT1-dependent increase in intestinal cell proliferation (Chiriac et al. 2017). The combined loss of IFN-I and III signaling causes more severe disease in DSS-induced colitis compared to the lack of individual signaling (McElrath et al. 2021; Rauch et al. 2015). IFN-I and III upregulate the ISG amphiregulin that promotes intestinal barrier repair by acting on lamina propria immune cells and epithelial cells respectively (McElrath et al. 2021). However, IFN-III can also disrupt the intestinal barrier by inducing cell death of Paneth cells, that are pivotal for stem cell survival in small intestine crypts, via caspase 8/mixed lineage kinase domain-like (MLKL) (Günther et al. 2019). Also, IFN-III are upregulated in the ileum and colon biopsies of CD and UC patients (Chiriac et al. 2017; Günther et al. 2019). Moreover, genome-wide association studies (GWAS) have identified several IBD-associated loci that are involved in type I and III IFN signaling (Andreou, Legaki, and Gazouli 2020; Jostins et al. 2012; J. Z. Liu et al. 2015). The possibility that similarly to type I IFNs, IFN-III might have opposing effects according to the phase of the disease in CD and UC is still under investigation.

The use of IFN-α and IFN-β has been tested in IBD patients with controversial outcomes. Some studies showed a beneficial effect (Madsen et al. 2001; E. Musch et al. 2007; Nikolaus et al. 2003) but

other studies failed to show efficacy (Eugen Musch et al. 2005; Pena Rossi et al. 2009; Pena-Rossi et al. 2008; Tilg et al. 2003) and the use of IFN-α in other pathological contexts was associated with the development of UC (Schott et al. 2007; Watanabe et al. 2006). So far, type III IFNs have not been evaluated for the treatment of IBD.

Antiproliferative and proapoptotic roles of type I / III IFNs.

Among the wide array of responses induced by IFNs is their ability to increase the susceptibility of cells to apoptosis triggers and to block cell proliferation (Chawla-Sarkar, Lindner, and Borden 2003; Li et al. 2008; Maher et al. 2008). Indeed, IFNs can regulate both intrinsic (or mitochondrial) and extrinsic (or death receptor-mediated) apoptosis pathways (Parker, Rautela, and Hertzog 2016; Thyrell et al. 2002). The antiproliferative and proapoptotic actions of IFNs enable them to contain viral spread in infected cells and to promote antitumor effects in malignant cells. However, enhanced apoptosis can interfere with tissue repair in different pathological contexts.

A useful mouse model to study gut epithelium repair is gastrointestinal damage following exposure to gamma radiation. Radiations trigger the production of reactive oxygen species (ROS) that damage cellular components including DNA. Total body irradiation (TBI) causes hematopoietic and intestinal damage. Partial or sub-total body irradiation (SBI) shields and preserves bone marrow to avoid hematopoietic syndrome. In SBI actively replicating cells such as intestinal stem cells and progenitor cells are more radiosensitive and are thought to die by p53-mediated cell death (Kim, Yang, and

Bialkowska 2017; Kirsch et al. 2010). Within the first two days from irradiation, crypt cells undergo apoptosis resulting in crypt and villus shortening (Kim, Yang, and Bialkowska 2017; Booth et al. 2012). This apoptotic phase is followed by a regenerative phase between days 2 and 4 in which the surviving crypt cells regenerate crypts and finally the system returns to homeostasis.

In this context IFNs can be induced downstream of PRRs that recognize damage-associated molecular patterns (DAMPs). In TBI, signaling downstream of TLR3 was shown to induce cell death of crypt cells in an IRF3 and IFNAR-independent manner (Takemura et al. 2014). Instead, IFN-β, and not IFN-α, downstream of cGAS-STING was shown to promote crypt regeneration via compensatory proliferation (Leibowitz et al. 2021). So far the role of IFN-III in gut repair following radiation injury has not been evaluated.

Scope of the thesis.

Despite a striking similarity in the ISG responses elicited by signaling via type I and III IFN receptors, unique functions of type III IFNs are increasingly being identified (Ye, Schnepf, and Staeheli 2019). IFN-III act on epithelial cells and on a restricted subset of immune cells mostly at mucosal barriers. They are considered frontline defenders of epithelia with the benefit of inducing less damage than IFN-I (Lazear, Schoggins, and Diamond 2019). In the course of my PhD, I have explored the possible contribution of IFN-III to immunopathology in the context of several pathological conditions namely viral respiratory infections, IBD and radiation-induced small intestinal damage.

In particular, in Chapters 2 and 3, my colleagues and I have mimicked the induction of an antiviral and tissue-damaging response in the lungs by injecting mice intratracheally with agonists of PRRs. Using this model, we investigated the cellular source and signaling pathways leading to IFN-III induction and assessed if and how they impact morbidity. Moreover, we measured the expression and production of IFN-III and IFN-I in nasopharyngeal swabs and BALF of COVID-19 patients. We correlated their levels and the transcriptional responses they elicit along the respiratory tract to disease severity. We also explored the pathways of detection of SARS-CoV-2 by epithelial and immune cells and how this impacts their differential production of specific members of the IFN-I and III families.

In Chapter 4 we tested if the responses elicited by IFN-III upon repair of the lung epithelium could also be observed in the gastrointestinal tract following radiation or DSS-induced injury.

References.

1. Abraham, Clara, and Judy H. Cho. 2009. “Inflammatory Bowel Disease.” *New England Journal of Medicine* 361 (21): 2066–78. https://doi.org/10.1056/NEJMra0804647.
2. Akamatsu, Milena Apetito, Júlia Tavares de Castro, Carolina Yumi Takano, and Paulo Lee Ho. 2021. “Off Balance: Interferons in COVID-19 Lung Infections.” *EBioMedicine* 73 (November). https://doi.org/10.1016/j.ebiom.2021.103642.
3. Andreou, Nicolaos-Panagiotis, Evangelia Legaki, and Maria Gazouli. 2020. “Inflammatory Bowel Disease Pathobiology: The Role of the Interferon Signature.” *Annals of Gastroenterology* 33 (2): 125–33. https://doi.org/10.20524/aog.2020.0457.
4. Ank, Nina, Marie B. Iversen, Christina Bartholdy, Peter Staeheli, Rune Hartmann, Uffe B. Jensen, Frederik Dagnaes-Hansen, et al. 2008. “An Important Role for Type III Interferon (IFN-λ/IL-28) in TLR-Induced Antiviral Activity.” *The Journal of Immunology* 180 (4): 2474–85. https://doi.org/10.4049/jimmunol.180.4.2474.
5. Bastard, Paul, Lindsey B. Rosen, Qian Zhang, Eleftherios Michailidis, Hans-Heinrich Hoffmann, Yu Zhang, Karim Dorgham, et al. 2020. “Autoantibodies against Type I IFNs in Patients with Life-Threatening COVID-19.” *Science (New York, N.Y.)* 370 (6515): eabd4585. https://doi.org/10.1126/science.abd4585.
6. Beer, Julius, Stefania Crotta, Angele Breithaupt, Annette Ohnemus, Jan Becker, Benedikt Sachs, Lisa Kern, et al. 2022. “Impaired Immune Response Drives Age-Dependent Severity of COVID-19.” *Journal of Experimental Medicine* 219 (12): e20220621. https://doi.org/10.1084/jem.20220621.
7. Blanco-Melo, Daniel, Benjamin E. Nilsson-Payant, Wen-Chun Liu, Skyler Uhl, Daisy Hoagland, Rasmus Møller, Tristan X. Jordan, et al. 2020. “Imbalanced Host Response to SARS-CoV-2 Drives Development of COVID-19.” *Cell* 181 (5): 1036-1045.e9. https://doi.org/10.1016/j.cell.2020.04.026.
8. Blumer, Tanja, Mairene Coto-Llerena, Francois H. T. Duong, and Markus H. Heim. 2017. “SOCS1 Is an Inducible Negative Regulator of Interferon λ (IFN-λ)–Induced Gene Expression in Vivo.” *Journal of Biological Chemistry* 292 (43): 17928–38. https://doi.org/10.1074/jbc.M117.788877.

9. Booth, Catherine, Gregory Tudor, Julie Tudor, Barry P. Katz, and Thomas J. MacVittie. 2012. “Acute Gastrointestinal Syndrome in High-Dose Irradiated Mice.” *Health Physics* 103 (4): 383–99. https://doi.org/10.1097/HP.0b013e318266ee13.
10. Broggi, Achille, Yunhao Tan, Francesca Granucci, and Ivan Zanoni. 2017. “IFN-λ Suppresses Intestinal Inflammation by Non-Translational Regulation of Neutrophil Function.” *Nature Immunology* 18 (10): 1084–93. https://doi.org/10.1038/ni.3821.
11. Channappanavar, Rudragouda. 2022. “Interferons in Coronavirus Pathogenesis: The Good, the Bad, and the Ugly.” *Cell Host & Microbe* 30 (4): 427–30. https://doi.org/10.1016/j.chom.2022.03.022.
12. Channappanavar, Rudragouda, Anthony R Fehr, Rahul Vijay, Matthias Mack, Jincun Zhao, David K Meyerholz, and Stanley Perlman. 2016. “Dysregulated Type I Interferon and Inflammatory Monocyte-Macrophage Responses Cause Lethal Pneumonia in SARS-CoV-Infected Mice.” *Cell Host & Microbe* 19 (2): 181–93. https://doi.org/10.1016/j.chom.2016.01.007.
13. Channappanavar, Rudragouda, Anthony R. Fehr, Jian Zheng, Christine Wohlford-Lenane, Juan E. Abrahante, Matthias Mack, Ramakrishna Sompallae, Paul B. McCray, David K. Meyerholz, and Stanley Perlman. 2019. “IFN-I Response Timing Relative to Virus Replication Determines MERS Coronavirus Infection Outcomes.” *The Journal of Clinical Investigation* 129 (9): 3625–39. https://doi.org/10.1172/JCI126363.
14. Chawla-Sarkar, M, D J Lindner, and Ernest C. Borden. 2003. “Apoptosis and Interferons: Role of Interferon-Stimulated Genes as Mediators of Apoptosis.” *Apoptosis*, 13.
15. Chen, Y. Grace, and Sun Hur. 2022. “Cellular Origins of DsRNA, Their Recognition and Consequences.” *Nature Reviews. Molecular Cell Biology* 23 (4): 286–301. https://doi.org/10.1038/s41580-021-00430-1.
16. Chiriac, Mircea T., Barbara Buchen, Alexandra Wandersee, Gheorghe Hundorfean, Claudia Günther, Yvonne Bourjau, Sean E. Doyle, et al. 2017. “Activation of Epithelial Signal Transducer and Activator of Transcription 1 by Interleukin 28 Controls Mucosal Healing in Mice With Colitis and Is Increased in Mucosa of Patients With Inflammatory Bowel Disease.”

Gastroenterology 153 (1): 123-138.e8. https://doi.org/10.1053/j.gastro.2017.03.015.

17. Chong, Zhenlu, Courtney E. Karl, Peter J. Halfmann, Yoshihiro Kawaoka, Emma S. Winkler, Shamus P. Keeler, Michael J. Holtzman, Jinsheng Yu, and Michael S. Diamond. 2022. "Nasally Delivered Interferon-λ Protects Mice against Infection by SARS-CoV-2 Variants Including Omicron." *Cell Reports* 39 (6): 110799. https://doi.org/10.1016/j.celrep.2022.110799.
18. Crotta, Stefania, Sophia Davidson, Tanel Mahlakoiv, Christophe J. Desmet, Matthew R. Buckwalter, Matthew L. Albert, Peter Staeheli, and Andreas Wack. 2013. "Type I and Type III Interferons Drive Redundant Amplification Loops to Induce a Transcriptional Signature in Influenza-Infected Airway Epithelia." *PLoS Pathogens* 9 (11): e1003773. https://doi.org/10.1371/journal.ppat.1003773.
19. Davidson, Sophia, Stefania Crotta, Teresa M. McCabe, and Andreas Wack. 2014. "Pathogenic Potential of Interferon Aβ in Acute Influenza Infection." *Nature Communications* 5 (1): 3864. https://doi.org/10.1038/ncomms4864.
20. Davidson, Sophia, Teresa M. McCabe, Stefania Crotta, Hans Henrik Gad, Edith M. Hessel, Soren Beinke, Rune Hartmann, and Andreas Wack. 2016. "IFN λ Is a Potent Anti-influenza Therapeutic without the Inflammatory Side Effects of IFN α Treatment." *EMBO Molecular Medicine* 8 (9): 1099–1112. https://doi.org/10.15252/emmm.201606413.
21. Dinnon, Kenneth H., Sarah R. Leist, Alexandra Schäfer, Caitlin E. Edwards, David R. Martinez, Stephanie A. Montgomery, Ande West, et al. 2020. "A Mouse-Adapted Model of SARS-CoV-2 to Test COVID-19 Countermeasures." *Nature* 586 (7830): 560–66. https://doi.org/10.1038/s41586-020-2708-8.
22. Durbin, Russell K., Sergei V. Kotenko, and Joan E. Durbin. 2013. "Interferon Induction and Function at the Mucosal Surface." *Immunological Reviews* 255 (1): 25–39. https://doi.org/10.1111/imr.12101.
23. Egli, Adrian, Deanna M Santer, Daire O'Shea, D Lorne Tyrrell, and Michael Houghton. 2014. "The Impact of the Interferon-Lambda Family on the Innate and Adaptive Immune Response to Viral

Infections." *Emerging Microbes & Infections* 3 (1): 1–12. https://doi.org/10.1038/emi.2014.51.

24. Feld, Jordan J., Christopher Kandel, Mia J. Biondi, Robert A. Kozak, Muhammad Atif Zahoor, Camille Lemieux, Sergio M. Borgia, et al. 2021. "Peginterferon Lambda for the Treatment of Outpatients with COVID-19: A Phase 2, Placebo-Controlled Randomised Trial." *The Lancet Respiratory Medicine* 9 (5): 498–510. https://doi.org/10.1016/S2213-2600(20)30566-X.
25. Forero, Adriana, Snehal Ozarkar, Hongchuan Li, Chia Heng Lee, Emily A. Hemann, Marija S. Nadjsombati, Matthew R. Hendricks, et al. 2019. "Differential Activation of the Transcription Factor IRF1 Underlies the Distinct Immune Responses Elicited by Type I and Type III Interferons." *Immunity* 51 (3): 451-464.e6. https://doi.org/10.1016/j.immuni.2019.07.007.
26. Frieman, Matthew B., Jun Chen, Thomas E. Morrison, Alan Whitmore, William Funkhouser, Jerrold M. Ward, Elaine W. Lamirande, et al. 2010. "SARS-CoV Pathogenesis Is Regulated by a STAT1 Dependent but a Type I, II and III Interferon Receptor Independent Mechanism." *PLoS Pathogens* 6 (4): e1000849. https://doi.org/10.1371/journal.ppat.1000849.
27. Fuchs, Sebastian, Petra Kaiser-Labusch, Julia Bank, Sandra Ammann, Anja Kolb-Kokocinski, Christine Edelbusch, Heymut Omran, and Stephan Ehl. 2016. "Tyrosine Kinase 2 Is Not Limiting Human Antiviral Type III Interferon Responses." *European Journal of Immunology* 46 (11): 2639–49. https://doi.org/10.1002/eji.201646519.
28. Galani, Nikoletta Rovina, Vicky Lampropoulou, Vasiliki Triantafyllia, Maria Manioudaki, Eleftherios Pavlos, Evangelia Koukaki, et al. 2021. "Untuned Antiviral Immunity in COVID-19 Revealed by Temporal Type I/III Interferon Patterns and Flu Comparison." *Nature Immunology* 22 (1): 32–40. https://doi.org/10.1038/s41590-020-00840-x.
29. Galani, Vasiliki Triantafyllia, Evridiki Evangelia Eleminiadou, Ourania Koltsida, Athanasios Stavropoulos, Maria Manioudaki, Dimitris Thanos, et al. 2017. "Interferon-λ Mediates Non-Redundant Front-Line Antiviral Protection against Influenza Virus Infection without Compromising Host Fitness." *Immunity*

46 (5): 875-890.e6. https://doi.org/10.1016/j.immuni.2017.04.025.
30. García-Sastre, Adolfo. 2011. “Induction and Evasion of Type I Interferon Responses by Influenza Viruses.” *Virus Research* 162 (0): 12–18. https://doi.org/10.1016/j.virusres.2011.10.017.
31. Groen, Rik A. de, Zwier M. A. Groothuismink, Bi-Sheng Liu, and André Boonstra. 2015. “IFN-λ Is Able to Augment TLR-Mediated Activation and Subsequent Function of Primary Human B Cells.” *Journal of Leukocyte Biology* 98 (4): 623–30. https://doi.org/10.1189/jlb.3A0215-041RR.
32. Günther, Claudia, Barbara Ruder, Iris Stolzer, Heidrun Dorner, Gui-Wei He, Mircea Teodor Chiriac, Konrad Aden, et al. 2019. “Interferon Lambda Promotes Paneth Cell Death Via STAT1 Signaling in Mice and Is Increased in Inflamed Ileal Tissues of Patients With Crohn’s Disease.” *Gastroenterology* 157 (5): 1310-1322.e13. https://doi.org/10.1053/j.gastro.2019.07.031.
33. Hadjadj, Jérôme, Nader Yatim, Laura Barnabei, Aurélien Corneau, Jeremy Boussier, Nikaïa Smith, Hélène Péré, et al. 2020. “Impaired Type I Interferon Activity and Inflammatory Responses in Severe COVID-19 Patients.” *Science (New York, N.Y.)* 369 (6504): 718–24. https://doi.org/10.1126/science.abc6027.
34. Halfmann, Peter J., Shun Iida, Kiyoko Iwatsuki-Horimoto, Tadashi Maemura, Maki Kiso, Suzanne M. Scheaffer, Tamarand L. Darling, et al. 2022. “SARS-CoV-2 Omicron Virus Causes Attenuated Disease in Mice and Hamsters.” *Nature* 603 (7902): 687–92. https://doi.org/10.1038/s41586-022-04441-6.
35. Hemann, Emily A., Michael Gale, and Ram Savan. 2017. “Interferon Lambda Genetics and Biology in Regulation of Viral Control.” *Frontiers in Immunology* 8 (DEC). https://doi.org/10.3389/fimmu.2017.01707.
36. Hemann, Emily A., Richard Green, J. Bryan Turnbull, Ryan A. Langlois, Ram Savan, and Michael Gale. 2019. “Interferon-λ Modulates Dendritic Cells to Facilitate T Cell Immunity during Infection with Influenza A Virus.” *Nature Immunology* 20 (8): 1035–45. https://doi.org/10.1038/s41590-019-0408-z.
37. Högner, Katrin, Thorsten Wolff, Stephan Pleschka, Stephanie Plog, Achim D. Gruber, Ulrich Kalinke, Hans-Dieter Walmrath, et

al. 2013a. “Macrophage-Expressed IFN-β Contributes to Apoptotic Alveolar Epithelial Cell Injury in Severe Influenza Virus Pneumonia.” *PLoS Pathogens* 9 (2): e1003188. https://doi.org/10.1371/journal.ppat.1003188.

38. ———. 2013b. “Macrophage-Expressed IFN-β Contributes to Apoptotic Alveolar Epithelial Cell Injury in Severe Influenza Virus Pneumonia.” *PLoS Pathogens* 9 (2): e1003188. https://doi.org/10.1371/journal.ppat.1003188.
39. Isaacs, and J. Lindenmann. 1957. “Virus Interference. I. The Interferon.” *Journal of Interferon Research* 7 (5): 429–38. https://doi.org/10.1089/jir.1987.7.429.
40. Isaacs, J. Lindenmann, R. C. Valentine, and Christopher Howard Andrewes. 1957. “Virus Interference. II. Some Properties of Interferon.” *Proceedings of the Royal Society of London. Series B - Biological Sciences* 147 (927): 268–73. https://doi.org/10.1098/rspb.1957.0049.
41. Israelow, Benjamin, Eric Song, Tianyang Mao, Peiwen Lu, Amit Meir, Feimei Liu, Mia Madel Alfajaro, et al. 2020. “Mouse Model of SARS-CoV-2 Reveals Inflammatory Role of Type I Interferon Signaling.” *Journal of Experimental Medicine* 217 (12): e20201241. https://doi.org/10.1084/jem.20201241.
42. Ivashkiv, Lionel B., and Laura T. Donlin. 2014. “Regulation of Type I Interferon Responses.” *Nature Reviews Immunology* 14 (1): 36–49. https://doi.org/10.1038/nri3581.
43. Iwasaki, Akiko, and Padmini S. Pillai. 2014. “Innate Immunity to Influenza Virus Infection.” *Nature Reviews Immunology* 14 (5): 315–28. https://doi.org/10.1038/nri3665.
44. Jagannathan, Prasanna, Jason R. Andrews, Hector Bonilla, Haley Hedlin, Karen B. Jacobson, Vidhya Balasubramanian, Natasha Purington, et al. 2021. “Peginterferon Lambda-1a for Treatment of Outpatients with Uncomplicated COVID-19: A Randomized Placebo-Controlled Trial.” *Nature Communications* 12 (1): 1967. https://doi.org/10.1038/s41467-021-22177-1.
45. Jaks, Eva, Martynas Gavutis, Gilles Uzé, Jacques Martal, and Jacob Piehler. 2007. “Differential Receptor Subunit Affinities of Type I Interferons Govern Differential Signal Activation.” *Journal of Molecular Biology* 366 (2): 525–39. https://doi.org/10.1016/j.jmb.2006.11.053.

46. Jensen, Søren, and Allan Randrup Thomsen. 2012. “Sensing of RNA Viruses: A Review of Innate Immune Receptors Involved in Recognizing RNA Virus Invasion.” *Journal of Virology* 86 (6): 2900–2910. https://doi.org/10.1128/JVI.05738-11.
47. Jewell, Nancy A., Troy Cline, Sara E. Mertz, Sergey V. Smirnov, Emilio Flaño, Christian Schindler, Jessica L. Grieves, Russell K. Durbin, Sergei V. Kotenko, and Joan E. Durbin. 2010. “Lambda Interferon Is the Predominant Interferon Induced by Influenza A Virus Infection in Vivo.” *Journal of Virology* 84 (21): 11515–22. https://doi.org/10.1128/JVI.01703-09.
48. Jhuti, Diya, Angeli Rawat, Christina M. Guo, Lindsay A. Wilson, Edward J. Mills, and Jamie I. Forrest. 2022. “Interferon Treatments for SARS-CoV-2: Challenges and Opportunities.” *Infectious Diseases and Therapy* 11 (3): 953–72. https://doi.org/10.1007/s40121-022-00633-9.
49. Jilg, Nikolaus, Wenyu Lin, Jian Hong, Esperance A. Schaefer, David Wolski, James Meixong, Kaku Goto, et al. 2014. “Kinetic Differences in the Induction of Interferon Stimulated Genes by Interferon-α and Interleukin 28B Are Altered by Infection with Hepatitis C Virus.” *Hepatology* 59 (4): 1250–61. https://doi.org/10.1002/hep.26653.
50. Jostins, Luke, Stephan Ripke, Rinse K. Weersma, Richard H. Duerr, Dermot P. McGovern, Ken Y. Hui, James C. Lee, et al. 2012. “Host-Microbe Interactions Have Shaped the Genetic Architecture of Inflammatory Bowel Disease.” *Nature* 491 (7422): 119–24. https://doi.org/10.1038/nature11582.
51. Kagan, Jonathan C., and Ruslan Medzhitov. 2006. “Phosphoinositide-Mediated Adaptor Recruitment Controls Toll-like Receptor Signaling.” *Cell* 125 (5): 943–55. https://doi.org/10.1016/j.cell.2006.03.047.
52. Kagan, Jonathan C., Tian Su, Tiffany Horng, Amy Chow, Shizuo Akira, and Ruslan Medzhitov. 2008. “TRAM Couples Endocytosis of Toll-like Receptor 4 to the Induction of Interferon-β.” *Nature Immunology* 9 (4): 361–68. https://doi.org/10.1038/ni1569.
53. Katakura, Kyoko, Jongdae Lee, Daniel Rachmilewitz, Gloria Li, Lars Eckmann, and Eyal Raz. 2005. “Toll-like Receptor 9–Induced Type I IFN Protects Mice from Experimental Colitis.” *The Journal*

of Clinical Investigation 115 (3): 695–702. https://doi.org/10.1172/JCI22996.

54. Kawai, Taro, and Shizuo Akira. 2006. "Innate Immune Recognition of Viral Infection." *Nature Immunology* 7 (2): 131–37. https://doi.org/10.1038/ni1303.
55. Kiesler, Patricia, Ivan J. Fuss, and Warren Strober. 2015. "Experimental Models of Inflammatory Bowel Diseases." *Cellular and Molecular Gastroenterology and Hepatology* 1 (2): 154–70. https://doi.org/10.1016/j.jcmgh.2015.01.006.
56. Kim, Chang-Kyung, Vincent W. Yang, and Agnieszka B. Bialkowska. 2017. "The Role of Intestinal Stem Cells in Epithelial Regeneration Following Radiation-Induced Gut Injury." *Current Stem Cell Reports* 3 (4): 320–32. https://doi.org/10.1007/s40778-017-0103-7.
57. Kirsch, David G., Philip M. Santiago, Emmanuelle di Tomaso, Julie M. Sullivan, Wu-Shiun Hou, Talya Dayton, Laura B. Jeffords, et al. 2010. "P53 Controls Radiation-Induced Gastrointestinal Syndrome in Mice Independent of Apoptosis." *Science* 327 (5965): 593–96. https://doi.org/10.1126/science.1166202.
58. Klinkhammer, Jonas, Daniel Schnepf, Liang Ye, Marilena Schwaderlapp, Hans Henrik Gad, Rune Hartmann, Dominique Garcin, Tanel Mahlakõiv, and Peter Staeheli. 2018. "IFN-λ Prevents Influenza Virus Spread from the Upper Airways to the Lungs and Limits Virus Transmission." Edited by Viviana Simon. *ELife* 7 (April): e33354. https://doi.org/10.7554/eLife.33354.
59. Koltsida, Ourania, Michael Hausding, Athanasios Stavropoulos, Sonja Koch, George Tzelepis, Caroline Übel, Sergei V. Kotenko, et al. 2011. "IL-28A (IFN-Λ2) Modulates Lung DC Function to Promote Th1 Immune Skewing and Suppress Allergic Airway Disease." *EMBO Molecular Medicine* 3 (6): 348–61. https://doi.org/10.1002/emmm.201100142.
60. Kotenko, Sergei V., Grant Gallagher, Vitaliy V. Baurin, Anita Lewis-Antes, Meiling Shen, Nital K. Shah, Jerome A. Langer, Faruk Sheikh, Harold Dickensheets, and Raymond P. Donnelly. 2003. "IFN-Lambdas Mediate Antiviral Protection through a Distinct Class II Cytokine Receptor Complex." *Nature Immunology* 4 (1): 69–77. https://doi.org/10.1038/ni875.

61. Kudva, Anupa, Erich V. Scheller, Keven M. Robinson, Chris R. Crowe, Sun Mi Choi, Samantha R. Slight, Shabaana A. Khader, et al. 2011. “Influenza A Inhibits Th17-Mediated Host Defense against Bacterial Pneumonia in Mice.” *The Journal of Immunology* 186 (3): 1666–74. https://doi.org/10.4049/jimmunol.1002194.
62. Lazear, Helen M., John W. Schoggins, and Michael S. Diamond. 2019. “Shared and Distinct Functions of Type I and Type III Interferons.” *Immunity* 50 (4): 907–23. https://doi.org/10.1016/j.immuni.2019.03.025.
63. Lee, Jeong Seok, Seongwan Park, Hye Won Jeong, Jin Young Ahn, Seong Jin Choi, Hoyoung Lee, Baekgyu Choi, et al. 2020. “Immunophenotyping of COVID-19 and Influenza Highlights the Role of Type I Interferons in Development of Severe COVID-19.” *Science Immunology* 5 (49): eabd1554. https://doi.org/10.1126/sciimmunol.abd1554.
64. Lee, Se-Jung, Wun-Jae Kim, and Sung-Kwon Moon. 2012. “Role of the P38 MAPK Signaling Pathway in Mediating Interleukin-28A-Induced Migration of UMUC-3 Cells.” *International Journal of Molecular Medicine* 30 (4): 945–52. https://doi.org/10.3892/ijmm.2012.1064.
65. Lei, Xiaobo, Xiaojing Dong, Ruiyi Ma, Wenjing Wang, Xia Xiao, Zhongqin Tian, Conghui Wang, et al. 2020. “Activation and Evasion of Type I Interferon Responses by SARS-CoV-2.” *Nature Communications* 11 (1): 3810. https://doi.org/10.1038/s41467-020-17665-9.
66. Leibowitz, Brian J., Guangyi Zhao, Liang Wei, Hang Ruan, Michael Epperly, Lujia Chen, Xinghua Lu, Joel S. Greenberger, Lin Zhang, and Jian Yu. 2021. “Interferon b Drives Intestinal Regeneration after Radiation.” *Science Advances* 7 (41): eabi5253. https://doi.org/10.1126/sciadv.abi5253.
67. Li, W., A. Lewis-Antes, J. Huang, M. Balan, and S. V. Kotenko. 2008. “Regulation of Apoptosis by Type III Interferons.” *Cell Proliferation* 41 (6): 960–79. https://doi.org/10.1111/j.1365-2184.2008.00558.x.
68. Lin, Jian-Da, Ningguo Feng, Adrish Sen, Murugabaskar Balan, Hsiang-Chi Tseng, Constance McElrath, Sergey V. Smirnov, et al. 2016. “Distinct Roles of Type I and Type III Interferons in

Intestinal Immunity to Homologous and Heterologous Rotavirus Infections." *PLOS Pathogens* 12 (4): e1005600. https://doi.org/10.1371/journal.ppat.1005600.

69. Liu, Shan Chen, Yujuan Guan, and Limin Chen. 2015. "Type III Interferon Induces Distinct SOCS1 Expression Pattern That Contributes to Delayed but Prolonged Activation of Jak/STAT Signaling Pathway: Implications for Treatment Non-Response in HCV Patients." *PLOS ONE* 10 (7): e0133800. https://doi.org/10.1371/journal.pone.0133800.
70. Liu, Jimmy Z., Suzanne van Sommeren, Hailiang Huang, Siew C. Ng, Rudi Alberts, Atsushi Takahashi, Stephan Ripke, et al. 2015. "Association Analyses Identify 38 Susceptibility Loci for Inflammatory Bowel Disease and Highlight Shared Genetic Risk across Populations." *Nature Genetics* 47 (9): 979–86. https://doi.org/10.1038/ng.3359.
71. Liu, Lin, Istvan Botos, Yan Wang, Joshua N. Leonard, Joseph Shiloach, David M. Segal, and David R. Davies. 2008. "Structural Basis of Toll-Like Receptor 3 Signaling with Double-Stranded RNA." *Science* 320 (5874): 379–81. https://doi.org/10.1126/science.1155406.
72. Loo, Yueh-Ming, and Michael Gale. 2011. "Immune Signaling by RIG-I-like Receptors." *Immunity* 34 (5): 680–92. https://doi.org/10.1016/j.immuni.2011.05.003.
73. Lopez, Jonathan, Marine Mommert, William Mouton, Andrés Pizzorno, Karen Brengel-Pesce, Mehdi Mezidi, Marine Villard, et al. 2021. "Early Nasal Type I IFN Immunity against SARS-CoV-2 Is Compromised in Patients with Autoantibodies against Type I IFNs." *The Journal of Experimental Medicine* 218 (10): e20211211. https://doi.org/10.1084/jem.20211211.
74. Lucas, Carolina, Patrick Wong, Jon Klein, Tiago B. R. Castro, Julio Silva, Maria Sundaram, Mallory K. Ellingson, et al. 2020. "Longitudinal Analyses Reveal Immunological Misfiring in Severe COVID-19." *Nature* 584 (7821): 463–69. https://doi.org/10.1038/s41586-020-2588-y.
75. Madsen, S. M., P. Schlichting, B. Davidsen, O. H. Nielsen, B. Federspiel, P. Riis, and P. Munkholm. 2001. "An Open-Labeled, Randomized Study Comparing Systemic Interferon-Alpha-2A and Prednisolone Enemas in the Treatment of Left-Sided Ulcerative

Colitis." *The American Journal of Gastroenterology* 96 (6): 1807–15. https://doi.org/10.1111/j.1572-0241.2001.03875.x.

76. Maher, Stephen G., Faruk Sheikh, Anthony J. Scarzello, Ana L. Romero-Weaver, Darren P. Baker, Raymond P. Donnelly, and Ana M. Gamero. 2008. "IFN-α and IFN-λ Differ in Their Antiproliferative Effects and Duration of JAK/STAT Signaling Activity." *Cancer Biology & Therapy* 7 (7): 1109–15. https://doi.org/10.4161/cbt.7.7.6192.
77. Mahlakõiv, Tanel, Pedro Hernandez, Konrad Gronke, Andreas Diefenbach, and Peter Staeheli. 2015. "Leukocyte-Derived IFN-α/β and Epithelial IFN-λ Constitute a Compartmentalized Mucosal Defense System That Restricts Enteric Virus Infections." *PLOS Pathogens* 11 (4): e1004782. https://doi.org/10.1371/journal.ppat.1004782.
78. Mahlakõiv, Tanel, Daniel Ritz, Markus Mordstein, Marta L. DeDiego, Luis Enjuanes, Marcel A. Müller, Christian Drosten, and Peter Staeheli. 2012. "Combined Action of Type I and Type III Interferon Restricts Initial Replication of Severe Acute Respiratory Syndrome Coronavirus in the Lung but Fails to Inhibit Systemic Virus Spread." *Journal of General Virology* 93 (12): 2601–5. https://doi.org/10.1099/vir.0.046284-0.
79. Major, Jack, Stefania Crotta, Miriam Llorian, Teresa M. McCabe, Hans Henrik Gad, Simon L. Priestnall, Rune Hartmann, and Andreas Wack. 2020. "Type I and III Interferons Disrupt Lung Epithelial Repair during Recovery from Viral Infection." *Science* 369 (6504): 712–17. https://doi.org/10.1126/science.abc2061.
80. Malakhova, Oxana A., Keun Kim, Jiann-Kae Luo, and Dong Er Zhang. 2006. "UBP43 Is a Novel Regulator of Interferon Signaling Independent of Its ISG15 Isopeptidase Activity." *The EMBO Journal*. https://doi.org/10.1038/sj.emboj.7601149.
81. Maloy, Kevin J., and Fiona Powrie. 2011. "Intestinal Homeostasis and Its Breakdown in Inflammatory Bowel Disease." *Nature* 474 (7351): 298–306. https://doi.org/10.1038/nature10208.
82. Marcello, Tobias, Arash Grakoui, Giovanna Barba–Spaeth, Erica S. Machlin, Sergei V. Kotenko, Margaret R. Macdonald, and Charles M. Rice. 2006. "Interferons α and λ Inhibit Hepatitis C Virus Replication With Distinct Signal Transduction and Gene

Regulation Kinetics." *Gastroenterology* 131 (6): 1887–98. https://doi.org/10.1053/j.gastro.2006.09.052.

83. McElrath, Constance, Vanessa Espinosa, Jian-Da Lin, Jianya Peng, Raghavendra Sridhar, Orchi Dutta, Hsiang-Chi Tseng, et al. 2021. "Critical Role of Interferons in Gastrointestinal Injury Repair." *Nature Communications* 12 (1): 2624. https://doi.org/10.1038/s41467-021-22928-0.
84. McNab, Finlay, Katrin Mayer-Barber, Alan Sher, Andreas Wack, and Anne O'Garra. 2015. "Type I Interferons in Infectious Disease." *Nature Reviews Immunology* 15 (2): 87–103. https://doi.org/10.1038/nri3787.
85. Megjugorac, Nicholas J., Grant E. Gallagher, and Grant Gallagher. 2009. "Modulation of Human Plasmacytoid DC Function by IFN-Λ1 (IL-29)." *Journal of Leukocyte Biology* 86 (6): 1359–63. https://doi.org/10.1189/jlb.0509347.
86. Mick, Eran, Jack Kamm, Angela Oliveira Pisco, Kalani Ratnasiri, Jennifer M. Babik, Gloria Castañeda, Joseph L. DeRisi, et al. 2020. "Upper Airway Gene Expression Reveals Suppressed Immune Responses to SARS-CoV-2 Compared with Other Respiratory Viruses." *Nature Communications* 11 (1): 5854. https://doi.org/10.1038/s41467-020-19587-y.
87. Moraga, Ignacio, Daniel Harari, Gideon Schreiber, Gilles Uzé, and Sandra Pellegrini. 2009. "Receptor Density Is Key to the Alpha2/Beta Interferon Differential Activities." *Molecular and Cellular Biology* 29 (17): 4778–87. https://doi.org/10.1128/MCB.01808-08.
88. Mordstein, Markus, Georg Kochs, Laure Dumoutier, Jean-Christophe Renauld, Søren R. Paludan, Kevin Klucher, and Peter Staeheli. 2008. "Interferon-λ Contributes to Innate Immunity of Mice against Influenza A Virus but Not against Hepatotropic Viruses." *PLOS Pathogens* 4 (9): e1000151. https://doi.org/10.1371/journal.ppat.1000151.
89. Mordstein, Markus, Eva Neugebauer, Vanessa Ditt, Birthe Jessen, Toni Rieger, Valeria Falcone, Frederic Sorgeloos, et al. 2010. "Lambda Interferon Renders Epithelial Cells of the Respiratory and Gastrointestinal Tracts Resistant to Viral Infections." *Journal of Virology* 84 (11): 5670–77. https://doi.org/10.1128/JVI.00272-10.

90. Moynagh, Paul N. 2005. “TLR Signalling and Activation of IRFs: Revisiting Old Friends from the NF-KB Pathway.” *Trends in Immunology* 26 (9): 469–76. https://doi.org/10.1016/j.it.2005.06.009.
91. Muñoz-Fontela, César, William E. Dowling, Simon G. P. Funnell, Pierre-S. Gsell, A. Ximena Riveros-Balta, Randy A. Albrecht, Hanne Andersen, et al. 2020. “Animal Models for COVID-19.” *Nature* 586 (7830): 509–15. https://doi.org/10.1038/s41586-020-2787-6.
92. Musch, E., T. Andus, M. Malek, A. Chrissafidou, and M. Schulz. 2007. “Successful Treatment of Steroid Refractory Active Ulcerative Colitis with Natural Interferon-β - an Open Long-Term Trial.” *Zeitschrift Für Gastroenterologie* 45 (12): 1235–40. https://doi.org/10.1055/s-2007-963378.
93. Musch, Eugen, Tilo Andus, Wolfgang Kruis, Andreas Raedler, Martina Spehlmann, Stefan Schreiber, Bernd Krakamp, et al. 2005. “Interferon-Beta-1a for the Treatment of Steroid-Refractory Ulcerative Colitis: A Randomized, Double-Blind, Placebo-Controlled Trial.” *Clinical Gastroenterology and Hepatology: The Official Clinical Practice Journal of the American Gastroenterological Association* 3 (6): 581–86. https://doi.org/10.1016/s1542-3565(05)00208-9.
94. Nell, Sandra, Sebastian Suerbaum, and Christine Josenhans. 2010. “The Impact of the Microbiota on the Pathogenesis of IBD: Lessons from Mouse Infection Models.” *Nature Reviews. Microbiology* 8 (8): 564–77. https://doi.org/10.1038/nrmicro2403.
95. Ng, Dianna L., Andrea C. Granados, Yale A. Santos, Venice Servellita, Gregory M. Goldgof, Cem Meydan, Alicia Sotomayor-Gonzalez, et al. 2021. “A Diagnostic Host Response Biosignature for COVID-19 from RNA Profiling of Nasal Swabs and Blood.” *Science Advances* 7 (6): eabe5984. https://doi.org/10.1126/sciadv.abe5984.
96. Nikolaus, S, P Rutgeerts, R Fedorak, A H Steinhart, G E Wild, D Theuer, J Möhrle, and S Schreiber. 2003. “Interferon β-1a in Ulcerative Colitis: A Placebo Controlled, Randomised, Dose Escalating Study.” *Gut* 52 (9): 1286–90.

97. Odendall, Charlotte, Evelyn Dixit, Fabrizia Stavru, Helene Bierne, Kate M. Franz, Ann Fiegen Durbin, Steeve Boulant, Lee Gehrke, Pascale Cossart, and Jonathan C. Kagan. 2014. “Diverse Intracellular Pathogens Activate Type III Interferon Expression from Peroxisomes.” *Nature Immunology* 15 (8): 717–26. https://doi.org/10.1038/ni.2915.
98. Odendall, Charlotte, Andrew A. Voak, and Jonathan C. Kagan. 2017. “Type III IFNs Are Commonly Induced by Bacteria-Sensing TLRs and Reinforce Epithelial Barriers during Infection.” *The Journal of Immunology* 199 (9): 3270–79. https://doi.org/10.4049/jimmunol.1700250.
99. Onoguchi, Kazuhide, Mitsutoshi Yoneyama, Azumi Takemura, Shizuo Akira, Tadatsugu Taniguchi, Hideo Namiki, and Takashi Fujita. 2007. “Viral Infections Activate Types I and III Interferon Genes through a Common Mechanism.” *Journal of Biological Chemistry* 282 (10): 7576–81. https://doi.org/10.1074/jbc.M608618200.
100. Osterlund, Pamela I., Taija E. Pietilä, Ville Veckman, Sergei V. Kotenko, and Ilkka Julkunen. 2007. “IFN Regulatory Factor Family Members Differentially Regulate the Expression of Type III IFN (IFN-Lambda) Genes.” *Journal of Immunology (Baltimore, Md.: 1950)* 179 (6): 3434–42. https://doi.org/10.4049/jimmunol.179.6.3434.
101. Park, Annsea, and Akiko Iwasaki. 2020. “Type I and Type III Interferons – Induction, Signaling, Evasion, and Application to Combat COVID-19.” *Cell Host & Microbe* 27 (6): 870–78. https://doi.org/10.1016/j.chom.2020.05.008.
102. Parker, Belinda S., Jai Rautela, and Paul J. Hertzog. 2016. “Antitumour Actions of Interferons: Implications for Cancer Therapy.” *Nature Reviews Cancer* 16 (3): 131–44. https://doi.org/10.1038/nrc.2016.14.
103. Pena Rossi, Claudia, Stephen B. Hanauer, Ratko Tomasevic, John O. Hunter, Ira Shafran, and Hans Graffner. 2009. “Interferon Beta-1a for the Maintenance of Remission in Patients with Crohn’s Disease: Results of a Phase II Dose-Finding Study.” *BMC Gastroenterology* 9 (March): 22. https://doi.org/10.1186/1471-230X-9-22.

104. Pena-Rossi, C., S. Schreiber, G. Golubovic, A. Mertz-Nielsen, J. Panes, D. Rachmilewitz, M. J. Shieh, V. I. Simanenkov, D. Stanton, and H. Graffner. 2008. "Clinical Trial: A Multicentre, Randomized, Double-Blind, Placebo-Controlled, Dose-Finding, Phase II Study of Subcutaneous Interferon-Beta-La in Moderately Active Ulcerative Colitis." *Alimentary Pharmacology & Therapeutics* 28 (6): 758–67. https://doi.org/10.1111/j.1365-2036.2008.03778.x.
105. Pestka, Sidney, Christopher D. Krause, and Mark R. Walter. 2004. "Interferons, Interferon-like Cytokines, and Their Receptors." *Immunological Reviews* 202 (1): 8–32. https://doi.org/10.1111/j.0105-2896.2004.00204.x.
106. Pestka, Sidney, and Jerome A. Langer. 1987. "Interferons and Their Actions." *Annual Review of Biochemistry*. https://www-annualreviews-org.unimib.idm.oclc.org/doi/pdf/10.1146/annurev.bi.56.070187.003455.
107. Piganis, Rebecca A. R., Nicole A. De Weerd, Jodee A. Gould, Christian W. Schindler, Ashley Mansell, Sandra E. Nicholson, and Paul J. Hertzog. 2011. "Suppressor of Cytokine Signaling (SOCS) 1 Inhibits Type I Interferon (IFN) Signaling via the Interferon α Receptor (IFNAR1)-Associated Tyrosine Kinase Tyk2 *." *Journal of Biological Chemistry* 286 (39): 33811–18. https://doi.org/10.1074/jbc.M111.270207.
108. Pires, Sílvia, and Dane Parker. 2018. *IL-1β Activation in Response to Staphylococcus Aureus Lung Infection Requires Inflammasome-Dependent and Independent Mechanisms*. *European Journal of Immunology*. Vol. 48. https://doi.org/10.1002/eji.201847556.
109. Planet, Paul J., Dane Parker, Taylor S. Cohen, Hannah Smith, Justinne D. Leon, Chanelle Ryan, Tobin J. Hammer, Noah Fierer, Emily I. Chen, and Alice S. Prince. 2016. "Lambda Interferon Restructures the Nasal Microbiome and Increases Susceptibility to Staphylococcus Aureus Superinfection." *MBio* 7 (1): 1–12. https://doi.org/10.1128/mBio.01939-15.
110. Pott, Johanna, Tanel Mahlakõiv, Markus Mordstein, Claudia U. Duerr, Thomas Michiels, Silvia Stockinger, Peter Staeheli, and Mathias W. Hornef. 2011. "IFN-Lambda Determines the

Intestinal Epithelial Antiviral Host Defense." *Proceedings of the National Academy of Sciences of the United States of America* 108 (19): 7944–49. https://doi.org/10.1073/pnas.1100552108.

111. Prokunina-Olsson, Ludmila, Brian Muchmore, Wei Tang, Ruth M. Pfeiffer, Heiyoung Park, Harold Dickensheets, Dianna Hergott, et al. 2013. "A Variant Upstream of IFNL3 (IL28B) Creating a New Interferon Gene IFNL4 Is Associated with Impaired Clearance of Hepatitis C Virus." *Nature Genetics* 45 (2): 164–71. https://doi.org/10.1038/ng.2521.
112. Rauch, Isabella, Eva Hainzl, Felix Rosebrock, Susanne Heider, Clarissa Schwab, David Berry, Dagmar Stoiber, et al. 2014. "Type I Interferons Have Opposing Effects during the Emergence and Recovery Phases of Colitis." *European Journal of Immunology* 44 (9): 2749–60. https://doi.org/10.1002/eji.201344401.
113. Rauch, Isabella, Felix Rosebrock, Eva Hainzl, Susanne Heider, Andrea Majoros, Sebastian Wienerroither, Birgit Strobl, et al. 2015. "Noncanonical Effects of IRF9 in Intestinal Inflammation: More than Type I and Type III Interferons." *Molecular and Cellular Biology* 35 (13): 2332–43. https://doi.org/10.1128/MCB.01498-14.
114. Rehwinkel, Jan, and Michaela U. Gack. 2020. "RIG-I-like Receptors: Their Regulation and Roles in RNA Sensing." *Nature Reviews Immunology* 20 (9): 537–51. https://doi.org/10.1038/s41577-020-0288-3.
115. Reis, L. F., H. Ruffner, G. Stark, M. Aguet, and C. Weissmann. 1994. "Mice Devoid of Interferon Regulatory Factor 1 (IRF-1) Show Normal Expression of Type I Interferon Genes." *The EMBO Journal* 13 (20): 4798–4806. https://doi.org/10.1002/j.1460-2075.1994.tb06805.x.
116. Schoenborn, Jamie R., and Christopher B. Wilson. 2007. "Regulation of Interferon-γ During Innate and Adaptive Immune Responses." In *Advances in Immunology*, 96:41–101. Elsevier. https://doi.org/10.1016/S0065-2776(07)96002-2.
117. Schott, Eckart, Friedemann Paul, Jens T Wuerfel, Frauke Zipp, Birgit Rudolph, Bertram Wiedenmann, and Daniel C Baumgart. 2007. "Development of Ulcerative Colitis in a Patient with Multiple Sclerosis Following Treatment with Interferonβ 1a."

World Journal of Gastroenterology : WJG 13 (26): 3638–40. https://doi.org/10.3748/wjg.v13.i26.3638.

118. Schroder, Kate, Paul J. Hertzog, Timothy Ravasi, and David A. Hume. 2004. "Interferon-γ: An Overview of Signals, Mechanisms and Functions." *Journal of Leukocyte Biology* 75 (2): 163–89. https://doi.org/10.1189/jlb.0603252.
119. Shahangian, Arash, Genhong Cheng, Jane C. Deng, Arash Shahangian, Edward K. Chow, Xiaoli Tian, Jason R. Kang, and Amir Ghaffari. 2009. "Type I IFNs Mediate Development of Postinfluenza Bacterial Pneumonia in Mice Find the Latest Version : Type I IFNs Mediate Development of Postinfluenza Bacterial Pneumonia in Mice." *The Journal of Clinical Investigation* 119 (7): 1910–20. https://doi.org/10.1172/JCI35412.1910.
120. Sheppard, Paul, Wayne Kindsvogel, Wenfeng Xu, Katherine Henderson, Stacy Schlutsmeyer, Theodore E. Whitmore, Rolf Kuestner, et al. 2003. "IL-28, IL-29 and Their Class II Cytokine Receptor IL-28R." *Nature Immunology* 4 (1): 63–68. https://doi.org/10.1038/ni873.
121. Siegel, Rachael, Joyce Eskdale, and Grant Gallagher. 2011. "Regulation of IFN-Λ1 Promoter Activity (IFN-Λ1/IL-29) in Human Airway Epithelial Cells." *Journal of Immunology (Baltimore, Md.: 1950)* 187 (11): 5636–44. https://doi.org/10.4049/jimmunol.1003988.
122. Sodeifian, Fatemeh, Mahsa Nikfarjam, Naghmeh Kian, Kawthar Mohamed, and Nima Rezaei. 2022. "The Role of Type I Interferon in the Treatment of COVID-19." *Journal of Medical Virology* 94 (1): 63–81. https://doi.org/10.1002/jmv.27317.
123. Sohn, Sook-Young, Janet Hearing, JoAnn Mugavero, Varvara Kirillov, Elena Gorbunova, Luke Helminiak, Smruti Mishra, et al. 2021. "Interferon-Lambda Intranasal Protection and Differential Sex Pathology in a Murine Model of SARS-CoV-2 Infection." *MBio* 12 (6): e02756-21. https://doi.org/10.1128/mBio.02756-21.
124. Stanifer, Megan L., Kalliopi Pervolaraki, and Steeve Boulant. 2019. "Differential Regulation of Type I and Type III Interferon Signaling." *International Journal of Molecular Sciences* 20 (6): 1445. https://doi.org/10.3390/ijms20061445.

125. Sun, Jing, Zhen Zhuang, Jian Zheng, Kun Li, Roy Lok-Yin Wong, Donglan Liu, Jicheng Huang, et al. 2020. “Generation of a Broadly Useful Model for COVID-19 Pathogenesis, Vaccination, and Treatment.” *Cell* 182 (3): 734-743.e5. https://doi.org/10.1016/j.cell.2020.06.010.
126. Takemura, Naoki, Takumi Kawasaki, Jun Kunisawa, Shintaro Sato, Aayam Lamichhane, Kouji Kobiyama, Taiki Aoshi, et al. 2014. “Blockade of TLR3 Protects Mice from Lethal Radiation-Induced Gastrointestinal Syndrome.” *Nature Communications* 5 (1): 3492. https://doi.org/10.1038/ncomms4492.
127. Thomson, Scott J. P., Fui G. Goh, Helen Banks, Thomas Krausgruber, Sergei V. Kotenko, Brian M. J. Foxwell, and Irina A. Udalova. 2009. “The Role of Transposable Elements in the Regulation of IFN-Lambda1 Gene Expression.” *Proceedings of the National Academy of Sciences of the United States of America* 106 (28): 11564–69. https://doi.org/10.1073/pnas.0904477106.
128. Thyrell, Lena, Sven Erickson, Boris Zhivotovsky, Katja Pokrovskaja, Olle Sangfelt, Juan Castro, Stefan Einhorn, and Dan Grandér. 2002. “Mechanisms of Interferon-Alpha Induced Apoptosis in Malignant Cells.” *Oncogene* 21 (8): 1251–62. https://doi.org/10.1038/sj.onc.1205179.
129. Tilg, H, H Vogelsang, O Ludwiczek, H Lochs, A Kaser, J-F Colombel, H Ulmer, et al. 2003. “A Randomised Placebo Controlled Trial of Pegylated Interferon α in Active Ulcerative Colitis.” *Gut* 52 (12): 1728–33.
130. Ueki, Iris F., Gundula Min-Oo, April Kalinowski, Eric Ballon-Landa, Lewis L. Lanier, Jay A. Nadel, and Jonathan L. Koff. 2013. “Respiratory Virus-Induced EGFR Activation Suppresses IRF1-Dependent Interferon λ and Antiviral Defense in Airway Epithelium.” *Journal of Experimental Medicine* 210 (10): 1929–36. https://doi.org/10.1084/jem.20121401.
131. Uematsu, Satoshi, and Shizuo Akira. 2008. “Toll-Like Receptors (TLRs) and Their Ligands.” *Handbook of Experimental Pharmacology*, no. 183: 1–20. https://doi.org/10.1007/978-3-540-72167-3_1.
132. Watanabe, T, M Inoue, K Harada, N Homma, M Uchida, N Ogata, R Funada, K Hasegawa, K Soga, and K Shibasaki. 2006. “A Case of Exacerbation of Ulcerative Colitis Induced by Combination

Therapy with PEG-interferon A-2b and Ribavirin." *Gut* 55 (11): 1682–83. https://doi.org/10.1136/gut.2006.105197.

133. Wheelock, E. F. 1965. "Interferon-Like Virus-Inhibitor Induced in Human Leukocytes by Phytohemagglutinin." *Science (New York, N.Y.)* 149 (3681): 310–11. https://doi.org/10.1126/science.149.3681.310.
134. Yamamoto, Masahiro, Shintaro Sato, Hiroaki Hemmi, Katsuaki Hoshino, Tsuneyasu Kaisho, Hideki Sanjo, Osamu Takeuchi, et al. 2003. "Role of Adaptor TRIF in the MyD88-Independent Toll-Like Receptor Signaling Pathway." *Science* 301 (5633): 640–43. https://doi.org/10.1126/science.1087262.
135. Ye, Liang, Daniel Schnepf, Jan Becker, Karolina Ebert, Yakup Tanriver, Valentina Bernasconi, Hans Henrik Gad, Rune Hartmann, Nils Lycke, and Peter Staeheli. 2019. "Interferon-λ Enhances Adaptive Mucosal Immunity by Boosting Release of Thymic Stromal Lymphopoietin." *Nature Immunology* 20 (5): 593–601. https://doi.org/10.1038/s41590-019-0345-x.
136. Ye, Liang, Daniel Schnepf, and Peter Staeheli. 2019. "Interferon-λ Orchestrates Innate and Adaptive Mucosal Immune Responses." *Nature Reviews Immunology* 19 (10): 614–25. https://doi.org/10.1038/s41577-019-0182-z.
137. Yoneyama, Mitsutoshi, Mika Kikuchi, Kanae Matsumoto, Tadaatsu Imaizumi, Makoto Miyagishi, Kazunari Taira, Eileen Foy, et al. 2005. "Shared and Unique Functions of the DExD/H-Box Helicases RIG-I, MDA5, and LGP2 in Antiviral Innate Immunity." *Journal of Immunology (Baltimore, Md.: 1950)* 175 (5): 2851–58. https://doi.org/10.4049/jimmunol.175.5.2851.
138. Zhang, Qian, Paul Bastard, Zhiyong Liu, Jérémie Le Pen, Marcela Moncada-Velez, Jie Chen, Masato Ogishi, et al. 2020. "Inborn Errors of Type I IFN Immunity in Patients with Life-Threatening COVID-19." *Science (New York, N.Y.)* 370 (6515): eabd4570. https://doi.org/10.1126/science.abd4570.
139. Zhao, Jincun, Kun Li, Christine Wohlford-Lenane, Sudhakar S. Agnihothram, Craig Fett, Jingxian Zhao, Michael J. Gale, et al. 2014. "Rapid Generation of a Mouse Model for Middle East Respiratory Syndrome." *Proceedings of the National Academy of Sciences of the United States of America* 111 (13): 4970–75. https://doi.org/10.1073/pnas.1323279111.

140. Zhou, Z., O. J. Hamming, N. Ank, S. R. Paludan, A. L. Nielsen, and R. Hartmann. 2007. “Type III Interferon (IFN) Induces a Type I IFN-Like Response in a Restricted Subset of Cells through Signaling Pathways Involving Both the Jak-STAT Pathway and the Mitogen-Activated Protein Kinases.” *Journal of Virology* 81 (14): 7749–58. https://doi.org/10.1128/jvi.02438-06.
141. Zhou, Zhuo, Lili Ren, Li Zhang, Jiaxin Zhong, Yan Xiao, Zhilong Jia, Li Guo, et al. 2020. “Heightened Innate Immune Responses in the Respiratory Tract of COVID-19 Patients.” *Cell Host & Microbe* 27 (6): 883-890.e2. https://doi.org/10.1016/j.chom.2020.04.017.
142. Zhu, Linnan, Penghui Yang, Yingze Zhao, Zhenkun Zhuang, Zhifeng Wang, Rui Song, Jie Zhang, et al. 2020. “Single-Cell Sequencing of Peripheral Mononuclear Cells Reveals Distinct Immune Response Landscapes of COVID-19 and Influenza Patients.” *Immunity* 53 (3): 685-696.e3. https://doi.org/10.1016/j.immuni.2020.07.009.
143. Ziegler, Carly G. K., Vincent N. Miao, Anna H. Owings, Andrew W. Navia, Ying Tang, Joshua D. Bromley, Peter Lotfy, et al. 2021. “Impaired Local Intrinsic Immunity to SARS-CoV-2 Infection in Severe COVID-19.” *Cell* 184 (18): 4713-4733.e22. https://doi.org/10.1016/j.cell.2021.07.023.

Chapter 2. Type III interferons disrupt the lung epithelial barrier upon viral recognition.

Achille Broggi[1,*], Sreya Ghosh[1,*], Benedetta Sposito[1,2,*], Roberto Spreafico[3], Fabio Balzarini[1,2], Antonino Lo Cascio[1,2], Nicola Clementi[4], Maria De Santis[5], Nicasio Mancini[4,6], Francesca Granucci[2,7], Ivan Zanoni[1,2,8,#].

[1] Harvard Medical School, Boston Children's Hospital, Division of Immunology, Boston, United States.

[2] Department of Biotechnology and Biosciences, University of Milano - Bicocca, Milan, Italy.

[3] Institute for Quantitative and Computational Biosciences, University of California, Los Angeles, United States.

[4] Laboratory of Medical Microbiology and Virology, Vita-Salute San Raffaele University, Milan, Italy.

[5] Rheumatology and Clinical Immunology, Humanitas Clinical and Research Center - IRCCS, Rozzano, Italy.

[6] IRCCS San Raffaele Hospital, Milan, Italy.

[7] INGM-National Institute of Molecular Genetics "Romeo ed Enrica Invernizzi" Milan, Italy.

[8] Harvard Medical School, Boston Children's Hospital, Division of Gastroenterology, Boston, United States.

* Equal contribution

[#] Corresponding author: ivan.zanoni@childrens.harvard.edu

Science *369, 706–712* (2020)
DOI: 10.1126/science.abc3545

Abstract.
Viral infections of the lower respiratory tract are a leading cause of mortality. Mounting evidence indicates that most severe cases are characterized by aberrant immune responses and do not depend on viral burden. In this study, we assessed how type III interferons (IFN-λ) contribute to the pathogenesis induced by RNA viruses. We report that IFN-λ is present in the lower, but not upper, airways of patients with coronavirus disease 2019 (COVID-19). In mice, we demonstrate that IFN-λ produced by lung dendritic cells in response to a synthetic viral RNA induces barrier damage, causing susceptibility to lethal bacterial superinfections. These findings provide a strong rationale for rethinking the pathophysiological role of IFN-λ and its possible use in clinical practice against endemic viruses, such as influenza virus as well as the emerging severe acute respiratory syndrome coronavirus 2 (SARS-CoV-2) infection.

Introduction.

The ability to resolve viral infections of the lung is dependent on the actions of interferons (IFNs) and inflammatory cytokines, yet their relative contributions to host defense and return to homeostasis remain undefined. In particular, type III IFNs (IFN-λ) have attracted much attention, as they operate primarily at mucosal surfaces (Broggi, Granucci, and Zanoni 2020). Recent work established that, unlike other IFNs, IFN-λ signaling induces antiviral activities while simultaneously limiting the tissue-damaging functions of neutrophils (Blazek et al. 2015; Broggi et al. 2017; Galani et al. 2017). When considered in the context of respiratory viral infections in which inflammation appears to be the primary driver of life-threatening symptoms, including the recently emerged severe acute respiratory syndrome (SARS)-coronavirus (CoV)-2 (Merad and Martin 2020), the ability of IFN-λ to limit immunopathology but maintain antiviral activity is noteworthy. Discussions on the possible use of IFN-λ against SARS-CoV-2 have begun (Prokunina-Olsson et al. 2020) and clinical trials have been initiated. However, despite this interest in the use of IFN-λ to treat viral infections, the long-term effects of IFN-λ on lung physiology remain largely overlooked. For example, during viral infections of the lung, immunopathology may predispose the host to opportunistic bacterial infections and IFN-λ impairs bacterial control during superinfections (Planet et al. 2016; Rich et al. 2019). It remains unresolved whether this is due to the anti-inflammatory activity of IFN-λ, which reduces host resistance, or to the capacity of IFN-λ to alter lung physiology upon a viral encounter. Indeed, superinfections represent the first

cause of lethality upon influenza virus infection (McCullers 2014) and correlate with severity in coronavirus disease 2019 (COVID-19) patients (Zhang et al. 2020).

Results.

Mouse models of SARS, Middle east respiratory syndrome (MERS) (Channappanavar et al. 2019; Frieman et al. 2010) and influenza (Broggi, Granucci, and Zanoni 2020; Major et al. 2020) are characterized by a robust induction of type I and III IFNs. However, the involvement of these cytokines in COVID-19 is controversial (Blanco-Melo et al. 2020; Zhou et al. 2020). To directly evaluate the capacity of SARS-CoV-2 to induce IFNs, we tested naso-oropharyngeal swabs of COVID-19 patients and healthy controls, as well as the bronchoalveolar lavage fluid (BALF) of SARS-CoV-2-positive patients with severe COVID-19. Levels of IFN mRNAs in the upper airways of COVID-19 patients were not significantly different from healthy controls. By contrast, BALF of patients with severe disease presented elevated levels of both inflammatory cytokines as well as type I and III IFNs (Fig. 1A-E).

To evaluate the contribution of IFN-λ to the immunopathology driven by RNA respiratory viruses uncoupled from its effect on viral replication, we devised an experimental system in which pattern recognition receptors (PRRs) involved in viral sensing were stimulated with their cognate ligands. RNA viruses are sensed via either endosomal Toll-like receptor (TLR) 3 and TLR7 or cytoplasmic retinoic acid-inducible gene I (RIG-I) and melanoma differentiation-associated protein 5 (MDA5) (Iwasaki and Pillai 2014). We intratracheally instilled

the TLR7 ligand, R848, or the synthetic analog of double-stranded RNA, polyinosine-polycytidylic acid [poly (I:C)], that stimulates both TLR3 and the RIG-I/MDA5 pathway in vivo (Kato et al. 2006). PRRs were stimulated over the course of 6 days to elicit prolonged innate immune activation in the lung. Both ligands induced hypothermia (Fig. 1F) and weight loss (fig. S1A), but only poly (I:C) compromised barrier function (Fig. 1G and fig. S1B). IFN mRNAs were strongly upregulated by poly (I:C) but not R848 (Fig. 1H, I). By contrast, R848 treatment induced the upregulation of proinflammatory cytokines (i.e. *Il1b*) but this did not correlate with barrier function decrease (Fig. 1G-J and fig. S1B).

Alterations in the epithelial barrier predispose mice to lethal bacterial superinfections (Jamieson et al. 2013). We therefore infected mice treated with either R848 or poly (I:C) with *Staphylococcus aureus*. Mice treated with poly (I:C) died upon *S. aureus* infection (Fig. 1K) and had higher bacterial burdens (Fig. 1L), more intense hypothermia, and greater barrier damage (fig. S2A, B). *S. aureus* infection did not alter the pattern of cytokine expression compared to that in mice treated with viral ligands only (fig. S2C-E). Upon poly (I:C) administration, IFN-β and IFN-λ transcript and protein levels were rapidly upregulated and plateaued (fig. S3A-D), whereas *S. aureus* bacterial burden increased with consecutive injections of poly (I:C) (fig. S3E). IFN-stimulated genes (ISGs), but not pro-inflammatory cytokines, were also sustained over time (fig. S3F-I). These data suggest that chronic exposure to IFNs aggravates bacterial superinfections. Because the protein levels of IFN-λ were very high compared to IFN-β (fig. S3C, D), we assessed whether IFN-λ was sufficient to exacerbate bacterial superinfections. We

administered exogenous IFN-λ either alone, or with R848, which induces inflammation but not IFN production (Fig. 1H-J). The administration of IFN-λ with R848, but not IFN-λ alone, was sufficient to induce sensitivity to *S. aureus* infection (Fig. 1M, N and fig. S3J). Thus, in an inflamed lung, IFN-λ is sufficient to aggravate superinfections.

In contrast to wild-type (WT) mice, mice deficient in IFN-λ receptor 1 (*Ifnlr1*) expression were protected from poly (I:C)-induced morbidity and barrier damage (Fig. 2A, B and fig. S4A, B). *Ifnlr1*$^{-/-}$ mice were also resistant to superinfection with *S. aureus* (Fig. 2C-F). By contrast, the absence of *Ifnlr1* did not affect mRNA or protein levels of IFNs or pro-inflammatory cytokines (fig. S4C-H). We next generated reciprocal bone marrow chimeras in which either the hematopoietic or the stromal compartments were defective for IFN-λ signaling. Absence of *Ifnlr1* in the stromal compartment, but not in hematopoietic cells, phenocopied complete *Ifnlr1* deficiency (Fig. 2G, H, and fig. S5). Furthermore, there was no difference in myeloid immune cell recruitment in *Ifnlr1*$^{-/-}$ compared to WT mice (fig. S6A-D) and depletion of neutrophils did not affect bacterial burden (fig. S6E). Thus, IFN-λ signaling in epithelial cells is necessary and sufficient to induce susceptibility to a secondary infection.

A targeted transcriptomic analysis on lung epithelial cells from mice treated with poly (I:C) revealed a potent downregulation of the IFN signature in *Ifnlr1*$^{-/-}$ compared to WT mice (Fig. 3A, B, fig. S7 and data Table S1). This finding confirmed the predominant role of IFN-λ as opposed to type I IFNs during prolonged viral sensing in the lung.

Consistent with the observed defect in barrier function, genes associated with apoptosis and the activation of the p53 pathway were enriched in WT compared to *Ifnlr1*$^{-/-}$ epithelial cells (Fig. 3B). By contrast, pathways involved in positive regulation of the cell cycle were enriched in *Ifnlr1*$^{-/-}$ cells (Fig. 3C). Accordingly, epithelial cells in *Ifnlr1*$^{-/-}$ mice, as well as in stromal *Ifnlr1*$^{-/-}$ chimeras, proliferated more efficiently after poly (I:C) administration, in the presence or absence of *S.aureus* (Fig. 3D-G). The most downregulated gene in *Ifnlr1*$^{-/-}$ epithelial cells compared with WT cells was the E3 ubiquitin-protein ligase makorin-1 *(Mrkn1*) (Fig. 3A, data Table S1). The protein encoded by this gene induces p21 degradation and favors apoptosis via p53 under oxidative stress conditions and after DNA damage (hallmarks of severe viral infections) (Lee et al. 2009). Indeed, *Ifnlr1*$^{-/-}$ epithelial cells showed elevated levels of p21 (Fig. 3H, I). Thus, the ability of IFN-λ to reduce tissue tolerance stems from its capacity to inhibit tissue repair by directly influencing epithelial cell proliferation and viability.

We next investigated the cellular source and molecular pathways that drive IFN-λ production. Upon poly (I:C) administration, lung resident dendritic cells (DCs) expressed the highest levels of IFN-λ transcript, during both the early and late phases after poly (I:C) administration (Fig. 4A, and fig. S8A). By contrast, epithelial cells, alveolar macrophages and monocytes, instead, expressed type I IFNs and proinflammatory cytokines but no IFN-λ transcript (fig. S8A-C). Depletion of CD11c^{+} DCs was sufficient to abolish the production of IFN-λ, but not type I IFNs (Fig. 4B, C, and fig. S8D-E). Alveolar macrophages were not depleted under diphtheria toxin

administration (fig. S8F) and did not produce IFN-λ in response to poly (I:C) (Fig. 4A). By using in vitro generated DCs, we found that IFN-λ was induced only when the TLR3 pathway was activated (Fig.4D, fig. S9A, B). Consistent with in vivo data, TLR7 stimulation in vitro induced only the upregulation of pro-inflammatory cytokines (Fig.4D, fig. S9A, B). Ex vivo analysis showed that conventional DC1 (cDC1) are the major producer of IFN-λ (fig. S10). Activation of RIG-I and MDA5 via intracellular delivery of poly (I:C) (Fig.4D, fig. S9A, B) and of triphosphate hairpin RNA (fig. S11A-E) induced high levels of type I IFNs, but not type III IFNs, in a mitochondrial antiviral signaling protein (MAVS)-dependent manner. Blockade of endosomal acidification via chloroquine treatment confirmed the importance of TLR3 activation for IFN-λ induction (fig. S12A, B). WT mice or mice that do not respond to TLR3 stimulation [toll-like receptor adaptor molecule 1 deficient (*Ticam1*$^{-/-}$)] were treated in vivo with poly (I:C). Only DCs sorted from *Ticam1*$^{-/-}$ mice did not express IFN-λ mRNA, although they still expressed type I IFN mRNA (Fig. 4E, F). Furthermore, *Ticam1*$^{-/-}$ mice were protected against *S. aureus* superinfections (Fig. 4G). *Ticam1*$^{-/-}$ mice also showed lower IFN-λ mRNA (but not type I IFN mRNA) than WT mice (Fig. 4H, I). Similar results were obtained when only hematopoietic cells were deficient in *Ticam1* (Fig. 4J-L).

Discussion.

The immune system evolved to protect against pathogens, but doing so often threatens host fitness and can cause immunopathologies (Medzhitov, Schneider, and Soares 2012). In COVID-19, SARS, MERS,

and flu, severe symptoms and death occur late, and after the peak in viral load, indicating a central role for the immune system in driving the pathology (Granados et al. 2017; Memish et al. 2020; Peiris et al. 2003; Wölfel et al. 2020). In our system, we isolated the effect of immune activation from resistance to lung viral infections and demonstrated that sustained IFN-λ is produced by DCs via TLR3. TLR3 detects replication intermediates from dying cells (Schulz et al. 2005) and thus is insensitive to viral immune evasion. IFN-λ acts on lung epithelial cells and compromises the lung barrier function, predisposing the host to lethal secondary bacterial infections.

Previous findings suggested that IFN-λ protects against viral infections (Ye, Schnepf, and Staeheli 2019, 20019) and increases the barrier functions of gut epithelial cells as well as of endothelial cells (Douam et al. 2017; Lazear et al. 2015; Odendall, Voak, and Kagan 2017). These discrepancies may have arisen because, in those studies, the particular cell types targeted by IFN-λ were different. Furthermore, our data support the hypothesis that the detrimental activities of IFN-λ occur only upon chronic exposure and in the presence of tissue damage. Early administration of IFN-λ in a mouse model of COVID-19 could instead confer protection (Dinnon et al. 2020). Our data enjoin clinicians to carefully analyze the duration of IFN-λ administration and to consider the severity of disease when IFN-λ is used as a therapeutic agent against lung viral infections.

Acknowledgments.
We thank J. C. Kagan for discussion, help, and support. Funding: I.Z. is supported by NIH grants 1R01AI121066 and 1R01DK115217 and NIAID-DAIT-NIHAI201700100. A.B. is supported by CCFA RFA 549868. F.G. is supported by AIRC (IG 2019Id.23512), Fondazione Regionale per la Ricerca Biomedica, FRRB (IANG-CRC - CP2_12/ 2018), and Ministero della Salute, Ricerca Finalizzata (RF-2018- 12367072).

Authors contributions.
A.B., S.G., and B.S. designed, performed, and analyzed the experiments; A.B. wrote the paper; R.S. performed the analysis of the sequencing data; F.B. and A.L.C. performed the experiments; N.C., M.D.S., and N.M. performed and analyzed human experiments; F.G. contributed to the design of the experiments; I.Z. conceived the project, designed the experiments, supervised the study and wrote the paper.

Figures.

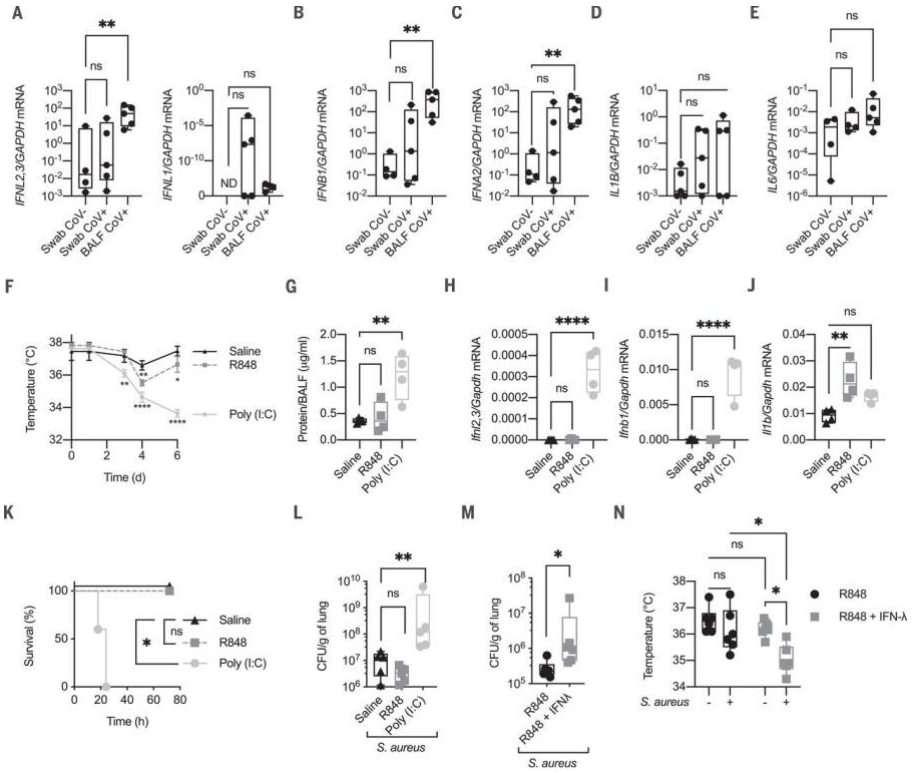

Figure 1. Morbidity correlates with the high expression of type I IFN and IFN-λ in the lung of COVID-19 patient BALF and of poly (I:C)-treated mice. (A to E) IFNL2,3, IFNL1 (A), IFNB (B), IFNA2 (C), IL1B (D), and IL6 (E) mRNA expression was evaluated in naso-oropharyngeal swabs from SARS-CoV-2– positive (Swab CoV+) and –negative (Swab CoV−) participants and from the BALF of intensive care unit (ICU)–hospitalized SARS-CoV-2–positive patients (BALF CoV+) (five participants per group). GAPDH, glyceraldehyde phosphate dehydrogenase; ND, not detectable. (F to J) Mice were intratracheally (i.t.) administered 2.5 mg of poly (I:C) per kilogram of body weight, 2.5 mg of R848 per kilogram of body weight, or saline daily for 6 days. (F)

Body temperatures of the treated mice measured over time. (G) Amount of total protein in the BALF measured after 6 days of poly (I:C) treatment. (H to J) Ifnl2,3 (H), Ifnb1 (I), and Il1b (J) mRNA expression was assessed in total lung lysate harvested 6 days after treatment. (K and L) Mice treated as in (F) to (J) were infected at day 6 with 5 × 107 colony-forming units (CFU) of S. aureus administered i.t. and were monitored for survival (K). Bacterial loads in the lungs of the treated mice normalized to lung weight were assessed 12 hours postinfection (hpi) (L). Mice were i.t. administered R848 (2.5 mg/kg) or a combination of R848 and IFN-l (50 mg/kg) daily for 6 days and were then infected as in (K). Lung bacterial burdens (M) and body temperatures (N) before and after S. aureus infection are shown [(G) to (J), (L) to (N)]. Each symbol represents one mouse. The median and range are represented. (F) Means ± SDs of five mice per group are represented. (G to J) Four, (L and M) five, and (N) six mice per group are represented, and median and range are shown. (K) Survival plot of five mice per group. (F to N) Representative data of three independent experiments. Statistics: ns, not significant ($P > 0.05$); *$P < 0.05$; **$P < 0.01$; ****$P < 0.0001$. Two-way analysis of variance (ANOVA) [(F) and (N)], one-way ANOVA [(G) to (J), (L)], or two-tailed t test (M) was performed. Logarithmic values were fitted when evaluating bacterial load [(L) and (M)]. Log-rank (Mantel-Cox) test, corrected for multiple comparisons, was performed to evaluate survival (K).

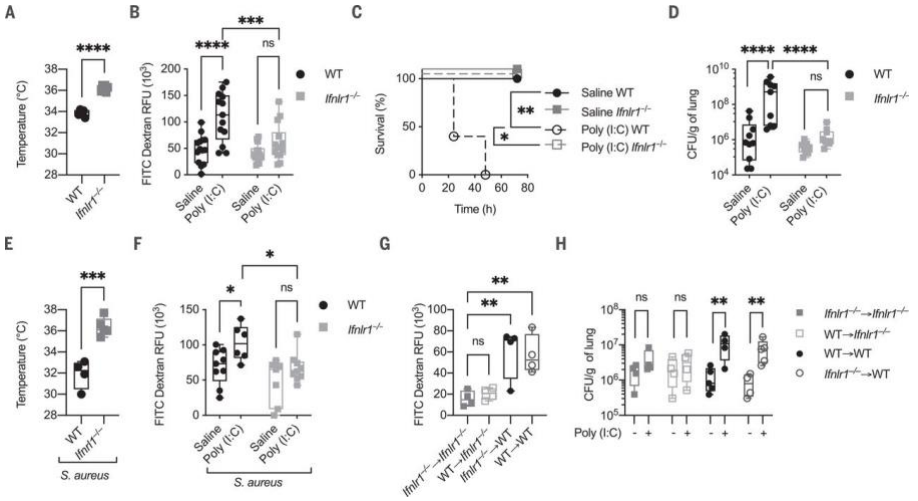

Figure 2. IFN-λ is necessary to increase susceptibility to bacterial infection induced by antiviral immunity. (A and B) WT and Ifnlr1−/− mice were i.t. treated with 2.5 mg/kg poly (I:C) or saline daily for 6 days. (A) Body temperatures of poly (I:C)–treated WT and Ifnlr1−/− mice were recorded on day 6. (B) On day 6, mice were i.t. treated with fluorescein isothiocyanate (FITC)– dextran (10 mg per mouse). Barrier permeability was measured as relative fluorescent units (RFU) of FITC-dextran leaked in plasma 1 hour after injection. (C to F) WT and Ifnlr1−/− mice i.t. treated with 2.5 mg/kg poly (I:C) or saline for 6 days were i.t. infected with 5 × 107 CFU of S. aureus and monitored for survival (C). Lung bacterial burdens normalized by lung weight (D), body temperature (E), and barrier permeability (F) [as in (B)] were assessed 12 hpi. (G and H) Lethally irradiated WT or Ifnlr1−/− recipients were reconstituted with donor bone marrow (Ifnlr1−/− or WT) for 6 weeks and were then treated as in (C) to (F). Resulting chimeric mice were defective for IFN-l signaling in either the hematopoietic compartment (Ifnlr1−/− → WT) or in the stromal compartment (WT →

Ifnlr1−/−). Ifnlr1−/− → Ifnlr1−/− and WT → WT chimeras were used as controls. (G) Barrier permeability [as in (B)] and (H) lung bacterial burdens were evaluated 12 hpi. Each symbol represents one mouse. The median and range are represented. (C) Survival plot of five mice per group. (A to H) Representative data of three independent experiments. (A, E, G, and H) Four, (B) 14, and (D and F) 10 mice per group; median and range are represented. Statistics: ns, not significant ($P > 0.05$); *$P < 0.05$; **$P < 0.01$; ***$P < 0.001$; ****$P < 0.0001$. Two-way ANOVA [(B), (D), (F), (H)], one-way ANOVA (G), or two-tailed t test [(A) and (E)] was performed. Logarithmic values were fitted when evaluating bacterial load [(D) and (H)]. Log-rank (Mantel-Cox) test, corrected for multiple comparisons, was performed to evaluate survival (C).

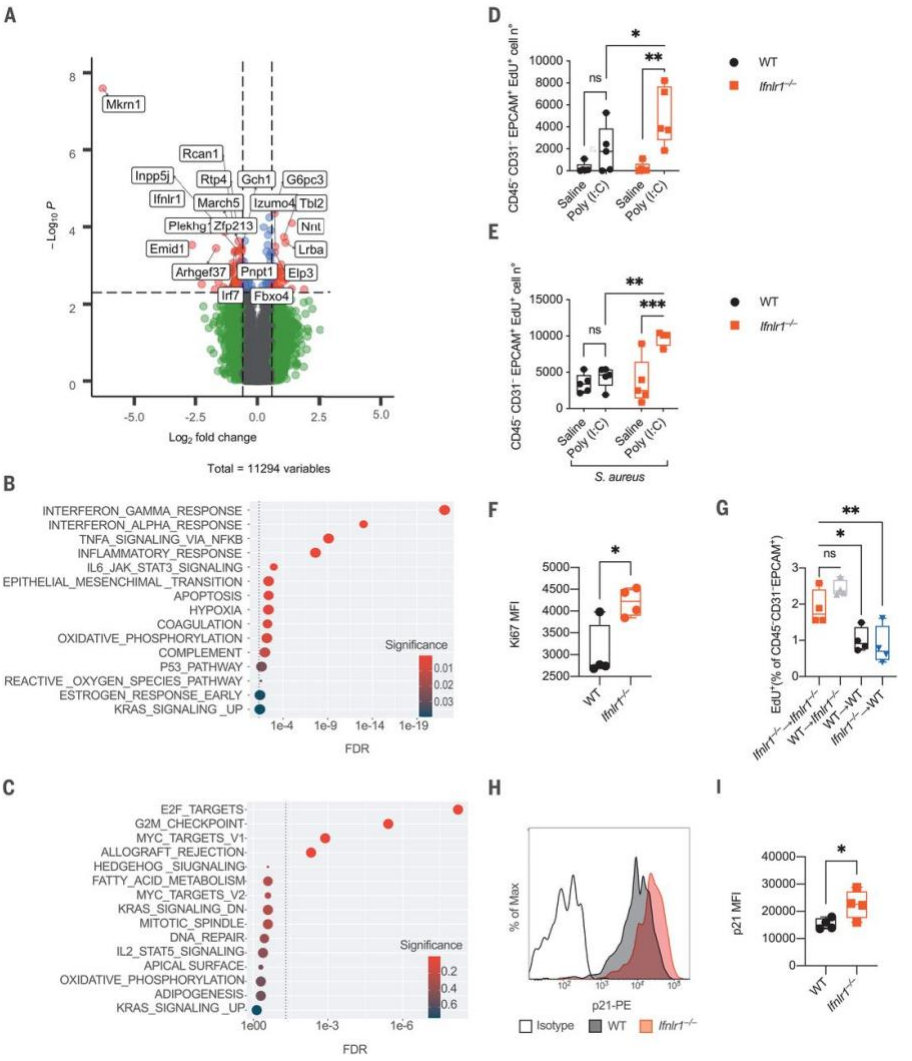

Figure 3. IFN-λ signaling directly inhibits lung epithelia proliferation and impairs repair upon viral recognition. (A to C) Targeted transcriptome sequencing was performed on lung epithelial cells isolated on day 6 from WT and Ifnlr1−/− mice i.t. treated with 2.5 mg/kg poly (I:C) daily for 6 days. (A) Volcano plot of differentially expressed genes (DEGs) between WT

and Ifnlr1−/−. DEGs (P < 0.005) with a fold change >1.5 (or <−1.5) are indicated in red; DEGs with a fold change <1.5 (or >−1.5) are in blue. Nonsignificant DEGs (P > 0.005) and genes not differentially expressed are indicated in green and gray, respectively. (B and C) Dot plot visualization of gene set enrichment analysis for pathways enriched in (B) WT epithelial cells compared to Ifnlr1−/− and (C) Ifnlr1−/− epithelial cells compared to WT. The color of the dots represents the adjusted P value (significance) for each enriched pathway; dot size represents the gene set size. FDR, false discovery rate. (D and E) Epithelial cell proliferation was assessed as 5-ethynyl-2′-deoxyuridine (EdU) incorporation in (D) lung epithelial cells (CD45−CD31−EPCAM+) in WT and Ifnlr1−/− mice treated as in (A) to (C) or (E) treated as in (A) to (C) and i.t. infected on day 6 with 5 × 107 CFU S. aureus for 12 hours. (F) Mean fluorescence intensity (MFI) of Ki67 in CD45−CD31−EPCAM+ cells of WT and Ifnlr1−/− mice treated as in (A) to (C). (G) EdU incorporation in lung epithelial cells of WT or Ifnlr1−/− chimeric mice reconstituted with Ifnlr1−/− or WT bone marrow treated as in (E). (H and I) p21 levels in lung epithelial cells (CD45−CD31−EPCAM+) from WT and Ifnlr1−/− mice treated as in (A) to (C). Representative histogram (H) and MFI (I) are depicted. (A to C) Four mice per genotype. (D and E) Five and (F to I) four mice per group; median and range are represented. (D to I) Representative data of three independent experi- ments. Statistics: ns, not significant (P > 0.05); *P < 0.05; **P < 0.01; ***P < 0.001. (D and E) Two-way ANOVA, (G) one-way ANOVA, and (F and I) and two-tailed t tests were performed.

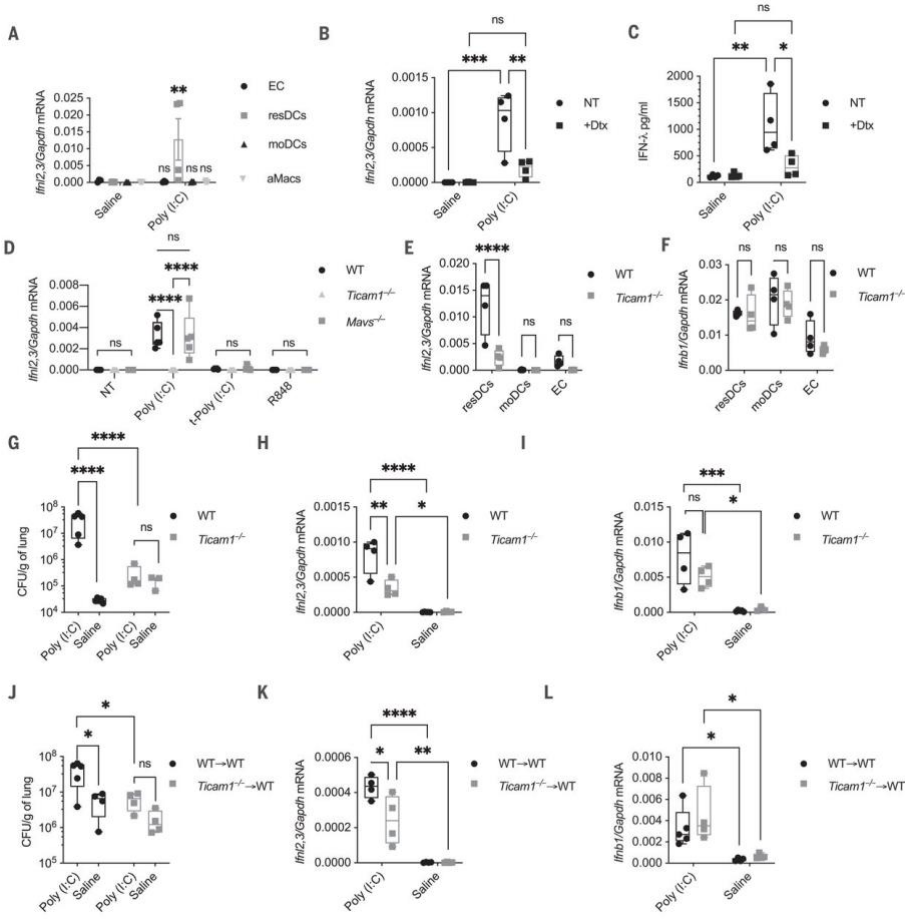

Figure 4. Lung resident DCs produce IFN-λ downstream of TLR3 upon viral recognition. (A) Ifnl2,3 relative mRNA expression in lung epithelial cells (EC), resident DCs (resDCs), monocyte-derived DCs (moDCs), and alveolar macro- phages (aMacs) sorted from WT mice i.t. treated with 2.5 mg/kg poly (I:C) or saline daily for 6 days measured on day 6. (B and C) CD11c-DTR mice were injected with diphtheria toxin (DTx) to deplete the CD11c+ cells in vivo. Relative Ifnl2,3 mRNA (B) and IFN-l protein levels (C) from lung homogenates were evaluated on day 6. NT, no toxin. (D) DCs differentiated from bone marrow cells

in the presence of FMS-like tyrosine kinase 3 ligand (Flt3l) for 9 days from WT, Ticam1−/−, or Mavs−/− mice were treated with 50 mg/ml poly (I:C), 1 mg transfected poly (I:C) per 106 cells, or 50 mg/ml R848 for 3 hours. Relative Ifnl2,3 mRNA expression was evaluated by quantitative polymerase chain reaction. (E and F) Ifnl2,3 (E) and Ifnb1 (F) relative mRNA expression in lung EC, resDCs, and moDCs sorted from WT and Ticam1−/− mice treated as in (A) was measured on day 6. (G to I) WT and Ticam1−/− mice were treated with poly (I:C) as in (A) and subsequently i.t. infected with 5 × 107 CFU of S. aureus on day 6 for 12 hours. Lung bacterial burden normalized by lung weight (G), Ifnl2,3 (H), and Ifnb1 (I) relative mRNA expression were evaluated. (J to L) WT chimeric mice recon- stituted with Ticam1−/− bone marrow (Ticam1−/− → WT) or WT bone marrow (WT → WT) were treated as in (G) to (I). Lung bacterial burden normalized by lung weight (J) and Ifnl2,3 (K) and Ifnb1 (L) relative mRNA expression 12 hpi were evaluated. Representative data of three independent experiments are shown. Statistics: ns, not significant ($P > 0.05$); *$P < 0.05$; **$P < 0.01$; ***$P < 0.001$; ***$P < 0.001$ (two-way ANOVA). Four mice per group; median and range are depicted [(A) to (C), (E) to (L)]. Means ± SEMs of four mice [(A) to (C), (E), and (F)] and of three independent experiments (D) are depicted.

Supplemental Figures.

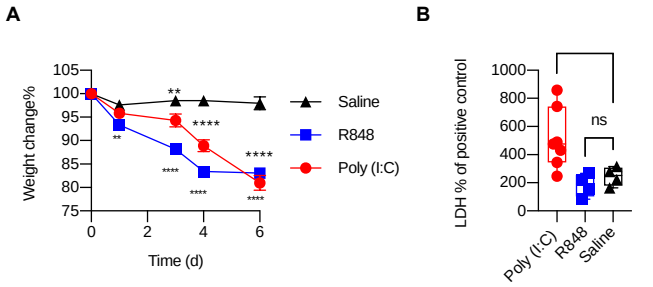

Figure S1. Intratracheal poly (I:C) treatment induces morbidity and lung damage. (A) Weight change and (B) LDH released in BALF of WT mice treated i.t. with 2.5 mg/kg poly (I:C), 2.5 mg/kg R848, or saline daily for 6 days. Statistics: ns, not significant (P>0.05); *P<0.05, **P<0.01 and ***P<0.001 (A) two-way ANOVA, (B) one-way ANOVA. (A) Mean +/− SEM of five mice per group is depicted. (B) Each mouse represents one point. Median and range are depicted.

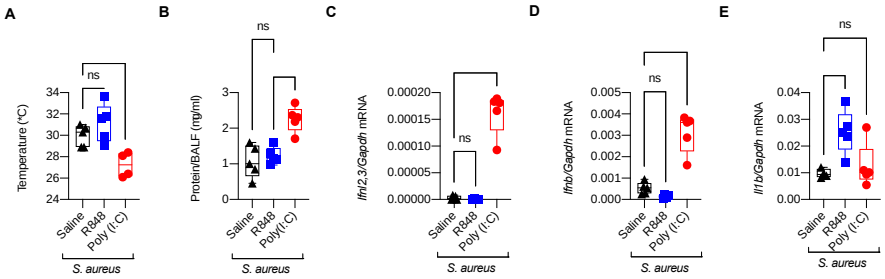

Figure S2. Intratracheal poly (I:C) treatment increases lung susceptibility to bacterial infection. WT mice were treated i.t. with 2.5 mg/kg poly (I:C), 2.5 mg/kg R848, or saline daily for 6 days and infected i.t. with 5×107 CFU of S. aureus on day 6. (A) Body temperature, (B) total protein in the BALF and Ifnl2,3 (C), Ifnb1 (D), and Il1b (E) relative mRNA expression in total lung lysates were evaluated 12 hpi. Statistics: ns, not significant (P>0.05); *P<0.05, **P<0.01 and ***P<0.001 (one-way ANOVA). Each mouse represents one point. Median and range are depicted.

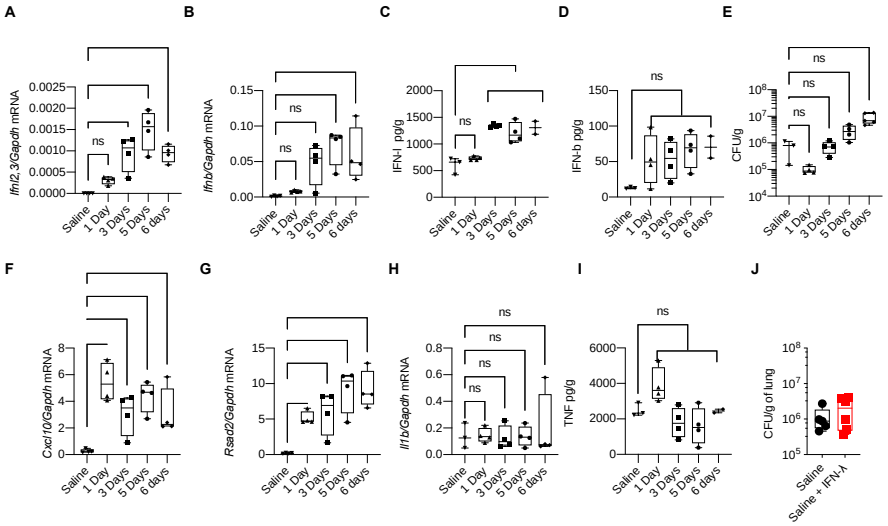

Figure S3. IFN-λ protein levels correlate with susceptibility to bacterial infections. (A-H) WT mice were treated i.t. with 2.5 mg/kg poly (I:C) daily for 1, 3, 5 or 6 days, or with saline for 6 days, and infected i.t. with 5×10^7 CFU of *S. aureus* for 12 hours. Total lung homogenates were analyzed by qPCR for *Ifnl2,3* (A), *Ifnb1* (B), *Cxcl10* (F), *Rsad2* (G), and *Il1b* (H) relative mRNA expression. Protein levels of IFN-λ (C), IFN-β (D), and TNF-α (I) were evaluated by ELISA on lung homogenates. (E) Bacterial burden was evaluated in total lung homogenate. (J) Bacterial burden in mice i.t. administered with saline alone, or saline with IFN-λ daily for 6 days and infected i.t. with 5×10^7 CFU of *S. aureus* were measured in total lung homogenates. Statistics: ns, not significant ($P>0.05$); *$P<0.05$, **$P<0.01$ and ***$P<0.001$ (one-way ANOVA compared to saline treatment). Each mouse represents one point. Median and range are depicted.

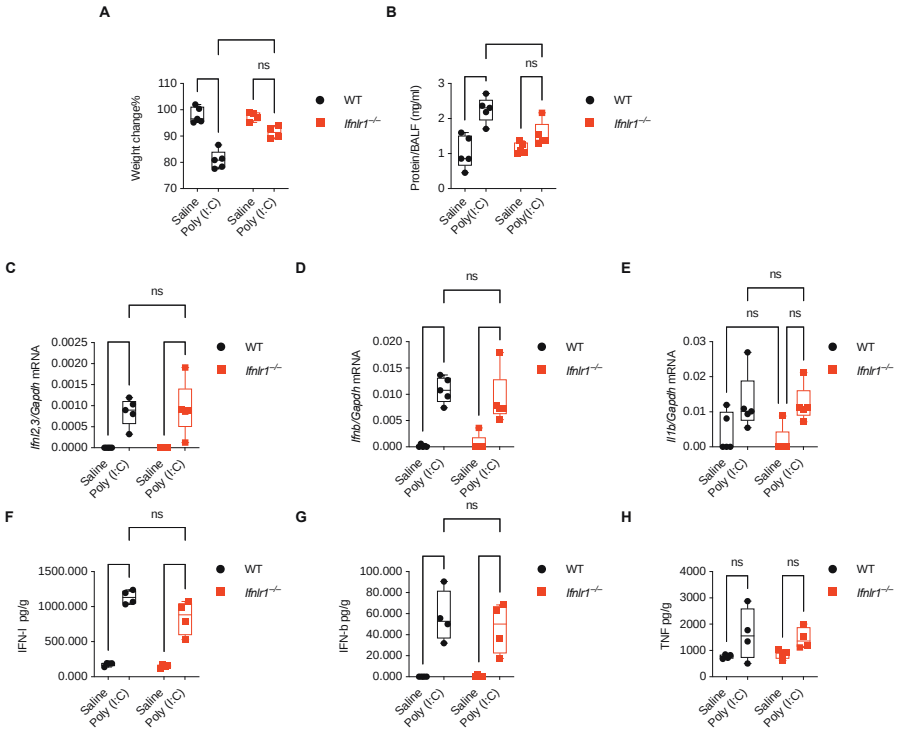

Figure S4. IFN-λ signaling is necessary to confer poly (I:C)-induced morbidity and susceptibility to bacterial infections. WT and *Ifnlr1*$^{-/-}$ mice were treated i.t. with 2.5 mg/kg poly (I:C) daily for 6 days and infected i.t. with 5×10^7 CFU of *S. aureus* for 12 hours. (A) Weight change, (B) total protein in the BALF, *Ifnl2,3* (C), *Ifnb1* (D), and *Il1b* (E) relative mRNA expression, and IFN-λ (F), IFN-β (G) and TNF (H) production in total lung homogenate were evaluated. Statistics: ns, not significant (P>0.05); *P<0.05, **P<0.01 and ***P<0.001 (two-way ANOVA). Each mouse represents one point. Median and range are depicted.

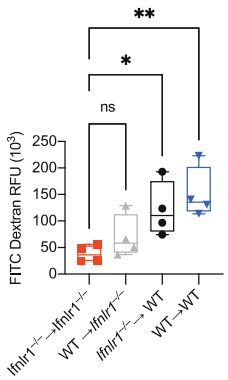

Figure S5. IFN-λ acts on epithelial cell to induce lung damage. Barrier function of *Ifnlr1*$^{-/-}$→*Ifnlr1*$^{-/-}$, WT→*Ifnlr1*$^{-/-}$, *Ifnlr1*$^{-/-}$→WT, and WT→WT chimeric mice was measured as the RFU of FITC-dextran in the plasma after mice were treated i.t. with 2.5 mg/kg poly (I:C) daily for 6 days and infected i.t. with 5×10^{7} CFU of *S. aureus* for 12 hours. Statistics: ns, not significant (P>0.05); *P<0.05, **P<0.01 and ***P<0.001 (one-way ANOVA). Each mouse represents one point. Median and range are depicted.

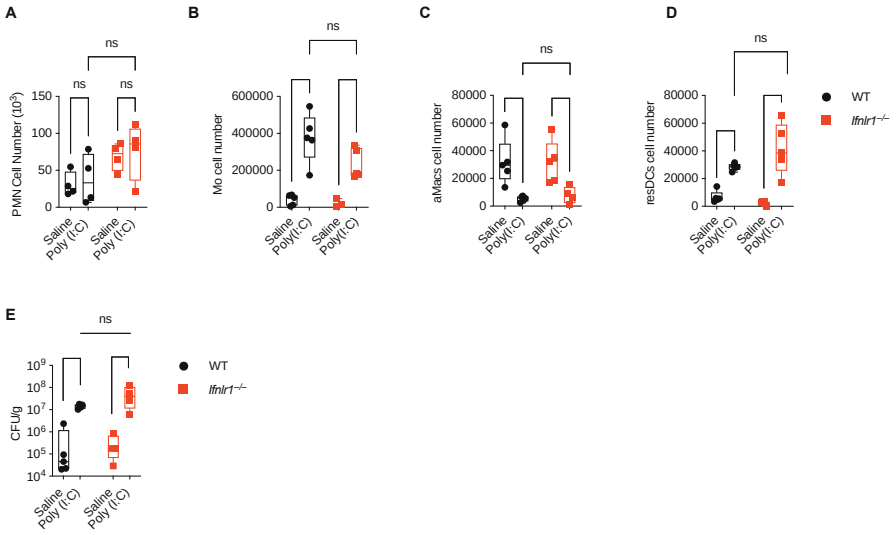

Figure S6. IFN-λ dependent loss of tolerance against bacterial infections is independent of neutrophil function or alteration in immune cell recruitment. Total number of (A) neutrophils (PMN), (B) monocyte and monocyte-derived cells (Mo), (C) alveolar macrophages (aMacs), and (D) resident DCs (resDCs) in lungs of WT and *Ifnlr1*$^{-/-}$ mice treated i.t. with 2.5 mg/kg poly (I:C) or saline daily for 6 days and infected with *S. aureus* as in Fig. 1K. (E) Wild-type mice were treated with either isotype or anti-Ly6G antibody to deplete Ly6G^{+} neutrophils in vivo. Mice were treated with poly (I:C) or saline for 6 days and infected with i.t. 5×10^{7} CFU of *S. aureus* for 12 hours. Bacterial loads in the lungs were calculated as CFU per gram of lung weights. Statistics: ns, not significant (P>0.05); *P<0.05, **P<0.01 and ***P<0.001 (two-way ANOVA). Each mouse represents one point. Median and range are depicted. Logarithmic data are fitted when depicting bacterial load (E).

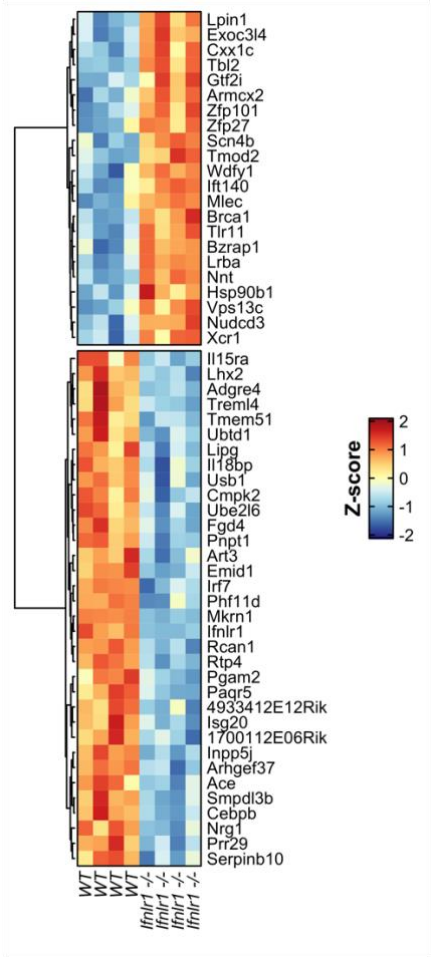

Figure S7. Differentially expressed genes in WT versus *Ifnlr1*$^{-/-}$ lung epithelial cells from poly (I:C)-treated mice. Heatmap of genes with a *P* value <0.005 and a fold change greater than 1.75 (or lower than −1.75) between *Ifnlr1*$^{-/-}$ and WT lung epithelial cells.

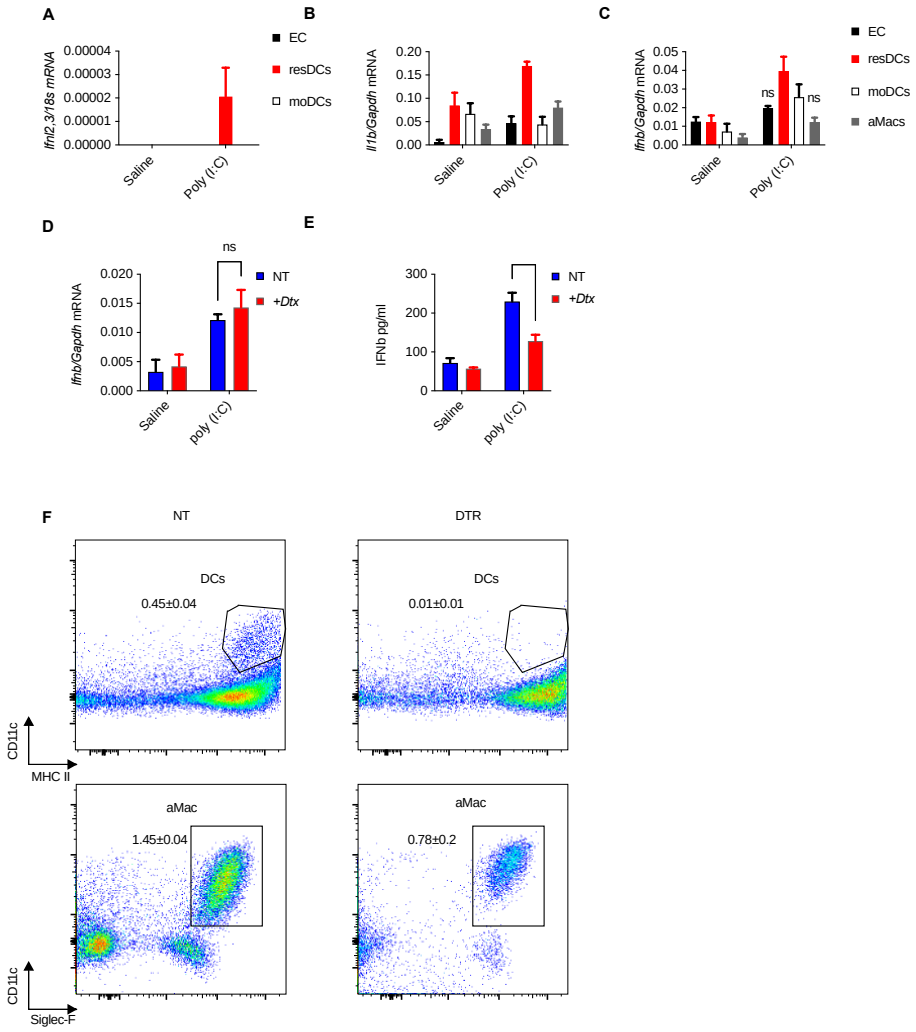

Figure S8. Lung resident DCs are the primary producers of IFN-λ upon poly (I:C) treatment. Lungs of mice treated i.t. with 2.5 mg/kg poly (I:C) or saline for 3 days or, 6 days were sorted for epithelial cells (EC), resident DCs (resDCs), monocyte-derived DCs (moDCs), and/or alveolar macrophages (aMacs) and assessed for (A) *Ifnl2,3* relative mRNA expression after 3 days, and (B) *Il1b* and (C) *Ifnb1* relative mRNA expressions after 6 days. CD11c-DTR mice depleted for $CD11c^{+}$ cells in vivo by DTx injections were treated daily with i.t. 0.5 mg/kg poly (I:C)

or saline for 6 days. Total lung lysates of the treated mice were analyzed for (D) *Ifnb1* relative mRNA expression, and (E) IFN-β protein expression by ELISA. (F) $Cd11c^{+}MHC\text{-}II^{+}$ DCs and $CD11c^{+}Siglec\text{-}F^{+}$ aMacs populations in the lungs of the mice treated with DTx (right panels) or not (left panels) were analyzed by flow cytometry. Percentage of total and standard deviations are depicted. Statistics: ns, not significant ($P>0.05$); *$P<0.05$, **$P<0.01$ and ***$P<0.001$ (two-way ANOVA). Mean +/− SEM of five mice per group are depicted.

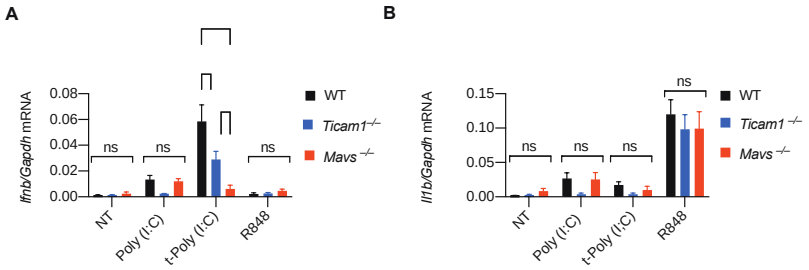

Figure S9. Flt3l-DCs responses to TLR3, RIG-I or TLR7 ligands. Flt3l-DCs from WT, *Ticam1*$^{-/-}$ or *Mavs*$^{-/-}$ mice were treated with 50 µg/ml poly (I:C), 1 µg transfected poly (I:C) per 10^6 cells, or 50 µg/ml R848 for 3 hours. *Ifnb1* (A), and *Il1b* (B) relative mRNA expression were evaluated by qPCR. Statistics: ns, not significant (P>0.05); *P<0.05, **P<0.01 and ***P<0.001 (two-way ANOVA). Mean and SEM of three independent experiments is depicted.

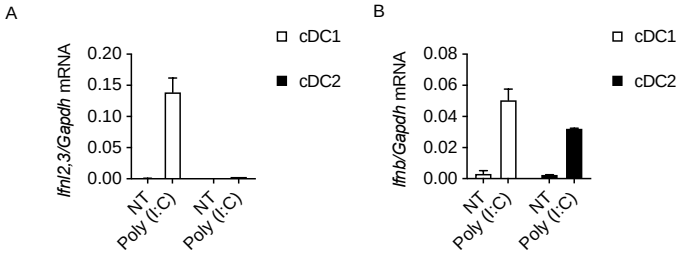

Figure S10. cDC1 are the primary producers of IFN-λ. In vivo differentiated splenic Flt3l-DCs were treated with 50 µg/ml poly (I:C) or, left untreated for 3 hours and sorted for cDC1 ($CD19^{-}B220^{-}CD11c^{+}MHC\text{-}II^{+}CD8\alpha^{+}$) and cDC2 ($CD19^{-}B220^{-}CD11c^{+}MHC\text{-}II^{+}CD8\alpha^{-}$). *Ifnl2,3* (A), and *Ifnb1* (B) relative mRNA expression in the sorted cells was evaluated by qPCR. Representative data of three independent experiments.

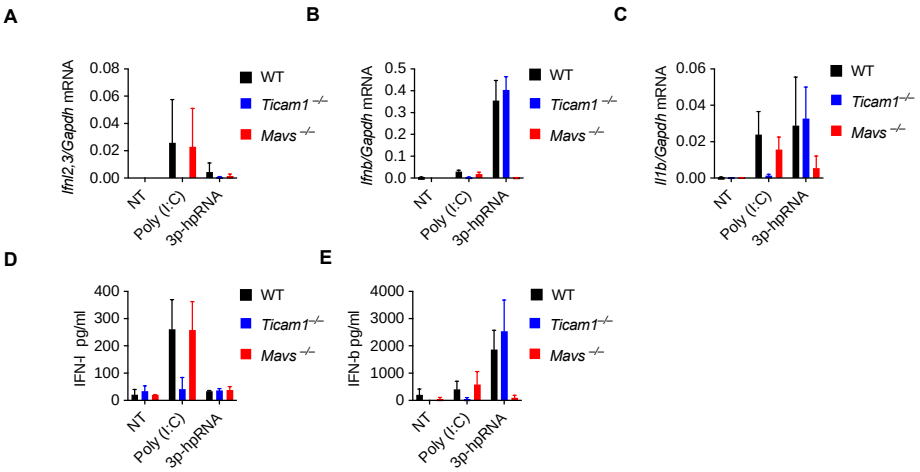

Figure S11. Flt3l-DCs upregulate IFN-λ uniquely upon activation of TLR3 signaling, and not in response to the RIG-I specific ligand 3p-hpRNA. Flt3l-DCs from WT, *Ticam1*$^{-/-}$ or *Mavs*$^{-/-}$ mice were treated with 50 µg/ml poly (I:C), or 1 µg transfected 3p-hpRNA per 10^6 cells for 3 or 6 hours. *Ifnl2,3* (A), *Ifnb1* (B), and *Il1b* (C) relative mRNA expression were evaluated by qPCR after 3 hours. IFN-λ (D), and IFN-β (E) levels in the supernatants were evaluated by ELISA after 6 hours. Mean +/− SEM of three independent experiments is depicted.

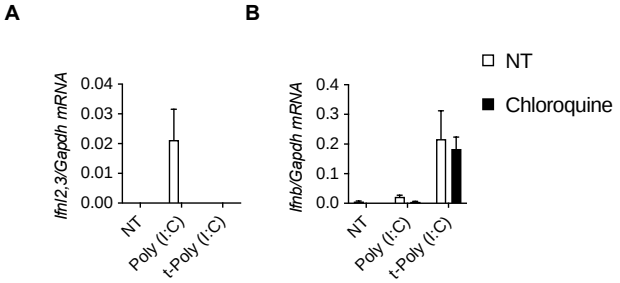

Figure S12. The endosomal TLR inhibitor Chloroquine inhibits poly (I:C) dependent IFN-λ expression in Flt3l-DCs. Flt3l-DCs from WT mice were treated with 50 μg/ml poly (I:C), or 1 μg transfected poly (I:C) per 10^6 cells for 3 hours in the presence or absence of 10 μg/ml Chloroquine. *Ifnl2,3* (A), and *Ifnb1* (B) relative mRNA expression were evaluated by qPCR. Mean +/− SEM of three independent experiments is depicted.

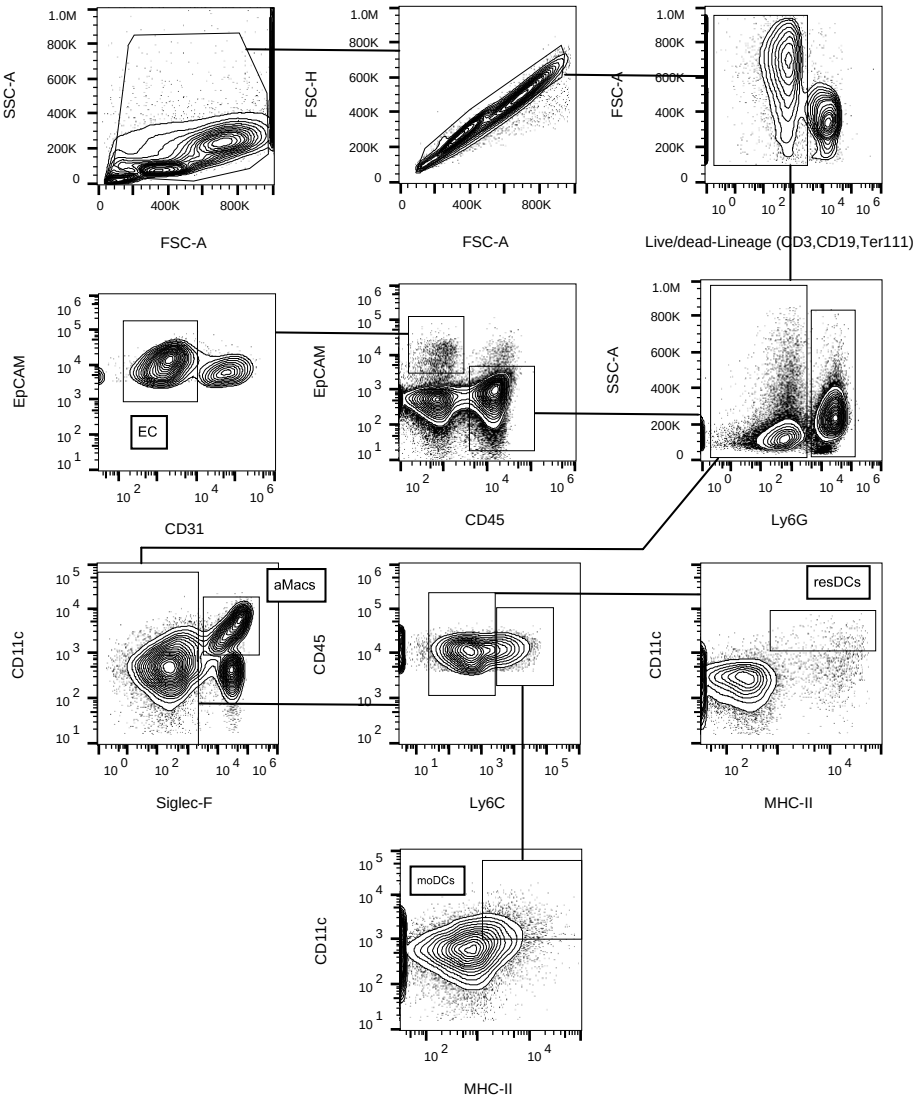

Figure S13. Sorting and cytofluorimetry strategy. Depiction of gating strategy for cell sorting. Cells were gated on FSC and SSC to eliminate debris, on FSC-A and FSC-H to select single cells and cells negative for live/dead dye and lineage markers (CD3, CD19, and Ter119). Epithelial cells (EC) were gated as $CD45^{-}EpCAM^{+}CD31^{-}$. The $EpCAM^{-}$ cells were sorted for immune cells as follows: aMacs were gated as

$CD45^{+}Ly6g^{-}CD11c^{hi}Siglec\text{-}F^{+}$, moDCs were gated as $CD45^{+}Ly6g^{-}Siglec\text{-}F^{-}Ly6C^{+}$ $CD11c^{+}MHC\text{-}II^{hi}$, and resDCs were gated as $CD45^{+}Ly6g^{-}Siglec\text{-}F^{-}Ly6C^{-}CD11c^{+}MHC\text{-}II^{hi}$.

Table S1. Flow cytometry antibodies and viability dyes.

Markers	Clone	Fluorochrome	Concentration	Provider
CD45.1	A20	PE	1:200	Biolegend
CD45.2	104	PerCP	1:200	Biolegend
CD45	30-F11	AF-700	1:200	Biolegend
EpCAM	G8.8	BV605	1:100	Biolegend
CD31	MEC13.3	APC	1:200	Biolegend
CD24	M1/69	PE-CF594	1:200	Biolegend
MHC-II I-A/I-E	M5/114.15.2	FITC	1:5000	Biolegend
Ly6G	1A8	APC	1:200	Biolegend
Ly6C	HK1.4	PerCP	1:200	Biolegend
CD11b	M1/70	PE-Cy5	1:5000	Biolegend
CD11c	N418	BV785	1:500	Biolegend
CD64	X54-5/71	BV711	1:200	Biolegend
Siglec F	S17007L	APC	1:200	Biolegend
CD8α	53-6.7	PE/Cy7	1:500	Biolegend
B220	RA3-6B2	APC	1:200	Biolegend
CD3	45.2C11	PE-CF594	1:200	Biolegend
CD19	6D5	PE-CF594	1:200	Biolegend
Erythroid cell marker	Ter119	PE-CF594	1:200	Biolegend
Ki67	16A8	PE	1:200	Biolegend
p21	F-5	PE	1:200	Santa Cruz

Table S2. q-RT-PCR Probes and Primers.

Gene	Probes or Primers	Assay ID
	Mouse	
Gapdh	Mouse Gapdh Endogenous Control (TaqMan™)	#4352932E
Ifnl2/3	TaqMan® Gene Expression Assays	Mm00663660_g1
Ifnb1	TaqMan® Gene Expression Assays	Mm00439552_s1
Il1b	TaqMan® Gene Expression Assays	Mm00434228_m1
Rsad2	TaqMan® Gene Expression Assays	Mm00491265_m1
Gapdh	IDT PrimeTime® Predesigned qPCR Assays	Mm.PT.39a.1
Rsad2	Sigma KiCqStart™ Primers	M_Rsad2_1
Cxcl10	Sigma KiCqStart™ Primers	M_Cxcl10_1
	Human	
IFNA2	TaqMan® Gene Expression Assays	Hs00265051_s1
IFNB1	TaqMan® Gene Expression Assays	Hs01077958_s1
IL6	TaqMan® Gene Expression Assays	Hs00174131_m1
IL1b	TaqMan® Gene Expression Assays	Hs01555410_m1
IFNL1	TaqMan® Gene Expression Assays	Hs01050642_gH
IFNL2,3	TaqMan® Gene Expression Assays	Hs04193048_gH

Table S3. Age and sex of patients.

Sample Type	Age	Sex
BALF Pos 1	58	M
BALF Pos 2	63	M
BALF Pos 3	48	M
BALF Pos 4	76	M
BALF Pos 5	65	M
Swab Pos 1	80	F
Swab Pos 2	51	F
Swab Pos 3	42	F
Swab Pos 4	30	F
Swab Pos 5	50	M
Swab Neg 1	48	M
Swab Neg 2	44	F
Swab Neg 3	43	F
Swab Neg 4	40	F
Swab Neg 5	40	F

Materials and Methods.

Mice.

C57BL/6J (Jax 00664) (wild-type; WT), B6.SJL-Ptprca Pepcb/BoyJ (*CD45.1*; Jax 002014), C57BL/6J-*Ticam1*^{Lps2}/J (*Ticam1*$^{-/-}$; Jax 005037), B6;129-*Mavs*^{tm1Zjc}/J (*Mavs*$^{-/-}$; Jax 008634, B6.FVB-*1700016L21RikTg(Itgax-DTR/EGFP)57Lan*/J (CD11c-DTR, Jax 004509) mice were purchased from Jackson Labs. C57BL/6 IL-28R$^{-/-}$ (*Ifnlr1*$^{-/-}$) mice were provided by Bristol-Myers Squibb. Mice were housed under specific pathogen-free conditions at Boston Children's Hospital. *Staphylococcus aureus* infections were conducted in the Biosafety Level-2 facility at Boston Children's Hospital. All procedures were approved under the Institutional Animal Care and Use Committee (IACUC) and conducted under the supervision of the department of Animal Resources at Children's Hospital (ARCH).

Reagents and antibodies.

Antibodies used in flow cytometry and sorting experiments are listed in Table S1. Live/dead cell markers, Zombie Red™ (423109) or Zombie Violet™ (423113) dyes were purchased from Biolegend. For in vitro and/or in vivo studies, poly (I:C) HMW (tlr-pic), R848 (tlr-r848) and 3p-hpRNA (tlrl-hprna) were purchased from Invivogen. For in vivo administration of type III IFN, we used polyethylene glycol-conjugated IFN-λ2 (PEG-IFN-λ) (gift from Bristol-Myers Squibb). Diphtheria toxin (unnicked) from *Corynebacterium diphtheriae* was purchased from Cayman Chemical. Anti-Ly6G antibody, clone 1A8 (BE0075-1) and rat IgG2a isotype control (BE0089) for in vivo administration was purchased from Bioxcell. 2'-Deoxy-5-ethynyl uridine (EdU) was

purchased from Carbosynth (NE08701). Chloroquine (PHR1258), fluorescein isothiocyanate (FITC), dextran (MW:10,000da) (FD10S), deoxyribonuclease (DNAse) I from bovine pancreas (DN25) and dispase II (D4693) were purchased from MilliporeSigma.

In vivo treatments and infection.

Intratracheal instillations (i.t.) were performed on anaesthetized mice (3% isoflurane) suspended by their incisors on an angled intubation stand with their tongue held to the side of the mouth by forceps. Inocula were dispensed in the oral cavity using a pipette. 2.5 mg/kg of poly (I:C) HMW, R848 or saline were administered i.t. daily for 6 days or as indicated in the figure legends. Where indicated, mice were treated i.t. with recombinant 50 μg/kg PEG-IFN-λ in combination with saline or R848 stimulation. *Staphylococcus aureus* subsp. *aureus* Rosenbach (ATCC® 25904™) was grown at 37°C in Tryptic Soy Broth (TSB) for 16 hours to the autolytic phase, then subcultured and grown to an optical density (OD_{600}) of 0.4, centrifuged and resuspended in PBS immediately prior to infection. Each mouse was infected by i.t. instillation of 5×10^7 CFU of *S. aureus* and sacrificed 12 hours post-infection, except for in survival studies. Rectal temperature and body weights were monitored daily.

Survival study and endpoints.

Mice were deemed to have reached endpoint at 75% of starting weight or after reaching body temperature of 25°C or lower.

Generation of bone-marrow chimeras.

To generate mice with hematopoietic-specific deletion of *Ifnlr1* or *Ticam1,* 6-week-old $CD45.1^+$ mice were exposed to lethal whole-body

irradiation (950 rads per mouse) and were reconstituted with 5×10^6 donor bone marrow cells from 6-week-old wild-type, *Ifnlr1*$^{-/-}$ or *Ticam1*$^{-/-}$ mice. Mice were treated with sulfatrim in the drinking water and kept in autoclaved cages for 2 weeks after reconstitution. After 2 weeks, mice were placed in cages with mixed bedding from wild-type, and *Ifnlr1*$^{-/-}$ or *Ticam1*$^{-/-}$ mice to replenish the microbiome and were allowed to reconstitute for two more weeks. A similar procedure was used to generate bone-marrow chimeras with stromal cells-specific deletion in *Ifnlr1*. Here, recipient WT or *Ifnlr1*$^{-/-}$ mice underwent irradiation and were reconstituted with BM cells derived from CD45.1$^+$ mice similarly as described above. To evaluate the percentage of chimerism, a sample of peripheral blood was taken from chimeric mice after 4 weeks of reconstitution and stained for CD45.1 and CD45.2 (antibodies as identified under "Reagents and antibodies") and were analyzed by flow cytometry.

Depletion of dendritic cells and neutrophils.

In order to deplete CD11c$^+$ cells, CD11c-DTR mice received 16 µg/kg diphtheria toxin (DTx) intravenously starting one day before TLR ligand or saline administration and continuing every other day until day 6 post-treatment to maintain depletion. In vivo depletion of neutrophils was carried out by injecting anti-Ly6G antibody (100 µg/mouse) intraperitoneally, starting one day before treatments and then continuing every other day through the duration of the treatment. As controls for no depletion, mice were injected with rat IgG isotype control.

Barrier permeability assessment.

To assess lung permeability, treated mice were administered FITC-dextran (10 μg/mouse) i.t. before or after *S. aureus* infection. After 1 hour of dextran instillation, blood was collected from the retro-orbital sinus, and the plasma was separated by centrifugation. Leakage of dextran in the bloodstream was measured as FITC fluorescence in the plasma compared to plasma from mock-treated mice.

BALF and lung collection.

Mice were euthanized by CO_2 inhalation. A capillary tube was inserted intratracheally, 3 ml of PBS were fluxed into the lungs (1ml at the time) and approximately 3 ml of BALF were collected. Samples were centrifuged (450g) and the supernatants were used for total protein measurement (Pierce BCA Protein Assay, Thermo Fisher Scientific #23227) and LDH quantification (Pierce LDH Cytotoxicity Assay, Thermo Fisher Scientific #C20301). Lungs were excised and used for RNA extraction using TRI Reagent (Zymo Research #R2050-1-200) (as described in "qRT-PCR and ELISA").

Bacterial load and lung cytokine production measurement.

The left lobe of the lung was weighed and homogenized in 1 ml of sterile deionized water in a Fisherbrand™ Bead Mill 24 Homogenizer. To calculate bacterial load, homogenate was serially diluted and plated on TSB-Agar plates in duplicate. Colonies were counted after a 16 hour-incubation, and bacterial burden in the lungs was calculated as CFU normalized to individual lung weight. Cytokines production in the lungs was measured in the supernatants collected after centrifuging the lung homogenates.

Flow cytometry and cell sorting.

Mice were euthanized by CO_2 inhalation and perfused by injection of 10 ml of PBS in the right ventricle. 2 ml of warm dispase solution (5 mg/ml) were instilled i.t. into the lungs followed by 0.5 ml of 1% low-melt agarose (Sigma #A9414) at 40°C and allowed to solidify on ice. Inflated lungs were incubated in dispase solution, for 30 min at RT. The lungs were then physically dissociated, incubated for 10 min with DNAse I (50 μg/ml), and filtered through 100-μm and 70-μm strainers. Red blood cells were lysed using ACK buffer. Single cell suspensions were stained with Zombie Red or Zombie Violet to discriminate between live and dead cells. Cells were then stained with antibodies against surface antigens diluted in PBS 0.2% BSA for 20 min at 4°C. Cells were then washed, fixed with 3.7% paraformaldehyde for 10 min at room temperature, washed again, and resuspended in PBS + 0.2% BSA. Samples were acquired on a BD LSRFortessa flow cytometer and data were analyzed using FlowJo v.10 software (BD Biosciences). CountBright Absolute Counting Beads (Invitrogen #C36950) were used to quantify absolute cell numbers.

For cell sorting, FACS samples were prepared as described above, excluding fixation, and sorted on Sony MA900 Cell Sorter following the sorting strategy indicated in fig. S12. The sorted cells were collected directly into TRI Reagent for RNA extraction. To detect cell proliferation, fixed cells were treated to assess 5-ethynyl-2'-deoxyuridine (EdU) incorporation as described below ("Epithelial cell proliferation") before being stained with antibodies against cell-surface antigens. Intracellular staining of Ki67 and p21 were carried

out using FoxP3 Fix/Perm Buffer set (Biolegend #421403) following the manufacturer's instructions.

Epithelial cell proliferation.

Proliferation of lung epithelial cells was monitored by assessing the incorporation of EdU (100 mg/kg, intraperitoneally, 12h before end-point euthanasia), and analyzed by flow cytometry or histology. Briefly, single cell suspensions of lung cells from mice injected with EdU were isolated as described before ("Flow cytometry and cell sorting"). Single cell suspensions were assessed for live/dead and fixed using 3.7% PFA. Staining for EdU was carried out by Click-chemistry reaction. Fixed cells were permeabilized with 0.1% Triton X100 (Millipore-Sigma) for 15 min. After permeabilization cells were washed and incubated with 4 mM Copper sulphate (Millipore-Sigma), 100 mM Sodium ascorbate (Millipore-Sigma) and 5 µM sulfo-Cyanine3-azide (Lumiprobe #A1330) in Tris Buffered Saline (TBS) 100mM, pH 7.6, for 30 min at room temperature.

Ion torrent.

For targeted transcriptome sequencing, 20 ng of RNA isolated from sorted cells was retro-transcribed to cDNA using SuperScript VILO cDNA Synthesis Kit (ThermoFisher Scientific). Barcoded libraries were prepared using the Ion AmpliSeq Transcriptome Mouse Gene Expression Kit as per the manufacturer's protocol and sequenced using an Ion S5 system (ThermoFisher Scientific). Differential gene expression analysis was performed using the Transcriptome Analysis Console (TAC) software with the ampliSeqRNA plugin (ThermoFisher Scientific).

Genes were called 'expressed' (n=11,294) if they had average $\log_2$ expression of 2 or greater in either WT or *Ifnlr1*$^{-/-}$. Differentially expressed genes (DEGs) between WT and *Ifnlr1*$^{-/-}$ were selected by thresholding on fold change ($\pm$1.5) and *P* value (0.005). In heatmaps, DEGs were Z-scaled and clustered (Euclidean distance, Ward linkage). Pathway analysis was performed with the R package hypeR, using Gene Set Enrichment Analysis on genes ranked according to their Log_2(Fold Change).

Cell culture.

In vitro FMS-like tyrosine kinase 3 ligand-differentiated dendritic cells (Flt3l-DCs) were derived from bone marrow cells in Iscove's Modified Dulbecco's Media (IMDM; Thermo Fisher Scientific), supplemented with 30% B16-Flt3l derived supernatant and 10% fetal bovine serum (FBS) for 9 days.

Splenic Flt3l-DCs were obtained by injecting mice subcutaneously with 2×10^6 B16-Flt3l cells and monitoring for tumor growth for two weeks. Spleens of the tumor-bearing mice were harvested, dissociated in PBS, filtered and the red blood cells were lysed. Cells from each spleen were resuspended in 3.5 ml Solution A (2.5 ml Dulbecco's Modified Eagle's Medium (DMEM) + 1 ml Opti-Prep (Millipore Sigma)), 4.5 ml Solution B (3.5 ml Buffer (0.88% NaCl, 1mM EDTA, 10mM HEPES, 0.5% BSA) + 1 ml Opti-Prep) and 2 ml Solution C (DMEM), in that order without disturbing the solution interfaces. The cells were centrifuged at 850 g for 20 min without brakes. Splenic Flt3l-DCs were obtained at the interface of Solutions C and B.

Flt3l-DCs were stimulated with poly (I:C), R848, or 3p-hpRNA. Where indicated, poly (I:C) and 3p-hpRNA were transfected with lipofectamine 300 (Invitrogen #L3000015) according to manufacturer's instructions at the concentrations indicated in the figure legends. Where indicated poly (I:C) stimulated cells were pre-treated with 10 μg/ml chloroquine for 5 min prior to stimulations. For sorting into cDC1 and cDC2, stimulated splenic Flt3l-DC were prepared similarly as described above ("Flow cytometry and cell sorting"). cDC1 were sorted as $B220^{-}CD11c^{+}MHC\text{-}II^{+}CD8a^{+}$ and cDC2 as $B220^{-}CD11c^{+}MHC\text{-}II^{+}CD8a^{-}$.

qRT-PCR and ELISA.

RNA was isolated from cell cultures using a GeneJET RNA Purification Kit (Thermo Fisher Scientific #K0731) according to manufacturer's instructions. RNA was extracted from excised lungs by homogenizing them in 1 ml of TRI Reagent. RNA was isolated from TRI Reagent samples using phenol-chloroform extraction or column-based extraction systems (Direct-zol RNA Microprep and Miniprep, Zymo Research #R2061 and #R2051) according to the manufacturer's protocol. RNA concentration and purity (260/280 and 260/230 ratios) were measured by NanoDrop (Thermo Fisher Scientific).

Purified RNA was analyzed for gene expression on a CFX384 real-time cycler (Bio-Rad) using a TaqMan RNA-to-CT 1-Step Kit (Thermo Fisher Scientific) or SYBR Green (Bio-Rad). Probes specific for *Ifnl2/3*, *Ifnb1*, *Il1b*, *Rsad2* and *Gapdh* were purchased from Thermo Fisher Scientific, and SYBR-Green primers for *Rsad2*, *Cxcl10*, *Gapdh* were purchased from Sigma (See Table S2).

Cytokine analyses were carried out using homogenized lung supernatants, and cell supernatants from stimulated FLT3L-DCs. Mouse IFNλ2/3 ELISA (R&D Systems DY1789B) and mouse IFNβ, IL1β, IL-6, and TNFα ELISAs (Invitrogen) were performed according to manufacturer's instructions.

Clinical samples.

BALF were obtained from five intensive care unit (ICU)-hospitalized SARS-CoV-2-positive patients. In parallel, five naso-oropharyngeal swabs were collected from both SARS-CoV-2-positive and -negative subjects. The negative swabs were obtained from subjects undergoing screening for suspected social contacts with COVID-19 subjects. Age and sex of patients is indicated in Table S3. Swabs were performed by using FLOQSwabs® (COPAN) in UTM® Universal Transport Medium (COPAN). All samples were stored at −80°C until processing. The study involving human participants was reviewed and approved by San Raffaele Hospital IRB in the COVID-19 Biobanking project. The patients provided informed written consent.

RNA extraction protocol and Real-Time PCR of clinical samples.

RNA extraction was performed by using PureLink™ RNA Thermo Fisher Scientific according to manufacturers' instruction. In particular, 500 µl for each BALF and swab analyzed sample were lysed and homogenized in the presence of RNase inhibitors. Ethanol was then added to homogenized samples, which were further processed through a PureLink™ Micro Kit Column for RNA binding. After washing, purified total RNA was eluted in 28 µl of RNase-free water. Reverse transcription was then performed according to SuperScript™ III First-

Strand Synthesis System (Invitrogen™) protocol by using 8 µl of RNA extracted from each BALF and swab sample. qRT-PCR analysis was then carried out to evaluate *IL6*, *IL1B*, *IFNB1*, *IFNA2*, *IFNL1* and *IFNL2* expression. All transcripts were tested in triplicate for each sample by using specific primers. *GAPDH* was also included. Probes were purchased from Thermo Fisher Scientific (See Table S2). Real-time analysis was then performed according to manufacturer instructions by using TaqMan® Fast Advanced Master Mix (Applied Biosystems™ by Thermo Fisher Scientific). Real-Time PCR Analysis was performed on ABI 7900 by Applied Biosystems.

Statistical Analyses.

Statistical significance for experiments with more than two groups was tested with one-way ANOVA, and Dunnett's multiple-comparison tests were performed. Two-way ANOVA with Tukey's multiple-comparison test was used to analyze kinetic experiments. Two-way ANOVA with Sidak's multiple-comparison test was used to analyze experiments with two grouped variables (i.e. treatment, genotype). Statistical significance for survival curves were evaluated with the log-rank (Mantel–Cox) test and corrected for multiple comparisons with Bonferroni's correction. To establish the appropriate test, normal distribution and variance similarity were assessed with the D'Agostino-Pearson omnibus normality test using Prism8 (Graphpad) software. When comparisons between only two groups were made, an unpaired two-tailed *t*-test was used to assess statistical significance. To determine the sample size, calculations were conducted in nQuery Advisor Version 7.0. Primary outcomes for each proposed experiment

were selected for the sample size calculation and sample sizes adequate to detect differences with an 80% power were selected. For animal experiments, 4-10 mice per group were used, as indicated in the figure legends.

References.

1. Blanco-Melo, Daniel, Benjamin E. Nilsson-Payant, Wen-Chun Liu, Skyler Uhl, Daisy Hoagland, Rasmus Møller, Tristan X. Jordan, et al. 2020. "Imbalanced Host Response to SARS-CoV-2 Drives Development of COVID-19." *Cell* 181 (5): 1036-1045.e9. https://doi.org/10.1016/j.cell.2020.04.026.
2. Blazek, Katrina, Hayley L. Eames, Miriam Weiss, Adam J. Byrne, Dany Perocheau, James E. Pease, Sean Doyle, Fiona McCann, Richard O. Williams, and Irina A. Udalova. 2015. "IFN-λ Resolves Inflammation via Suppression of Neutrophil Infiltration and IL-1β Production." *Journal of Experimental Medicine* 212 (6): 845–53. https://doi.org/10.1084/jem.20140995.
3. Broggi, Achille, Francesca Granucci, and Ivan Zanoni. 2020. "Type III Interferons: Balancing Tissue Tolerance and Resistance to Pathogen Invasion." *Journal of Experimental Medicine* 217 (1): e20190295. https://doi.org/10.1084/jem.20190295.
4. Broggi, Achille, Yunhao Tan, Francesca Granucci, and Ivan Zanoni. 2017. "IFN-λ Suppresses Intestinal Inflammation by Non-Translational Regulation of Neutrophil Function." *Nature Immunology* 18 (10): 1084–93. https://doi.org/10.1038/ni.3821.
5. Channappanavar, Rudragouda, Anthony R. Fehr, Jian Zheng, Christine Wohlford-Lenane, Juan E. Abrahante, Matthias Mack, Ramakrishna Sompallae, Paul B. McCray, David K. Meyerholz, and Stanley Perlman. 2019. "IFN-I Response Timing Relative to Virus Replication Determines MERS Coronavirus Infection Outcomes." *The Journal of Clinical Investigation* 129 (9): 3625–39. https://doi.org/10.1172/JCI126363.
6. Dinnon, Kenneth H., Sarah R. Leist, Alexandra Schäfer, Caitlin E. Edwards, David R. Martinez, Stephanie A. Montgomery, Ande West, et al. 2020. "A Mouse-Adapted Model of SARS-CoV-2 to Test COVID-19 Countermeasures." *Nature* 586 (7830): 560–66. https://doi.org/10.1038/s41586-020-2708-8.
7. Douam, Florian, Yentli E. Soto Albrecht, Gabriela Hrebikova, Evita Sadimin, Christian Davidson, Sergei V. Kotenko, and Alexander Ploss. 2017. "Type III Interferon-Mediated Signaling Is Critical for Controlling Live Attenuated Yellow Fever Virus Infection In Vivo." *MBio* 8 (4): e00819-17. https://doi.org/10.1128/mBio.00819-17.

8. Frieman, Matthew B., Jun Chen, Thomas E. Morrison, Alan Whitmore, William Funkhouser, Jerrold M. Ward, Elaine W. Lamirande, et al. 2010. “SARS-CoV Pathogenesis Is Regulated by a STAT1 Dependent but a Type I, II and III Interferon Receptor Independent Mechanism.” *PLoS Pathogens* 6 (4): e1000849. https://doi.org/10.1371/journal.ppat.1000849.
9. Galani, Ioanna E., Vasiliki Triantafyllia, Evridiki Evangelia Eleminiadou, Ourania Koltsida, Athanasios Stavropoulos, Maria Manioudaki, Dimitris Thanos, et al. 2017. “Interferon-λ Mediates Non-Redundant Front-Line Antiviral Protection against Influenza Virus Infection without Compromising Host Fitness.” *Immunity* 46 (5): 875-890.e6. https://doi.org/10.1016/j.immuni.2017.04.025.
10. Granados, Andrea, Adriana Peci, Allison McGeer, and Jonathan B. Gubbay. 2017. “Influenza and Rhinovirus Viral Load and Disease Severity in Upper Respiratory Tract Infections.” *Journal of Clinical Virology: The Official Publication of the Pan American Society for Clinical Virology* 86 (January): 14–19. https://doi.org/10.1016/j.jcv.2016.11.008.
11. Iwasaki, Akiko, and Padmini S. Pillai. 2014. “Innate Immunity to Influenza Virus Infection.” *Nature Reviews Immunology* 14 (5): 315–28. https://doi.org/10.1038/nri3665.
12. Jamieson, Amanda M., Lesley Pasman, Shuang Yu, Pia Gamradt, Robert J. Homer, Thomas Decker, and Ruslan Medzhitov. 2013. “Role of Tissue Protection in Lethal Respiratory Viral-Bacterial Coinfection.” *Science* 340 (6137): 1230–34. https://doi.org/10.1126/science.1233632.
13. Kato, Hiroki, Osamu Takeuchi, Shintaro Sato, Mitsutoshi Yoneyama, Masahiro Yamamoto, Kosuke Matsui, Satoshi Uematsu, et al. 2006. “Differential Roles of MDA5 and RIG-I Helicases in the Recognition of RNA Viruses.” *Nature* 441 (7089): 101–5. https://doi.org/10.1038/nature04734.
14. Lazear, Helen M., Brian P. Daniels, Amelia K. Pinto, Albert C. Huang, Sarah C. Vick, Sean E. Doyle, Michael Gale, Robyn S. Klein, and Michael S. Diamond. 2015. “Interferon-λ Restricts West Nile Virus Neuroinvasion by Tightening the Blood-Brain Barrier.” *Science Translational Medicine* 7 (284): 284ra59. https://doi.org/10.1126/scitranslmed.aaa4304.

15. Lee, Eun-Woo, Min-Sik Lee, Suzanne Camus, Jaewang Ghim, Mi-Ran Yang, Wonkyung Oh, Nam-Chul Ha, David P Lane, and Jaewhan Song. 2009. “Differential Regulation of P53 and P21 by MKRN1 E3 Ligase Controls Cell Cycle Arrest and Apoptosis.” *The EMBO Journal* 28 (14): 2100–2113. https://doi.org/10.1038/emboj.2009.164.
16. Major, Jack, Stefania Crotta, Miriam Llorian, Teresa M. McCabe, Hans Henrik Gad, Simon L. Priestnall, Rune Hartmann, and Andreas Wack. 2020. “Type I and III Interferons Disrupt Lung Epithelial Repair during Recovery from Viral Infection.” *Science* 369 (6504): 712–17. https://doi.org/10.1126/science.abc2061.
17. McCullers, Jonathan A. 2014. “The Co-Pathogenesis of Influenza Viruses with Bacteria in the Lung.” *Nature Reviews Microbiology* 12 (4): 252–62. https://doi.org/10.1038/nrmicro3231.
18. Medzhitov, Ruslan, David S. Schneider, and Miguel P. Soares. 2012. “Disease Tolerance as a Defense Strategy.” *Science (New York, N.Y.)* 335 (6071): 936–41. https://doi.org/10.1126/science.1214935.
19. Memish, Ziad A, Stanley Perlman, Maria D Van Kerkhove, and Alimuddin Zumla. 2020. “Middle East Respiratory Syndrome.” *Lancet (London, England)* 395 (10229): 1063–77. https://doi.org/10.1016/S0140-6736(19)33221-0.
20. Merad, Miriam, and Jerome C. Martin. 2020. “Pathological Inflammation in Patients with COVID-19: A Key Role for Monocytes and Macrophages.” *Nature Reviews Immunology* 20 (6): 355–62. https://doi.org/10.1038/s41577-020-0331-4.
21. Odendall, Charlotte, Andrew A. Voak, and Jonathan C. Kagan. 2017. “Type III IFNs Are Commonly Induced by Bacteria-Sensing TLRs and Reinforce Epithelial Barriers during Infection.” *The Journal of Immunology* 199 (9): 3270–79. https://doi.org/10.4049/jimmunol.1700250.
22. Peiris, J. S. M., C. M. Chu, V. C. C. Cheng, K. S. Chan, I. F. N. Hung, L. L. M. Poon, K. I. Law, et al. 2003. “Clinical Progression and Viral Load in a Community Outbreak of Coronavirus-Associated SARS Pneumonia: A Prospective Study.” *Lancet (London, England)* 361 (9371): 1767–72. https://doi.org/10.1016/s0140-6736(03)13412-5.

23. Planet, Paul J., Dane Parker, Taylor S. Cohen, Hannah Smith, Justinne D. Leon, Chanelle Ryan, Tobin J. Hammer, Noah Fierer, Emily I. Chen, and Alice S. Prince. 2016. “Lambda Interferon Restructures the Nasal Microbiome and Increases Susceptibility to Staphylococcus Aureus Superinfection.” *MBio* 7 (1): 1–12. https://doi.org/10.1128/mBio.01939-15.
24. Prokunina-Olsson, Ludmila, Noémie Alphonse, Ruth E. Dickenson, Joan E. Durbin, Jeffrey S. Glenn, Rune Hartmann, Sergei V. Kotenko, et al. 2020. “COVID-19 and Emerging Viral Infections: The Case for Interferon Lambda.” *The Journal of Experimental Medicine* 217 (5): e20200653. https://doi.org/10.1084/jem.20200653.
25. Rich, Helen E., Collin C. McCourt, Wen Quan Zheng, Kevin J. McHugh, Keven M. Robinson, Jieru Wang, and John F. Alcorna. 2019. “Interferon Lambda Inhibits Bacterial Uptake during Influenza Superinfection.” *Infection and Immunity* 87 (5): 1–12. https://doi.org/10.1128/IAI.00114-19.
26. Schulz, Oliver, Sandra S. Diebold, Margaret Chen, Tanja I. Näslund, Martijn A. Nolte, Lena Alexopoulou, Yasu Taka Azuma, Richard A. Flavell, Peter Liljeström, and Caetano Reis E. Sousa. 2005. “Toll-like Receptor 3 Promotes Cross-Priming to Virus-Infected Cells.” *Nature* 433 (7028): 887–92. https://doi.org/10.1038/nature03326.
27. Wölfel, Roman, Victor M. Corman, Wolfgang Guggemos, Michael Seilmaier, Sabine Zange, Marcel A. Müller, Daniela Niemeyer, et al. 2020. “Virological Assessment of Hospitalized Patients with COVID-2019.” *Nature* 581 (7809): 465–69. https://doi.org/10.1038/s41586-020-2196-x.
28. Ye, Liang, Daniel Schnepf, and Peter Staeheli. 2019. “Interferon-λ Orchestrates Innate and Adaptive Mucosal Immune Responses.” *Nature Reviews Immunology* 19 (10): 614–25. https://doi.org/10.1038/s41577-019-0182-z.
29. Zhang, Guqin, Chang Hu, Linjie Luo, Fang Fang, Yongfeng Chen, Jianguo Li, Zhiyong Peng, and Huaqin Pan. 2020. “Clinical Features and Short-Term Outcomes of 221 Patients with COVID-19 in Wuhan, China.” *Journal of Clinical Virology: The Official Publication of the Pan American Society for Clinical Virology* 127 (June): 104364. https://doi.org/10.1016/j.jcv.2020.104364.

30. Zhou, Zhuo, Lili Ren, Li Zhang, Jiaxin Zhong, Yan Xiao, Zhilong Jia, Li Guo, et al. 2020. “Heightened Innate Immune Responses in the Respiratory Tract of COVID-19 Patients.” *Cell Host & Microbe* 27 (6): 883-890.e2. https://doi.org/10.1016/j.chom.2020.04.017.

Chapter 3. The interferon landscape along the respiratory tract impacts the severity of COVID-19.

Benedetta Sposito[1,2,*], Achille Broggi[1,*,^], Laura Pandolfi[3], Stefania Crotta[4], Nicola Clementi[5,6], Roberto Ferrarese[5], Sofia Sisti[5], Elena Criscuolo[5], Roberto Spreafico[7], Jaclyn M Long[1], Alessandro Ambrosi[8], Enju Liu[9,10], Vanessa Frangipane[3], Laura Saracino[3], Sara Bozzini[3], Laura Marongiu[2], Fabio A Facchini[2], Andrea Bottazzi[11], Tommaso Fossali[12], Riccardo Colombo[12], Massimo Clementi[5,6], Elena Tagliabue[13], Janet Chou[1], Antonio E Pontiroli[14], Federica Meloni[3,15], Andreas Wack[4], Nicasio Mancini[5,6,#,^], Ivan Zanoni[1,8,#,^,$].

[1] Harvard Medical School, Boston Children's Hospital, Division of Immunology, Boston, 02115, US.

[2] Dep. of Biotechnology and Biosciences and Ph.D. program in Molecular and Translational Medicine (DIMET), University of Milano - Bicocca, Milan, 20100, Italy.

[3] Respiratory Disease Unit IRCCS San Matteo Hospital Foundation, Pavia, 27100, Italy.

[4] Immunoregulation Laboratory, The Francis Crick Institute, London, NW1 1AT, UK.

[5] Laboratory of Medical Microbiology and Virology, Vita-Salute San Raffaele University, Milan, 20100, Italy.

[6] IRCCS San Raffaele Hospital, Milan, 20100, Italy.

[7] Institute for Quantitative and Computational Biosciences, University of California, Los Angeles, United States.

[8] Faculty of Medicine and Surgery, Vita-Salute San Raffaele University, Milan, 20100, Italy.

[9] Harvard Medical School, Boston Children's Hospital, Division of Gastroenterology, Boston, 02115, US.

[10] Institutional Centers for Clinical and Translational Research, Boston Children's Hospital, Boston, MA, 02115, USA.

[11] Department of Anesthesia and Critical Care Medicine, IRCCS Policlinico San Matteo Foundation, Pavia, 27100, Italy.

[12] Division of Anesthesiology and Intensive Care, ASST Fatebenefratelli Sacco, Luigi Sacco Hospital, University of Milan, Milan, 20100, Italy.

[13] Value-based healthcare unit, IRCCS Multimedica, Milan, 20100, Italy.

[14] Department of Health Sciences, University of Milan, Milan, 20100, Italy.

[15] Department of Internal Medicine and Pharmacology, University of Pavia, Pavia, 27100, Italy.

* These authors contributed equally [#] These authors contributed equally

[$] Lead contact

^ Corresponding authors: ivan.zanoni@childrens.harvard.edu, mancini.nicasio@hsr.it, achille.broggi@childrens.harvard.edu

Cell *184, 4953–4968* (2021)

DOI: 10.1016/j.cell.2021.08.016

Abstract.

Severe coronavirus disease 2019 (COVID-19) is characterized by overproduction of immune mediators, but the role of interferons (IFNs) of the type I (IFN-I) or type III (IFN-III) families remains debated. We scrutinized the production of IFNs along the respiratory tract of COVID-19 patients and found that high levels of IFN-III, and to a lesser extent IFN-I, characterize the upper airways of patients with high viral burden but reduced disease risk or severity. Production of specific IFN-III, but not IFN-I, members denotes patients with a mild pathology and efficiently drives the transcription of genes that protect against severe acute respiratory syndrome corona- virus 2 (SARS-CoV-2). In contrast, compared to subjects with other infectious or noninfectious lung pathologies, IFNs are overrepresented in the lower airways of patients with severe COVID-19 that exhibit gene pathways associated with increased apoptosis and decreased proliferation. Our data demonstrate a dynamic production of IFNs in SARS-CoV-2-infected patients and show IFNs play opposing roles at distinct anatomical sites.

Graphical Abstract.

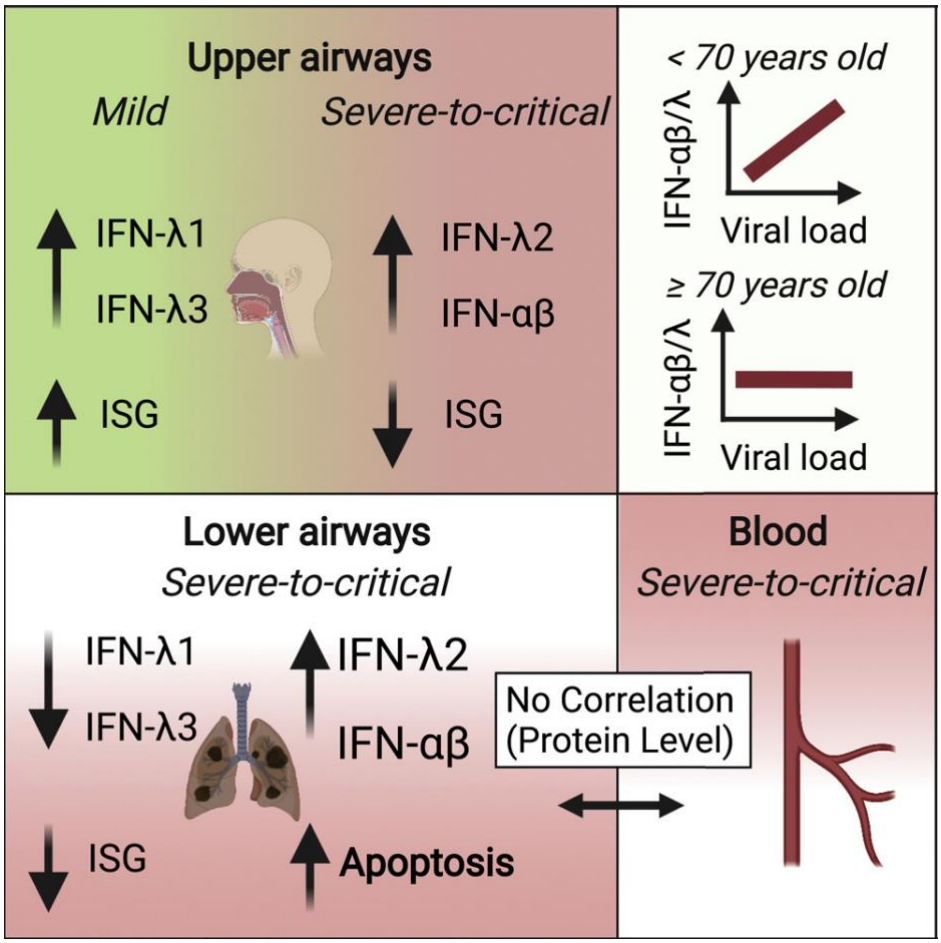

Introduction.

Since the outbreak of the coronavirus disease 2019 (COVID-19) in late 2019, the novel, severe acute respiratory syndrome coronavirus 2 (SARS-CoV-2) has infected over 188 million people globally and caused more than 4 million deaths as of July 2021. SARS-CoV-2 infection can lead to acute respiratory distress syndrome (ARDS) characterized by elevated levels of pro-inflammatory cytokines in the bloodstream (Guan et al. 2020; Lee et al. 2020; Lucas et al. 2020; F. Zhou et al. 2020). Mouse models and retrospective human studies suggest that severity and death following SARS-CoV-2 encounter is correlated with exaggerated inflammation rather than viral load (Bergamaschi et al. 2021; Guan et al. 2020; Karki et al. 2021; Lee et al. 2020; Lucas et al. 2020; Ruan et al. 2020; Winkler et al. 2020; F. Zhou et al. 2020). Nevertheless, how a balance between the benefits (restricting viral replication and spread) and risks (inducing a cytokine storm) of efficient immune cell activation is achieved during COVID-19 remains a mystery.

Of the many inflammatory mediators produced upon infection with SARS-CoV-2, interferons (IFNs) have attracted much attention since the inception of the pandemic. IFNs belong to three major families: IFN-I (mainly represented by IFN-αs and IFN-β), IFN-II (IFN-γ), and IFN-III (IFN-λ1-4). Upregulation of IFN-II in patients with severe COVID-19 (Karki et al. 2021; Lucas et al. 2020) is associated with increased PANoptosis, which exacerbates pathology and death (Karki et al. 2021). In contrast, the roles of IFN-I and IFN-III during SARS-CoV-2 infection have been a matter of debate. Indeed, IFN-I and IFN-III exert

potent anti-viral functions via the induction of IFN-stimulated genes (ISGs). Several studies showed that SARS-CoV-2, compared to other viruses, boosts the production of inflammatory mediators, while delaying and/or dampening anti-viral IFN responses in patients with severe COVID-19 (Blanco-Melo et al. 2020; Galani et al. 2021; Hadjadj et al. 2020; Mudd et al. 2020). Nevertheless, regulation of IFN-I and IFN-III production following infection with SARS-CoV-2 appears to be more complex. In fact, analyses of the nasopharyngeal swabs (Cheemarla et al. 2021; Lieberman et al. 2020; Ziegler et al. 2021), the bronchoalveolar lavage fluid (BALF) (Z. Zhou et al. 2020), or the peripheral blood monocytes (Lee et al. 2020) of COVID-19 patients have revealed potent ISG induction. Production of IFNs is also sustained in the blood of a longitudinal cohort of severe COVID-19 patients compared to subjects with a mild illness (Lucas et al. 2020).

Aside from the challenge of understanding the pattern of expression of IFNs, a major unanswered question is whether IFNs serve protective or detrimental functions in COVID-19. Recent studies show that patients with severe COVID-19 have defective IFN responses (Bastard et al. 2020; Combes et al. 2021; Laing et al. 2020; Pairo-Castineira et al. 2021; Wang et al. 2021; Zhang et al. 2020). Other studies, however, report that heightened and prolonged production of IFNs in patients infected with SARS-CoV-2 is correlated with negative clinical outcomes (Lee et al. 2020; Lucas et al. 2020). We and others have also recently demonstrated that the production of IFN-III, and to a lesser extent of IFN-I, impairs lung function and may trigger a severe disease in mouse models of lung viral infections (Broggi et al. 2020; Major et al. 2020).

Thus, it is urgent to fully unravel the role of IFNs in the pathogenesis of COVID-19.

To define how IFN production impacts the progression of COVID-19, here we analyzed the pattern and level of expression of IFNs and the transcriptional programs associated with the IFN landscape in the upper or lower respiratory tract of COVID-19 patients, subjects with infectious and non-infectious lung diseases and healthy controls.

Results.

High viral loads drive the efficient production of IFN-III, and to a lesser extent of IFN-I, in an age-dependent manner in the upper airways of COVID-19 patients.

We initially analyzed IFN gene expression in nasopharyngeal swabs derived from SARS-CoV-2 positive and negative subjects (**Table S1 and Supplemental Figure 1A-C**) and found that, in subjects positive for SARS-CoV-2, *IFNL1* and *IFNL2,3* (amongst type III interferons) and *IFNB1 and IFNA2* (amongst IFN-I) were significantly upregulated **(Figure 1A-F)**. As controls, *IL1B* and *IL6* were also analyzed in the same cohort of subjects (**Supplemental Figure 1D, E**). To account for the bimodal distribution of cytokine gene expression, we transformed gene expression data in discrete variables (expressed or undetected) and obtained results similar to what we observed with continuous gene expression (**Supplemental Figure 1F-M**).

Next, we examined the distribution of IFN levels relative to the viral load. Of the IFN-III family members, IFN-λ1 and IFN-λ2,3 positively correlated with viral load (**Figure 1G-I**). Amongst IFN-I, IFN-β and IFN-

α4 also showed a positive correlation with the viral load (**Figure 1J-L**). Transcript levels of the proinflammatory cytokines *IL1B* and *IL6* were also positively correlated with the viral load (**Supplemental Figure 1N-O**). Next, we divided our patient cohort into terciles based on the viral load (**Table S1**), and analyzed gene expression using discrete variables. These analyses confirmed that IFN-λ1, IFN-λ2,3, IFN-β, IL-1β and IL-6 were preferentially expressed in high, compared to low, viral load samples (**Supplemental Figure 1P-W**).

We, then, evaluated how IFN gene expression relates to the age of patients, a key determinant of severity and lethality of COVID-19 (McPadden et al. 2020; Williamson et al. 2020). Our analyses demonstrated that IFN-III and IFN-I expression is significantly associated with the viral load for the < 70 cohort (**Figure 1M-R**). In contrast, IFN expression in the ≥70 patient cohort either completely lost association with the viral load and/or showed a significantly lower correlation coefficient compared to the < 70 cohort (**Figure 1M-R**). IL-1β and IL-6 maintained their association with the viral load independent of age and were not significantly different in the two age cohorts (**Supplemental Figure 1X, Y**). When we analyzed gene expression as a discrete variable, we found that response patterns to viral load were significantly different between elderly (≥70) and younger (<70) patients for IFN-λ2,3 and IFN-α4 (**Supplemental Figure 1Z-AE and Table S2**). This analysis also showed that only younger patients have a dose-response relationship between IFN gene expression and viral load. In contrast to IFNs, no difference in the dose-response relationship between IL-1β and IL-6 expression and viral load

was observed between age groups (**Supplemental Figure 1AF, AG, and Table S2**). These results indicate that in COVID-19 patients the production of IFNs correlates with the viral load in the upper respiratory tract and that elderly patients, who are at risk of developing severe disease, have dysregulated IFN induction which correlates more loosely with the viral load compared to younger patients.

Mild COVID-19 is characterized by high levels of IFN-III, not IFN-I, in response to high viral loads in the upper airways.

To explore the link between IFN production and disease severity, we analyzed nasopharyngeal swabs from a subset of patients with known clinical follow-up. Disease severity was assessed as follows: patients with mild disease manifestations discharged from the emergency room without being hospitalized (home-isolated, HI); severe patients that required hospitalization (HOSP); and critically ill patients admitted to the intensive care unit (ICU) (**Table S3**). When gene expression levels were plotted against the viral load in HI vs. HOSP/ICU (**Figure 2A-H**), patients with a mild disease showed a positive correlation with expression of several members of the IFN-III family (**Figure 2A-C**). In HOSP/ICU patients this correlation was lost for IFN-λ2,3 and was significantly reduced for IFN-λ1 compared to HI patients (**Figure 2A, B**). In contrast to IFN-III, the positive correlation between *IL6* levels and viral load was maintained only for HOSP/ICU patients (**Figure 2H**). When members of the IFN-I family, or *IL1B* expression, were analyzed, no positive correlation was found in either hospitalized or HI patients (**Figure 2D**-**G**). To control for possible differences due to random

sampling, we assessed how the viral load varies based on the day from symptom onset in patients with different disease severity (**Table S3**) and found no significant difference (**Figure 2I**).

To further investigate the distribution of IFN-III production in subjects with mild, severe or critical illness, we performed K-mean clustering based on the expression of IFN-I, IFN-III and IL-1β. Our results reveal that cluster 3, characterized by the highest expression of IFN-III, was enriched in patients with milder disease manifestations and high viral load (**Figure 2J-M**, **Supplemental Figure 2A-E**). Notably, patients in cluster 2 (characterized by low levels of IFN-III and the highest levels of IFN-I) were 10 times more likely to have severe illness resulting in hospitalization or ICU admission than patients in cluster 3, and patients in cluster 1 (that presented low IFN-I and IFN-III expression and high IL-1β expression) showed a similar trend (**Figure 2J-M**, **Supplemental Figure 2A-C**). Overall, these data support the hypothesis that efficient production of IFN-III in the upper airways of COVID-19 patients with high viral load protects against severe COVID-19.

IFN-λ1 and IFN-λ3, but not IFN-λ2 or IFN-I, characterize the upper airways of patients with mild COVID-19 and drive ISGs that protect against SARS-CoV-2.

To gain more insight into the transcriptional programs linked to expression of specific IFN members, we used targeted RNA sequencing (RNA-seq) to examine the swabs of a subset of COVID-19 patients (**Table S4**). We found that IFN-λ1 and IFN-λ3 (now distinguishable from IFN-λ2 because of sequencing) segregated with subjects with mild

COVID-19 and a high viral load compared to healthy controls or more severely ill COVID-19 patients (**Figure 3A**). IFN-γ was expressed in patients with mild and severe COVID-19, while IFN-I as well as IFN-λ2 were mostly associated with critical, and to a lesser extent with severe, patients (**Figure 3A**). When gene set enrichment analysis was performed, the IFN responses were the most significantly enriched in subjects with mild, compared to severe or critical, COVID-19 (**Figure 3B** and **Supplemental Figure 3A, B**). When compared to swabs from SARS-CoV-2 negative subjects, only patients with mild and severe, but not critical, COVID-19 were enriched in IFN responses (**Supplemental Figure 3C**). To determine whether the pattern of IFNs found in HI patients drove a protective response against SARS-CoV-2, we tested expression of >50 ISGs that directly restrain SARS-CoV-2 infection (Martin-Sancho et al., 2021). RNA-seq data demonstrate that only patients with mild manifestations efficiently upregulated this set of protective ISGs (**Figure 3C and Supplemental Figure 3D, E**). and that this set of ISGs was significantly enriched compared to controls (**Supplemental Figure 3F**).

Due to the high sequence identity of the IFN-III family members (Broggi et al., 2020b), we, next, compared the capacity of IFN-λ1, IFN-λ2, and IFN-λ3 to induce specific ISGs. We stimulated human bronchial epithelial cells (hBECs) with different type III IFNs and found that IFN-λ1 induces and sustains the transcription of several ISGs more efficiently than IFN-λ2, and, to some extent, than IFN-λ3 (**Figure 3D-G**). Overall, our data demonstrate that specific members of the IFN families associate with mild or severe COVID-19. Also, that the

landscape of IFNs determines the ISGs induced in the upper airways and that IFN-λ1 is uniquely capable of inducing potent anti-SARS-CoV-2 ISGs in patients with mild COVID-19.

Members of the IFN-III and IFN-I families are over-represented in the lower airways of COVID-19 patients.

A detailed analysis of the IFNs produced in the lower airways of SARS-CoV-2 infected subjects is lacking. We, thus, analyzed BALF samples derived from COVID-19 hospitalized patients, including ICU-admitted subjects, and, as controls, samples derived from patients with non-infectious lung pathologies (sex and age distribution reported in **Table S5 and Supplemental Figure 4A-C**).

Transcripts of IFN-λ2,3, IFN-β, IFN-α2 and IFN-α4 were significantly upregulated in COVID-19 patients compared to controls (**Figure 4A-F**), while a similar percentage of subjects expressed the genes analyzed (**Supplemental Figure 4D-I**). No difference was observed for *IL1B* transcripts, while *IL6* mRNA levels appeared to be slightly increased in controls compared to COVID-19 patients (**Figure 4G, H and Supplemental Figure 4J, K**).

We next compared the expression of IFNs between the lower and upper airways of COVID-19 patients with similar disease severity. Sex and age were distributed as reported in **Table S5**. We found that, except for IFN-λ1, levels of IFNs in severe-to-critical patients were higher in the lower compared to the upper airways (**Figure 4I-N**), while a similar percentage of patients expressed IFNs in the upper or lower respiratory tract, except for IFN-α4 (**Supplemental Figure 4L-Q**). *IL1B* mRNA levels were not different in the upper and lower airways of

hospitalized COVID-19 patients, while *IL6* transcripts appeared to be predominantly expressed in the nasopharyngeal swabs compared to the BALF (**Figure 4 O, P and Supplemental Figure 4R, S**). These data demonstrate that selected members of both IFN-III and IFN-I families are over-represented in the lower airways compared to the upper airways of hospitalized COVID-19 patients.

Critical COVID-19 is characterized by the induction of a similar IFN landscape in the upper and lower airways.

We, next, performed RNA-seq of the BALF of a subset of ICU-isolated patients and of subjects with non-infectious lung pathologies (**Table S6**). Gene set enrichment analysis confirmed that IFN responses characterize COVID-19 patients, compared to non-microbially infected patients (**Figure 5A, B**). In keeping with the capacity of IFNs to increase apoptosis and facilitate lung tissue damage (Broggi et al. 2020; Major et al. 2020), gene enrichment also revealed that the p53 pathway is significantly upregulated in COVID-19 patients (**Figure 5A, C**). Notably, the IFNs landscape in the upper and lower airways of critical patients was strikingly similar (**Figure 5D**). Also, the induction of ISGs that protect against SARS-CoV2 was significantly decreased in the lower airways of critical COVID-19 patients, compared with the upper airways of patients with milder, as well as similar, disease severity (**Supplemental Figure 5A-C**). The gene signatures in the upper airways of mildly ill patients, compared with either the upper or lower airways of critical patients, were enriched for pathways associated with the induction of ISGs and other inflammatory pathways, (**Figure 5E**). In keeping with the capacity of IFNs to dampen cell proliferation and

delay tissue repair (Broggi et al. 2020; Major et al. 2020), gene programs linked to proliferation were significantly downmodulated in the lower airways of critical patients compared to the upper airways of subjects with a mild disease (**Supplemental Figure 5D**).

Overall, these data demonstrate that a unique IFN signature characterizes severe-to-critical COVID-19 patients along the respiratory tract and that the induction of unique set of IFNs is coupled with either protective ISGs, or gene programs associated with apoptosis and reduced proliferation.

A unique protein IFN signature characterizes the lower airways of COVID-19 patients compared to patients with other ARDS or non-infectious lung pathologies.

Our data show unique patterns of IFN gene expression in the lower airways of severe COVID-19 patients. However, whether the relative distribution of the IFN members, as measured by mRNA transcripts, correlates with their protein levels remains unknown. We thus assessed protein levels of IFNs and other inflammatory cytokines in the BALF of subjects infected with COVID-19 compared to the BALFs of patients with ARDS not driven by SARS-CoV-2 or patients with non-infectious lung involvement including fibrosis, sarcoidosis, or lung transplant (going forward, referred to as “controls”) (**Table S7**). In keeping with results of the transcriptional analyses, the levels of IFN-III and IFN-I measured in BALF from patients with COVID-19 were elevated (**Figure 6A-D and STAR Methods**), and, among IFN-III, showed a predominant induction of IFN-λ2,3 compared to IFN-λ1 (**Supplemental Figure 6A**). IFN-III and IFN-I were also significantly

upregulated in COVID-19 patients relative to controls, as well as when compared to patients with ARDS of different etiologies (except for IFN-λ1) (**Figure 6A-D and STAR Methods**). Finally, we found no correlation between age and protein levels in the lower airways of severe COVID-19 patients (**Supplemental Figure 6B-H and STAR Methods**).

When we compared the protein levels in the BALF and in the plasma of a subset of COVID-19 patients (**STAR Methods**), no correlation between these levels for any protein analyzed was found (**Figure 6E-J** and **Supplemental Figure 6I**), confirming at the protein level the transcriptional differences recently highlighted between the peripheral blood and the lungs of COVID-19 patients (Overholt et al. 2021).

When we performed unbiased K-means clustering of the protein analyzed, we found that COVID-19 patients were significantly enriched in cluster 3 which is characterized by a unique signature of IFNs (which encompasses all three IFN families) and IL-10 production (**Figure 6K-O** and **STAR Methods**). Many proinflammatory cytokines are also upregulated in cluster 2 which is enriched in patients who have ARDS that is not driven by SARS-CoV-2 (**Figure 6L and Supplemental Figure 6J**); most of these patients also express IFN-λ1, but not other IFNs. Control patients were, in contrast, enriched in cluster 1, characterized by low pro-inflammatory cytokine and IFN responses (**Figure 6L and Supplemental Figure 6K**).

Overall, these data demonstrate that COVID-19 patients are characterized by a unique IFN signature in the lower airways relative to patients with ARDS of different etiology.

Epithelial and immune cells dictate the IFN landscape.

Based on the heterogenous induction of IFNs along the respiratory tract of COVID-19 patients with different disease severity, we hypothesized that different populations of cells contribute to production of specific IFNs by activating discrete pattern recognition receptors (PRRs). Our finding that the mRNA for *IFNL1* is absent in the lower airways of COVID-19 patients (**Figure 4A**), but protein levels for IFN-λ1 are present at the same anatomical site (**Figure 6A**) suggests that cells that actively produce the mRNA for *IFNL1* are underrepresented in the BALF. However, *IFNL1* is one of the most upregulated genes in the upper airways, supporting the hypothesis that the cells that produce it are highly represented in the swabs. We, thus, explored the cellular composition of the swabs and BALFs by deconvoluting our bulk RNAseq data (**Figure 7A-C** and **Supplemental Figure 7A, B**). We found that the epithelial compartment, represented by several epithelial cell lineages, is more represented than the hematopoietic compartment in swabs from SARS-CoV-2 negative and positive subjects (**Figure 7A, C** and **Supplemental Figure 7A**). In contrast, BALFs from both SARS-CoV-2 negative and positive patients present very diversified hematopoietic populations (**Figure 7B** and **Supplemental Figure 7B**) that are more represented than epithelial cells (**Figure 7C**).

We, thus, explored how epithelial cells, or phagocytes, differentially contribute to the production of IFNs during SARS-CoV-2 encounter (**Figure 7D**). We confirmed that polarized hBECs of healthy individuals are sensitive to SARS-CoV-2 infection (**Supplemental Figure 7C**) and

respond by expressing IFNs (**Figure 7E-H**) and pro-inflammatory cytokines (**Supplemental Figure 7D, E**). Notably, hBECs infected with SARS-CoV-2 mostly produced IFN-λ1 compared to other IFNs (**Figure 7E-H**). Among human phagocytes, plasmacytoid (p)DCs respond to SARS-CoV-2 by producing mainly IFN-I (Onodi et al. 2021). Based on the potent induction of IFN-III in patients with mild COVID-19, we focused our attention on conventional (c)DCs that we recently described as major producers of IFN-III in the lungs of mice (Broggi et al. 2020). Human cDCs isolated from the blood of healthy donors did not produce IFNs or other inflammatory cytokines when exposed to SARS-CoV-2 *in vitro* (*data not shown*). To test the possible involvement of cDCs during COVID-19, we infected a human lung epithelial cell (hLEC) line with SARS-CoV-2 and exposed cDCs to the supernatant of these cells. We found that only cDCs exposed to the supernatant of virally-infected hLECs upregulated the expression of IFN-λ2,3 (but not IFN-λ1), members of the IFN-I family, as well as IL-1B and IL-6, (**Figure 7I-L and Supplemental Figure 7F, G**).

To identify the PRRs involved in the production of IFNs by either human epithelial cells or cDCs, we tested different PRR ligands (**Figure 7M)**. In keeping with a central role of the RIG-I/MDA-5 pathway in epithelial cells for sensing SARS-CoV-2 (Liu et al. 2021; Wu et al. 2021; Yin et al. 2021), stimulation of the RIG-I pathway, and to a lesser extent of TLR3, in epithelial cells potently induced the transcripts of IFN-III and IFN-I, but not of other pro-inflammatory mediators (**Supplemental Figure 7H,** and **STAR Methods**). The analysis of protein levels confirmed the transcriptional data (**Figure 7N, Supplemental Figure 7I,**

J, and **STAR Methods**). In keeping with SARS-CoV-2 infection, epithelial cells were more potent producers of IFN-λ1 compared to IFN-λ2,3 upon stimulation of TLR3, RIG-I and MDA-5 pathways (**Figure 7N, Supplemental Figure 7I**).

We next evaluated the response of cDCs. As a comparison, we also treated bulk peripheral blood mononuclear cells (PBMCs), monocytes isolated from PBMCs, as well as monocyte-derived DCs (moDCs). While PBMCs were particularly able to produce IFN-II in response to viral and bacterial ligands, cDCs were uniquely capable of producing very high levels of IFN-λ2,3, and to a lesser extent of IFN-λ1, solely in response to TLR3 stimulation (**Figure 7O, Supplemental Figure 7K-M,** and **STAR Methods**). Monocytes and moDCs were poor producers of IFNs in response to all the stimuli tested. When these analyses were extended to other inflammatory mediators, each cell type revealed a unique pattern of protein production (**Supplemental Figure 7N,** and **STAR Methods**), underscoring the complexity and cell-specificity of the inflammatory response.

Collectively, these data demonstrate that epithelial cells preferentially produce IFN-λ1 upon SARS-CoV-2 infection and suggest that IFN production is driven via RIG-I/MDA-5 or TLR3 stimulation. Also, that cDCs only respond to the supernatant of SARS-CoV-2-infected cells, and that TLR3 is the major driver of IFN-III production by human cDCs

Discussion.

COVID-19 has caused millions of deaths, and has had devastating societal and economic effects. Notwithstanding the efficacy of the

COVID-19 vaccines, a better understanding of the molecular underpinnings that drive the severe disease in patients infected with the SARS-CoV-2 virus is imperative to implement effective additional prophylactic and/or therapeutic interventions. IFN-I and IFN-III are potent anti-viral cytokines and the potential of using clinical grade recombinant IFN-I or IFN-III as therapeutics has raised much hope and interest (Prokunina-Olsson et al. 2020). To date, though, opposing evidence has complicated our view of the role played by members of the IFN-I and IFN-III families during SARS-CoV-2 infection.

We found that in the upper airways of patients with mild manifestations, the presence of IFN-λ1 and IFN-λ3, but not IFN-λ2 or IFN-I, was associated with the induction of ISGs known to efficiently contain SARS-CoV-2. Our data also demonstrated that critically ill patients express high levels of IFN-I (and IFN-λ2) compared to subjects with a mild disease or healthy controls. These patients show a reduced induction of protective ISGs and, in general, of IFN responses. Two non-mutually exclusive explanations for this behavior may be that: i) the pattern of IFN expression of critically ill patients is less capable of inducing the protective ISGs; ii) other factors, such as the production of specific antibodies that block ISG induction (Combes et al. 2021), or viral adaptation to evade control by IFN-I (Lei et al. 2020; Xia et al. 2020), restrain the capacity of this set of IFNs to mount a strong response.

The present in-depth analysis shows not only that high viral loads of SARS-CoV-2 induce the efficient production of IFN-III in the upper airways of younger and/or milder patients, but also that severely ill

COVID-19 patients are characterized by the highest levels of IFNs (at the mRNA as well as protein levels) in the lower airways. These data support the hypothesis that IFNs have opposing roles along the respiratory tract, and reconcile some of the seemingly contradictory findings on IFNs in COVID-19 patients. Efficient initiation of IFN production in the upper airways can lead to a more rapid elimination of the virus and may limit viral spread to the lower airways, as suggested by studies that report defects in IFN signaling of severe COVID-19 patients (Bastard et al. 2020; Pairo-Castineira et al. 2021; Wang et al. 2021; Zhang et al. 2020). On the other hand, when the virus escapes immune control in the upper airways, the IFN production that is potently boosted in the lungs likely contributes to the cytokine storm and associated tissue damage, that are typical of patients with severe-to-critical COVID-19, characterized by reduced proliferation and increased pro-apoptotic p53 transcriptional signatures.

Another novel finding in the present study is that the type of IFN produced in response to different PRR pathways varies according to cell types. In keeping with $ACE2^{+}$ cells being the primary cells infected by SARS-CoV-2, we measured a potent immune response in human bronchial epithelial cells, but not in cDCs infected with SARS-CoV-2. Nevertheless, we found that cDCs efficiently express specific members of the IFN-III and IFN-I families when exposed to the supernatant of lung epithelial cells previously infected with SARS-CoV-2, or in response to dsRNA. These data suggest that cDCs, despite not responding directly to SARS-CoV-2 infection, may play fundamental

roles in recognizing intermediates of viral replication and/or DAMPs released by dying cells.

Finally, our findings highlight the importance of the timing of production and/or administration of IFNs during COVID-19 and suggest that early administration (before infection or early after symptom onset) of specific recombinant IFN-III may be an effective therapeutic intervention, and that targeting the upper airways, while avoiding systemic administration as previously proposed (Park and Iwasaki 2020), represents the best way to exploit the anti-viral activities of IFNs.

In conclusion, our data define the anatomical map of inter and intra-family production of IFNs during COVID-19, and highlight how IFN production is linked to the different clinical outcomes, based on the location of the IFN response. Our findings reconcile a large portion of the literature on IFNs, and further stress the key role played by IFN-III, compared to IFN-I, at mucosal surfaces during life-threatening viral infections. These findings will be fundamental for designing appropriate pharmacological interventions to prevent infection with SARS-CoV-2 or to dampen the severity of COVID-19 and will help to better understand how the IFN landscape affects human immune responses to respiratory viral infections.

Limitations of the Study.

Our findings shed new light on the nature of the IFNs and on the molecular pathways that drive intrinsic immunity. The capacity of lung epithelial cells to recognize and respond to viral components is confounded by the presence of SARS-CoV-2 effector proteins which block immune recognition and IFN production (Banerjee et al. 2020; Konno et al. 2020; Lei et al. 2020; Wu et al. 2021). We show that high viral load in the upper airways of COVID-19 patients induces a potent immune response and that viral loads are not correlated *per se* with disease severity. High viral loads in the upper airways may therefore be associated to a protective immune response in young individuals, whilst eliciting a dysregulated inflammatory response in older patients, as observed in our study. Nevertheless, additional studies are needed to directly link specific IFNs to particular cell types and, above all, to specific protective or detrimental immune cell functions. As an example, our data suggest that cDCs do not directly sense SARS-CoV-2. Intriguingly, a recent report showed that specific cDC subtypes may instead respond to SARS-CoV-2 encounter (Marongiu et al. 2022), but the capacity of these subtypes to produce specific IFNs remains an open question. Furthermore, understanding the specific contribution of different PRRs to the IFN response elicited in patients infected with SARS-CoV-2 also requires further analyses.

Acknowledgments.

We thank the members of the Zanoni and Mancini laboratories for thoughtful discussion and comments on the project. IZ is supported by NIH grants 2R01AI121066, 5R01DK115217, NIAID-DAIT-NIHAI201700100, Lloyd J. Old STAR Program CRI3888, and holds an Investigators in the Pathogenesis of Infectious Disease Award from the Burroughs Wellcome Fund. NM is supported by IRCSS San Raffaele Hospital Program Project Covid-19 funds. Research done in the Wack lab was funded in whole, or in part, by the Wellcome Trust [FC001206]. For the purpose of Open Access, the author has applied a CC BY public copyright license to any Author Accepted Manuscript version arising from this submission. SC and AW were supported by the Francis Crick Institute which receives its core funding from Cancer Research UK (FC001206), the UK Medical Research Council (FC001206) and the Wellcome Trust (FC001206). We thank: Dr. Renato Ostuni (TIGET, Hospital San Raffaele) for granting access to the ViiA7 Real-Time PCR System; Saira Hussain (Francis Crick Institute) for preparing the virus stock used in lung epithelial cell infection experiments; and Drs. Daniele Lilleri and Chiara Fornara (IRCCS Policlinico San Matteo Foundation) for granting the use of the cytofluorimeter. RS thanks the UCLA Institute for Quantitative and Computational Biosciences (QCBio) Collaboratory community directed by Matteo Pellegrini.

Author Contributions.

BS and A Broggi designed, performed, analyzed experiments and edited the text; LP, VF, LS, A Bottazzi, TF, CR, FM, SB performed protein analyses on the BALF fluids; SC and AW designed and performed analyses on human lung epithelial cells; AA, EL, ET and AEP helped with statistical analyses; RF, SS, NC, MC, LM, FAF, helped in the analyses of the gene quantification from the swabs; NC and EC designed, performed and analyzed experiments with infected epithelial cells and cDCs; JML performed qPCR analyses in vitro and edited the text; RS, SW, JC helped with targeted RNAseq analyses; NM designed the experiments, supervised the project and edited the text; IZ conceived and supervised the project, designed the experiments and wrote the paper.

Figures.

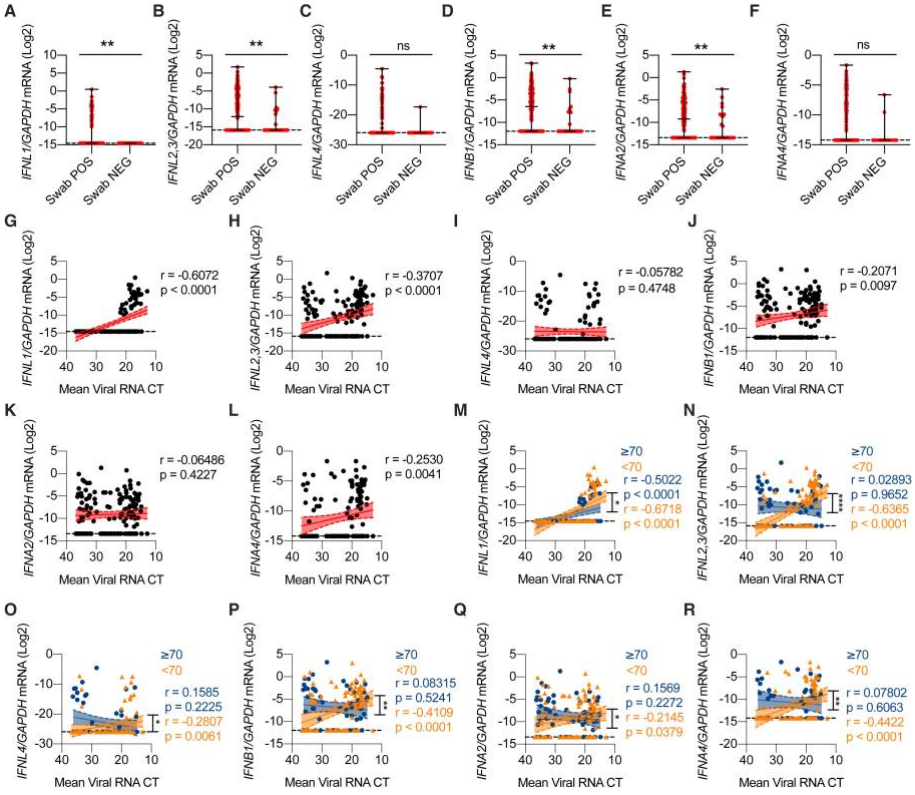

Figure 1. High viral loads drive the efficient production of IFN-III, and to a lesser extent of IFN-I, in an age-dependent manner in the upper airways of COVID-19 patients. (**A-F**) *IFNL1* (**A**)*, IFNL2,3* (**B**)*, IFNL4* (**C**), *IFNB1* (**D**), *IFNA2* (**E**), *IFNA4* (**F**) mRNA expression was evaluated in nasopharyngeal swabs from SARS-CoV-2-negative (Swab NEG) and -positive (Swab POS) subjects. Each dot represents a patient. Median with range is depicted. Dashed line represents limit of detection. (**G-L**) *IFNL1* (**G**)*, IFNL2,3* (**H**)*, IFNL4* (**I**), *IFNB1* (**J**), *IFNA2* (**K**), *IFNA4* (**L**) mRNA expression is plotted against mean viral RNA CT in swabs from SARS-CoV-2^{+} patients. Each dot represents a patient. Linear regression lines (continuous line) and 95% confidence interval (dashed line and shaded

area) are depicted in red. Spearman correlation coefficients (r) and p-value (p) are indicated. (**M-R**) *IFNL1* (**M***), IFNL2,3* (**N***), IFNL4* (**O**), *IFNB1* (**P**), *IFNA2* (**Q**), *IFNA4* (**R**) mRNA expression is plotted against mean viral RNA CT in swabs from SARS-CoV-2^{+} patients over 70-year-old (≥ 70, blue dots and lines) and below 70-year-old (< 70, orange dots and lines). Each dot represents a patient. Linear regression (continuous lines) and 95% confidence interval (dashed line and shaded area) are depicted. Spearman correlation coefficients (r) and p-value (p) are indicated in blue and in orange for ≥70 and <70 year-old patients respectively. (**A-R)** Expression is plotted as log2 (*gene*/*GAPDH* mRNA + 0.5 x gene-specific minimum). Statistics: (**A-F**) Mann-Whitney test: ns, not significant (P>0.05); *P<0.05, **P<0.01, ***P<0.001, and ****P<0.0001. (**M-R**) Test difference between simple linear regression slopes: ns, not significant (P>0.05); *P<0.05, **P<0.01, ***P<0.001, and ****P<0.0001. See also **Figure S1** and **Table S1**.

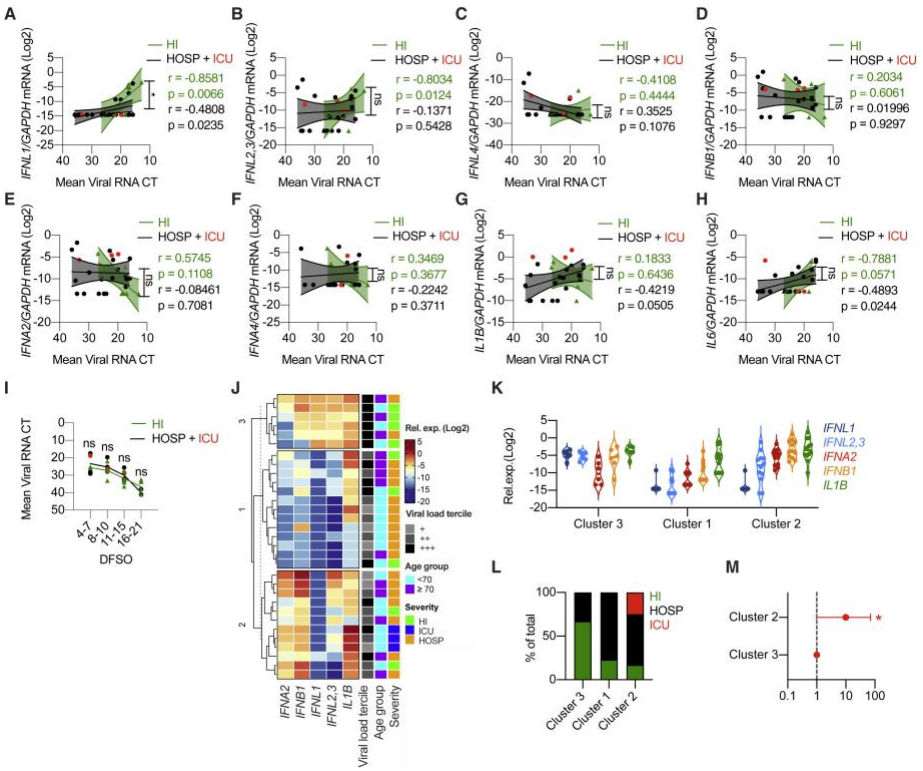

Figure 2. Mild COVID-19 is characterized by high levels of IFN-III, not IFN-I, in response to high viral loads in the upper airways. (**A-M**) Swabs from a cohort of SARS-CoV-2^{+} patients with known disease severity hospitalized patients and ICU inpatients (HOSP, black dots, ICU, red dots, both HOSP and ICU black lines and analyzed together) and home-isolated patients (HI, green dots and lines) were analyzed. (**A-H**) *IFNL1* (**A**)*, IFNL2,3* (**B**)*, IFNL4* (**C**), *IFNB1* (**D**), *IFNA2* (**E**), *IFNA4* (**F**), *IL1B* (**G**), and *IL6* (**H**) mRNA expression is plotted against mean viral RNA CT. Each dot represents a patient. Linear regression lines (continuous line) and 95% confidence interval (dashed line and shaded area) are depicted. Spearman correlation coefficients (r) and p-value (p) are indicated in black and in green for "HOSP + ICU" and "HI"

patients respectively. (**I**) Mean viral RNA CT values are plotted against days from symptom onset (DFSO). Each dot represents a patient. Lines connect mean values for each range of DFSO. (**J**) K-means clustering based on the expression of *IFNA2, IFNB1 IFNL1, IFNL2,3*, *IL1B* was used to determine clusters 1-3 (Cluster 1 n=13, Cluster 2 n=12, Cluster 3 n=6). The color indicates the relative gene expression. Viral load tercile, age group and severity are annotated. Viral load terciles ("+++", "++", "+") are defined by mean viral RNA CT (<20, >20 and <30, > 30). Age groups are defined as <70 or ≥70-year old patients. (**K**) *IFNL1, IFNL2,3*, *IFNA2, IFNB1, IL1B* mRNA expression within clusters identified in **Figure 2J**. Each dot represents a patient. Violin plots are depicted. (**L**) Percentage of patients with the indicated disease severity within clusters identified in **Figure 2J.** (**M**) Odds ratio of patients in Cluster 2 being hospitalized or admitted to the ICU relative to patients in Cluster 3 (Clusters identified in **Figure 2J).** Symbols represent the odds ratio. Error bars represent the 95% confidence interval associated to the odds ratio. (**A-H, K**) Expression is plotted as log2 (*gene*/*GAPDH* mRNA + 0.5 x gene-specific minimum). Statistics: (**A-H**) Test difference between simple linear regression slopes: ns, not significant (P>0.05); *P<0.05, **P<0.01, ***P<0.001, and ****P<0.0001. (**I**) Two-way ANOVA: ns, not significant (P>0.05); *P<0.05, **P<0.01, ***P<0.001, and ****P<0.0001. (**L**) Chi Square test for odds ratio: ns, not significant (P>0.05); *P<0.05, **P<0.01, ***P<0.001. See also **Figure S2** and **Table S3**.

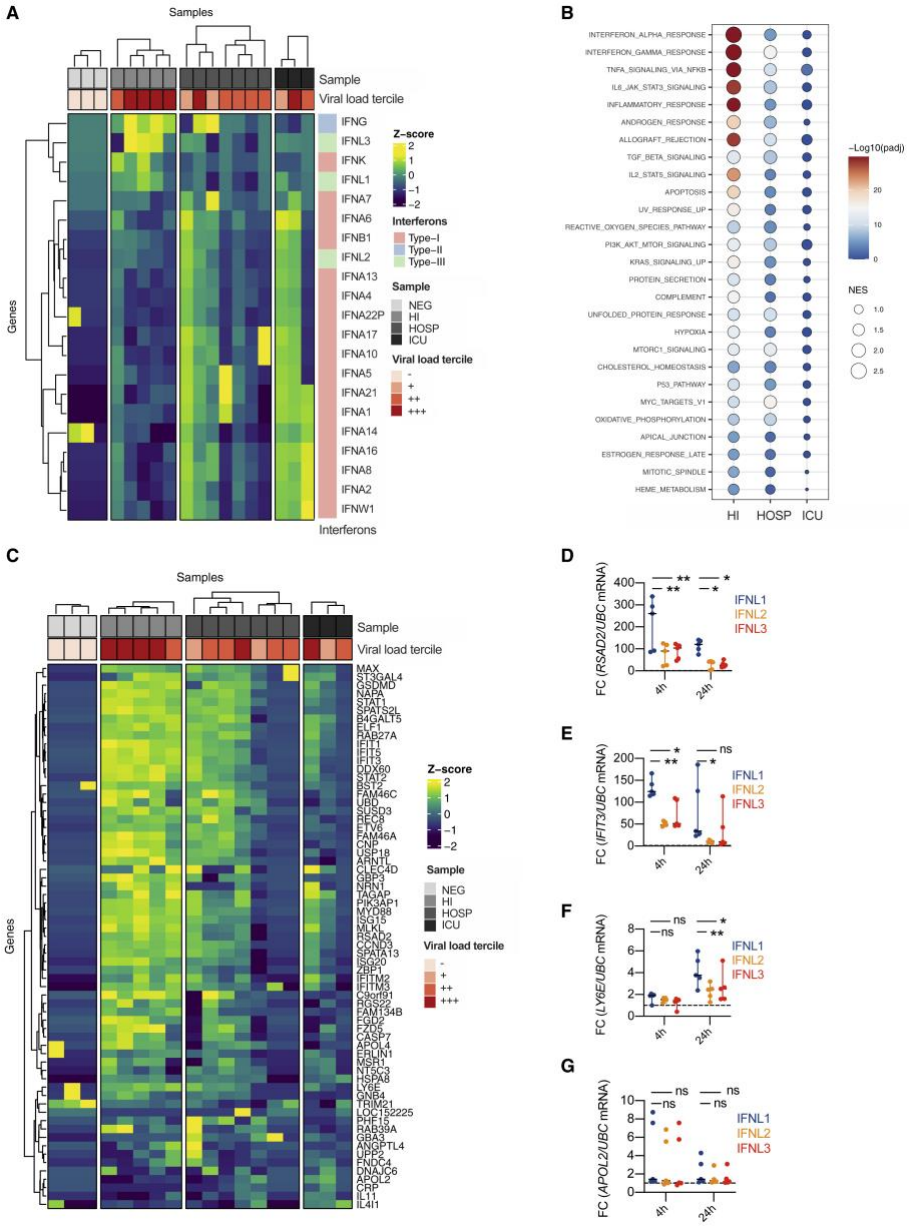

Figure 3. IFN-λ1 and IFN-λ3, but not IFN-λ2 or IFN-I, characterize the upper airways of patients with mild COVID-19 and drive ISGs that protect against SARS-CoV-2. (A-C) Targeted RNA-sequencing of nasopharyngeal swabs from SARS-CoV-2 negative (NEG, 3) and

positive patients with known disease severity: home-isolated patients (HI, 5), hospitalized patients (HOSP, 7), ICU inpatients (ICU, 3). (**A**) Heatmap depicting expression of type I / II / III IFNs. The color is proportional to the Z Score. (**B**) Bubble plot visualization of gene set enrichment analysis (GSEA) for pathways enriched in HI, HOSP and ICU patients. Normalized enrichment score (NES) is depicted. Color coding corresponds to -Log10 (p adjusted value). Pathway with padj val <0.05 in either group are represented. (**C**) Heatmap depicting expression of ISG genes that protect against SARS-CoV-2. The color is proportional to the Z Score. (**D-G**) Human bronchial epithelial cells (hBECs) were treated with human recombinant IFN-λ1, IFN-λ2, IFN-λ3 at a concentration of 2ng/ml for 4 or 24 hours. *RSAD2* (**D**) *IFIT3* (**E**), *LY6E* (**F**), *APOL2* (**G**) mRNA expression was evaluated. Each dot represents a biological replicate. Median with range is depicted. FC = Fold change compared to untreated cells. Statistics: (**D-G**) Two-way ANOVA: ns, not significant ($P>0.05$); *$P<0.05$, **$P<0.01$, ***$P<0.001$, and ****$P<0.0001$. See also **Figure S3** and **Table S4**.

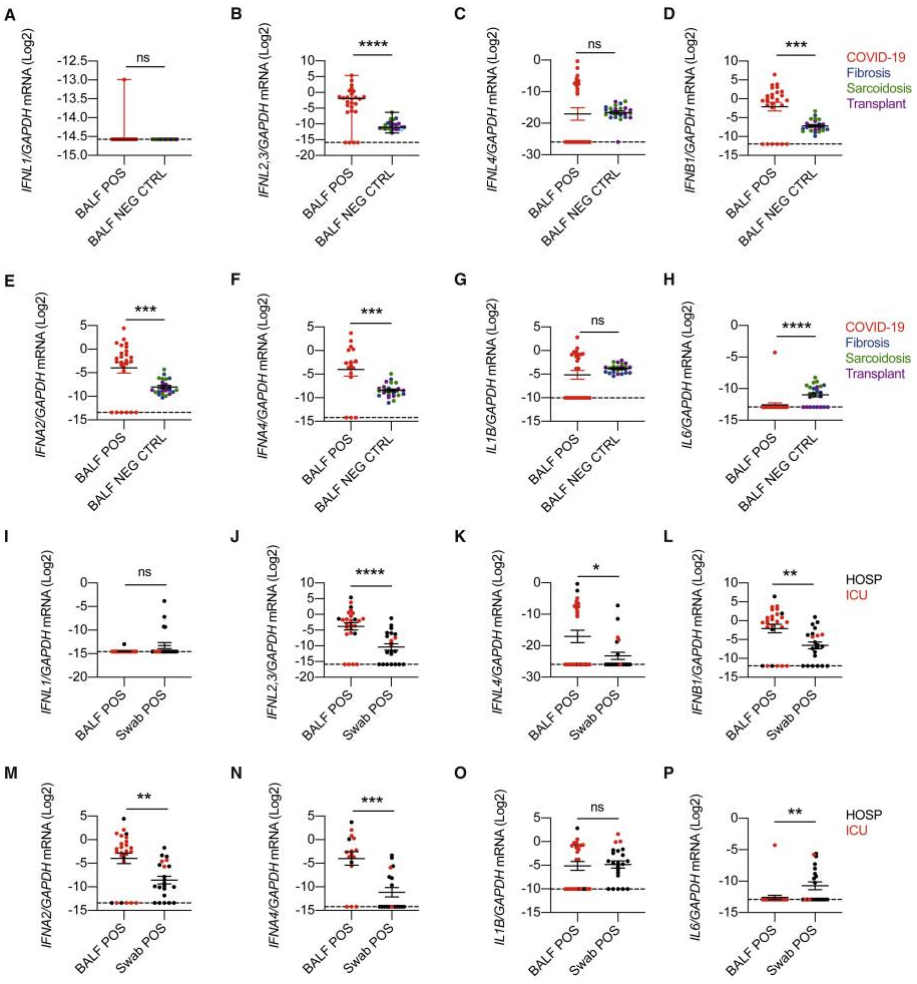

Figure 4. Members of the IFN-III and IFN-I families are over-represented in the lower airways of COVID-19 patients. (**A-H**) *IFNL1* (**A**)*, IFNL2,3* (**B**)*, IFNL4* (**C**), *IFNB1* (**D**), *IFNA2* (**E**), *IFNA4* (**F**), *IL1B* (**G**), and *IL6* (**H**) mRNA expression was evaluated in BALF from SARS-CoV-2-positive (BALF POS, 26, black dot) and -negative (BALF NEG CTRL, 24) patients with non-infectious lung involvement such as fibrosis (8, blue dot), sarcoidosis (8, green dot) or lung transplant (8, purple dot). (**I-P**) *IFNL1* (**I**)*, IFNL2,3* (**J**)*, IFNL4* (**K**), *IFNB1* (**L**), *IFNA2* (**M**), *IFNA4* (**N**), *IL1B* (**O**), and *IL6* (**P**) mRNA expression was evaluated in BALF (BALF POS,

26) and swabs (Swab POS, 21) from SARS-CoV-2-positive subjects that were either hospitalized (black dots) or ICU inpatients (red dots). (**A-P**) Expression is plotted as log2 (*gene*/*GAPDH* mRNA + 0.5 x gene-specific minimum). Each dot represents a patient. Median with range is depicted. Statistics: (**A-P**) Mann-Whitney test: ns, not significant ($P>0.05$); *$P<0.05$, **$P<0.01$, ***$P<0.001$, and ****$P<0.0001$. See also **Figure S4** and **Table S5**.

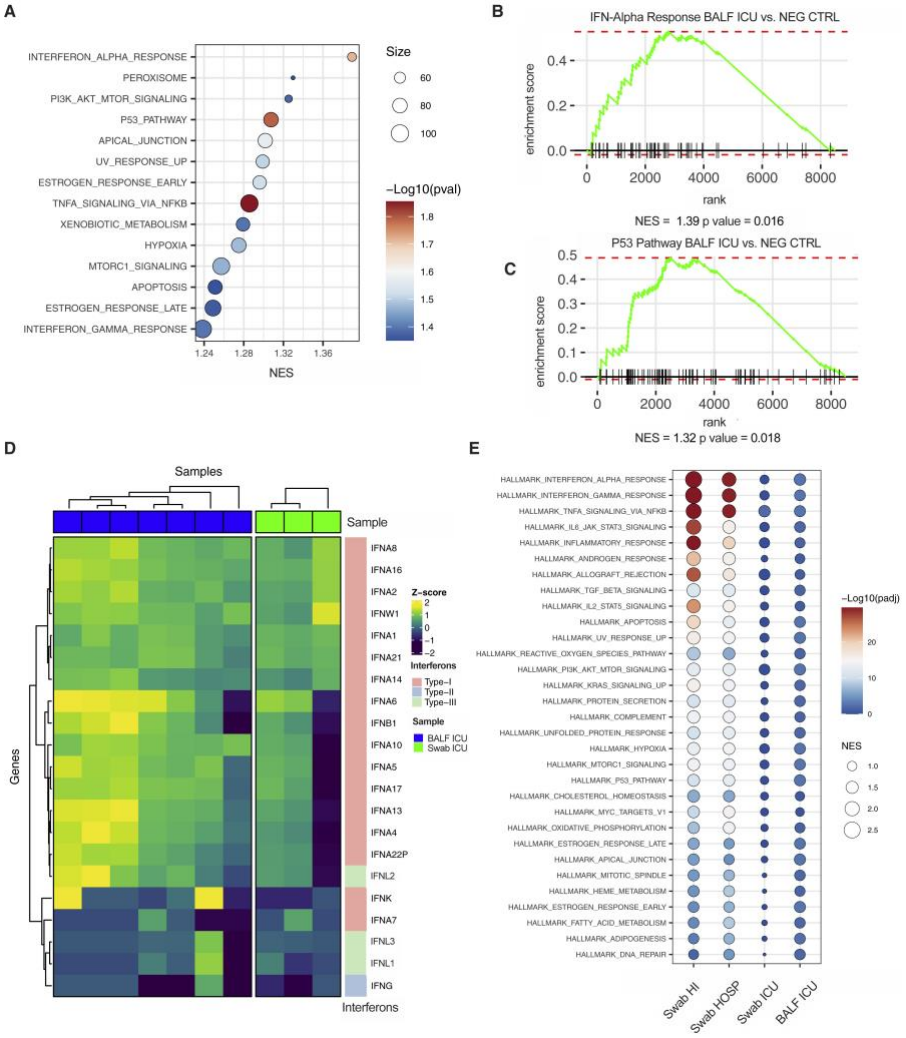

Figure 5. Critical COVID-19 is characterized by the induction of a similar IFN landscape in the upper and lower airways. (**A-E**) Targeted RNA-sequencing of BALF from SARS-CoV-2 positive patients (BALF ICU, 7), from patients with non-infectious lung pathologies (BALF NEG CTRL, 5) and from nasopharyngeal swabs from SARS-CoV-2 positive patients that were either ICU inpatients (Swab ICU, 3) hospitalized (Swab HOSP, 7) or home-isolated (Swab HI, 5). The color is proportional to the Z Score (**A**) Bubble plot visualization of gene set

enrichment analysis (GSEA) for pathways enriched in BALF ICU compared to BALF NEG CTRL samples. Normalized enrichment score (NES) is depicted. Color coding corresponds to -Log10(p adjusted value), size corresponds to the number of genes detected for each pathway. Pathways with pval <0.05 are depicted. (**B-C**) GSEA enrichment plot for genes belonging to the interferon alpha response (**B**) and p53 pathway (**C**) in BALF ICU and BALF NEG CTRL samples. (**D**) Heatmap depicting expression of type I / II / III IFNs in BALF ICU and Swab ICU samples. (**E**) Dot plot visualization of gene set enrichment analysis (GSEA) for pathways enriched in the lower airways of critical patients (BALF ICU) and the upper airways of patients with different disease severity (Swab HI, Swab HOSP, Swab ICU). NES is depicted. Color coding corresponds to -Log10(p adjusted value). Pathways with padj<0.05 in any of the groups are depicted. See also **Figure S5** and **Table S6**.

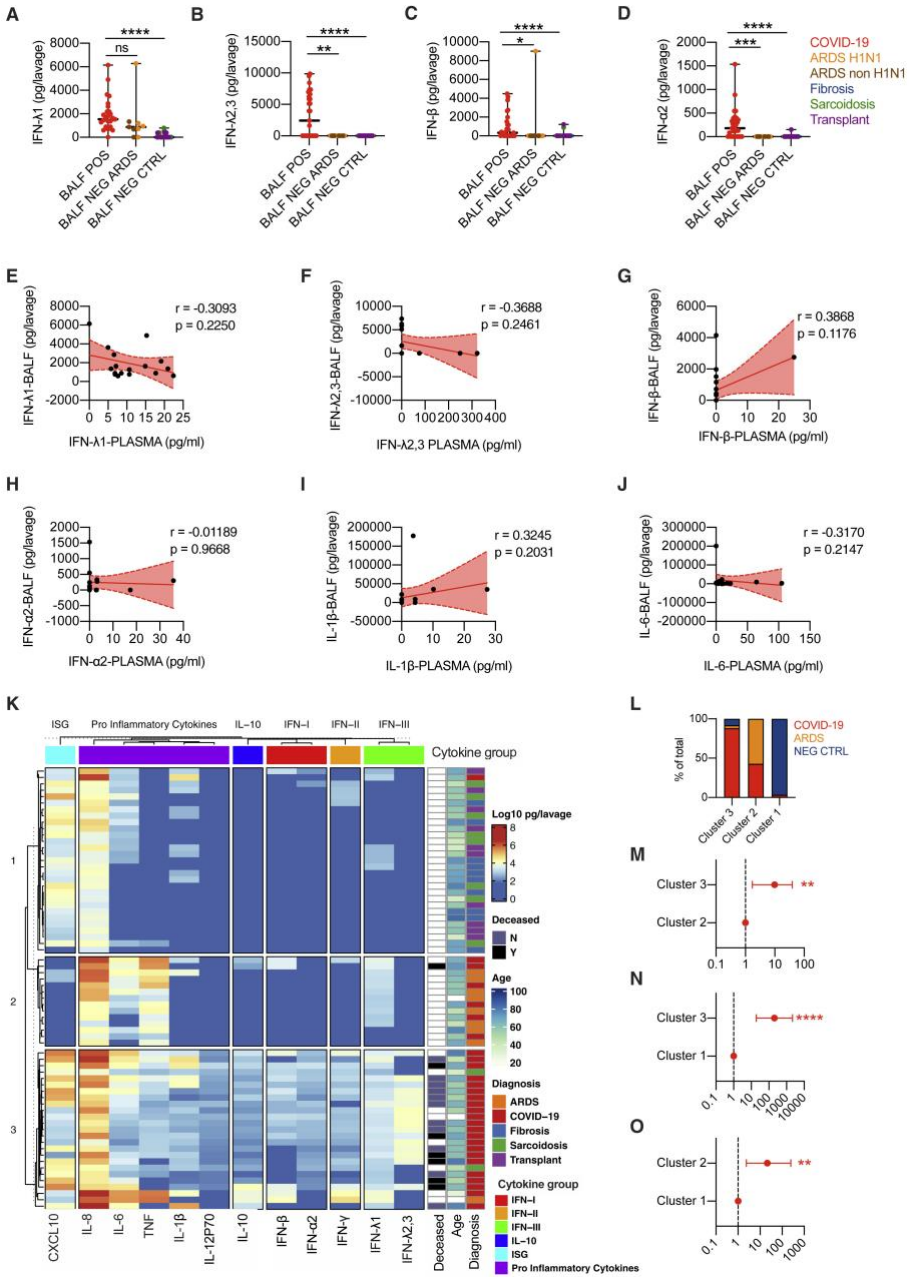

Figure 6. A unique protein IFN signature characterizes the lower airways of COVID-19 patients compared to patients with other ARDS or non-infectious lung pathologies. (**A-D**) IFN-λ1 (**A**), IFN-λ2,3 (**B**), IFN-β (**C**), IFN-α2 (**D**) protein levels were measured in the BALF of COVID-

19 (BALF POS, 29, are depicted with red dots), ARDS (BALF NEG ARDS, 5 were diagnosed H1N1 and are depicted with orange dots, the remaining 4 are depicted with brown dots), non-microbially infected (BALF NEG CTRL, 10 affected by Fibrosis are depicted with blue dots, 10 affected by Sarcoidosis are depicted with green dots, and 10 Transplant patients are depicted with purple dots). Each dot represents a patient. Median with range is depicted. (**E-J**) IFN-λ1 (**E**), IFN-λ2,3 (**F**), IFN-β (**G**), IFN-α2 (**H**), IL-1β (**I**), and IL-6 (**J**) protein levels in the BALF of COVID-19 patients (17) are plotted against protein levels in the plasma of the same patient. Each dot represents a patient. Linear regression lines (continuous line) and 95% confidence interval (dashed line and shaded area) are depicted in red. Spearman correlation coefficients (r) and p-value (p) are indicated. (**K**) Heatmap comparison of IFN-α2, IFN-β, IFN-γ, IFN-λ1, IFN-λ2,3, IL-10, CXCL-10, IL-1β, IL-6, TNF-α, IL-8, IL12p70 protein levels in the BALF of COVID-19 (29), ARDS (9), Transplant (10), Fibrosis (10) and Sarcoidosis (10) patients. The color is proportional to the Log10 transformed value of the amount of cytokine normalized for sample volume (pg/lavage) of each cytokine. Rows in each group represent different patients. Unbiased K-means clustering was performed. Diagnosis, mortality and age are annotated. (**L**) Percentage of patients with the indicated diagnosis within clusters identified in **Figure 6K.** (**M-O**) Odds ratio of containing COVID-19 patients in Cluster 3 as compared to Cluster 2 (**M**) and Cluster 1 (**N**), and in Cluster 2 as compared to Cluster 1 (**O**). (Clusters identified in **Figure 6J).** Statistics: (**A-D**) Kruskal-Wallis test with Dunn's post-hoc test: ns, not significant (P>0.05); *P<0.05,

P<0.01, ***P<0.001, and ****P<0.0001. (L-M**) Chi Square test for odds ratio: ns, not significant (P>0.05); *P<0.05, **P<0.01, ***P<0.001. See also **Figure S6** and **Table S7**.

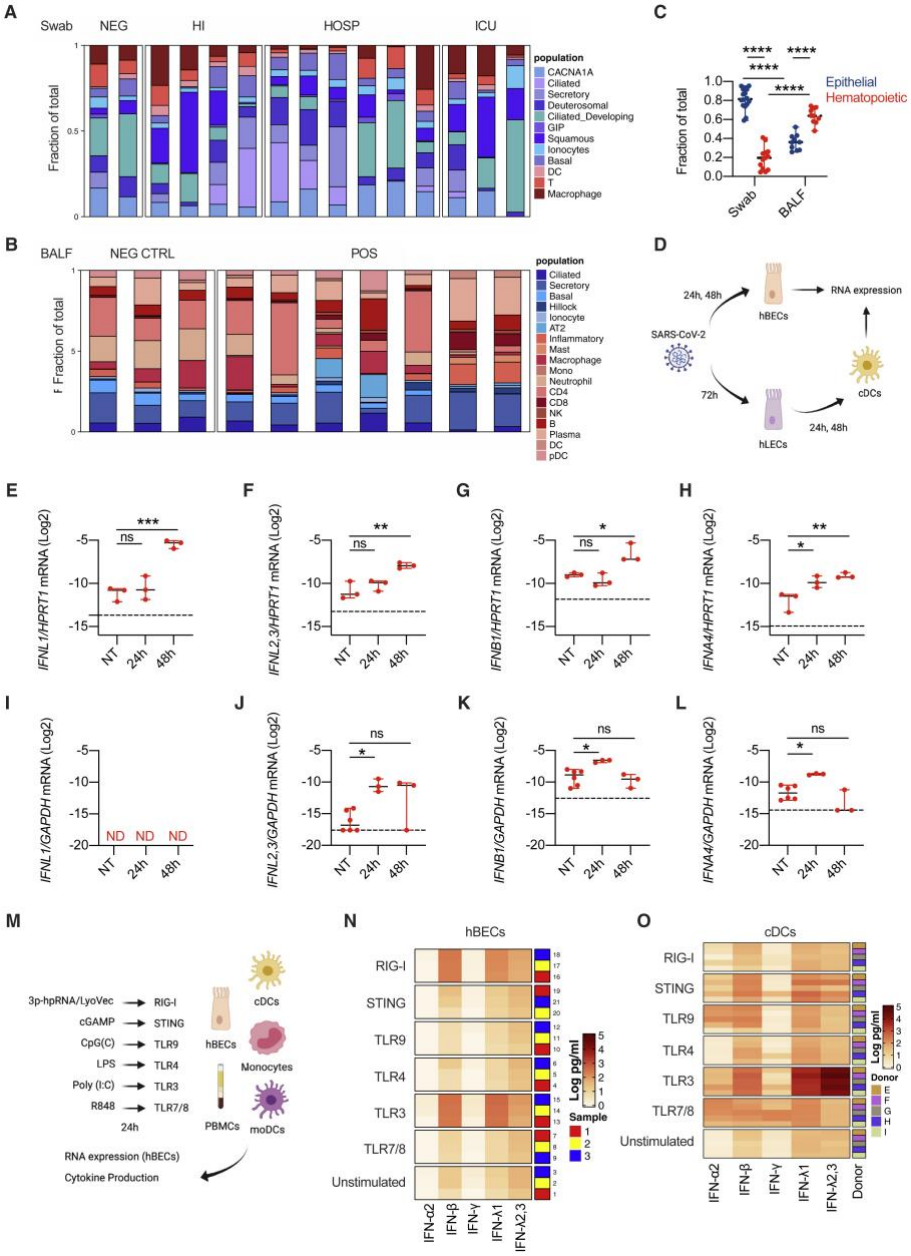

Figure 7. Epithelial and immune cells dictate the IFN landscape. (A-C) Targeted RNA-sequencing of nasopharyngeal swabs from SARS-CoV-2 positive patients that were either ICU inpatients (Swab ICU, 3) hospitalized (Swab HOSP, 6) or home-isolated (Swab HI, 4) and from

SARS-CoV-2 negative (Swab NEG, 2) patients, and BALF from SARS-CoV-2 positive patients (BALF POS, 7) and from patients with non-infectious lung pathologies (BALF NEG CTRL, 3) was performed. Data was deconvoluted based on publicly available scRNAseq datasets (Ziegler et al. 2021) using CIBERSORTx (Newman et al. 2019) to extrapolate the relative cellular composition of samples. (**A-B**) Each cell population in Swab (**A**) and BALF (**B**) samples is depicted as a fraction of total cells. (**C**) Fraction of epithelial or hematopoietic cells in Swab and BALF samples is depicted. Each dot represents a patient. Median with range is depicted. (**D**) Schematic of experimental setup. hBECs were infected with SARS-CoV-2 for 24 and 48 hours. hLECs were infected with SARS-CoV-2 for 72 hours. cDCs were treated with supernatants from hLECs, infected or not, for 24 and 48 hours. Gene expression was evaluated in hBECs and cDCs (created with BioRender). (**E-H**) *IFNL1* (**E***), IFNL2,3* (**F***), IFNB1* (**G**) and *IFNA4* (**H**) mRNA expression was evaluated in hBECs 24 and 48 hours after infection with SARS-CoV-2. Each dot represents a biological replicate. Median with range is depicted. Dashed line represents limit of detection. (**I-L**) *IFNL1* (**I***), IFNL2,3* (**J***), IFNB1* (**K**) and *IFNA4* (**L**) mRNA expression was evaluated in cDCs 24 and 48 hours after treatment with supernatants of uninfected or SARS-CoV-2-infected hLECs. Each dot represent a technical replicate. Median with range is depicted. Dashed line represents limit of detection. ND= Not detected. (**M**) Schematic of experimental setup. hBECs, PBMCs, Monocytes, cDCs and moDCs were treated for 24 hours with 3p-hpRNA/LyoVec, cGAMP, CpG(C), LPS, Poly (I:C), R848 for stimulation of RIG-I, STING, TLR9, TLR4, TLR3, TLR7/8 respectively.

Cytokine expression was evaluated on RNA extracted from cell lysates and cytokine production was evaluated in supernatants (created with BioRender). (**N-O**) Heatmap representation of IFN-α2, IFN-β, IFN-γ, IFN-λ1 and IFN-λ2,3 production by hBECs (**N**), cDCs (**O**) 24 hours after treatment. The color is proportional to the Log10 transformed concentration (pg/ml) of each cytokine. (**N**) Rows in each group represent a biological replicate. (**O**) Rows in each group represent different donors as depicted in the annotation. (**E-L)** Expression is plotted as log2 (*gene*/*GAPDH* mRNA + 0.5 x gene-specific minimum). Statistics: (**C**) Two-way ANOVA: ns, not significant ($P>0.05$); *$P<0.05$, **$P<0.01$, ***$P<0.001$, and ****$P<0.0001$. (**E-L)** One-Way ANOVA with Dunnett's post-hoc test: ns, not significant ($P>0.05$); *$P<0.05$, **$P<0.01$, ***$P<0.001$, and ****$P<0.0001$. See also **Figure S7** and **STAR Methods**.

Supplemental Figures.

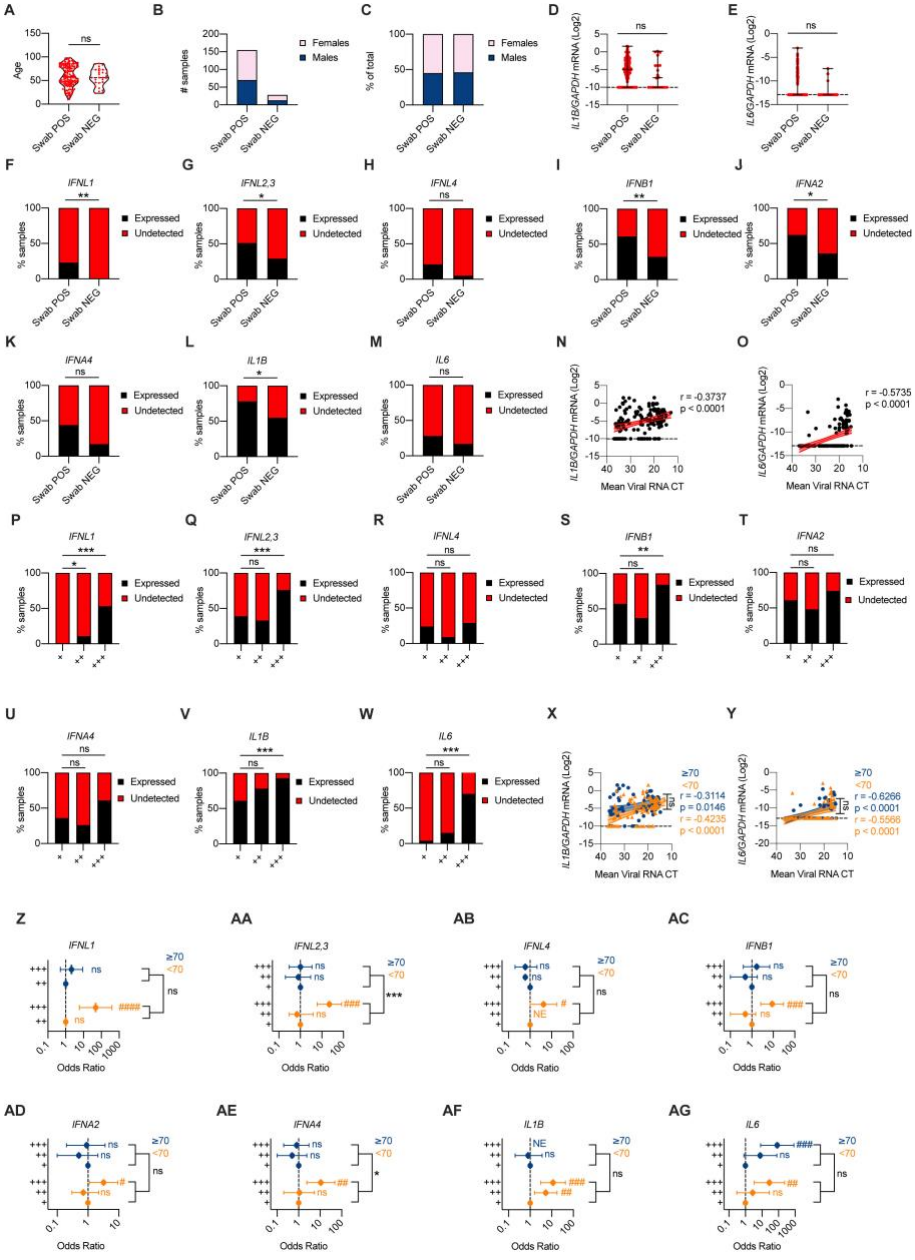

Supplemental Figure 1. High viral loads drive the efficient production of IFN-III, and to a lesser extent of IFN-I, in an age-dependent manner in the upper airways of COVID-19 patients. Related to Figure 1. (**A-C**)

Age distribution (**A**), number (**B**) and percentage (**C**) of females and males in cohorts of patients (Swab NEG, Swab POS) analyzed in **Figure 1A-L and Supplemental Figure 1D-O.** (**A**) Each dot represents a patient. Violin plots are depicted. (**D, E**) *IL1B* (**D**), and *IL6* (**E**) mRNA expression was evaluated in nasopharyngeal swabs from SARS-CoV-2-negative (Swab NEG) and -positive (Swab POS) subjects. Each dot represents a patient. Median with range is depicted. Dashed line represents limit of detection. (**F-M**) Percentage of patients that express (Expressed, black bars) or not (Undetected, red bars) *IFNL1* (**F***), IFNL2,3* (**G***), IFNL4* (**H**), *IFNB1* (**I**), *IFNA2* (**J**), *IFNA4* (**K**), *IL1B* (**L**), and *IL6* (**M**) in Swab POS and Swab NEG cohorts. (**N-O**) *IL1B* (**N**), and *IL6* (**O**) mRNA expression is plotted against mean viral RNA CT in Swab POS cohorts. Each dot represents a patient. Linear regression lines (continuous line) and 95% confidence interval (dashed line and shaded area) are depicted in red. Spearman correlation coefficients (r) and p-value (p) are indicated. (**P-W**) Percentage of patients that express (Expressed, black bars) or not (Undetected, red bars) *IFNL1* (**P***), IFNL2,3* (**Q***), IFNL4* (**R**), *IFNB1* (**S**), *IFNA2* (**T**), *IFNA4* (**U**), *IL1B* (**V**), and *IL6* (**W**) in viral load tercile cohorts ("+", "++", "+++"). (**X, Y**) *IL1B* (**X**), and *IL6* (**Y**) mRNA expression is plotted against mean viral RNA CT in swabs from SARS-CoV-2 positive patients over 70-year-old (≥ 70, blue dots and lines) and below 70-year-old (< 70, orange dots and lines). Each dot represents a patient. Linear regression (continuous lines), 95% confidence interval (dashed line and shaded area), Spearman correlation coefficients (r) and p-value (p) are indicated in blue and in orange for ≥70 and <70 year-old patients respectively. (**Z-AG**) Odds

ratio of expressing *IFNL1* (**Z**) mRNA in "+++" with respect to "++" SARS-CoV-2 positive swabs and *IFNL2,3* (**AA***), IFNL4* (**AB**), *IFNB1* (**AC**), *IFNA2* (**AD**), *IFNA4* (**AE**), *IL1B* (**AF**), and *IL6* (**AG**) mRNA in "+++" and "++" with respect to "+" SARS-CoV-2 positive swabs in ≥70 (blue dots and lines) and < 70 (orange dots and lines) patients. Symbols represent the odds ratio. Error bars represent the 95% confidence interval associated to the odds ratio. NE: not estimable, **AB**) no patient in group expresses *IFNL4*, **AF**) all patients in group express *IL1B*. (**D, E, N, O, X, Y**) Expression is plotted as log2 (*gene*/*GAPDH* mRNA + 0.5 x gene-specific minimum). Statistics: (**A**) Unpaired t test: ns, not significant (P>0.05); *P<0.05, **P<0.01, ***P<0.001, and ****P<0.0001. (**D, E**) Mann-Whitney test: ns, not significant (P>0.05); *P<0.05, **P<0.01, ***P<0.001, and ****P<0.0001. (**F-M and P-W**) Fisher's exact test with Bonferroni correction: ns, not significant (P>0.05); *P<0.05, **P<0.01, ***P<0.001, and ****P<0.0001. (**Z-AG**) Odds ratio: ns, not significant (P>0.05); #P<0.05, ##P<0.01, ###P<0.001. Interaction analysis: ns, not significant (P>0.05); *P<0.05, **P<0.01, ***P<0.001. See also **Table S1, S2**.

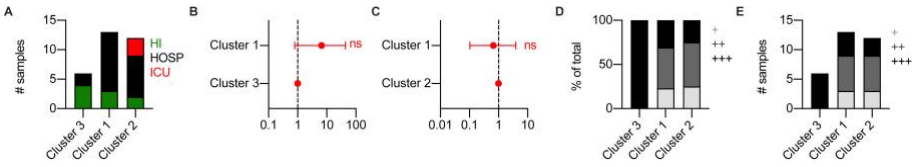

Supplemental Figure 2. Mild COVID-19 is characterized by high levels of IFN-III, not IFN-I, in response to high viral loads in the upper airways. **Related to Figure 2.** (**A**) Number of samples from each disease severity group (HI=home-isolated, HOSP=hospitalized and ICU=Intensive care unit) within each cluster identified in **Figure 2J**. (**B-C**) Odds ratio of patients in Cluster 1 being hospitalized or admitted to the ICU relative to patients in Cluster 3 (**B**) and Cluster 2 (**C**) (Clusters identified in **Figure 2J).** Symbols represent the odds ratio. Error bars represent the 95% confidence interval associated to the odds ratio. (**D-E**) Percentage (**D**) and number (**E**) of samples from each viral load tercile ("+++", "++", "+") within each cluster identified in **Figure 2J**. Viral load terciles ("+++", "++", "+") are defined by mean viral RNA CT (<20, >20 and <30, > 30). Statistics: (**B-C**) Chi Square test for odds ratio: ns, not significant (*P*>0.05); **P*<0.05, ***P*<0.01, ****P*<0.001. See also **Table S3**.

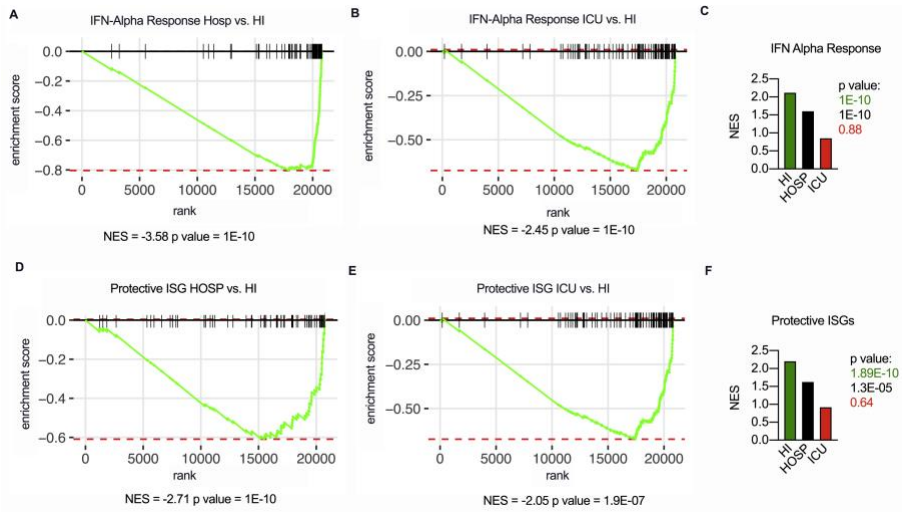

Supplemental Figure 3. IFN-λ1 and IFN-λ3, but not IFN-λ2 or IFN-I, characterize the upper airways of patients with mild COVID-19 and drive ISGs that protect against SARS-CoV-2. Related to Figure 3. (A-F) Targeted RNA-sequencing of nasopharyngeal swabs from SARS-CoV-2 negative (NEG, 3) and positive patients with known disease severity: home-isolated patients (HI, 5), hospitalized patients (HOSP, 7), ICU inpatients (ICU, 3). (**A-B**) Gene set enrichment analysis (GSEA) enrichment plot for genes belonging to the interferon alpha response (HALLMARK Pathways) between HOSP and HI (**A**) and ICU and HI (**B**) cohorts of patients. (**C**) Normalized enrichment score (NES) and p value of interferon alpha response geneset (HALLMARK Pathways) in HI, HOSP and ICU patients as compared to NEG. (**D-E**) GSEA enrichment plot for protective ISG geneset (Curated Geneset derived from (Martin-Sancho et al. 2021)) between HOSP and HI (**D**) and ICU and HI (**E**) cohorts of patients. (**F**) Normalized enrichment score (NES) of protective ISG geneset in HI, HOSP and ICU patients as compared to NEG. See also **Table S4**.

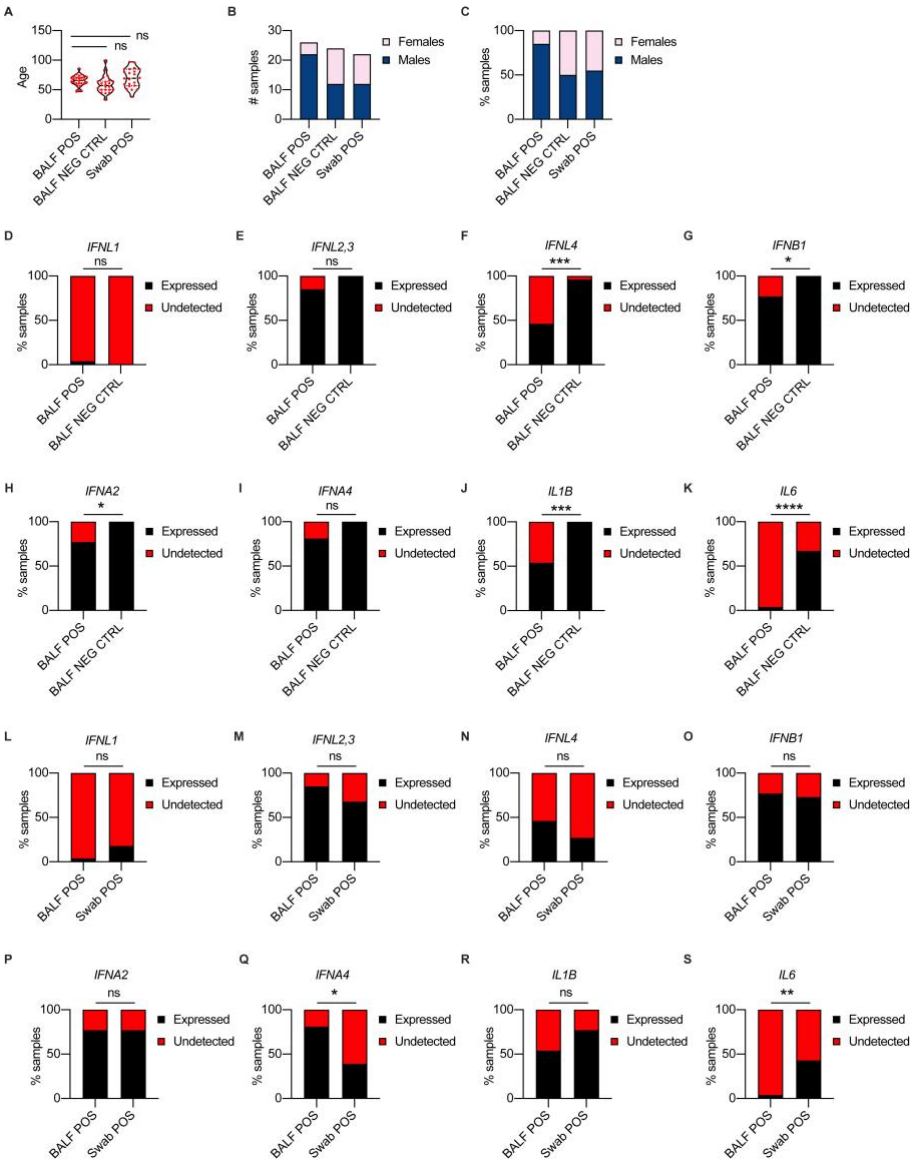

Supplemental Figure 4. Members of the IFN-III and IFN-I families are over-represented in the lower airways of COVID-19 patients. Related to Figure 4. (**A-C**) Age distribution (**A**), number (**B**) and percentage (**C**) of females and males in cohorts of patients (BALF POS, BALF NEG CTRL and Swab POS) analyzed in **Figure 4A-P.** (**A**) Each dot represents a

patient. Violin plots are depicted. (**D-K)** Percentage of patients in BALF from SARS-CoV-2-positive (BALF POS, 26) and -negative (BALF NEG CTRL, 24) that express (Expressed, black bars) or not (Undetected, red bars) *IFNL1* (**D***), IFNL2,3* (**E***), IFNL4* (**F**), *IFNB1* (**G**), *IFNA2* (**H**), *IFNA4* (**I**), *IL1B* (**J**), and *IL6* (**K**). (**L-S)** Percentage of patients (BALF POS, 26) and swabs (Swab POS, 21) from SARS-CoV-2-positive subjects that express (Expressed, black bars) or not (Undetected, red bars) *IFNL1* (**L***), IFNL2,3* (**M***), IFNL4* (**N**), *IFNB1* (**O**), *IFNA2* (**P**), *IFNA4* (**Q**), *IL1B* (**R**), and *IL6* (**S**). Statistics: (**D-S**) Fisher's exact test: ns, not significant (P>0.05); *P<0.05, **P<0.01, ***P<0.001, and ****P<0.0001. See also **Table S5**.

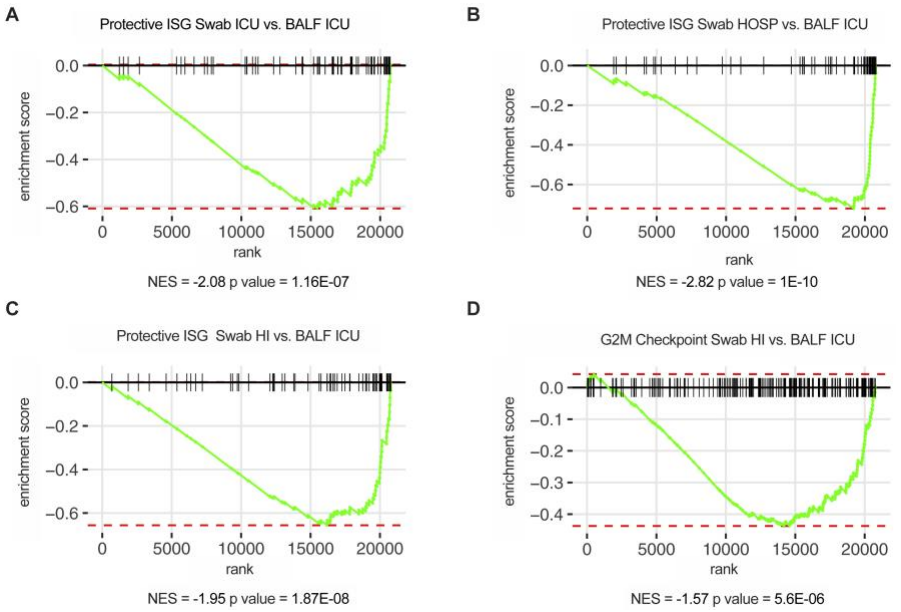

Supplemental Figure 5. Critical COVID-19 is characterized by the induction of a similar IFN landscape in the upper and lower airways. Related to Figure 5. (**A-C**) Targeted RNA-sequencing of BALF from SARS-CoV-2 positive patients (BALF ICU, 7), and from nasopharyngeal swabs from SARS-CoV-2 positive patients that were either ICU inpatients (Swab ICU, 3) hospitalized (Swab HOSP, 7) or home-isolated (Swab HI, 5). (**A-C**) GSEA enrichment plot for protective ISG genes (curated Geneset derived from (Martin-Sancho et al. 2021)) between Swab ICU and BALF ICU (**A**), Swab HOSP and BALF ICU (**B**), Swab HI and BALF ICU (**C**). (**D**) GSEA enrichment plot for genes involved in the G2M checkpoint (HALLMARK Pathways) between Swab HI and BALF ICU. (**A-D**) NES: Normalized enrichment score. See also **Table S6**.

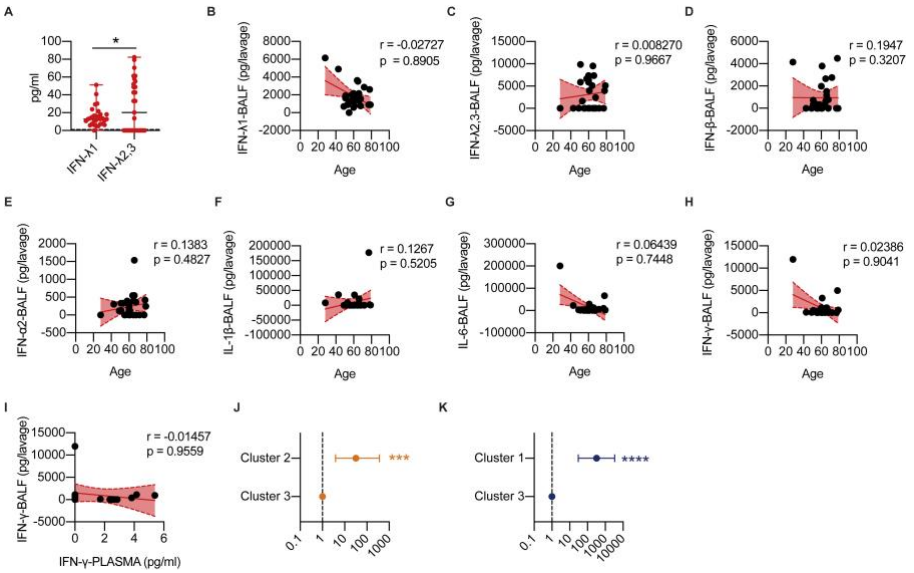

Supplemental Figure 6. A unique protein IFN signature characterizes the lower airways of COVID-19 patients compared to patients with other ARDS or non-infectious lung pathologies. Related to Figure 6. (**A**) IFN-λ1 and IFN-λ2,3 protein levels were measured in the BALF of COVID-19 patients (29). Each dot represents a patient. Median and range are depicted. Dashed line represents limit of detection. (**B-H**) IFN-λ1 (**B**), IFN-λ2,3 (**C**), IFN-β (**D**), IFN-α2 (**E**), IL-1β (**F**), IL-6 (**G**) and IFN-γ (**H**) protein levels in the BALF of COVID-19 patients (29) are plotted over age. (**I**) IFN-γ protein levels in the BALF of COVID-19 patients (17) are plotted against protein levels in the plasma**.** (**J-K**) Odds ratio of containing ARDS patients in Cluster 2 as compared to Cluster 3 (**J**) and of containing non-microbially infected control patients in Cluster 1 as compared to Cluster 3 (**K**) (Clusters identified in **Figure 6J**) (**B-I**) Each dot represents a patient. Linear regression lines (continuous line) and 95% confidence interval (dashed line and shaded area) are depicted in red. Spearman correlation coefficients (r) and p-value (p) are

indicated. Statistics: (**A**) Unpaired t-test**:** ns, not significant ($P>0.05$); *$P<0.05$, **$P<0.01$, ***$P<0.001$, and ****$P<0.0001$. (**J-K**) Chi Square test for odds ratio: ns, not significant ($P>0.05$); *$P<0.05$, **$P<0.01$, ***$P<0.001$. See also **Table S7**.

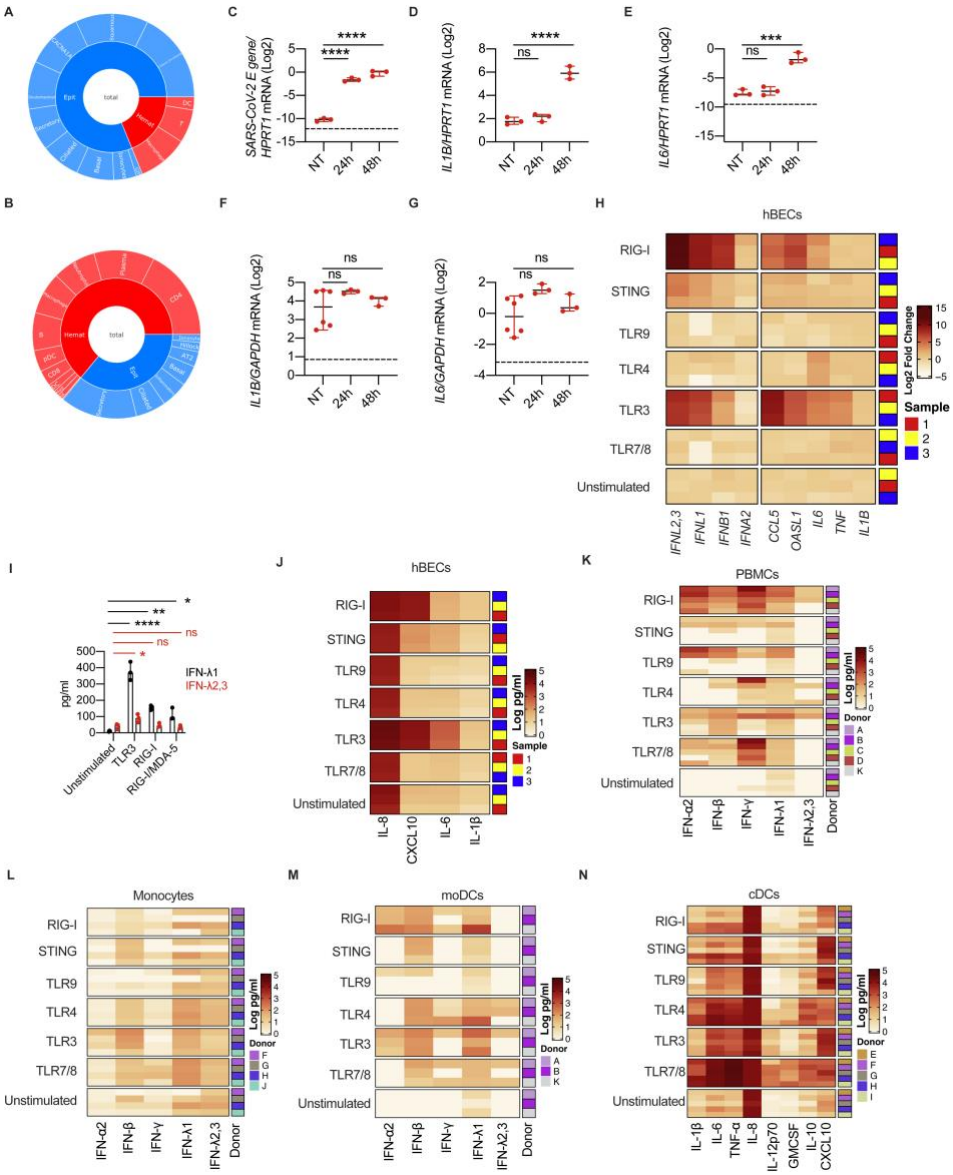

Supplemental Figure 7. Epithelial and immune cells dictate the IFN landscape. Related to Figure 7. (**A-B**) Sunburst plots representing cell population fractions in Swabs (**A**) and BALF (**B**) as identified in Figure **7A, B**. (**C-E**) SARS-CoV-2 E gene (**C**), *IL1B* (**D**)*, IL6* (**E***)* mRNA expression was evaluated in hBECs 24 and 48 hours after infection with SARS-CoV-

2. Each dot represents a biological replicate. Median with range is depicted. Dashed line represents limit of detection. (**F-G**) *IL1B* (**D***), IL6* (**E***)* mRNA expression was evaluated in cDCs 24 and 48 hours after treatment with supernatants of uninfected or SARS-CoV-2-infected hLECs. Each dot represents a biological replicate. Median with range is depicted. Dashed line represents limit of detection. (**H-J**) hBECs were treated with 3p-hpRNA/LyoVec, cGAMP, CpG(C), LPS, Poly (I:C) and R848 for stimulation of RIG-I, STING, TLR9, TLR4, TLR3 and TLR7/8 respectively. Each dot represents a technical replicate. Median with range is depicted. **(H)** Heatmap representation of *IFNL2,3*, *IFNL1, IFNB1, IFNA2, CCL5, OASL1, IL6, TNF* and *IL1B* mRNA expression 24 hours after treatment. The color is proportional to Log2 (Fold Change) of each gene. Rows in each group represent biological replicates distributed as indicated in the legend. (**I**) IFN-λ1 and IFN-λ2,3 production by hBECs treated for 24h with PRR ligands. Poly (I:C) (TLR3), 3p-hpRNA/LyoVec (RIG-I) and transfected Poly (I:C) (RIG-I/MDA5) were used. Each dot represents a biological replicate. Median with range is depicted. (**J**) Heatmap representation of IL-8, CXCL10, IL-6 and IL-1β production 24 hours after stimulation. The color is proportional to the Log10 transformed concentration (pg/ml) of each cytokine. Rows in each group represent a biological replicate. (**K-M**) Heatmap representation of IFN-α2, IFN-β, IFN-γ, IFN-λ1 and IFN-λ2,3 production by PMBCs (**K**), Monocytes (**L**), moDCs (**M**) 24 hours after treatment. The color is proportional to the Log10 transformed concentration (pg/ml) of each cytokine. (**N**) Heatmap representation of IL-1β, IL-6, TNF-α, IL-8, IL-12p70, GMCSF, IL-10 and CXCL10 production cDCs 24

hours after treatment. (**J-N**) The color is proportional to the Log10 transformed concentration (pg/ml) of each cytokine. Rows in each group represent different donors as depicted in the annotation on the right. (**C-E, F, G**) Expression is plotted as log2 (*gene*/*GAPDH* mRNA + 0.5 x gene-specific minimum). Statistics: (**C-E, F,G, I**) One-Way ANOVA with Dunnett's post-hoc test: ns, not significant ($P>0.05$); *$P<0.05$, **$P<0.01$, ***$P<0.001$, and ****$P<0.0001$. See also **STAR Methods**.

		Swab NEG	Swab POS total	Swab POS +	Swab POS ++	Swab POS +++
	Samples (#)	28(183)	155(183)	51(155)	46(155)	58(155)
Age	Minimum	23	10	17	10	26
	Maximum	86	98	93	98	97
	Q1	46	44	46	46	48
	Q3	72	80	83	80	79
	IQR	26	36	37	34	31
	Median	56	58	68	55	61
	Mean	57	60	62	58	62
	≥ 70 (#)	8(28)	61(155)	25(51)	16(46)	20(58)
	< 70 (#)	20(28)	94(155)	26(51)	30(46)	38(58)
	≥ 70 (%)	29	39	49	35	34
	< 70 (%)	71	61	51	65	66
Sex	F (#)	15(28)	85(155)	27(51)	27(46)	31(58)
	M (#)	13(28)	70(155)	24(51)	19(46)	27(58)
	F (%)	54	55	53	59	53
	M (%)	46	45	47	41	47

Supplemental Table 1. Patient information for Swab NEG and Swab POS samples used for gene expression. Related to Figure and Supplemental Figure 1. Age, sex and severity characteristics of patient cohorts analyzed in **Figure 1 and Supplemental Figure 1**. Nasopharyngeal swabs from SARS-CoV-2-negative (Swab NEG) and -positive (Swab POS total) subjects, that were further divided in viral load terciles ("Swab POS +", "Swab POS++", "Swab POS+++"), were analyzed by qPCR. Q1=quartile 1, Q3=quartile 3, IQR=interquartile range, ≥ 70=over or equal to 70 years old, <70=under 70 years old, F=female, M=male, #=number of samples, %=percentage of samples.

		Age <70		Age ≥70		
Outcome/gene	Viral load tercile	Odds ratio	P value	Odds ratio	P value	P value for interaction
IFNA2	+	Reference(1.0)		Reference(1.0)		0.38
	++	0.7(0.3,2.2)	0.59	0.5(0.1,2.1)	0.36	
	+++	3.2(1.1,9.2)	0.03	0.9(0.2,3.6)	0.89	
IFNA4	+	Reference(1.0)		Reference(1.0)		0.03
	++	1.1(0.2,5.5)	0.92	0.5(0.1,2.4)	0.38	
	+++	10.7(2.4,47.9)	0.002	0.8(0.2,3.0)	0.70	
IFNB1	+	Reference(1.0)		Reference(1.0)		0.14
	++	0.5(0.1,1.5)	0.19	0.5(0.1,1.8)	0.29	
	+++	8.8(2.6,30.2)	<0.001	1.7(0.4,6.8)	0.49	
IFNL1	+	NE		NE		0.06
	++	Reference(1.0)		Reference(1.0)		
	+++	48.0(5.8,399.0)	<0.001	2.1(0.5,8.9)	0.33	
IFNL2,3	+	Reference(1.0)		Reference(1.0)		<0.001
	++	1.0(0.3,3.9)	0.96	0.8(0.2,3.0)	0.80	
	+++	22.1(6.0,82.0)	<0.001	1.0(0.3,3.5)	0.95	
IFNL4	+	Reference(1.0)		Reference(1.0)		0.13
	++	NE		0.6(0.1,3.2)	0.47	
	+++	4.2(1.0,17.6)	0.049	0.6(0.2,2.1)	0.39	
IL1B	+	Reference(1.0)		Reference(1.0)		0.13
	++	5.3(1.6,17.6)	0.005	0.8(0.2,3.6)	0.73	
	+++	11.5(3.1,42.6)	<0.001	NE		
IL6	+	Reference(1.0)		Reference(1.0)		0.80
	++	2.7(0.3,27.8)	0.40	7.8(0.8,79.3)	0.08	
	+++	28.1(3.4,233.1)	0.002	83.90(8.2,857.3)	<0.001	

Supplemental Table 2. Odds ratio of expressing/not each gene across viral load terciles and age groups in swabs from SARS-CoV-2 positive patients. Related to Figure Supplemental 1. Odds ratio of expressing *IFNL1* in "+++" with respect to "++" *and IFNL2,3*, *IFNL4*, *IFNB1*, *IFNA2*, *IFNA4*, *IL1B*, and *IL6* mRNA in "+++" and "++" with respect to "+" swabs from SARS-CoV-2 positive ≥ 70 and < 70 patients was calculated. Odds ratio column indicates the odds ratio and associated 95% confidence interval in brackets. P value column indicates the associated P value for each cohort of patients. Interaction between viral load terciles and age groups (≥70 years vs <70 years) was tested and P values for interaction are indicated. NE=not estimable.

		Gene Expression			Mean Viral RNA CT progression		
		HI	HOSP	ICU	HI	HOSP	ICU
	Samples (#)	9(31)	19(31)	3(31)	6(12)	5(12)	1(12)
Age	Minimum	22	38	60	50	32	NA
	Maximum	78	97	69	84	84	NA
	Q1	42	57	64	54	51	NA
	Q3	51	85	69	73	81	NA
	IQR	9	29	5	19	30	NA
	Median	47	76	68	68	73	91
	Mean	50	71	66	66	64	91
Sex	F (#)	4(9)	9(19)	1(3)	3(6)	2(5)	1(1)
	M (#)	5(9)	10(19)	2(3)	3(6)	3(5)	0(1)
	F (%)	44	47	33	50	40	100
	M (%)	56	53	67	50	60	0

Supplemental Table 3. Patient information for HI, HOSP and ICU Swab samples for gene expression and for Mean Viral RNA CT progression analysis. Related to Figure 2 and Supplemental Figure 2. Age, sex and severity characteristics of patient cohorts analyzed in **Figure 2 and Supplemental Figure 2**. Nasopharyngeal swabs from SARS-CoV-2 positive subjects that were either home-isolated (HI), hospitalized (HOSP)) or hospitalized and admitted to the ICU (ICU) were analyzed by qPCR for gene expression or were analyzed longitudinally for mean viral RNA CT. Q1=quartile 1, Q3=quartile 3, IQR=interquartile range, F=female, M=male, #=number of samples, %=percentage of samples.

		Swab NEG	Swab POS
	Samples (#)	3(18)	15(18)
Viral load tercile	+ (#)	NA	3(15)
	++ (#)	NA	6(15)
	+++ (#)	NA	6(15)
Severity	HI (#)	NA	5(15)
	HOSP (#)	NA	7(15)
	ICU (#)	NA	3(15)
Age	Minimum	29	42
	Maximum	86	96
	Q1	51	51
	Q3	80	77
	IQR	29	27
	Median	73	68
	Mean	63	65
Sex	F (#)	1(3)	6(15)
	M (#)	2(3)	9(15)
	F (%)	33	40
	M (%)	67	60

Supplemental Table 4. Patient information for swab samples used for RNA-Seq. Related to Figure and Supplemental Figure 3. Age and sex characteristics of patient cohorts analyzed in **Figure 3 and Supplemental Figure 3**. Nasopharyngeal swabs from SARS-CoV-2 positive patients divided in viral load terciles ("+++", "++", "+") and that were either home-isolated (HI), hospitalized (HOSP)) or hospitalized and admitted to the ICU (ICU) were analyzed by RNA-Seq. Q1=quartile 1, Q3=quartile 3, IQR=interquartile range, ≥ 70=over or equal to 70 years old, <70=under 70 years old, F=female, M=male, #=number of samples, %=percentage of samples.

		BALF NEG CTRL	BALF POS	Swab POS
	Samples (#)	24(72)	26(72)	22(72)
Severity	HOSP (#)	NA	5(26)	19(22)
	ICU (#)	NA	21(26)	3(22)
Diagnosis	Fibrosis (#)	8(24)	NA	NA
	Sarcoidosis (#)	8(24)	NA	NA
	Transplant (#)	8(24)	NA	NA
Age	Minimum	33	47	38
	Maximum	100	86	97
	Q1	50	61	58
	Q3	64	71	84
	IQR	14	10	27
	Median	57	66	69.5
	Mean	59	65	70
Sex	F (#)	12(24)	4(26)	12(22)
	M (#)	12(24)	22(26)	10(22)
	F (%)	50	15	55
	M (%)	50	85	45

Supplemental Table 5. Patient information for swab and BALF samples used for gene expression. Related to Figure and Supplemental Figure 4. Age and sex characteristics of patient cohorts analyzed in **Figure 4 and Supplemental Figure 4**. Nasopharyngeal swabs and BALF from SARS-CoV-2 positive patients that were either home-isolated (HI), hospitalized (HOSP)) or hospitalized and admitted to the ICU (ICU) and BALF from SARS-CoV-2 negative patients were analyzed by qPCR. Q1=quartile 1, Q3=quartile 3, IQR=interquartile range, , F=female, M=male, #=number of samples, %=percentage of samples.

		BALF NEG CTRL	BALF POS	Swab POS
	Samples (#)	5(27)	7(27)	15(27)
Viral load tercile	**+ (#)**	NA	NA	3(15)
	++ (#)	NA	NA	6(15)
	+++ (#)	NA	NA	6(15)
Diagnosis	**Fibrosis (#)**	1(5)	NA	NA
	Sarcoidosis (#)	2(5)	NA	NA
	Transplant (#)	2(5)	NA	NA
Severity	**HI (#)**	NA	0(7)	5(15)
	HOSP (#)	NA	0(7)	7(15)
	ICU (#)	NA	7(7)	3(15)
Age	**Minimum**	45	48	42
	Maximum	64	72	96
	Q1	53	66	51
	Q3	63	71	77
	IQR	10	5	27
	Median	63	69	68
	Mean	58	66	65
Sex	**F (#)**	2(5)	3(7)	6(15)
	M (#)	3(5)	4(7)	9(15)
	F (%)	40	43	40
	M (%)	60	57	60

Supplemental Table 6. Patient information for swab and BALF samples used for RNA-Seq. Related to Figure and Supplemental Figure 5. Age and sex characteristics of patient cohorts analyzed in **Figure 5 and Supplemental Figure 5**. Nasopharyngeal swabs and BALF from SARS-CoV-2 positive patients that were either home-isolated (HI), hospitalized (HOSP)) or hospitalized and admitted to the ICU (ICU) and BALF from SARS-CoV-2 negative patients were analyzed by RNA-Seq. Q1=quartile 1, Q3=quartile 3, IQR=interquartile range, , F=female, M=male, #=number of samples, %=percentage of samples.

		COVID-19	ARDS H1N1+	ARDS H1N1-	Fibrosis	Sarcoidosis	Transplant
	Samples (#)	29(68)	5(68)	4(68)	10(68)	10(68)	10(68)
Age	**Minimum**	28	42	44	64	35	35
	Maximum	79	67	76	83	77	67
	Q1	56	54	54	66	39	53
	Q3	66	62	70	74	53	58
	IQR	10	8	16	8	14	5
	Median	60	59	63	70	46	56
	Mean	61	57	61	71	50	53
Sample	**BALF (#)**	29(29)	5(5)	4(4)	10(10)	10(10)	10(10)
	Plasma (#)	17(29)	0(5)	0(4)	0(10)	0(10)	0(10)

Supplemental Table 7. Patient information for BALF and plasma samples used for cytokine quantification. Related to Figure and Supplemental Figure 6. Age and type of collected sample of patient cohorts analyzed in **Figure and Supplemental Figure 6**. BALF and plasma from patients with COVID-19 was analyzed. BALF from patients suffering from: non-COVID-19 ARDS (divided in H1N1 Influenza A virus positive or not), fibrosis, sarcoidosis, and that received lung transplant was analyzed. Q1=quartile 1, Q3=quartile 3, IQR=interquartile range.

Materials and Methods.

RESOURCE AVAILABILITY

Lead contact

Further information and requests for resources and reagents should be directed to and will be fulfilled by the lead contact, Ivan Zanoni (ivan.zanoni@childrens.harvard.edu).

Materials availability

This study did not generate new unique reagents.

Data and code availability

- Targeted transcriptomics data have been deposited at GEO and are publicly available as of the date of publication. Accession numbers are listed in the Key Resources Table.
- Gene expression matrix from targeted transcriptomics, Gene expression matrix from qPCR experiments, cytokine expression matrix from multiplex analysis of BALF, Plasma and supernatants of phagocytes are deposited at Mendeley and are publicly available as of the date of publication. The DOI is listed in the Key Resources Table.
- The code used to analyze the data is available upon request to the corresponding authors.

EXPERIMENTAL MODEL AND SUBJECT DETAILS

Clinical samples for gene expression analysis and targeted RNA-sequencing.

Nasopharyngeal swabs were collected using FLOQSwabs® (COPAN Cat#306C) in UTM® Universal Transport Medium (COPAN Cat#306C)

from 155 SARS-CoV-2 positive patients and from 28 negative subjects undergoing screening for suspected social contacts with SARS-CoV-2 positive subjects. Nasopharyngeal swabs were collected at San Raffaele Hospital (Milan, Italy) from April to December 2020. BALF was obtained from 26 SARS-CoV-2-positive patients hospitalized at San Raffaele Hospital (Milan, Italy) from March to May 2020. BALF was obtained from 24 non-infected patients: lung fibrosis patients (8) were collected from May 2018 to September 2020; sarcoidosis patients (8) were collected from August to July 2020; lung transplant patients (8) were collected from January 2018 to September 2020 by IRCCS Policlinico San Matteo Foundation (Pavia, Italy). See **Table S1**, **S3, S4, S5, S6** for patient information. All samples were stored at −80°C until processing. 500 µl of each BALF and swab sample were lysed and used for RNA extraction (see *RNA extraction protocol and Real-Time PCR for clinical samples and hBECs*).

Clinical metadata were obtained from the COVID-BioB clinical database of the IRCCS San Raffaele Hospital. The study was approved by the Ethics Committee of San Raffaele Hospital (protocol 34/int/2020). All of these patients signed an informed consent form. Our research was in compliance to the Declaration of Helsinki.

Clinical samples for cytokine quantification in BALF and plasma.

BALF from 29 SARS-CoV-2 positive patients hospitalized in the Intensive Care Unit (ICU) at Luigi Sacco Hospital (Milan, Italy) were collected from September to November 2020. The total volume for each lavage was 120ml. Blood from 17 of these patients was also collected on the same day. BALF from patients affected by ARDS (9 in

total, 5 of which were diagnosed H1N1 influenza A virus) were collected from February 2014 to March 2018. Samples from: lung fibrosis patients (10) were collected from May 2018 to September 2020; sarcoidosis patients (10) were collected from August to July 2020; lung transplant patients (10) were collected from January 2018 to September 2020 by IRCCS Policlinico San Matteo Foundation (Pavia, Italy). The total volume for each lavage was 150ml. None of the patients affected by lung fibrosis, sarcoidosis or that received lung transplant was diagnosed a respiratory viral or bacterial infection. See **Table S7** for patient information.

Research and data collection protocols were approved by the Institutional Review Boards (Comitato Etico di Area 1) (protocol 20100005334) and by IRCCS Policlinico San Matteo Foundation Hospital (protocol 20200046007). All patients signed an informed consent form. Our research was in compliance to the Declaration of Helsinki.

Isolation of human phagocytes.

Human phagocytes were isolated from collars of blood received from Boston Children's Hospital blood donor center for in vitro stimulations and from San Raffaele Hospital blood donor center for SARS-CoV-2 infections. Briefly, blood was diluted 1:2 in PBS and PBMCs were isolated using a Histopaque (Sigma Cat# 1077-1) gradient. Monocytes were positively selected from PBMCs with CD14 MicroBeads (Miltenyi Biotec Cat# 130-050-201) by MACS technology. MoDCs were differentiated from monocytes in the presence of GM-CSF 20ng/ml (PeproTech Cat# 300-03) and IL-4 20ng/ml (PeproTech Cat# 200-04)

for 7 days. MoDCs differentiation was tested for CD14 downregulation and HLA-DR expression. cDCs were positively selected from PBMCs with CD141 (BDCA-3) MicroBead Kit (Miltenyi Biotec Cat# 130-090-512) by MACS technology. Purity and differentiation were assessed by FACS and representative plots are available on Mendeley (see Key Resources Table)

hBECs were expanded in a T-75 flask to 60% confluence and then trypsinized and seeded either on 48 well plates ($2x10^5$ cells/well) for IFN stimulations or ($3x10^4$ cells/transwell) onto 0.4 μm pore size clear polyester membranes (Corning Cat# 3470) coated with a collagen solution for PRR agonist stimulations and SARS-CoV-2 infections.

SARS-CoV-2 propagation and titration.

For hBECs infection experiments with SARS-CoV-2, the isolate England/02/2020 (GISAID accession ID: EPI_ISL_407073) was propagated and titrated in Vero E6 cells (ATCC Cat# CRL-1586). For cDCs infection experiments with SARS-CoV-2 the isolate hCoV-19/Italy/UniSR1/2020 (GISAID accession ID: EPI_ISL_413489) was propagated and titrated in Vero E6 cells (ATCC Cat# CRL-1586). All infection experiments were performed in a biosafety level-3 (BLS-3) laboratory.

Evaluation of SARS-CoV-2 RNA amount in clinical samples.

The viral load was inferred on nasopharyngeal swabs through cycle threshold (Ct) determination with Cobas® SARS-CoV-2 Test (Roche Cat# P/N 09175431190), a real-time PCR dual assay targeting ORF-1a/b and E-gene regions on SARS-CoV-2 genome. The mean between ORF-1a/b and E Ct was used as an indirect measure of the viral load.

Non-infectious plasmid DNA containing a specific SARS-CoV-2 sequence and a pan-Sarbecovirus sequence is used in the test as positive control. A non-Sarbecovirus related RNA construct is used as internal control. The test is designed to be performed on the automated Cobas® 6800 Systems under Emergency Use Authorization (EUA). The test is available as a CE-IVD test for countries accepting the CE-mark.

Culture of primary NHBE (hBECs) and Calu3 cells (hLECs).

NHBE (hBECs) were expanded in a T-75 flask to 60% confluence and then trypsinized and seeded either on 48 well plates ($2x10^5$ cells/well) for IFN stimulations or ($3x10^4$ cells/transwell) onto 0.4 µm pore size clear polyester membranes (Corning Cat# 3470) coated with a collagen solution for PRR agonist stimulations and SARS-CoV-2 infections.

Calu-3 (hLECs, ATCC Cat# HTB-55) were cultured in MEM (Gibco Cat# 41090036) and supplemented with MEM non-essential amino acids solution (Gibco Cat#11140050), Penicillin-Streptomycin (Gibco Cat#11140050), Sodium Pyruvate and 10% FBS (Gibco Cat#10437-028).

METHOD DETAILS.

In vitro stimulation and SARS-CoV-2 infection of hBECs.

IFN stimulations were performed one day after seeding by treating cells with 2ng/ml IFN-λ1, IFN-λ2 and IFN-λ3 for 4 and 24 hours. Cell lysates were processed for RNA extraction as described below. For PRR agonist stimulations and SARS-CoV-2 infections cells were grown in submersion until confluent, and then exposed to air to establish an air-liquid interface (ALI). At ALI day 15, cells were stimulated with LPS (100

ng/ml), R848 (10 µg/ml), CpG(C) (1 µM), Poly (I:C) (50 µg/ml), Poly (I:C) (1 µg/10^6 cells) + Lipofectamine, 3p-hpRNA/LyoVec (100 ng/ml), and cGAMP (10 µg /ml). Supernatants and cell lysates were collected 24 hours post treatment. Supernatants were processed with LEGENDplex™ (BioLegend Cat# 740390) according to manufacturer's instructions and read by flow cytometry. Lysates were processed for RNA extraction as described below. For SARS-CoV-2 infections on day 15 of ALI cells were washed apically with PBS and infected at a multiplicity of infection (MOI) of 10^{-1} for 30 minutes at 37°C. The inoculum was then removed, and cell lysates were collected at 24 or 48 hours post infection for RNA extraction as described below.

Measurement of cytokine levels on BALF and plasma samples.

BALF specimens from COVID-19 patients were managed in a biosafety level 3 laboratory until viral inactivation with a 0.2% SDS and 0.1% Tween-20 solution and heating at 65 °C for 15 min. Cell-free BALF supernatants were stored at − 20 °C until analysis. Blood was centrifuged at 400g for 10 minutes without brake and plasma was stored at − 20 °C until analysis. Samples were processed with LEGENDplex™ (BioLegend Cat# 740390) according to manufacturer's instructions and read by flow cytometry.

In vitro stimulation of human phagocytes with PRR agonists and supernatant from SARS-CoV-2-infected hLECs.

PBMCs, monocytes, moDCs and cDCs were stimulated with LPS (100 ng/ml), R848 (10 µg/ml), CpG(C) (1 µM), Poly (I:C) (50 µg/ml), 3p-hpRNA/LyoVec (2.5 µg/ml), and cGAMP (10 µg/ml). Supernatants were collected 24 hours post treatment and stored at − 20 °C until analysis.

cDCs were also stimulated with conditioned media from hLECs. hLECs were infected or not with SARS-CoV-2 at an MOI of 10^{-1} and supernatant was collected 72 hours post infection. Cell lysates were collected 24 and 48 hours after treatment for RNA extraction as described below.

RNA extraction protocol and Real-Time PCR from clinical samples and hBECs.

RNA was extracted from nasopharyngeal swabs, BALFs, hBECs (stimulated with PRR agonists, with IFNs and infected with SARS-CoV-2) lysates and cDCs (stimulated with supernatant from SARS-CoV-2 infected hLECs) using Pure Link RNA Micro Scale kit (Invitrogen Cat# 12183016) according to manufacturer's instruction, including in-column DNase treatment. Reverse transcription was performed on all samples except IFN-treated hBECs using SuperScript™ III First-Strand Synthesis System (Invitrogen Cat# 18080051) according to manufacturer's instruction. qRT-PCR analysis was then carried out with Taqman™ Fast Advanced Master Mix (Applied Biosystems Cat#4444963) by using specific Taqman™ Gene Expression Assays from Thermo Fisher. *IFNL1 (*Hs01050642_gH)*, IFNL2,3 (*Hs04193047_gH)*, IFNL4* (Hs04400217_g1), *IFNB1* (Hs01077958_s1), *IFNA2* (Hs00265051_s1)*, IFNA4* (Hs01681284_sH)*, IL1B* (Hs01555410_m1) and *IL6* (Hs00174131_m1) expression was assessed with respect to the housekeeping gene *GAPDH* (Hs99999905_m1) or *HPRT1* (Hs99999909_m1). qRT-PCR was performed on IFN-treated hBECs with Power SYBR Green RNA-to-CT 1-step kit (Applied Biosystems Cat#4389986) from Thermo Fisher using primers (Sigma)

for the following genes: *UBC, RSAD2, IFIT3, LY6E, APOL2*. Expression was assessed with respect to the housekeeping *UBC*. SARS-CoV-2 E gene expression in infected hBECs was quantified by real-time reverse transcription PCR. All transcripts were tested in triplicate for each sample on ViiA7 Real-Time PCR System (Thermo Fisher) for clinical samples, on Quantastudio 3 Real-Time PCR System (Thermo Fisher) for hBECs stimulated with PRR agonists and infected with SARS-CoV-2 and on CFX384 real time cycler (Bio-rad) for hBECs stimulated with IFNs and cDCs infected with SARS-CoV-2.

Targeted Transcriptomics.

For targeted transcriptome sequencing, RNA (15ng) isolated from clinical samples described in **Table 4** and **Table 6** was retro-transcribed to cDNA using SuperScript VILO cDNA Synthesis Kit (Invitrogen Cat# 11754-05). Barcoded libraries were prepared using the Ion AmpliSeq Transcriptome Human Gene Expression Kit (Ion Torrent Cat# A26325) as per the manufacturer's protocol and sequenced using an Ion S5 system (Ion Torrent Cat# A27212). Differential gene expression analysis was performed using the Transcriptome Analysis Console (TAC) software with the ampliSeqRNA plugin (ThermoFisher Scientific). We used CIBERSORTx (Newman et al. 2019) to estimate the abundances of epithelial end hematopoietic cell types using using bulk gene expression data as an input and scRNAseq signature matrices from single-cell RNA sequencing data to provide the reference gene expression profiles of pure cell populations. The scRNAseq signature matrix used to deconvolute RNAseq dataset from swabs or BALFs were derived from (Wauters et al. 2021; Ziegler et al. 2021).

Gene set enrichment analysis and enrichment plot were generated in R using the Fast Gene Set Enrichment Analysis package (fGSEA) (Korotkevich et al. 2021). Heatmaps were generated in R and visualized with the ComplexHeatmap package (Gu, Eils, and Schlesner 2016). Clustering analysis was performed using Euclidean distances on individual z-scores. Code available upon request.

Quantification And Statistical Analysis.

One-way ANOVA with Turkey's post-hoc test was used to compare continuous variables among multiple groups. Kruskal-Wallis test with Dunn's post-hoc test or Multiple Mann-Whitney tests with Holm-Šídák method were used instead when data did not meet the normality assumption. Fisher's exact test was used to compare categorical variables. Spearman correlation analysis was used to examine the degree of association between two continuous variables. To establish the appropriate test, normal distribution and variance similarity were assessed with the D'Agostino-Pearson omnibus normality test.

Cluster analysis with unbiased K-mean methods based on the expression of IFN-I, IFN-III and the proinflammatory cytokine IL-1β were used to classify a subset of COVID-19 patients into 3 exclusive clusters.

Cluster analysis with unbiased K-mean methods based on the expression of Interferons and pro-inflammatory cytokines in the BALF were used to classify COVID-19 patients, non-COVID-19 ARDS patients, and controls into 3 exclusive clusters. Heatmaps and K-mean clustering were generated in R and visualized with the ComplexHeatmap package. Clustering analysis was performed using Euclidean distances.

Estimated (K) value was selected based on the elbow point cluster number. Logistic regression models were performed to estimate the association of gene expression as binary outcome within viral load terciles (defined by mean viral RNA CT <20, >20 and <30, > 30), and clusters (cluster 1, cluster 2 and cluster 3). Interaction between viral load terciles and age groups (≥70 years vs <70 years) were tested to detect significant difference between elder patients and young patients in their gene expression response to different levels of viral load. All statistical analyses were two-sided and performed using Prism9 (Graphpad) software or SAS version 9.4 (SAS Institute). All statistical analyses are indicated in figure legends. Throughout the paper significant is defined as follows : ns, not significant (P>0.05); *P<0.05, **P<0.01, ***P<0.001, and ****P<0.0001.

Additional Resources.

A subset of samples included in this study were obtained from the following clinical trial: NCT04318366, https://www.clinicaltrials.gov/ct2/show/NCT04318366

References.

1. Banerjee, Abhik K., Mario R. Blanco, Emily A. Bruce, Drew D. Honson, Linlin M. Chen, Amy Chow, Prashant Bhat, et al. 2020. "SARS-CoV-2 Disrupts Splicing, Translation, and Protein Trafficking to Suppress Host Defenses." *Cell* 183 (5): 1325-1339.e21. https://doi.org/10.1016/j.cell.2020.10.004.
2. Bastard, Paul, Lindsey B. Rosen, Qian Zhang, Eleftherios Michailidis, Hans-Heinrich Hoffmann, Yu Zhang, Karim Dorgham, et al. 2020. "Autoantibodies against Type I IFNs in Patients with Life-Threatening COVID-19." *Science (New York, N.Y.)* 370 (6515): eabd4585. https://doi.org/10.1126/science.abd4585.
3. Bergamaschi, Laura, Federica Mescia, Lorinda Turner, Aimee L. Hanson, Prasanti Kotagiri, Benjamin J. Dunmore, Hélène Ruffieux, et al. 2021. "Longitudinal Analysis Reveals That Delayed Bystander CD8+ T Cell Activation and Early Immune Pathology Distinguish Severe COVID-19 from Mild Disease." *Immunity* 54 (6): 1257-1275.e8. https://doi.org/10.1016/j.immuni.2021.05.010.
4. Blanco-Melo, Daniel, Benjamin E. Nilsson-Payant, Wen-Chun Liu, Skyler Uhl, Daisy Hoagland, Rasmus Møller, Tristan X. Jordan, et al. 2020. "Imbalanced Host Response to SARS-CoV-2 Drives Development of COVID-19." *Cell* 181 (5): 1036-1045.e9. https://doi.org/10.1016/j.cell.2020.04.026.
5. Broggi, Achille, Sreya Ghosh, Benedetta Sposito, Roberto Spreafico, Fabio Balzarini, Antonino Lo Cascio, Nicola Clementi, et al. 2020. "Type III Interferons Disrupt the Lung Epithelial Barrier upon Viral Recognition." *Science* 369 (6504): 706–12. https://doi.org/10.1126/science.abc3545.
6. Cheemarla, Nagarjuna R., Timothy A. Watkins, Valia T. Mihaylova, Bao Wang, Dejian Zhao, Guilin Wang, Marie L. Landry, and Ellen F. Foxman. 2021. "Dynamic Innate Immune Response Determines Susceptibility to SARS-CoV-2 Infection and Early Replication Kinetics." *Journal of Experimental Medicine* 218 (8): e20210583. https://doi.org/10.1084/jem.20210583.
7. Combes, Alexis J., Tristan Courau, Nicholas F. Kuhn, Kenneth H. Hu, Arja Ray, William S. Chen, Nayvin W. Chew, et al. 2021. "Global Absence and Targeting of Protective Immune States in

Severe COVID-19." *Nature* 591 (7848): 124–30. https://doi.org/10.1038/s41586-021-03234-7.

8. Galani, Ioanna-Evdokia, Nikoletta Rovina, Vicky Lampropoulou, Vasiliki Triantafyllia, Maria Manioudaki, Eleftherios Pavlos, Evangelia Koukaki, et al. 2021. "Untuned Antiviral Immunity in COVID-19 Revealed by Temporal Type I/III Interferon Patterns and Flu Comparison." *Nature Immunology* 22 (1): 32–40. https://doi.org/10.1038/s41590-020-00840-x.
9. Gu, Zuguang, Roland Eils, and Matthias Schlesner. 2016. "Complex Heatmaps Reveal Patterns and Correlations in Multidimensional Genomic Data." *Bioinformatics (Oxford, England)* 32 (18): 2847–49. https://doi.org/10.1093/bioinformatics/btw313.
10. Guan, Wei-jie, Zheng-yi Ni, Yu Hu, Wen-hua Liang, Chun-quan Ou, Jian-xing He, Lei Liu, et al. 2020. "Clinical Characteristics of Coronavirus Disease 2019 in China." *New England Journal of Medicine* 382 (18): 1708–20. https://doi.org/10.1056/NEJMoa2002032.
11. Hadjadj, Jérôme, Nader Yatim, Laura Barnabei, Aurélien Corneau, Jeremy Boussier, Nikaïa Smith, Hélène Péré, et al. 2020. "Impaired Type I Interferon Activity and Inflammatory Responses in Severe COVID-19 Patients." *Science (New York, N.Y.)* 369 (6504): 718–24. https://doi.org/10.1126/science.abc6027.
12. Karki, Rajendra, Bhesh Raj Sharma, Shraddha Tuladhar, Evan Peter Williams, Lillian Zalduondo, Parimal Samir, Min Zheng, et al. 2021. "Synergism of TNF-α and IFN-γ Triggers Inflammatory Cell Death, Tissue Damage, and Mortality in SARS-CoV-2 Infection and Cytokine Shock Syndromes." *Cell* 184 (1): 149-168.e17. https://doi.org/10.1016/j.cell.2020.11.025.
13. Konno, Yoriyuki, Izumi Kimura, Keiya Uriu, Masaya Fukushi, Takashi Irie, Yoshio Koyanagi, Daniel Sauter, Robert J. Gifford, So Nakagawa, and Kei Sato. 2020. "SARS-CoV-2 ORF3b Is a Potent Interferon Antagonist Whose Activity Is Increased by a Naturally Occurring Elongation Variant." *Cell Reports* 32 (12): 108185. https://doi.org/10.1016/j.celrep.2020.108185.
14. Korotkevich, Gennady, Vladimir Sukhov, Nikolay Budin, Boris Shpak, Maxim N. Artyomov, and Alexey Sergushichev. 2021.

"Fast Gene Set Enrichment Analysis." *BioRxiv*, February, 060012. https://doi.org/10.1101/060012.

15. Laing, Adam G., Anna Lorenc, Irene Del Molino Del Barrio, Abhishek Das, Matthew Fish, Leticia Monin, Miguel Muñoz-Ruiz, et al. 2020. "Author Correction: A Dynamic COVID-19 Immune Signature Includes Associations with Poor Prognosis." *Nature Medicine* 26 (10): 1663. https://doi.org/10.1038/s41591-020-1079-x.
16. Lee, Jeong Seok, Seongwan Park, Hye Won Jeong, Jin Young Ahn, Seong Jin Choi, Hoyoung Lee, Baekgyu Choi, et al. 2020. "Immunophenotyping of COVID-19 and Influenza Highlights the Role of Type I Interferons in Development of Severe COVID-19." *Science Immunology* 5 (49): eabd1554. https://doi.org/10.1126/sciimmunol.abd1554.
17. Lei, Xiaobo, Xiaojing Dong, Ruiyi Ma, Wenjing Wang, Xia Xiao, Zhongqin Tian, Conghui Wang, et al. 2020. "Activation and Evasion of Type I Interferon Responses by SARS-CoV-2." *Nature Communications* 11 (1): 3810. https://doi.org/10.1038/s41467-020-17665-9.
18. Lieberman, Nicole A. P., Vikas Peddu, Hong Xie, Lasata Shrestha, Meei-Li Huang, Megan C. Mears, Maria N. Cajimat, et al. 2020. "In Vivo Antiviral Host Transcriptional Response to SARS-CoV-2 by Viral Load, Sex, and Age." *PLOS Biology* 18 (9): e3000849. https://doi.org/10.1371/journal.pbio.3000849.
19. Liu, GuanQun, Jung-Hyun Lee, Zachary M. Parker, Dhiraj Acharya, Jessica J. Chiang, Michiel van Gent, William Riedl, et al. 2021. "ISG15-Dependent Activation of the Sensor MDA5 Is Antagonized by the SARS-CoV-2 Papain-like Protease to Evade Host Innate Immunity." *Nature Microbiology* 6 (4): 467–78. https://doi.org/10.1038/s41564-021-00884-1.
20. Lucas, Carolina, Patrick Wong, Jon Klein, Tiago B. R. Castro, Julio Silva, Maria Sundaram, Mallory K. Ellingson, et al. 2020. "Longitudinal Analyses Reveal Immunological Misfiring in Severe COVID-19." *Nature* 584 (7821): 463–69. https://doi.org/10.1038/s41586-020-2588-y.
21. Major, Jack, Stefania Crotta, Miriam Llorian, Teresa M. McCabe, Hans Henrik Gad, Simon L. Priestnall, Rune Hartmann, and Andreas Wack. 2020. "Type I and III Interferons Disrupt Lung

Epithelial Repair during Recovery from Viral Infection." *Science* 369 (6504): 712–17. https://doi.org/10.1126/science.abc2061.

22. Marongiu, Laura, Giulia Protti, Fabio A. Facchini, Mihai Valache, Francesca Mingozzi, Valeria Ranzani, Anna Rita Putignano, et al. 2022. "Maturation Signatures of Conventional Dendritic Cell Subtypes in COVID-19 Suggest Direct Viral Sensing." *European Journal of Immunology* 52 (1): 109–22. https://doi.org/10.1002/eji.202149298.
23. Martin-Sancho, Laura, Mary K. Lewinski, Lars Pache, Charlotte A. Stoneham, Xin Yin, Mark E. Becker, Dexter Pratt, et al. 2021. "Functional Landscape of SARS-CoV-2 Cellular Restriction." *Molecular Cell* 81 (12): 2656-2668.e8. https://doi.org/10.1016/j.molcel.2021.04.008.
24. McPadden, Jacob, Frederick Warner, H. Patrick Young, Nathan C. Hurley, Rebecca A. Pulk, Avinainder Singh, Thomas JS Durant, et al. 2020. "Clinical Characteristics and Outcomes for 7,995 Patients with SARS-CoV-2 Infection." *MedRxiv*, November, 2020.07.19.20157305. https://doi.org/10.1101/2020.07.19.20157305.
25. Mudd, Philip A., Jeremy Chase Crawford, Jackson S. Turner, Aisha Souquette, Daniel Reynolds, Diane Bender, James P. Bosanquet, et al. 2020. "Distinct Inflammatory Profiles Distinguish COVID-19 from Influenza with Limited Contributions from Cytokine Storm." *Science Advances* 6 (50): eabe3024. https://doi.org/10.1126/sciadv.abe3024.
26. Newman, Aaron M., Chloé B. Steen, Chih Long Liu, Andrew J. Gentles, Aadel A. Chaudhuri, Florian Scherer, Michael S. Khodadoust, et al. 2019. "Determining Cell Type Abundance and Expression from Bulk Tissues with Digital Cytometry." *Nature Biotechnology* 37 (7): 773–82. https://doi.org/10.1038/s41587-019-0114-2.
27. Onodi, Fanny, Lucie Bonnet-Madin, Laurent Meertens, Léa Karpf, Justine Poirot, Shen-Ying Zhang, Capucine Picard, et al. 2021. "SARS-CoV-2 Induces Human Plasmacytoid Predendritic Cell Diversification via UNC93B and IRAK4 SARS-CoV-2 and Plasmacytoid Predendritic Cells." *Journal of Experimental Medicine* 218 (4): e20201387. https://doi.org/10.1084/jem.20201387.

28. Overholt, Kalon J., Jonathan R. Krog, Ivan Zanoni, and Bryan D. Bryson. 2021. “Dissecting the Common and Compartment-Specific Features of COVID-19 Severity in the Lung and Periphery with Single-Cell Resolution.” *IScience* 24 (7): 102738. https://doi.org/10.1016/j.isci.2021.102738.
29. Pairo-Castineira, Erola, Sara Clohisey, Lucija Klaric, Andrew D. Bretherick, Konrad Rawlik, Dorota Pasko, Susan Walker, et al. 2021. “Genetic Mechanisms of Critical Illness in COVID-19.” *Nature* 591 (7848): 92–98. https://doi.org/10.1038/s41586-020-03065-y.
30. Park, Annsea, and Akiko Iwasaki. 2020. “Type I and Type III Interferons – Induction, Signaling, Evasion, and Application to Combat COVID-19.” *Cell Host & Microbe* 27 (6): 870–78. https://doi.org/10.1016/j.chom.2020.05.008.
31. Prokunina-Olsson, Ludmila, Noémie Alphonse, Ruth E. Dickenson, Joan E. Durbin, Jeffrey S. Glenn, Rune Hartmann, Sergei V. Kotenko, et al. 2020. “COVID-19 and Emerging Viral Infections: The Case for Interferon Lambda.” *The Journal of Experimental Medicine* 217 (5): e20200653. https://doi.org/10.1084/jem.20200653.
32. Ruan, Qiurong, Kun Yang, Wenxia Wang, Lingyu Jiang, and Jianxin Song. 2020. “Clinical Predictors of Mortality Due to COVID-19 Based on an Analysis of Data of 150 Patients from Wuhan, China.” *Intensive Care Medicine* 46 (5): 846–48. https://doi.org/10.1007/s00134-020-05991-x.
33. Wang, Eric Y., Tianyang Mao, Jon Klein, Yile Dai, John D. Huck, Jillian R. Jaycox, Feimei Liu, et al. 2021. “Diverse Functional Autoantibodies in Patients with COVID-19.” *Nature* 595 (7866): 283–88. https://doi.org/10.1038/s41586-021-03631-y.
34. Wauters, Els, Pierre Van Mol, Abhishek Dinkarnath Garg, Sander Jansen, Yannick Van Herck, Lore Vanderbeke, Ayse Bassez, et al. 2021. “Discriminating Mild from Critical COVID-19 by Innate and Adaptive Immune Single-Cell Profiling of Bronchoalveolar Lavages.” *Cell Research* 31 (3): 272–90. https://doi.org/10.1038/s41422-020-00455-9.
35. Williamson, Elizabeth J., Alex J. Walker, Krishnan Bhaskaran, Seb Bacon, Chris Bates, Caroline E. Morton, Helen J. Curtis, et al. 2020. “Factors Associated with COVID-19-Related Death Using

OpenSAFELY." *Nature* 584 (7821): 430–36. https://doi.org/10.1038/s41586-020-2521-4.

36. Winkler, Emma S., Adam L. Bailey, Natasha M. Kafai, Sharmila Nair, Broc T. McCune, Jinsheng Yu, Julie M. Fox, et al. 2020. "SARS-CoV-2 Infection of Human ACE2-Transgenic Mice Causes Severe Lung Inflammation and Impaired Function." *Nature Immunology* 21 (11): 1327–35. https://doi.org/10.1038/s41590-020-0778-2.
37. Wu, Jing, Yuheng Shi, Xiaoyan Pan, Shuang Wu, Ruixia Hou, Yong Zhang, Tiansheng Zhong, et al. 2021. "SARS-CoV-2 ORF9b Inhibits RIG-I-MAVS Antiviral Signaling by Interrupting K63-Linked Ubiquitination of NEMO." *Cell Reports* 34 (7): 108761. https://doi.org/10.1016/j.celrep.2021.108761.
38. Xia, Hongjie, Zengguo Cao, Xuping Xie, Xianwen Zhang, John Yun-Chung Chen, Hualei Wang, Vineet D. Menachery, Ricardo Rajsbaum, and Pei-Yong Shi. 2020. "Evasion of Type I Interferon by SARS-CoV-2." *Cell Reports* 33 (1): 108234. https://doi.org/10.1016/j.celrep.2020.108234.
39. Yin, Xin, Laura Riva, Yuan Pu, Laura Martin-Sancho, Jun Kanamune, Yuki Yamamoto, Kouji Sakai, et al. 2021. "MDA5 Governs the Innate Immune Response to SARS-CoV-2 in Lung Epithelial Cells." *Cell Reports* 34 (2): 108628. https://doi.org/10.1016/j.celrep.2020.108628.
40. Zhang, Qian, Paul Bastard, Zhiyong Liu, Jérémie Le Pen, Marcela Moncada-Velez, Jie Chen, Masato Ogishi, et al. 2020. "Inborn Errors of Type I IFN Immunity in Patients with Life-Threatening COVID-19." *Science (New York, N.Y.)* 370 (6515): eabd4570. https://doi.org/10.1126/science.abd4570.
41. Zhou, Fei, Ting Yu, Ronghui Du, Guohui Fan, Ying Liu, Zhibo Liu, Jie Xiang, et al. 2020. "Clinical Course and Risk Factors for Mortality of Adult Inpatients with COVID-19 in Wuhan, China: A Retrospective Cohort Study." *The Lancet* 395 (10229): 1054–62. https://doi.org/10.1016/S0140-6736(20)30566-3.
42. Zhou, Zhuo, Lili Ren, Li Zhang, Jiaxin Zhong, Yan Xiao, Zhilong Jia, Li Guo, et al. 2020. "Heightened Innate Immune Responses in the Respiratory Tract of COVID-19 Patients." *Cell Host & Microbe* 27 (6): 883-890.e2. https://doi.org/10.1016/j.chom.2020.04.017.

43. Ziegler, Carly G. K., Vincent N. Miao, Anna H. Owings, Andrew W. Navia, Ying Tang, Joshua D. Bromley, Peter Lotfy, et al. 2021. “Impaired Local Intrinsic Immunity to SARS-CoV-2 Infection in Severe COVID-19.” *Cell* 184 (18): 4713-4733.e22. https://doi.org/10.1016/j.cell.2021.07.023.

Chapter 4. Type III interferons induce pyroptosis in gut epithelial cells and delay tissue restitution upon acute intestinal injury.

Benedetta Sposito[1, 2], Julien Mambu[3], Katlynn Bugda Gwilt[4], Lionel Spinelli[3], Natalia Andreeva[1], Franck Galland[3], Philippe Naquet[3], Vanessa Mitsialis[4], Jay R Thiagarajah[4], Scott B Snapper[4], Achille Broggi[3, *], Ivan Zanoni[1, 4, *]

[1] Harvard Medical School, and Boston Children's Hospital, Division of Immunology, Boston, USA.

[2] Dep. of Biotechnology and Biosciences and Ph.D. program in Molecular and Translational Medicine (DIMET), University of Milano - Bicocca, Milan, 20100, Italy

[3] Aix Marseille Université, CNRS, INSERM, Centre d'Immunologie de Marseille-Luminy (CIML), 13288 Marseille Cedex 9, France.

[4] Harvard Medical School, Boston Children's Hospital, Division of Gastroenterology, Boston, USA.

* These authors contributed equally.

Correspondence:

ivan.zanoni@childrens.harvard.edu

broggi@ciml.univ-mrs.fr

bioRxiv 2022.03.04.482997

DOI: 10.1101/2022.03.04.482997

Abstract.

Tissue damage and repair are hallmarks of the inflammatory process. Despite a wealth of information focused on the mechanisms that govern tissue damage, mechanistic insight on how inflammatory immune mediators affect the restitution phase is lacking. Here, we investigated how interferons influence tissue restitution after damage of the intestinal mucosa driven by inflammatory or physical injury. We found that type III, but not type I, interferons serve a central role in the restitution process. Type III interferons induce the upregulation of ZBP1, caspase activation, and cleavage of gasdermin C, and drive epithelial cell death by pyroptosis, thus delaying tissue restitution. We also found that this pathway is transcriptionally regulated in IBD patients. Our findings highlight a new molecular signaling cascade initiated by the immune system that affects the outcome of the immune response by delaying tissue repair and that may have important implications for human inflammatory disorders.

Introduction.

The immune system evolved to protect the host from external or internal threats, as well as to maintain homeostasis of the organs and tissues. The strong interrelationship between these two functions of the immune system is best exemplified during the restitution phase that follows mucosal damage, occurring as a consequence of an immune response. The skin, the lungs, the gut, and other mucosae are constantly exposed to microbial and/or physical perturbations and harbor multiple immune and non-immune cells that sense the presence of hostile environmental or endogenous factors and mount a defensive response. The causative agent of this response, the response itself, or both, may lead to tissue damage. Tissue damage sensing by tissue-resident as well as newly recruited cells initiates a complex cascade of cellular and molecular processes to restore tissue functionality and homeostasis, or to adapt to persistent perturbations (Meizlish et al. 2021).

The gastrointestinal tract represents an ideal tissue to explore the mechanisms underlying the exquisite balance between tissue damage and repair orchestrated by the immune system. In the intestine, immune cells, epithelial cells, and commensal microbes are in a dynamic equilibrium. A monolayer of highly specialized epithelial cells separates the gut lumen from the underlying lamina propria. The interplay between microbiota-derived inflammatory cues and the host cells in the intestine profoundly impacts the biology of the gut, both during homeostasis, inflammation, and damage responses. The lamina propria hosts a large variety of immune and non-immune cells that

detect alterations in the functioning as well as in the integrity of the epithelial barrier and mount an immune response. The fine equilibrium between the microbiota, the epithelial barrier, and the immune system is lost during inflammatory bowel diseases (IBDs). IBDs are a group of heterogeneous diseases, whose pathogenesis is associated with genetic and environmental factors, that are characterized by a dysregulated immune response (Danese and Fiocchi 2011; Roda et al. 2020). Along with a heightened inflammatory response, IBDs are characterized by the breach of the intestinal barrier and a defective repair response that compromises mucosal homeostasis. Therefore, the ability of immune mediators to influence epithelial repair has an important impact on the pathogenesis of IBDs. Indeed, the promotion of mucosal healing has been recognized as a major therapeutic challenge for the management of IBDs (Pineton de Chambrun et al. 2010).

We previously showed that a group of interferons (IFNs), known as type III IFNs or IFN-λ (Kotenko et al. 2003; Sheppard et al. 2003; Prokunina-Olsson et al. 2013), limits inflammation in a mouse model of colitis by dampening the tissue-damaging functions of neutrophils (Broggi et al. 2017). IFN-λ, as type I IFNs, plays potent anti-microbial roles, but, in contrast to type I IFNs, also preserves gut functionality by limiting excessive damage (Broggi, Granucci, and Zanoni 2020). The limited damage is largely explained by the fact that the expression of the IFN-λ receptor (IFNLR) is mainly restricted to epithelial cells and neutrophils. In contrast, type I IFNs act systemically and play potent inflammatory activities on immune and non-immune cells thanks to

the broad expression of the type I IFN receptor (IFNAR). The local activity of IFN-λ at mucosal tissues, thus, limits the extent of activation of immune cells, preventing excessive tissue damage, while preserving the anti-microbial functions of IFN-λ (Broggi, Granucci, and Zanoni 2020).

Although we and others have shown that IFN-λ limits intestinal tissue damage, the involvement of this group of IFNs during tissue restitution of the gut is more controversial. Indeed, IFN-λ and type I IFNs have been shown to function in a balanced and compartmentalized way to favor re-epithelization by acting, respectively, on epithelial cells or immune cells resident in the lamina propria (McElrath et al. 2021). IFN-λ has been also proposed to facilitate the proliferation of intestinal epithelial cells via STAT1 signaling (Chiriac et al. 2017) and to partially enhance gut mucosal integrity during graft versus host disease (Henden et al. 2021). On the other hand, though, IFN-λ and/or the IFNLR were found to be upregulated in IBD patients (Chiriac et al. 2017; Günther et al. 2019). Also, systemic and prolonged overexpression of IFN-λ in mice favored the death of Paneth cells, a group of cells that can facilitate epithelial cell regeneration by acquiring stem-like features (Schmitt et al. 2018), and by regulating the balance of epithelial growth factors in the stem cell niche (Sato, van Es, et al. 2011).

In keeping with a possible detrimental role of IFN-λ during an inflammatory response at mucosal surfaces, we and others have recently demonstrated that IFN-λ delays the proliferation of lung epithelial cells in murine models of persistent viral infections (Broggi

et al. 2020; Major et al. 2020). Also, that IFN-λ production in the lower respiratory tract of COVID-19 patients is associated with increased apoptotic and decreased proliferative transcriptional programs, and characterizes SARS-CoV-2-infected individuals with severe-to-critical outcomes (Sposito et al. 2021). Whether IFN-λ plays similar roles in the intestine, and the molecular mechanisms initiated by this group of IFNs to exert their functions during gut restitution, remain unknown.

Here, by exploiting conditional knock-out mice that do not respond to IFN-λ only in intestinal epithelial cells or in neutrophils, *ex vivo* transcriptomics, and biochemical assays, as well as intestinal organoids *in vitro*, we dissected the role of IFN-λ during tissue repair secondary to either an inflammatory insult or to radiation damage. Our data reveal a new molecular cascade initiated by IFN-λ that culminates in the activation of ZBP1 and of gasdermin C (GSDMC), in the induction of pyroptosis and results in delayed gut restitution.

Results.

IFN-λ delays tissue repair of the inflamed gut.

We previously showed that, in the acute inflammatory phase of the dextran sulfate sodium (DSS) model of colitis, IFN-λ signaling in neutrophils dampens reactive oxygen species production and neutrophil degranulation, and thus restrains intestinal damage (Broggi et al. 2017). To assess the involvement of IFN-λ during the restitution phase of the DSS colitis model, we injected, or not, recombinant (r)IFN-λ in mice after DSS-induced inflammation has peaked. We confirmed that rIFN-λ administration upregulated interferon-stimulated genes

(ISGs) in the colon of DSS-treated mice (**Figure S1A**). Mice administered rIFN-λ, but not vehicle controls, showed persistent weight loss, reduced colon length, and prolonged tissue damage as measured by histology (**Figure 1A-C**). These data suggest that IFN-λ delays tissue restitution in mice encountering colitis.

Next, we tested whether the endogenous IFN-λ, which is produced during colitis development (Broggi et al. 2017), also affects the restitution phase. After the peak of the inflammatory process induced by DSS administration, mice were treated with a blocking antibody directed against IFN-λ and compared to mice treated with DSS, in the presence or absence of rIFN-λ. Our data demonstrated that inhibition of endogenous IFN-λ facilitates tissue restitution as measured by increased weight gain and colon lengthening (**Figure 1D, E**). Notably, we found that ISG levels in epithelial cells were significantly decreased in mice treated with the anti-IFN-λ antibody (**Figure S1A**), suggesting that IFN-λ, rather than type I IFNs, plays a major role in driving gene transcription during the repair phase of colitis. To directly test the involvement of type I IFNs in the restitution phase of DSS-induced colitis, we either blocked type I IFN signaling using an anti-IFNAR antibody, or added rIFNβ, 7 days after DSS administration. In keeping with a key role of IFN-λ in regulating mucosal epithelial responses, none of the treatments aimed at targeting type I IFNs affected tissue repair (**Figure 1F, G**). Accordingly, ISG levels in colonocytes were not altered under these experimental conditions compared to control mice (**Figure S1B**).

While intestinal epithelial cells are the major effector cell type during mucosal restitution, other cells, including immune cells, can participate in modulating tissue repair. Since intestinal epithelial cells and neutrophils are the two cell types that respond to IFN-λ in the gut of mice (Broggi et al. 2017), we used conditional knock out mice that do not express the IFNLR either in intestinal epithelial cells (*Vil*^{CRE}*Ifnlr1*$^{fl/fl}$ mice) or neutrophils (*Mrp8*^{CRE}*Ifnlr1*$^{fl/fl}$ mice). *Ifnlr1*$^{fl/fl}$ (WT) littermates were used as controls. In contrast to WT littermates, administration of rIFN-λ to *Vil*^{CRE}*Ifnlr1*$^{fl/fl}$ mice did not delay tissue restitution as measured by weight change (**Figure 1H**). *Vil*^{CRE}*Ifnlr1*$^{fl/fl}$ mice in which intestinal epithelial cells do not respond to IFN-λ showed a faster recovery as measured by a significant increase in colon length, regardless of the presence or absence of rIFN-λ (**Figure 1I**). In contrast to *Vil*^{CRE}*Ifnlr1*$^{fl/fl}$ mice, *Mrp8*^{CRE}*Ifnlr1*$^{fl/fl}$ behaved similarly to their WT counterpart, in the presence or absence of rIFN-λ (**Figure S1C**). These data demonstrate that, in contrast to the acute inflammatory phase of colitis, epithelial cells, not neutrophils, are the major responders to endogenous, as well as exogenous, IFN-λ and that IFN-λ signaling in epithelial cells delays tissue restitution.

IFN-λ delays the tissue restitution phase that follows radiation damage.

Repair of the gut epithelial monolayer is a complex process, and the regenerative capacity of intestinal stem cells (ISCs) plays a critical role (Blanpain and Fuchs 2014). To target ISCs and assess the direct involvement of IFN-λ during gut restitution, we employed a well-characterized model of epithelial damage resulting from exposure to

ionizing radiations (Kim, Yang, and Bialkowska 2017). In this model, radiation induces widespread epithelial cell death in the small intestine, with a particularly dramatic effect on cycling ISCs that reside at the bottom of the small intestinal crypt. Cell death is followed by repair of the damaged epithelial crypts and return to homeostasis. Three to four days after radiation injury, during the peak of the repair response, crypt regeneration was assessed in WT mice, WT mice administered exogenous rIFN-λ, or *Ifnlr1*$^{-/-}$ mice. We found that mice that received rIFN-λ showed reduced regeneration of the crypts, while *Ifnlr1*$^{-/-}$ mice had an increased number of crypts (**Figure 2A**). Notably, in the small intestine of irradiated mice, similarly to what we observed in the colon of mice exposed to DSS, endogenous IFN-λ, but not type I IFN, signaling caused the delay in tissue restitution (**Figure 2B**). Similarly, ISG induction in epithelial cells was dependent on IFN-λ, rather than type I IFNs (**Figure S2A**).

Next, we assessed the nature of the cell types that respond to IFN-λ in the irradiated small intestine. When *Vil*^{CRE}*Ifnlr1*$^{fl/fl}$ mice and WT littermates were used, we found that the number of crypts three days post-radiation was significantly increased in *Vil*^{CRE}*Ifnlr1*$^{fl/fl}$ mice compared to WT mice (**Figure 2C, S2B**). We also demonstrated that exogenous rIFN-λ does not affect the number of crypts in *Vil*^{CRE}*Ifnlr1*$^{fl/fl}$ mice, while delaying tissue restitution in WT littermates (**Figure 2C, S2B**). In keeping with a key role for epithelial cells, but not neutrophils, in responding to IFN-λ during tissue restitution, we found that *Mrp8*^{CRE}*Ifnlr1*$^{fl/fl}$ mice didn't show significant differences compared to their WT littermates (**Figure S2C**). No differences were measured in

the number of crypts of non-irradiated mice regardless of their capacity to respond, or not, to IFN-λ (**Figure S2D**). Finally, we followed over time irradiated *Vil*^{CRE}*Ifnlr1*$^{fl/fl}$ mice or WT littermates, treated or not with rIFN-λ. We found that WT mice irradiated and treated with rIFN-λ lost significantly more weight than irradiated WT mice, and all died (**Figure 2D, E**). Notably, WT littermates lost significantly more weight compared to *Vil*^{CRE}*Ifnlr1*$^{fl/fl}$ mice, treated or not with rIFN-λ (**Figure 2D**). In contrast, *Vil*^{CRE}*Ifnlr1*$^{fl/fl}$ mice treated or not with rIFN-λ showed a very similar behavior (**Figure 2D, E**). Overall, these data demonstrate that epithelial cell regeneration and tissue restitution in the small intestine of irradiated mice is inhibited in the presence of IFN-λ. Also, that IFN-λ delays repair by acting on intestinal epithelial cells.

IFN-λ dampens regenerative and proliferative transcriptional programs in intestinal epithelial cells.

To determine the transcriptional programs initiated by IFN-λ to delay tissue restitution, we isolated intestinal crypts from the small intestine of *Vil*^{CRE}*Ifnlr1*$^{fl/fl}$ mice or WT littermates that have been irradiated and performed targeted transcriptomics analysis (RNAseq). In keeping with a major role of IFN-λ-dependent responses in the intestine, when we performed gene ontology (GO) enrichment analyses, IFN-signaling related pathways, as well as anti-viral or anti-bacterial pathways, were highly enriched in WT epithelial cells, compared to *Vil*^{CRE}*Ifnlr1*$^{fl/fl}$ (**Figure 3A**). In contrast, GO terms associated with cell migration and extracellular remodeling, which are linked to higher efficiency in the

closure of mucosal wounds (Quirós and Nusrat 2019), were mostly represented in epithelial cells that do not respond to IFN-λ (**Figure 3A**). Gene set enrichment analysis (GSEA) confirmed that genes associated with IFN responses were significantly enriched in WT, compared to knock-out, epithelial cells (**Figure 3B, S3A**). We next assessed the relative enrichment of a previously identified colitis-associated regenerative epithelial gene-set (Yui et al. 2018), as well as gene-sets associated with epithelial cell proliferation. Both gene-sets were significantly enriched when epithelial cells did not respond to IFN-λ (**Figure 3C, D, S3B, C**).

To assess whether IFN-λ-dependent delayed tissue restitution is characterized by reduced cell proliferation *in vivo*, we administered the thymidine analog 2'-deoxy-5-ethynyluridine (EdU) two hours before mice were euthanized and measured cell proliferation in either WT littermates or $Vil^{CRE}Ifnlr1^{fl/fl}$ mice, administered or not rIFN-λ. We found that exogenous rIFN-λ reduced the number of EdU-positive cells per crypt in WT but not $Vil^{CRE}Ifnlr1^{fl/fl}$ mice (**Figure 3E**). Also, that $Vil^{CRE}Ifnlr1^{fl/fl}$ mice had a significant increased number of proliferating cells per crypts, compared to WT littermates, irrespectively of the administration of rIFN-λ (**Figure 3E**).

During tissue repair that follows radiation damage (Metcalfe et al. 2014) or colitis (VanDussen, Sonnek, and Stappenbeck 2019), specialized ISCs drive re-epithelialization by massively proliferating. Therefore, the decreased number of proliferating epithelial cells we observed in WT mice may reflect the lack of reparatory ISCs that proliferate. To assess whether endogenous

IFN-λ affected the cellular composition of the small intestine in WT or *Vil*^{CRE}*Ifnlr1*$^{fl/fl}$ mice that were irradiated, we used CIBERSORTx (Newman et al. 2019) and deconvoluted our bulk RNAseq data based on single-cell RNAseq data previously published (Haber et al. 2017). Our deconvolution analysis revealed that, while most epithelial cell types did not present major significant differences, the ISC compartment was significantly expanded in mice that were irradiated and whose epithelial cells do not respond to IFN-λ (**Figure 3F**). In keeping with retro-differentiation of transit-amplifying (TA) cells to replenish the ISC compartment upon ISC depletion (Wang et al. 2019; Ohara, Colonna, and Stappenbeck 2022), TA cells were significantly decreased in the small intestine of *Vil*^{CRE}*Ifnlr1*$^{fl/fl}$ mice, compared to WT controls (**Figure 3F**). The expansion of the Lrg5^{+} compartment in mice that do not respond to IFN-λ was confirmed by qPCR (**Figure S3D**). We also confirmed that the major epithelial cell populations analyzed were not different under homeostatic conditions in *Vil*^{CRE}*Ifnlr1*$^{fl/fl}$ mice or WT littermates (**Figure S3E**). Overall, these data demonstrate that IFN-λ initiates a transcriptional program that reduces tissues restitution, limits ISC cell expansion, and, thus, dampens the overall capacity of epithelial cells to proliferate.

IFN-λ controls the expression of ZBP1 and the activation of Gasdermin C.

The reduced expansion of ISC can be driven either by increased cell death of ISCs and/or TA cells, reduced proliferative programs, or both. To determine the molecular mechanisms regulated by IFN-λ to dampen tissue restitution, we identified the genes that were

significantly differentially regulated in epithelial cells derived from irradiated *Vil*^{CRE}*Ifnlr1*$^{fl/fl}$, compared to WT, mice (**Figure 4A**). As expected, multiple ISGs were among the genes significantly downregulated in cells that cannot respond to IFN-λ (**Figure 4A**). Intriguingly, *Zbp1* was among these genes. ZBP1 is a key component in the multiprotein complex PANoptosome, which encompasses effectors of several forms of cell death, and is an important regulator of cell fate (Kuriakose and Kanneganti 2018). We also found that protein levels of ZBP1, as well as another ISG such as RSAD2, were upregulated in epithelial cells of the small intestine upon *in vivo* administration of rIFN-λ in non-irradiated WT mice (**Figure S4A**). Upregulation of these proteins was prevented in epithelial cells derived from *Vil*^{CRE}*Ifnlr1*$^{fl/fl}$ mice and was not different in the absence of rIFN-λ in the two backgrounds (**Figure S4A**). Among other genes significantly downregulated in cells that do not respond to IFN-λ there were two members of the gasdermin C (GSDMC) family. GSDMs are critical effectors of pyroptosis, a form of inflammatory cell death (Kovacs and Miao 2017). Compared to other GSDMs, very little is known about the functions of GSDMC, and scattered reports have involved GSDMC in the lytic death of tumor cells (Hou et al. 2020; Zhang et al. 2021), or of enterocytes during helminth infections (Xi et al. 2021). Of note, non-irradiated mice administered with rIFN-λ do not show upregulation of the GSDMC protein (**Figure S4A**), demonstrating that additional pathways associated with irradiation and/or tissue damage and repair regulate *Gsdmc* gene expression and/or protein synthesis.

IBD patients present increased levels of IFN-λ and/or *Ifnlr1* (Günther et al. 2019; Chiriac et al. 2017). Prompted by our findings in irradiated mice, we assessed the expression levels of *ZBP1* and *GSDMC* (the only GSDMC present in humans) in the biopsy derived from a cohort of IBD patients with active or inactive disease, or non-IBD controls (see Material and Methods for details). We found a significant increase in the expression of *ZBP1* as well as *GSDMC* in patients with active IBD, compared to non-IBD controls (**Figure 4B**). Similar expression trends were observed in RNAseq datasets derived from rectal mucosal biopsies from ulcerative colitis (UC) pediatric patients (PROTECT cohort) and from ileal biopsies from Crohn's disease (CD) pediatric patients (RISK cohort) in two independent cohorts previously published (Haberman et al. 2014; 2019) (**Figure S4B**). In keeping with a key role of IFNs also in IBD patients, we found that genes regulated in response of IFNs (evaluated as mean expression of genes that belong to the "HALLMARK _IFN_ALPHA_RESPONSE" gene-set (Liberzon et al. 2015) and indicated as "IFN response score") were significantly enriched in IBD patients with active disease, compared to controls or patients with inactive disease (**Figure 4B**). In support of a role of IFN-λ in modulating GSDMC expression, *GSDMC* levels positively correlated with the IFN response score in patients with active disease, but not in the other subjects analyzed (**Figure 4C**). These data indicate that IFN induction and upregulation of the genes that encode for ZBP1 and GSDMC are hallmarks of intestinal damage both in mice and humans.

GSDMs exert their pyroptotic function upon cleavage by caspases (Kovacs and Miao 2017), when the N-terminal cleavage product oligomerizes to form lytic pores in the cell membrane, leading to the loss of ionic homeostasis and cell death (Broz, Pelegrín, and Shao 2020). We, thus, tested whether GSDMC-2/-3 were cleaved in epithelial cells of the small intestine upon irradiation and confirmed that irradiated, but not non-irradiated, mice not only showed increased levels of GSDMC-2/-3, but also that GSDMC-2/-3 were efficiently cleaved in WT, but not *Vil*^{CRE}*Ifnlr1*$^{fl/fl}$, mice (**Figure 4D**). In contrast, another key effector of pyroptosis, GSDMD, was not activated.

GSDMC is primarily cleaved by Caspase-8 (Hou et al. 2020; Zhang et al. 2021). Indeed, the pattern of bands of cleaved GSDMC-2/-3 is compatible with the activity of Caspase-8 (Julien and Wells 2017). We thus investigated the activation of Caspase-8. Caspase-8 was not activated in WT or *Vil*^{CRE}*Ifnlr1*$^{fl/fl}$ mice in the absence of irradiation (**Figure S4A**). In contrast, epithelial cells derived from irradiated WT littermates, but not *Vil*^{CRE}*Ifnlr1*$^{fl/fl}$ mice, efficiently activated Caspase-8 (**Figure 4D**). Of note, we found that expression of *CASP8* was increased in patients with active IBD compared to non-IBD controls (**Figure 4B, S4B**). In keeping with the capacity of ZBP1 to control the activation of multiple caspases (Kuriakose and Kanneganti 2018), we found that a similar pattern of activation was also true for Caspase-3 (**Figure 4D**).

Overall, these data demonstrate that IFN-λ initiates in the small intestine of irradiated mice a signaling cascade that allows the upregulation of ZBP1, the activation of Caspase-8/-3, and the

induction and cleavage of GSDMC, an executor of pyroptosis. Also, that similar programs are transcriptionally upregulated in IBD patients with active disease.

The ZBP1-GSDMC axis induced by IFN-λ controls epithelial cell death and proliferation.

To assess directly the role of the signaling cascade initiated by IFN-λ in driving cell death, we used intestinal organoids. Mouse and human small intestinal organoids seeded in the presence of rIFN-λ died between 48 and 72h from treatment (**Figure 5A, S5A**). Dying cells assumed typical changes associated with pyroptosis including swelling and sudden disruption of the plasma membrane and liberation of nuclear DNA (**Figure 5A**). By using organoids derived from WT or *Stat1*$^{-/-}$ mice, we also confirmed that gene transcription induced by IFN-λ was necessary to induce cell death (**Figure 5B**). No differences were observed between the two genotypes in the absence of rIFN-λ (**Figure 5B**). Similar to what we observed in irradiated epithelial cells *in vivo*, we found that rIFN-λ administration to small intestine organoids profoundly diminished the level of *Lgr5* expression, suggesting a defect in the maintenance and/or proliferation of ISCs (**Figure S5B**). In agreement with a reduced number of ISCs that proliferate, we also found that cell proliferation (as measured by EdU incorporation) was significantly decreased in IFN-λ-treated mouse, as well as human organoids (**Figure 5C, S5C**).

To assess the involvement of ZBP1 in these processes, we derived organoids from either WT or *Zbp1*$^{-/-}$ mice. Organoids were differentiated in the presence or absence of IFN-λ and their survival

and/or growth was followed for 72h. Survival and growth of organoids, derived either from the small or large intestine, differentiated from WT, but not *Zbp1*$^{-/-}$, mice were significantly reduced upon the administration of rIFN-λ (**Figure 5D, S5D**). In agreement with the capacity of IFN-λ to activate a ZBP1/Caspase-8/GSDMC axis, organoids grown for 6 days and then administered with rIFN-λ showed ZBP1 upregulation and cleavage of GSDMC-2/-3 and Caspase-8 and Caspase-3 (**Figure 5E**). Furthermore, inhibition of caspase activity with the pan-caspase inhibitor Z-VAD-FMK protected the organoids from cell death induced by IFN-λ (**Figure 5F**). To directly assess the involvement of GSDMC in this process, we knocked down *Gsdmc-2 and Gsdmc-3* in small intestine organoids and found that, similar to *Zbp1*$^{-/-}$ organoids, upon exposure to rIFN-λ, survival of organoids that do not express *Gsdmc2, 3* was significantly increased compared to controls (**Figure 5G**).

To better reflect the cycles of injury and repair characteristic of IBD and mouse models of colitis, we implemented a previously described model of long-term organoid culture (Wang et al. 2019). We grew organoids in a two-dimensional (2D) epithelial monolayer system and exposed their apical side to air, to obtain a self-organizing monolayer that mimics cells in homeostasis. This monolayer can then be re-submerged in medium (to elicit damage response mimicking *in vivo* epithelial injuries) and re-exposed to air (which induces epithelial regeneration responses) (**Figure 5H**). When we treated with IFN-λ the epithelial monolayer after re-exposure to air, the proliferative repair

response was curbed, as demonstrated by the failure to incorporate EdU (**Figure 5I**).

Overall, our data demonstrate that IFN-λ signaling induces a ZBP-1-GSDMC axis that controls epithelial cell survival, and dampens the capacity of ISCs to proliferate and orchestrate tissue restitution.

Discussion.

In our work, we revealed that IFN-λ restrains the restitution of the intestinal mucosae secondary to either inflammatory damage or ionizing radiations toxicity. We reveal the capacity of IFN-λ to initiate a previously overlooked molecular cascade in intestinal epithelial cells that allows the induction of ZBP1, the activation of caspases, and the induction and cleavage of GSDMCs. We also found that similar pathways are transcriptionally upregulated in IBD patients with active disease. Induction of epithelial cell death via the ZBP1-GSDMC axis reduces the number of ISCs, and dampens the proliferation and restitution of epithelial cells, thus affecting the re-epithelization of the injured intestine. Finally, we revealed that IFN-λ, but not type I IFNs, are the major drivers of the delayed restitution *in vivo* in mouse models of gut damage.

The immune system is endowed with the capacity not only to protect against pathogen invasion but also to maintain tissue homeostasis. Fundamental to exert these activities, is the fine balance between anti-microbial functions of the immune system that can drive tissue damage, and the regenerative capacity of organs and tissues. Many cellular and molecular mediators of the immune system are involved

in exerting anti-microbial and potentially damaging functions, but several can also modulate mucosal repair. Here, we focused our attention on a group of IFNs, known as type III IFNs or IFN-λ. IFN-λ activities at mucosal surfaces are essential to limit pathogen spread while reducing inflammation and immune cell infiltration (Broggi, Granucci, and Zanoni 2020). IFN-λ and type I IFNs regulate very similar transcriptional programs, but the limited expression of the IFNLR restricts the activity of IFN-λ to epithelial cells, hepatocytes, neutrophils and few other cell types and, thus, reduces the extent of the inflammation (Broggi, Granucci, and Zanoni 2020). The limited number of cells that respond to IFN-λ signaling, and the reduced capacity of IFN-λ, compared to type I IFNs, to activate IRF1 (Forero et al. 2019) allow to preserve the functionality of mucosal tissues during an immune response. Although the protective functions of IFN-λ in the gut, and in general at mucosal surfaces, are well known (Broggi, Granucci, and Zanoni 2020), much less is known about the functions of this group of IFNs during the healing phase that follows intestinal tissue damage. Our data reveal the unique capacity of IFN-λ, compared to type I IFNs, to negatively affect tissue restitution in the intestine, possibly opening new ways of therapeutic intervention for individuals that encounter tissue damage such as IBD patients or subjects exposed to radiation therapies.

A common feature revealed by our analyses is that IFN-λ affects the survival of the cells, decreases the number of ISCs, and dampens the proliferation of the cells in the crypts, both *in vivo* in mice and *in vitro* in both human and mouse organoids. Tissue restitution in the gut is

regulated by a complex crosstalk between epithelial cells, immune cells, microbial stimuli, and mesenchymal cells and culminates in the proliferation of ISCs. Treatment with ionizing radiation induces widespread epithelial damage and targets in particular proliferating ISCs in the intestinal crypt, making it an ideal model to understand the dynamics of ISCs proliferation and intestinal healing. $Lrg5^{+}$ ISCs support normal cell turnover as well as injury-induced restitution (Metcalfe et al. 2014). When ISC are depleted by radiation, or by immune-mediated tissue-damaging events, TA cells retro-differentiate and acquire new stem-like properties in the small, as well as in the large, intestine (Wang et al. 2019; Ohara, Colonna, and Stappenbeck 2022). These cells then proliferate to allow the re-epithelization of the damaged tissue. We and others previously described the capacity of IFN-λ to dampen lung epithelial cell proliferation (Broggi et al. 2020; Major et al. 2020) and to instruct anti-proliferative transcriptional programs in the lung of patients infected with SARS-CoV-2 (Sposito et al. 2021). Nevertheless, our new findings in the gut suggest that decreased proliferation assessed at transcriptional and cellular levels is due to augmented cell death, possibly occurring in newly generated ISCs or in TA cells. If similar processes also take place in the lung, it remains an open question that will require further investigation.

Another interesting observation we made is that exogenous administration of IFN-λ does not induce caspase or GSDMC activation *in vivo* in the absence of tissue damage, although it induces ZBP1 upregulation at the transcriptional as well as protein level. ZBP1 is a Z-DNA binding protein, and is part of the PANoptosome, a multiprotein

complex that governs the cell fate (Place, Lee, and Kanneganti 2021). PANoptosis is a form of cell death that encompasses pyroptosis, apoptosis, and necroptosis. ZBP1 can interact directly or indirectly with proteins that regulate cell death and drive the activation of apoptotic caspases 8, 3 and 7, the necroptosis effector MLKL, or pyroptosis effectors Casp-1, 11 and GSDMD. So far, GSDMC was not associated with ZBP1 and/or PANoptosis. Our data highlight the existence of a ZBP1-GSDMC axis that appears to be the preferential pathway of cell death that is active during cycles of intestinal epithelial damage and restitution. Upregulation of ZBP1 alone is not sufficient to trigger the full activation of the PANoptosome, which is consistent with our inability to detect toxic effects of IFN-λ in the absence of inflammation or tissue damage. Conversely, ZBP1 can be activated both by binding microbial-derived nucleic acids (Kuriakose et al. 2018; Muendlein et al. 2021) or by binding host-derived Z-DNA following oxidative damage of the mitochondria (Szczesny et al. 2018). It is, thus, possible that *in vivo*, under tissue-damaging conditions, either microbiota- or host-derived DNA becomes available to induce the assembly and activation of the PANoptosome downstream of ZBP1. In contrast to our *in vivo* data, administration of IFN-λ to murine or human intestinal organoids induces the ZBP1-GSDMC axis and drives cell death. We, thus, speculate that under our *in vitro* experimental conditions a “tissue damage” signal, e.g. Z-DNA from dying cells that are differentiating *in vitro*, is available, thus making additional signals unnecessary.

Linked to the above-mentioned observations, we also found that the ISC compartment is not altered under homeostatic conditions in *Vil*^{CRE}*Ifnlr1*$^{fl/fl}$ mice compared to WT mice, suggesting that the basal level of IFNs present during homeostasis (Van Winkle et al. 2022) does not affect the normal turnover of gut epithelial cells. Intriguingly, it has been recently shown that IFN-λ-dependent responses at homeostasis are restricted to pockets of mature enterocytes in the small intestine and in the colon (Van Winkle et al. 2022). In contrast, when mice are injected with rIFN-λ, or infected with murine rotavirus, a type of virus potently controlled by IFN-λ (Walker, Sridhar, and Baldridge 2021), responses to IFN-λ broadly distribute along the epithelial layer. These data, together with our new findings, suggest that the compartmentalization of IFN-λ signaling at homeostasis preserves the functions of ISCs and the normal turnover of gut epithelial cells.

Our models of intestinal damage either of the colon, in the DSS-colitis model, or of the small intestine, in the radiation model, highlight the centrality of IFN-λ and its capacity to delay tissue restitution. Two previous studies suggested that IFN-λ may play an opposite role and favor tissue restitution during colitis (Chiriac et al. 2017; McElrath et al. 2021). Nevertheless, both studies were performed by inducing colitis in total *Ifnlr1*$^{-/-}$ mice and thus they suffer the confounding activity of IFN-λ on neutrophils. The absence of IFN-λ signaling in neutrophils potentiates tissue damage (Broggi et al. 2017), making it hard to compare the tissue restitution phase with WT mice that start from a different level of damage. Indeed, we always administered or blocked IFNs in our colitis model after the peak of the inflammatory

phase. Alternatively, we used mice deficient for the IFNLR only in epithelial cells. Total knock-out mice were solely used in the radiation model in which damage and/or inflammation are not driven by neutrophils but by the ionizing radiations. The compartmentalized activity of IFN-λ in different cell types appears to be, thus, a key feature of this group of IFNs.

Overall, our data unveiled a new axis between IFN-λ, ZBP1 and GSDMC that governs tissue restitution in the gut and open new perspectives to future therapeutic interventions.

Acknowledgements.

IZ is supported by NIH grants 1R01AI121066, 1R01DK115217, 1R01AI165505 and contract no. 75N93019C00044, Lloyd J. Old STAR Program CRI3888, and holds an Investigators in the Pathogenesis of Infectious Disease Award from the Burroughs Wellcome Fund. AB is supported by the excellence initiative of Aix Marseille Université-A*Midex, a French “investissements d’Avenir” program: AMX-20-CE-01; the FRM amorçage de jeunes equipes grant AJE202010012468; and the ANR-JCJC grant “INTERMICI” ANR-21-CE15-0022. The French National Research Agency through the "Investments for the Future" program (France-BioImaging, ANR-10-INBS-04) contributed to support this work. We thank the imaging core facility (ImagImm) of the Centre d'Immunologie de Marseille-Luminy (CIML).

Author contributions.

BS designed, performed, analyzed the experiments; JM performed and analyzed murine organoid experiments; KBG and JT participated to experiments with human organoids and performed and analyzed the knock-down experiment; LS performed the RNAseq data analyses and the transcriptome analysis of IBD patients; NA participated to the histological analyses and *to in vitro* experiments; FG and PN performed the studies on IBD patients; VM and SBS gave advice on *in vitro* and *in vivo* experiments and analyzed human data from publicly available databases; AB conceived the project, designed and performed the experiments, supervised the study, and edited the paper; IZ conceived the project, designed the experiments, supervised the study, and wrote the paper. All authors reviewed and provided input to the manuscript. All authors declare no conflicts of interest.

Figures.

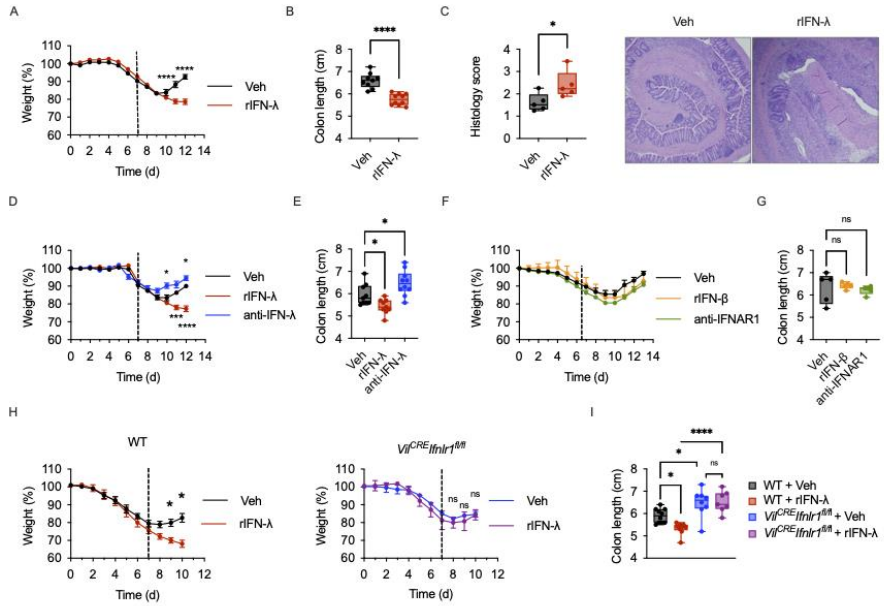

Figure 1. IFN-λ inhibits tissue recovery after DSS-colitis. (**A-C**) WT mice were treated with 2.5% DSS for 7 days (dotted line indicates the end of DSS administration). Upon DSS withdrawal on Day 7, mice were injected intraperitoneally (i.p.) with 50 µg $kg^{-1}day^{-1}$ of rIFN-λ for five consecutive days. Weight (**A**), colon length (**B**), histological score and representative histology images (**C**) are depicted. (**D, E**) WT mice were treated with DSS for 7 days as in (**A-C**). Upon DSS withdrawal mice were injected i.p. with either 50 µg kg-1day-1 of rIFN-λ or 12.5 mg $kg^{-1}day^{-1}$ of anti-IFN-λ2,3 antibody. Weight (**D**), and colon length (**E**) are depicted. (**F, G**) Mice were treated with DSS as in (**A-C**). Upon DSS withdrawal mice were injected i.p. with 50 mg $kg^{-1}day^{-1}$ of rIFN-β or 12.5 mg $kg^{-1}day^{-1}$ of anti-IFNAR1 antibody. Weight (**F**), and colon length (**G**) are depicted. (**H, I**) WT (**H**, *left panel*) or *Vil*^{CRE}*Ifnlr1*$^{fl/fl}$ mice (**H**, *right panel*) were treated with 2.5% DSS for seven days (dotted

line). Upon DSS withdrawal mice were injected i.p. with 50 µg $kg^{-1}day^{-1}$ of rIFN-λ. Weight (**H**), and colon length (**I**) are depicted.

(**A, D, F, H**) Mean and SEM of 5 mice per group are depicted. Two-way ANOVA with Tukey correction for multiple comparisons was utilized. (**B, C, E, G, I**) Box plots are depicted. Each dot represents a mouse. Median, range and interquartile range are depicted. Statistics: (**B, C**) Unpaired t test. (**E, G**) One-way ANOVA with Dunnett correction for multiple comparisons. (**I**) Two-way ANOVA with Šidak correction for multiple comparisons. Data representative of 3 independent experiments. ns= not significant ($p > 0.05$); *$p < 0.05$;**$p < 0.01$; ***$p < 0.001$; ****$p < 0.0001$.

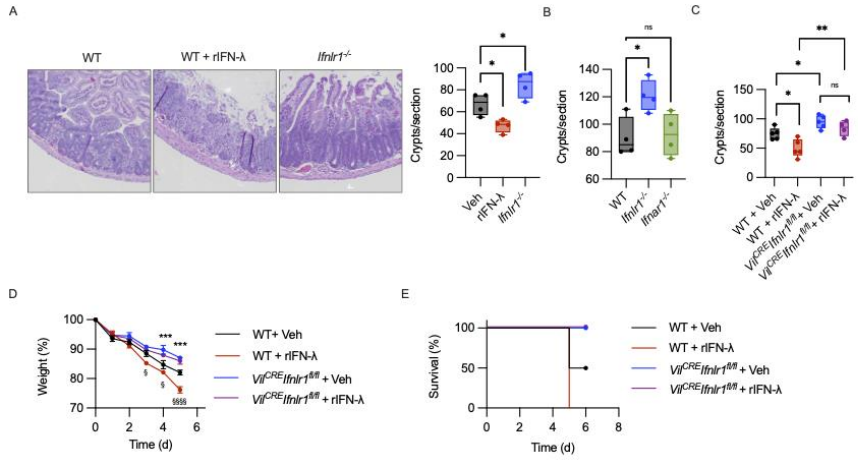

Figure 2. IFN-λ impairs epithelial regeneration after radiation damage. (**A**) WT mice and *Ifnlr1*$^{-/-}$ received 11 Gy ionizing radiation, with lead shielding of the upper body. WT mice were either administered 50 mg kg^{-1}day^{-1} of rIFN-λ (WT + rIFN-λ), or the same volume of saline vehicle (WT + Veh). Tissue repair in the small intestine was evaluated 96h after irradiation by counting the number of intact crypts per histological section (Crypts/section). *Left panel*: Representative histological images; *right panel*: quantification. (**B**) WT, *Ifnlr1*$^{-/-}$, or *Ifnar1*$^{-/-}$ mice were irradiated as in (**A**). Quantification of intact crypts per histological section is depicted. (**C**) *Vil*^{CRE} *Ifnlr1*$^{fl/fl}$ mice or WT mice were irradiated as in (**A**) and treated with either 50 mg kg^{-1}day^{-1} of rIFN-λ (rIFN-λ), or saline vehicle (Veh). Quantification of intact crypts per histological section is depicted. (**D, E**) *Vil*^{CRE} *Ifnlr1*$^{fl/fl}$ mice or WT mice were treated with 14 Gy of ionizing radiation and treated with either 50 mg kg^{-1}day^{-1} of rIFN-λ (rIFN-λ), or saline vehicle (Veh) and followed over time. Weight (**D**) and survival (**E**) are depicted. Statistical comparison between "WT+ Veh" and "*Vil*^{CRE}*Ifnlr1*$^{fl/fl}$ + Veh" are

depicted as (*), comparison between “WT+ Veh” and “WT + rIFN-λ” is depicted as (§).

(**A-C**) Box plots are depicted. Each dot represents a mouse. Median, range and interquartile range are depicted. (**D**) Mean and SEM are depicted. Statistics: (**A, B**) One-way ANOVA with Dunnett correction for multiple comparisons. (**C**) Two-way ANOVA with Šidak correction for multiple comparison. (**D**) Two-way ANOVA with Tukey correction for multiple comparisons. ns= not significant ($p > 0.05$); *$p < 0.05$;**$p < 0.01$; ***$p < 0.001$; ****$p < 0.0001$.

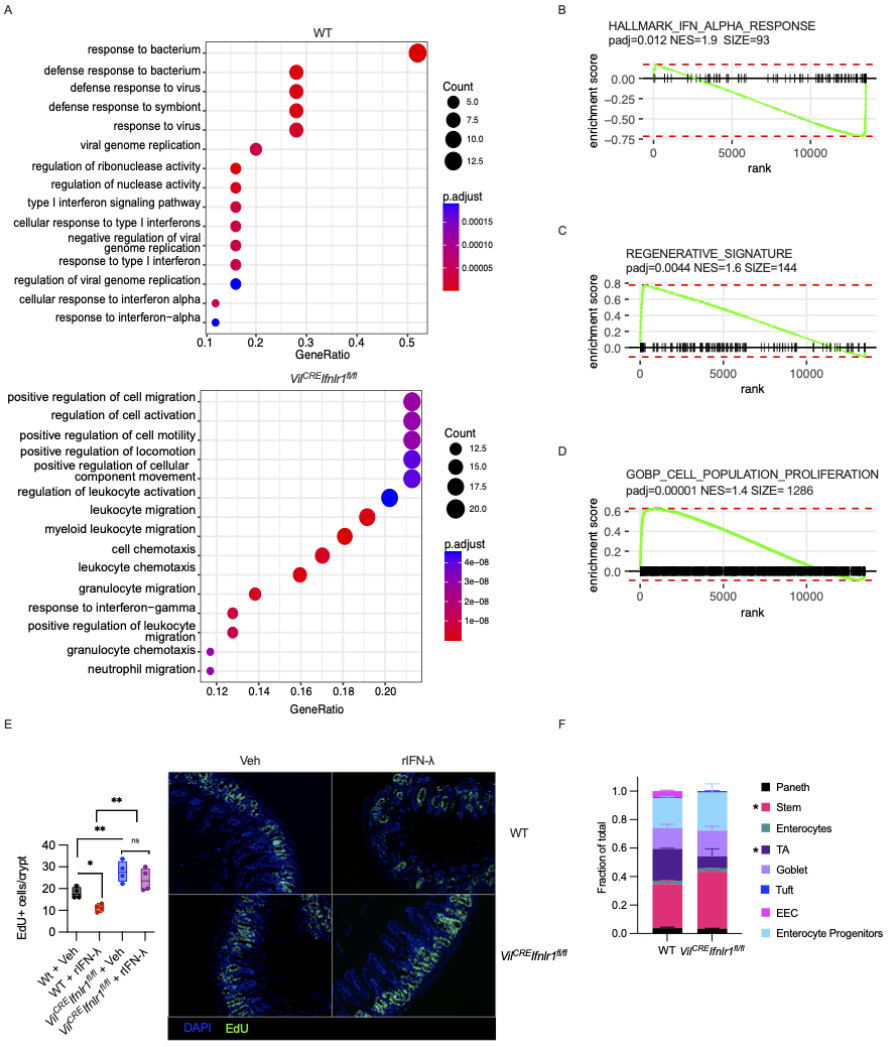

Figure 3. IFN-λ signaling induces an antiproliferative program in small intestine epithelia. (**A-D, F**) *Vil*^{CRE} *Ifnlr1*$^{fl/fl}$ mice or WT mice received 11 Gy ionizing radiation, with lead shielding of the upper extremities. Targeted transcriptomics was performed on small intestinal crypts isolated 96h after irradiation. (**A**) Dot plots of Gene Ontology (GO) enrichment analysis. GO terms enriched in crypts from WT mice (*upper panel*) or *Vil*^{CRE} *Ifnlr1*$^{fl/fl}$ mice (*lower panel*) are shown. Gene ratio (x

axis), adjusted p-value (color) and gene count (dot size) are depicted. (**B-D**) GSEA enrichment plots of the HALLMARK_IFN_ALPHA_RESPONSE (**B**), REGENERATIVE SIGNATURE (as previously described (Yui et al. 2018)) (**C**), and the GO biological process Cell Population proliferation ("GOBP_CELL_POP_PROLIF) (**D**) are depicted. padj: adjusted p-value, NES: Normalized enrichment score, SIZE: size. (**E**) *Vil*^{CRE} *Ifnlr1*$^{fl/fl}$ mice or WT mice were irradiated as in (**A-D**) and treated with either 50 mg kg^{-1}day^{-1} of rIFN-λ (rIFN-λ), or saline vehicle (Veh). After 96h mice were pulsed with EdU for 2h. Number of EdU^{+} cells per crypt quantified by immunohistochemistry (IHC) (*left panel*), and representative IHC sections (*right panel*) are depicted. (**F**) Targeted transcriptomics data from WT or *Vil*^{CRE} *Ifnlr1*$^{fl/fl}$ small intestinal crypts were deconvoluted based on publicly available single-cell RNA-seq (scRNA-seq) datasets (Haber et al. 2017) using CIBERSORTx (Newman et al. 2019) to extrapolate the relative cellular composition of samples. Paneth: Paneth cells; Stem: Intestinal stem cells; Enterocytes: small intestine enterocytes; TA: Transit amplifying cells; Goblet: Goblet cells; Tuft: tuft cells; EEC: Enteroendocrine cells; EP: Enterocyte progenitors. (**E**) Box plots are depicted. Each dot represents a mouse. Median, range and interquartile range are depicted. (**F**) Mean and SEM of 4 samples (WT) and 3 samples (*Vil*^{CRE} *Ifnlr1*$^{fl/fl}$) are depicted. Statistics: (**E, F**) Two-way ANOVA with Šidak correction for multiple comparisons. ns= not significant ($p > 0.05$); *$p < 0.05$;**$p < 0.01$; ***$p < 0.001$; ****$p < 0.0001$.

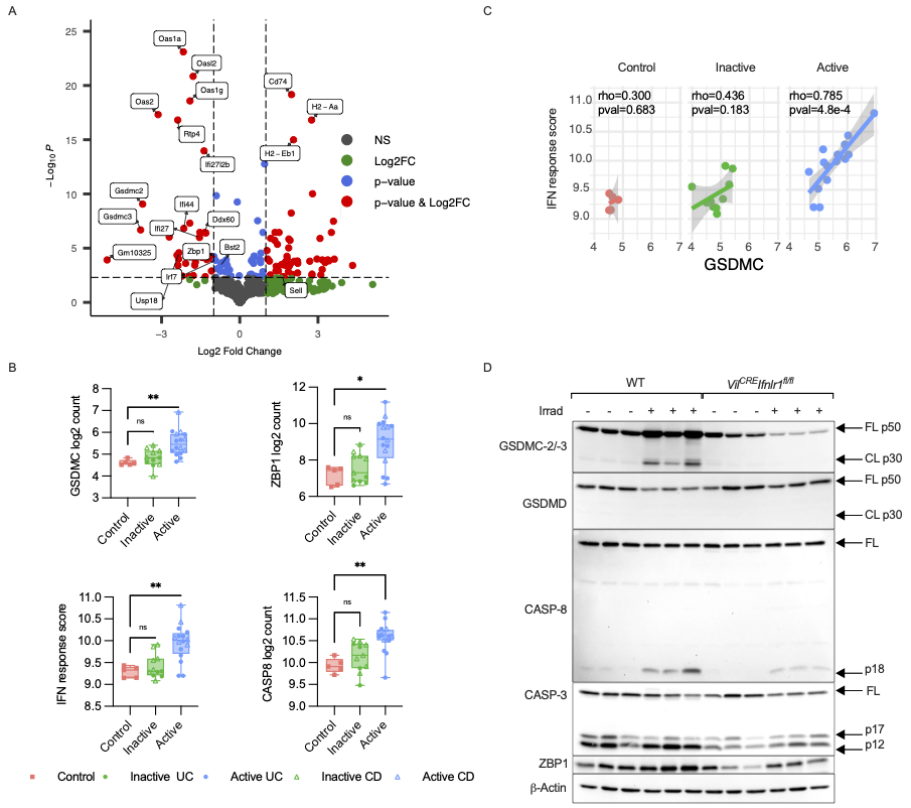

Figure 4. IFN-λ controls the expression of ZBP1 and the activation of gasdermin C. (**A**) *Vil*^{CRE} *Ifnlr1*$^{fl/fl}$ mice or WT mice were irradiated as in **Figure 2A**. Targeted transcriptomics was performed on freshly isolated small intestinal crypts. Volcano plot depicting differentially expressed genes (DEGs) between *Vil*^{CRE} *Ifnlr1*$^{fl/fl}$ and WT small intestinal crypts. DEGs (P< 0.005) with a fold change >2 (or <−2) are indicated in red; DEGs with a fold change <2 (or >−2) are indicated in blue. Nonsignificant DEGs (P> 0.005) and genes not differentially expressed are indicated in green and gray, respectively. Positive values represent genes overexpressed in *Vil*^{CRE} *Ifnlr1*$^{fl/fl}$, negative values represent genes overexpressed in WT. (**B**) RNA sequencing was performed on colon

biopsies from control patients, IBD patients with inactive disease, and IBD patients with active disease, (see Materials and Methods). Square symbols represent controls, round symbols represent ulcerative colitis (UC) patients, triangles represent Crohn's disease patients (CD). Box plots with median, range and interquartile range are depicted. Each symbol represents one patient. Expression of *GSDMC* (*top left panel*), *ZBP1* (*top right panel*), *CASP8* (*bottom right panel*) expressed as normalized log2 count is depicted. Mean expression of genes belonging to the GSEA HALLMARK_IFN _ALPHA_RESPONSE gene set (IFN Response score), is depicted (*bottom left panel*). (**C**) Dot plot depicting the correlation between GSDMC expression and the IFN Response score performed on the same samples as (**B**). Each point represents a patient, solid lines represent linear regression, shaded area depicts the confidence interval. Spearman correlation coefficient (rho) and the relative p-value (pval) are indicated for each graph. (**D**) Small intestinal crypts were isolated from *Vil*^{CRE} *Ifnlr1*$^{fl/fl}$ mice or WT mice irradiated as in **Figure 2A** (Irrad +) or not (Irrad -). Immunoblot analysis of the indicated proteins was performed. GSDMC-2/-3 FL p50: full length 50 kDa GSDMC-2/3; GSDMC-2/-3 CL p30: N-terminal 30 kDa cleaved protein; GSDMD FL p50: full length GSDMD 50 kDa; GSDMD CL p30: N-terminal 30 kDa cleaved protein; CASP-8 FL: full length CASP-8; CASP-8 p18: 18 kDa CASP-8 cleavage fragment; CASP-3 FL: full length CASP-3; CASP-3 p17: 17 kDa CASP-3 cleavage fragment; CASP-3 p12: 12 kDa CASP-3 cleavage fragment. Each lane represents one mouse. Representative data of 3 independent experiments is depicted. Statistics: (**B**) Kruskal Wallis test with Dunn correction for multiple

comparisons was performed. ns= not significant ($p > 0.05$); *$p < 0.05$;**$p < 0.01$; ***$p < 0.001$; ****$p < 0.0001$.

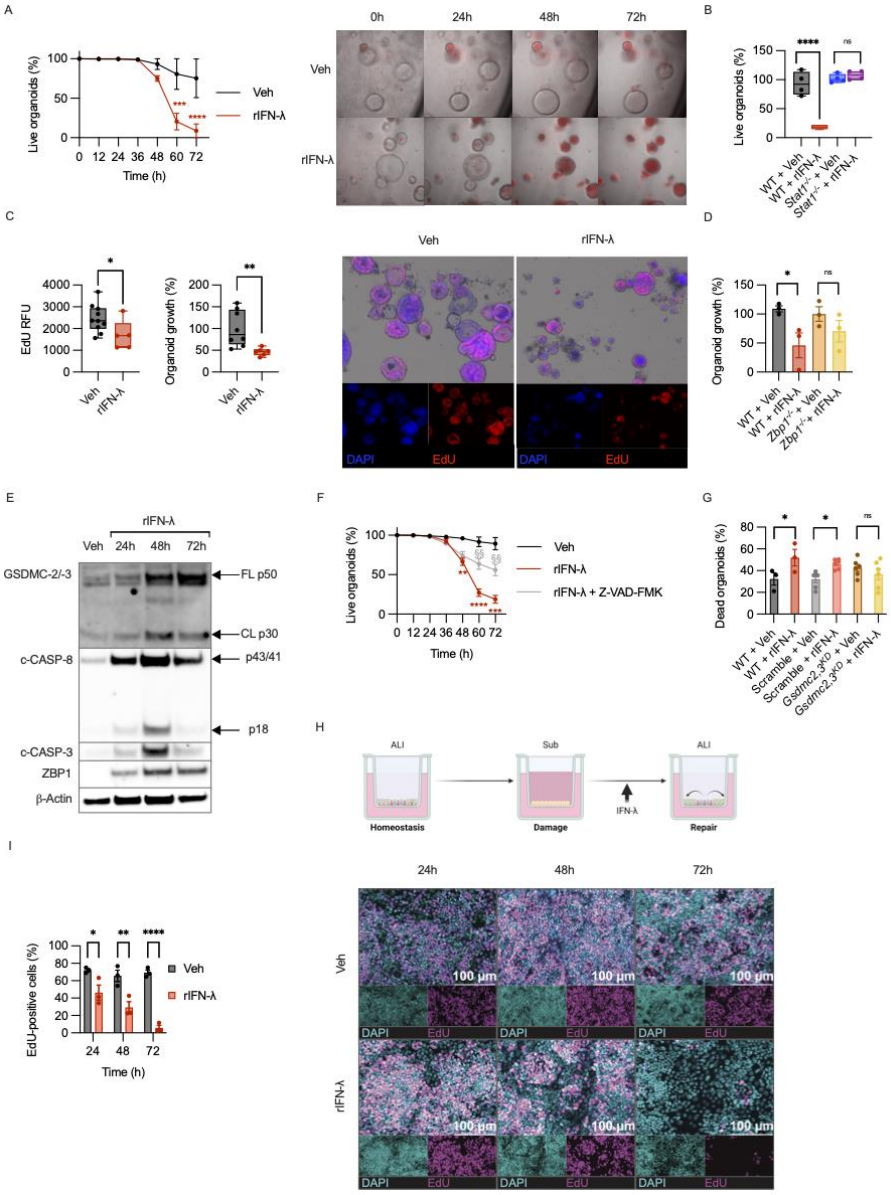

Figure 5. IFN-λ inhibits epithelial proliferation and survival in intestinal organoids *in vitro*. (**A**) Mouse small intestinal organoids were seeded from freshly isolated crypts and allowed to grow for 48h. Organoids were then treated with 200ng/ml of rIFN-λ in the presence of 1ug/ml propidium iodide (PI) and imaged every 12h over 72h.

Percentage of live organoids (*left panel*) was calculated as percentage of PI^- organoids over the total number of live organoids in each well. Representative image of 3 independent experiments is depicted (*right panel*). (**B**) Small intestinal organoids derived from WT or *Stat1*$^{-/-}$ mice were seeded and treated as in (**A**). Percentage of live organoids was calculated as percentage of PI^- organoids over the total number of live organoids in each well. (**C**) Small intestinal organoids were seeded and treated as in (**A**) for 72h. Organoids were pulsed with EdU for 6h. Organoids were stained for EdU incorporation (RED), and DAPI (BLUE). Mean fluorescence of EdU staining (*left panel*), relative organoid growth (*middle panel*) and representative images (*right panel*), are depicted. The relative growth of organoids is measured as the % of their area over untreated control organoids. (**D**) Small intestinal organoids derived from WT or *Zbp1*$^{-/-}$ mice were seeded and treated with 200ng/ml of rIFN-λ and imaged at 48h. The relative growth of organoids measured as in (**C**) is depicted. (**E**) Small intestinal organoids were treated as in (**A**) for 24, 48 and 72h. Immunoblot analysis of the indicated proteins was performed. GSDMC-2/-3 FL p50: full length 50kDa GSDMC-2/-3; GSDMC-2/-3 CL p30: N-terminal 30kDa cleaved protein; c-CASP-8 p43: 43 kDa CASP-8 cleavage fragment; c-CASP-8 p18: 18 kDa CASP-8 cleavage fragment. Representative blot of three independent experiments. (**F**) Small intestinal organoids were seeded as in (**A**) and either treated with 200ng/ml of rIFN-λ alone (rIFN-λ) or with rIFN-λ in the presence of the pan caspase inhibitor Z-VAD-FMK (40uM). Organoids were then followed for 72h and % of live organoids was evaluated as in (**A**). Statistical comparison between “rIFN-λ” and

"Veh" are depicted in red (*), comparison between "rIFN-λ + Z-VAD-FMK" and "rIFN-λ" is depicted in grey (§). (**G**) Small intestinal organoids were either left untreated (WT) or infected with a lentivirus expressing GFP and either a Gasdermin-2/Gasdermin-3 targeting (*Gsdmc2, 3^{KD}*) small harpin (sh)RNA, or a scrambled control shRNA (Scramble). Organoids were grown for 5 days and then treated with 200ng/ml of rIFN-λ or vehicle control for 48h. Survival of WT controls or lentiviral-infected GFP^{+} cells was assessed by cytofluorimetry by staining with Zombie dye and calcein. % of dead cells represent cells positive for Zombie dye staining and negative for calcein. (**H**) Experimental scheme for the establishment of 2D Air Liquid Interface (ALI) organoid cultures and modeling of damage and repair responses. Organoids were seeded in transwells and grown to confluence. The apical side was then exposed to air up to 14 days, which favored differentiation of a homeostatic monolayer. Organoids were then submerged for 7 days to induce damage responses. After 7 days they were re-exposed to air to stimulate repair responses. Concomitantly with re-exposure to air, organoids were treated with 200ng/ml of rIFN-λ for 3 days. (**I**) Organoids treated as in (**H**) were pulsed with EdU for 2h to mark proliferating cells. Quantification of the percentage of EdU^{+} cells per field of view (*lelft panel*) and representative images (*right panel*) are depicted. Edu (MAGENTA), and DNA stain DAPI (CYAN) are depicted. Representative image of 3 independent experiments. (**A, F**) Mean and SEM of 3 (**A**) and 5 (**F**) biological replicates per group are depicted. (**B, C**) Box plots are depicted. Each dot represents a biological replicate. Median, range and interquartile range are depicted. (**D, G, I**) Scatter

plots are depicted. Each dot represents a biological replicate. Statistics: (**A, F**) Two-way ANOVA with Tukey correction for multiple comparisons. (**B, C, D, G, I**) Two-way ANOVA with Šidak correction for multiple comparison. (**C**) Unpaired t test. ns= not significant ($p > 0.05$); *or §$p < 0.05$;**or §§$p < 0.01$; ***or §§§$p < 0.001$; ****or §§§§$p < 0.0001$.

Supplemental Figures.

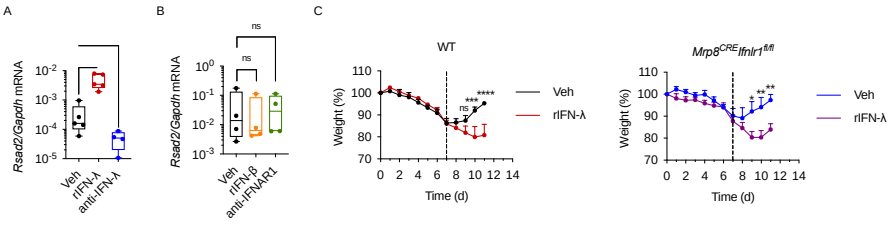

Figure S1. IFN-λ inhibits tissue recovery after DSS-colitis. (A) WT mice were treated with 2.5% DSS for 7 days. Upon DSS withdrawal mice were injected i.p. with either 50 µg kg-1day-1 of rIFN-λ or 12.5 mg $kg^{-1}day^{-1}$ of anti-IFN-λ2,3 antibody for five days. *Rsad2* relative mRNA expression in colonocytes on Day 14 is depicted. (**B**) Mice were treated with DSS as in (**A**). Upon DSS withdrawal mice were injected i.p. with either 50 mg $kg^{-1}day^{-1}$ of rIFN-β or 12.5 mg $kg^{-1}day^{-1}$ of anti-IFNAR1 antibody. *Rsad2* relative mRNA expression in colonocytes on Day 14 is depicted. (**C**) WT (*left panel*) or *Mrp8*^{CRE}*Ifnlr1*$^{fl/fl}$ mice (*right panel*) were treated with 2.5% DSS for seven days. Upon DSS withdrawal mice were injected i.p. with 50 µg $kg^{-1}day^{-1}$ of rIFN-λ. Weight is depicted. (**A, B**) Box plots are depicted. Each dot represents a mouse. Median, range and interquartile range are shown. (**C**) Mean and SEM of 5 mice per group are depicted. Statistics: (**A, B**) One-way ANOVA with Dunnett correction for multiple comparisons. (**C**) Two-way ANOVA with Tukey correction for multiple comparisons. ns= not significant ($p > 0.05$); *$p < 0.05$;**$p < 0.01$; ***$p < 0.001$; ****$p < 0.0001$.

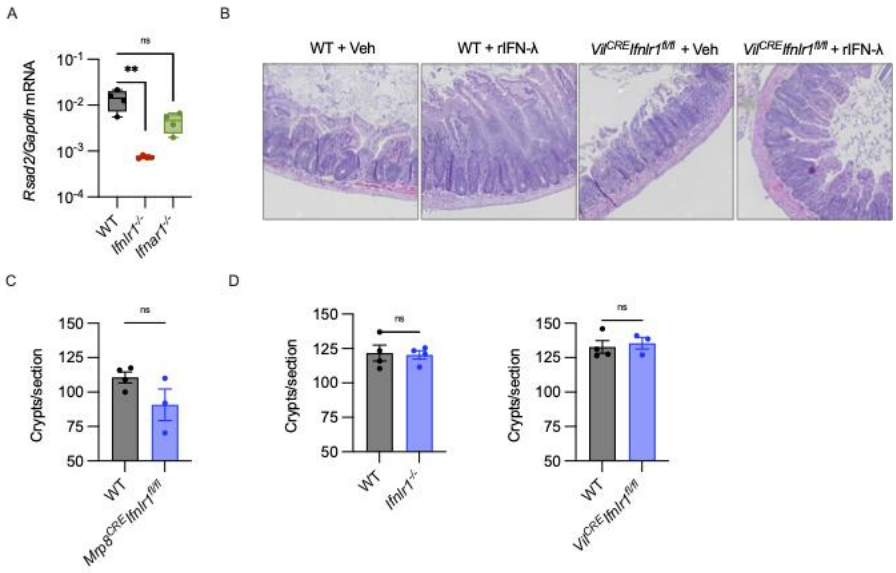

Figure S2. IFN-λ impairs epithelial regeneration after radiation damage. (**A**) WT, *Ifnlr1*$^{-/-}$, or *Ifnar1*$^{-/-}$ mice received 11 Gy ionizing radiation, with lead shielding of the upper body. *Rsad2* relative mRNA expression in small intestinal crypt cells was evaluated 96h after irradiation. (**B**) *Vil*^{CRE} *Ifnlr1*$^{fl/fl}$ mice or WT mice were irradiated as in (**A**) and treated with either 50 mg kg^{-1}day^{-1} of rIFN-λ (rIFN-λ), or saline vehicle (Veh). Tissue repair in the small intestine was evaluated 96h after irradiation. Representative histological images of the small intestine are depicted. (**C**) WT mice and *Mrp8*^{CRE}*Ifnlr1*$^{fl/fl}$ were irradiated as in (**A**). Tissue repair in the small intestine was evaluated 96h after irradiation by counting the number of intact crypts per histological section (Crypts/section). (**D**) Number of small intestinal intact crypts per histological section (Crypts/section) was evaluated in WT and *Ifnlr1*$^{-/-}$ (*left panel*) and WT and *Vil*^{CRE}*Ifnlr1*$^{fl/fl}$ (*right panel*) mice at homeostasis. (**A**) Box plots are depicted. Each dot represents a

mouse. Median, range and interquartile range are depicted. (**C, D**) Scatter plots are depicted. Each dot represents a mouse. Mean with SEM are depicted. Statistics: (**A**) One-way ANOVA with Dunnett correction for multiple comparisons. (**B**) Unpaired t test. ns= not significant ($p > 0.05$); *$p < 0.05$;**$p < 0.01$; ***$p < 0.001$; ****$p < 0.0001$.

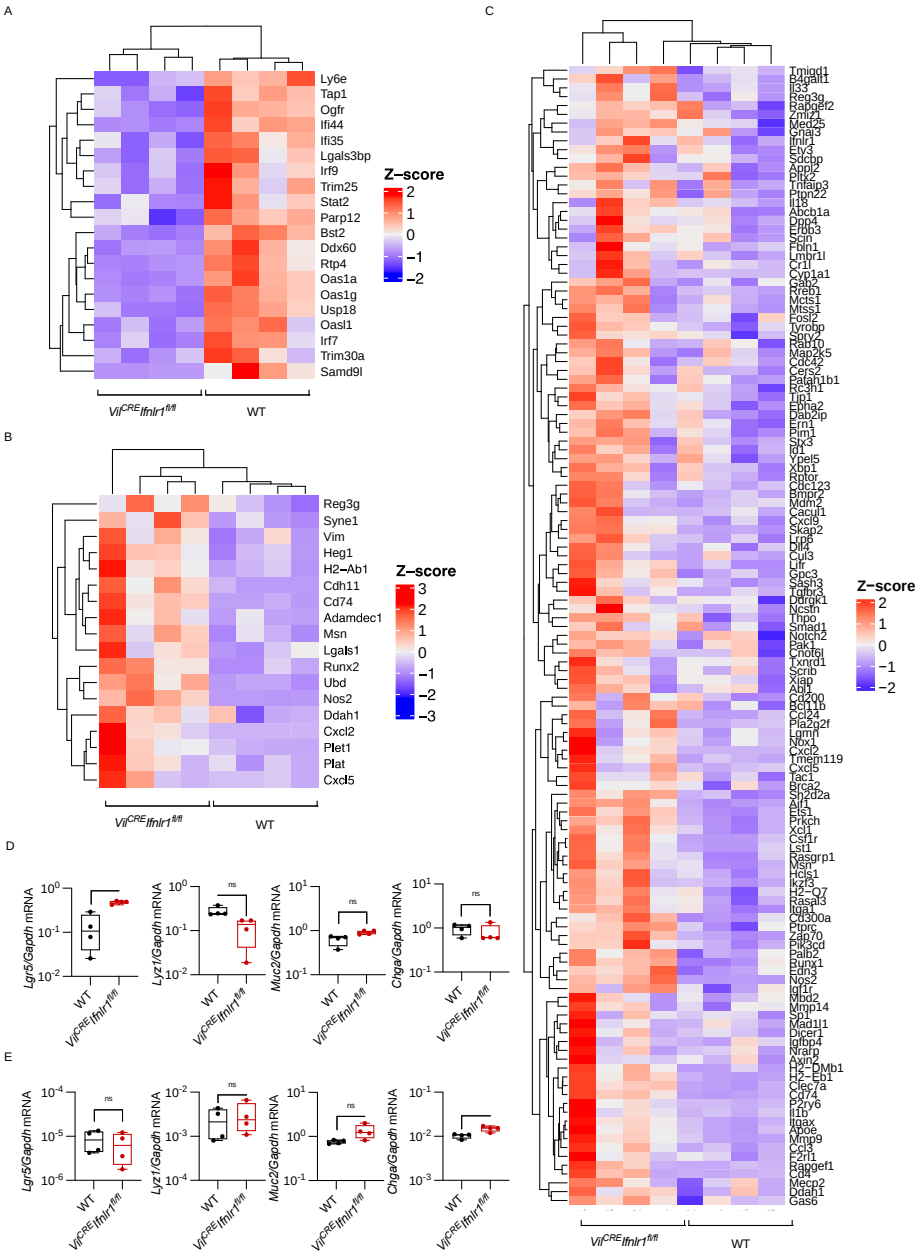

Figure S3. IFN-λ signaling induces an antiproliferative program in small intestine epithelia. (**A-D**) *Vil*^{CRE} *Ifnlr1*$^{fl/fl}$ mice or WT mice received 11 Gy ionizing radiation, with lead shielding of the upper body. (**A, B**) Targeted transcriptomics was performed on small

intestinal crypts isolated 96h after irradiation. (**A**) Heatmap depicting expression of genes in the leading edge of the enriched HALLMARK_IFN_ALPHA_RESPONSE gene set. The color is proportional to the Z Score. (**B**) Heatmap depicting expression of genes in the leading edge of the REGENERATION SIGNATURE gene set. The color is proportional to the Z Score. (**C**) Heatmap depicting expression of genes in the leading edge of the enriched GOBP_CELL_POPULATION_PROLIFERATION gene set. The color is proportional to the Z Score. (**D**) *Lgr5, Lyz1, Muc2, Chga* relative mRNA expression in small intestinal crypt cells was evaluated 96h after irradiation. (**E**) *Lgr5, Lyz1, Muc2, Chga* relative mRNA expression in small intestinal crypt cells isolated from *Vil*^{CRE} *Ifnlr1*$^{fl/fl}$ mice or WT mice at homeostasis was evaluated. (**D, E**) Box plots are depicted. Each dot represents a mouse. Median, range and interquartile range are depicted. Statistics: (**D, E**) Unpaired t test. ns= not significant ($p > 0.05$); *$p < 0.05$;**$p < 0.01$; ***$p < 0.001$; ****$p < 0.0001$.

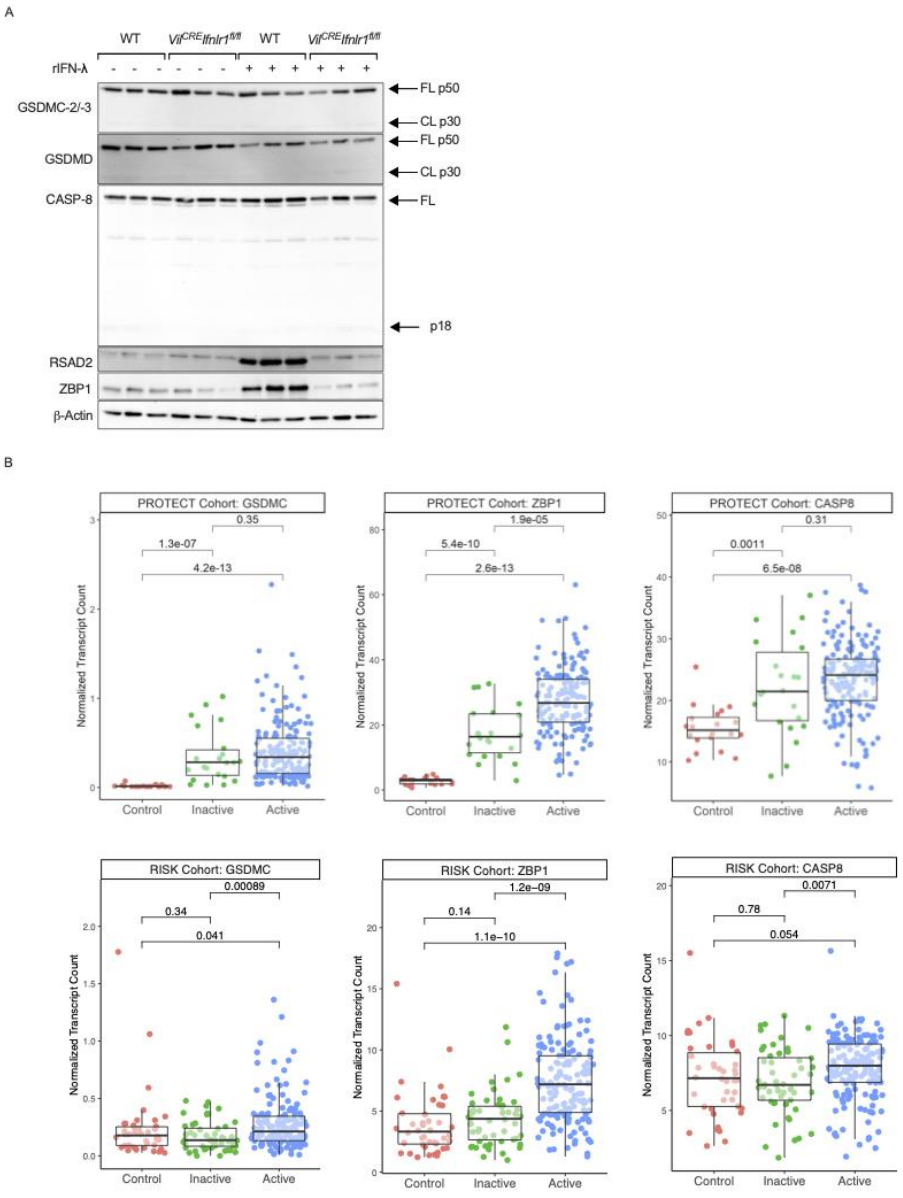

Figure S4. IFN-λ controls the expression of ZBP1 and the activation of Gasdermin C. (**A**) *Vil*^{CRE} *Ifnlr1*$^{fl/fl}$ mice or WT mice were treated with either 50 mg kg^{-1}day^{-1} of rIFN-λ (rIFN-λ), or saline vehicle (Veh). Immunoblot analysis of the indicated proteins was performed. Each lane represents one mouse. GSDMC-2/-3 FL p50: full length 50 kDa

GSDMC-2/-3; GSDMC-2/-3 CL p30: N-terminal 30 kDa cleaved protein; GSDMD FL p50: full length 50 kDa GSDMD; GSDMD CL p30: N-terminal 30 kDa cleaved protein; CASP-8 FL: full length CASP-8; CASP-8 p18: 18 kDa cleavage fragment. (**B**) Expression (defined by normalized transcript counts; Transcripts Per Kilobase Million [TPM] for PROTECT cohort and Reads Per Kilobase Million [RPKM] for RISK cohort) of the indicated genes was assessed in bulk RNA-seq data from the PROTECT (pediatric UC) and RISK (pediatric ileal CD) cohorts and comparisons made between control patients, uninflamed IBD and inflamed IBD patients. P-values are based on non-parametric t-testing between assessed groups (Wilcoxon test).

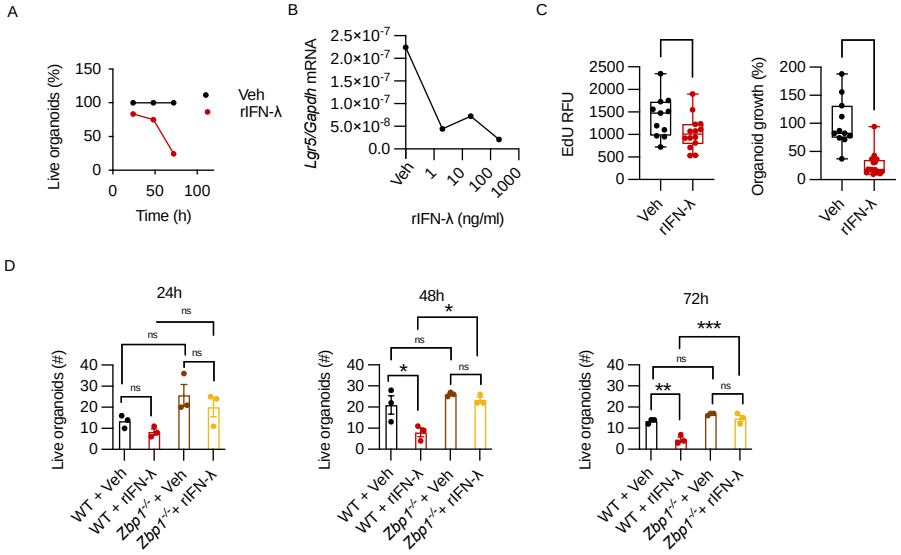

Figure S5. IFN-λ inhibits epithelial proliferation and survival in intestinal organoids *in vitro*. (**A**) Human duodenoids were seeded and treated (rIFN-λ), or not (Veh) with 200ng/ml of human IFN-λ2 for 72h. Cell viability was measured with CellTiter-Blue. Percentage of live organoids in rIFN-λ treated wells compared to Veh is depicted. (**B**) Mouse small intestinal organoids were grown for 6 days and then treated with mouse recombinant IFN-λ2 (rIFN-λ) at the indicated concentrations. *Lgr5* relative mRNA expression is depicted. (**C**) Human duodenoids were seeded and treated with 200ng/ml of IFN-λ2 for 72h. Organoids were pulsed with EdU for 6hr. Organoids were stained for EdU incorporation. Mean fluorescence of EdU staining (*left panel*), relative organoid growth (*right panel*), are depicted. The relative growth of organoids is measured as the % of their area over untreated control organoids. (**D**) Colon organoids derived from WT or *Zbp1*$^{-/-}$ mice were seeded and treated with 200ng/ml of rIFN-λ and imaged at

24h, 48h and 72h. The number of formed organoids is depicted. (**C**) Box plots are depicted. Each dot represents a biological replicate. Median, range and interquartile range are depicted. (**D**) Scatter box with bars are depicted. Each dot represents a biological replicate. Mean and SEM are depicted. Statistics: (**C**) Unpaired t-test. (**D**) Two-way ANOVA with Šidak correction for multiple comparisons. ns= not significant ($p > 0.05$); *$p < 0.05$;**$p < 0.01$; ***$p < 0.001$; ****$p < 0.0001$.

Materials and Methods.

Mouse strains. C57BL/6J (Jax 00664) (wild-type), *Ifnar1*$^{-/-}$ (Jax 028288), *Mrp8*^{CRE} recombinase (Jax 021614), and *Vil*^{CRE} recombinase (Jax 004586) mice were purchased from Jackson Labs. C57BL/6 IL-28R$^{-/-}$ (*Ifnlr1*$^{-/-}$) mice were provided by Bristol-Myers Squibb. Cells from the intestine of C57BL/6 *Zbp1*$^{-/-}$ mice were kindly provided by Dr. A Poltorak. Cells from the intestine of B6.129S(Cg)-Stat1tm1Dlv (Stat1−/−, JAX 012606) were kindly provide by Dr. S.B. Snapper. The mutant mouse line *Ifnlr1*$^{tm1a(EUCOMM)Wtsi}$ was provided by the Wellcome Trust Sanger Institute Mouse Genetics Project (Sanger MGP) and its funders (funding and associated primary phenotypic Information, http://www.sanger.ac.uk/mouseportal). Mice were housed under specific pathogen-free conditions at Boston Children's Hospital, and all the procedures were approved under the Institutional Animal Care and Use Committee (IACUC) and operated under the supervision of the department of Animal Resources at Children's Hospital (ARCH).

Reagents and antibodies. To treat murine organoids *in vitro* and for *in vivo* administration, we used recombinant mouse IFNλ-2 (rIFN-λ) attached to polyethylene glycol (provided by Bristol-Myers Squibb), mouse recombinant IFN-β (12401-1; PBL interferonsource), anti-IFN-λ2-3 (MAB17892; R&D systems) and anti-IFNAR1 (BE00241; BioXCell), the pan caspase inhibitor Z-VAD-FMK (HY-16658B; MedChem Express), EdU (NE08701; Carbosynth). To treat human organoids *in vitro* we used recombinant human IFNλ-2 (300-02K; Peprotech). The following

antibodies were used for immunoblotting: β-Actin (Mouse monoclonal; A5441; AC-15 clone; Lot# 127M4866V; Sigma-Aldrich), Rsad2 (Mouse monoclonal custom made; BioLegend) Zbp1 (Mouse monoclonal; AG-20B-0010-c100; Lot# A28231605; AdipoGen), gasderminC-2/-3 (Rabbit monoclonal; 229896; Lot# GR3317481-6; abcam), gasdermin D (Rabbit polyclonal; 20770-1-AP; Proteintech), Caspase 8 (D35G2; 4790; Lot#2; CST), Caspase 3 (9662; Lot# 19; CST), cleaved caspase 8 (Rabbit monoclonal; Asp387; D5B2; 8592; Lot#4; CST), cleaved caspase 3 (Rabbit monoclonal; D175; 5A1E; 9664; Lot#22; CST).

DSS-colitis induction. To induce colitis, mice were given 2.5% (w/v) dextran sulfate sodium (DSS, Affymetrix) in drinking water for 7 days and were then administered water for 7 days. Where indicated in the figure legends, mice were received daily intraperitoneal injections of 50 mg $kg^{-1}day^{-1}$ rIFN-λ or rIFN-β, and, to deplete endogenous IFN-λ or to block type I IFN signaling, mice received daily intraperitoneal injections of 12.5 mg $kg^{-1}day^{-1}$ of anti-IFN-λ2-3 or anti-IFNAR1 antibody respectively. Body weight, stool consistency and the presence of blood in the stool were monitored daily. Weight change was calculated as percentage of initial weight.

Partial body irradiation. Mice were sedated with a mix of ketamine (100 mg/ml) and xylazine (20 mg/ml) intraperitoneally. Mice then received gamma irradiation in a Best Theratronics Gammacell 40 Cesium 137-based irradiator with lead shielding of the head, thorax, and upper extremities to prevent bone marrow failure. In one sitting mice received either 11 Grey of gamma irradiation to assess tissue

restitution in small intestinal crypts or 14 Grey of gamma irradiation for survival experiments. To assess proliferation, mice were intraperitoneally administered a 100 mg/kg dose of EdU in saline, final volume 500µl.

Histological Analysis and Immunofluorescence. For morphologic analysis of irradiation experiments, fragments of the small intestine were fixed overnight in 4% paraformaldehyde (PFA) and embedded in paraffin for sectioning. Intestinal sections were stained with hematoxylin and eosin. Images were acquired with an EVOS M7000 (Thermo Fisher Scientific). Intact crypts were counted in 3 sections per animal blindly with ImageJ software. Proliferation was assessed by measuring the number of EdU^+ cells per intestinal crypt. A minimum of 10 crypts per section and 3 sections per mouse were evaluated. For Immunofluorescence analysis, paraffin sections were deparaffinized with sequential washes in xylene and ethanol. Deparaffinized sections were then stained for EdU incorporation. All quantifications were executed in a blinded fashion.

For histology of DSS-colitis experiments, colons were flushed with PBS, flattened and rolled into a 'Swiss roll'. Colon rolls were fixed in 10% formalin (Fisher Scientific), dehydrated in 70% Ethanol and embedded in paraffin. Paraffin sections were stained with hematoxylin and eosin and histological features were evaluated. Histological scoring was performed in a blinded fashion by assignment of a score of 1–5 to segments of the colon roll (1, presence of leukocyte infiltrate, loss of goblet cells; 2, bottom third of the crypt compromised; 3, two thirds of the crypt compromised; 4, complete crypt architecture loss; 5,

complete crypt loss and lesion of the epithelial layer). Each segment was then measured with ImageJ software, and the final histological score of each sample was obtained by 'weighting' the score of each segment against the length of the segment and divided by the total length of the colon roll.

EdU incorporation staining. Deparaffinized slides or organoids fixed on transwell were stained for 30 minutes with 2mM Sulfo-Cyanine5-azide (Lumiprobe) in the presence of 1mM $CuSO_4$ and 2mg/ml Sodium ascorbate, in PBS. After EdU staining, slides were stained with DAPI (Sigma) to detect nuclei, and mounted with ProLongGold antifade reagent (Thermo Fisher Scientific).

Crypt extraction. Small intestines were longitudinally cut and rinsed in PBS. Mucus was washed away by incubation with 1mM DTT at 4°C for 5 minutes. The tissue was moved to 10mM EDTA, 1% FBS, 1% sucrose at 37°C for 5 minutes. Samples were vortexed and small intestine fragments were moved to a new tube with 10mM EDTA, 1% FBS, 1% sucrose at 37°C for 10 minutes. Samples were vortexed. The supernatant was filtered through a 70uM strainer and kept on ice. Small intestine fragments were moved to a new tube with 10mM EDTA, 1% FBS, 1% sucrose at 37°C for 10 minutes. Samples were vortexed and the supernatant was combined with the previous fraction. The isolated crypts were resuspended in Trizol for RNA extraction and in RIPA Buffer with protease and phosphatase inhibitors for Western Blot analysis.

Measure cytokine gene expression in the colon, small intestine crypts and organoids. Samples were collected in Trizol (Thermo Scientific) and RNA was isolated using phenol-chloroform extraction. Purified RNA was analyzed for gene expression by qPCR on a CFX384 real-time cycler (Bio-rad) using *Power* SYBR™ Green RNA-to-C_T™ *1-Step* Kit (Thermo Scientific, 4389986) and pre-designed KiCqStart SYBR Green Primers (MilliporeSigma) specific for *Rsad2* (RM1_Rsad2 and FM1_Rsad2), *Lgr5* (RM1_Lgr5 and FM1_Lgr5) and IDT PrimeTime Predesigned qPCR Assays *specific for Gapdh* (Mm.PT.39a.1;).

RNA sequencing. For targeted transcriptome sequencing, RNA (15ng) isolated from small intestinal crypts was retro-transcribed to cDNA using SuperScript VILO cDNA Synthesis Kit (11754-05; Invitrogen). Barcoded libraries were prepared using the Ion AmpliSeq Transcriptome Mouse Gene Expression Panel, Chef-Ready Kit (A36412; Thermo Scientific) as per the manufacturer's protocol. Sequencing, read alignment, de-multiplexing, quality control and normalization was performed using an Ion S5 system (A27212; Ion Torrent). The generated count matrixes were analyzed using custom scripts in R (v 4.1.1). Differential Expression of Gene analysis was performed using the R package DEseq2 (v 1.34) with shrinkage of log2 fold changes. Volcano plots were created using the R package EnhancedVolcano (v 1.12). The differentially expressed genes with an adjusted p-value lesser that 0.1 and a log2 fold change greater than 1.5 were selected for downstream analysis. Functional enrichment analysis in Gene Ontology was performed using the R package ClusterProfiler (v 4.2) with the Biological Process terms and Benjamin-Hochberg multi-test

correction with 5% of FDR threshold. Geneset Enrichment Analysis (GSEA) of hallmarks was performed using the R package fgsea (v 1.20) using the hallmark genesets (v 7.4) from the Broad Institute MSigDB or custom genesets. Leading edges of the different selected genesets were selected to build heatmaps of their expression in the different conditions and samples. The R package ComplexHeatmap (v 2.10) was used to plot the heatmaps. We used CIBERSORTx (Newman et al. 2019) to estimate the abundances of epithelial cell types using using bulk gene expression data as an input and scRNAseq signature matrices from single-cell RNA sequencing data to provide the reference gene expression profiles of pure cell populations. The scRNAseq signature matrix used to deconvolute RNAseq dataset from small intestine crypts was taken from (Haber et al. 2017). Code available upon request.

Western blot. Western blot was performed with standard molecular biology techniques. Blots were probed for: β-Actin, Rsad2, Zbp1, gasdermin C-2/-3, gasdermin D, caspase 8, caspase 3, cleaved caspase 8 and cleaved caspase 3.

RNAseq on IBD patient's biopsies. The IBD biobank was generated starting with biopsy samples collected from patients suffering from CD or UC and diagnosed as clinically quiescent or in an active phase of the disease with various degrees. Controls were taken from non-inflammatory healthy portions of the colon. This investigation was registered under ClinicalTrials.gov Identifier: NCT02304666. A detailed description of the biobank as well as the RNAseq studies are described elsewhere (V. Millet et al., submitted). All raw and processed

sequencing data generated in this study are accessible on the NCBI Gene Expression Omnibus (GEO) under the meta-series GSE174159: https://www.ncbi.nlm.nih.gov/geo/query/acc.cgi?acc=GSE174166

Samples were divided in three groups according to the disease status of the patient: control, inactive and active. The mean of genes for the tested hallmarks were computed by mean of their expression across the samples of each group. Linear regression analyses were performed using the geom_smooth function of the R package ggplot (v 3.3.5) with the "lm" method. Correlation analysis were performed by a Spearman test using the cor.test function of the R base package stats.

Bulk RNA-seq sequencing data was downloaded from NCBI GEO for the RISK (https://www.ncbi.nlm.nih.gov/geo/query/acc.cgi; TPM-normalized counts matrix) and PROTECT (https://www.ncbi.nlm.nih.gov/geo/query/acc.cgi?acc=GSE109142; RPKM-normalized count matrix) cohorts. For the RISK data, samples with “undetermined” histopathology data were excluded from the analysis, and IBD samples labeled as macroscopically or microscopically inflammation were categorized as “Active” with the rest as “Inactive”. For the PROTECT cohort, samples lacking histology scores were excluded from the analysis and all other IBD samples were categorized as “Active” if they had a Histology Severity Score (for chronic and active acute neutrophil inflammation) > 1 and “Inactive” if they had a Histology Severity Score of 0-1 (Boyle et al. 2017). Group comparisons between healthy controls, inactive and active IBD were performed using non-parametric t-testing (Wilcoxon test) and p values reported.

Organoid culture and stimulation. Mouse intestinal spheroids were derived and maintained as previously described (Miyoshi and Stappenbeck 2013). Briefly, 1cm long segments of the small intestine were incubated in 5 ml of 2mM EDTA for 30 min at 4°C under rotation. Following the incubation period, the tubes were vigorously shaken, and the supernatant was passed through a 70µm strainer to collect small intestinal crypts and exclude villi fragments. The crypt compartment was collected by centrifugation, washed with advanced DMEM/F12 media (Thermo Fisher Scientific), resuspended in cold Matrigel (Corning) and plated in 40µl domes with 50% L-WRN (Wnt3, R-spondin, Noggin) supplemented medium.

Human organoids derived from healthy patients' duodenal biopsies were kindly provided by Dr. Jay Thiagarajah. Duodenal biopsy samples were obtained from routine diagnostic endoscopy under Boston Children's Hospital IRB protocol P00027983 and cultured with methods modified from (Sato, Stange, et al. 2011). Briefly, crypts were dissociated from duodenal biopsy samples obtained from age-matched (<3 years) healthy control individuals. Isolated crypts were suspended in Matrigel and plated in 50µL domes with 50% L-WRN supplemented media.

For maintenance, organoids were liberated from the extracellular matrix by incubating in cell recovery solution (Corning) at 4°C for 30 minutes, then a single cell preparation was obtained by incubating in TrypLE express (Thermo Fisher Scientific) at 37°C for 5 minutes. Single cells were then re-plated in Matrigel with 50% L-WRN supplemented media and 10mM Rock inhibitor Y-27632. For western blot

experiments, organoids were plated for 6 days. Organoids were then treated as indicated in the figure legends by adding cytokines and reagents to the medium overlaying the organoids. At the indicated timepoints, organoids were liberated from the extracellular matrix and lysed in RIPA buffer (Sigma). For microscopy of 3D organoids, freshly isolated crypts were seeded in 10µL of extracellular matrix in µ-Slide Angiogenesis (Ibidi) and overlayed with 45 µl of 50% L-WRN conditioned medium supplemented with 10mM Rock inhibitor Y-27632 for 24 hours. After 24 hours organoids were treated according to the figure legend in the presence of 1ug/ml Propidium Iodide (PI) (Sigma), and incubated in the video microscope ”Observer Z.1 Zeiss with Hamamatsu ORCA Flash 4.0 LT”, equipped with a temperature-controlled and CO_2 chamber. Wells were scanned every 12 hours and mosaic brightfield and fluorescence images were taken. Organoids were identified by ImageJ and were followed over time for PI incorporation as hallmark of cell death. % of live organoids was expressed as % of organoids that never incorporated PI. Where indicated in the figure legends, organoids viability was measured with CellTiter-Blue (Promega) according to the manufacturer’s instruction. Percentage of live organoids is expressed based on relative CellTiter-Blue signal compared to untreated organoids.

For experiments with 2D organoids in Air-Liquid Interface (ALI), we followed a previously described protocol (Wang et al. 2019). Briefly, cultured mouse small intestinal organoids were dissociated in single cells and seeded on polycarbonate transwells, with 0.4µM pores (CORNING). Initially, cells were seeded in the presence of 50% L-WRN

media with 10μM Rock inhibitor Y-27632 in both the lower and the upper chamber. After 7 days, the media was removed from the upper chamber to create an ALI. Cells were maintained in these conditions for 14 days to establish a homeostatic monolayer. The ALI culture was then resubmerged with 200μL 50% L-WRN medium, for 7 days and re-exposed to air for 3 days in the presence or absence of rIFN-λ, as indicated in the figure legends. After 3 days from re-exposure to air, cells were pulsed with 10 μM EdU for 2 hours, fixed in 10% formalin and stained for EdU incorporation. Samples were examined using a Zeiss LSM 880 confocal microscope (Carl Zeiss) and data were collected with fourfold averaging at a resolution of 2100 × 2100 pixels. The percentage of EdU-positive-cells was calculated as the ratio of the number EdU-positive foci and DAPI-positive foci.

***Gsdmc-2* and *Gsdmc-3* knock down in small intestine organoids and analysis by cytofluorimetry.** GSDMC knockdown (*Gsdmc2, 3*^{KD}) stable cell lines were produced using commercially designed lentivirus particles targeting mouse *Gsdmc2* (NM_001168274.1) and *Gsdmc3* (NM_183194.3) (Origene #HC108542): shRNA HC1008542A–AGTATTCAATACCTATCCCAAAGGGTTCG, HC108542B–AGTTGTGTTGTCCAGTTTCCTGTCCATGC and scrambled negative control non-effective shRNA (Origene Item no: TR30023). Lentivirus was packaged by co-transfecting shRNA and psPAX2 and pVSVG packaging plasmids into HEK293T cells. Transfection efficiency was monitored by GFP fluorescence, media was changed 24 hours post transfection and lentivirus particles were harvested in cell culture media 72 hours after transfection. Lentivirus particles were

concentrated with Lenti-X^{TM} Concentrator (Takara 631232) with the manufacturers protocol. Concentrated particles were resuspended in 100% WRN conditioned media and titers were checked using Lenti-X^{TM} GoStix^{TM} Plus (Takara 631280). Only high titer lenti-particles were used to transduce duodenoids. For transduction, duodenoids were removed from Matrigel with Cell Recovery Solution and dissociated into single cells in Trypsin-EDTA for 10 minutes. Debris was removed by filtering over a 70uM Cell strainer (Stem Cell Technologies #27260) and single cells isolated at 300RCF for 10 minutes. Single cells were resuspended in 1ml of Organoid Growth Media + 500ul of concentrated lentivirus particles in a 15ml conical tube supplemented with 4ug/mL polybrene. Cells were spin-transduced in a pre-warmed 32C centrifuge in a swinging bucket rotor at 500 x g for 1 hour. Organoid pellet was resuspended in matrigel, plated onto a Corning 24 Well plate, and incubated in a 37C +5%CO2 incubator for 2 hours. After two hours 500ul of organoid growth media was added. Media was changed every other day. Transduction efficiency was assessed by GFP fluorescence, and positively transduced wells were expanded. Vehicle (Veh) treated, scramble shRNA, and *Gsdmc2, 3^{KD}* duodenoids were treated with 200ng/ml of rIFN-λ in Organoid Growth Media. After 48 hours duodenoids were removed from Matrigel in Cell Recovery Solution for 1hr at 4ºC, washed with PBS and resuspended in Organoid FACS Buffer (1X PBS+ 1%BSA + 2mM EDTA + 10uM Y27632). Duodenoids were stained with Zombie Aqua (Biolegend) and Calcein Red AM (Thermofisher) in Organoid FACS buffer, diluted according to manufacturer's protocol. Cells were washed twice with PBS and

mechanically disrupted by pipetting with a P200 pipet tip, then incubated with prewarmed Trypsin-EDTA for 10 minutes at 37C. After 10 minutes trypsin was quenched with Organoid FACS buffer, cells were spun at 300 x g for 10 minutes at 4ºC, and resuspended in Organoid FACS Buffer for flow cytometry. Fluorescent positive gates were positioned relative to vehicle-treated and DMSO treated controls.

Quantification and Statistical Analysis. Statistical significance was assessed by: Unpaired t-test to compare two groups, One-way ANOVA with Dunnett correction for multiple comparisons to compare 3 or more independent groups, Two-way ANOVA with Turkey or Šidak correction for multiple comparisons to compare two groups with two conditions. Kruskal-Wallis test with Dunn's post hoc test was used to compare 3 or more independent groups when data did not meet the normality assumption. Spearman correlation analysis was used to examine the degree of association between two continuous variables. To establish the appropriate test, normal distribution and variance similarity were assessed with the D'Agostino-Pearson omnibus normality test. Statistical analyses were two-sided and performed using Prism9 (Graphpad) software or using custom scripts in R (v 4.1.1) and details are indicated in figure legends. Throughout the paper statistical significancy is defined as follows: ns, not significant ($p > 0.05$); *$p < 0.05$, **$p < 0.01$, ***$p < 0.001$, and ****$p < 0.0001$.

References.

1. Blanpain, Cédric, and Elaine Fuchs. 2014. “Stem Cell Plasticity. Plasticity of Epithelial Stem Cells in Tissue Regeneration.” *Science (New York, N.Y.)* 344 (6189): 1242281. https://doi.org/10.1126/science.1242281.
2. Boyle, Brendan, Margaret H. Collins, Zhu Wang, David Mack, Anne Griffiths, Cary Sauer, James Markowitz, et al. 2017. “Histologic Correlates of Clinical and Endoscopic Severity in Children Newly Diagnosed With Ulcerative Colitis.” *The American Journal of Surgical Pathology* 41 (11): 1491–98. https://doi.org/10.1097/PAS.0000000000000939.
3. Broggi, Achille, Sreya Ghosh, Benedetta Sposito, Roberto Spreafico, Fabio Balzarini, Antonino Lo Cascio, Nicola Clementi, et al. 2020. “Type III Interferons Disrupt the Lung Epithelial Barrier upon Viral Recognition.” *Science* 369 (6504): 706–12. https://doi.org/10.1126/science.abc3545.
4. Broggi, Achille, Francesca Granucci, and Ivan Zanoni. 2020. “Type III Interferons: Balancing Tissue Tolerance and Resistance to Pathogen Invasion.” *Journal of Experimental Medicine* 217 (1): e20190295. https://doi.org/10.1084/jem.20190295.
5. Broggi, Achille, Yunhao Tan, Francesca Granucci, and Ivan Zanoni. 2017. “IFN-λ Suppresses Intestinal Inflammation by Non-Translational Regulation of Neutrophil Function.” *Nature Immunology* 18 (10): 1084–93. https://doi.org/10.1038/ni.3821.
6. Broz, Petr, Pablo Pelegrín, and Feng Shao. 2020. “The Gasdermins, a Protein Family Executing Cell Death and Inflammation.” *Nature Reviews Immunology* 20 (3): 143–57. https://doi.org/10.1038/s41577-019-0228-2.
7. Chiriac, Mircea T., Barbara Buchen, Alexandra Wandersee, Gheorghe Hundorfean, Claudia Günther, Yvonne Bourjau, Sean E. Doyle, et al. 2017. “Activation of Epithelial Signal Transducer and Activator of Transcription 1 by Interleukin 28 Controls Mucosal Healing in Mice With Colitis and Is Increased in Mucosa of Patients With Inflammatory Bowel Disease.” *Gastroenterology* 153 (1): 123-138.e8. https://doi.org/10.1053/j.gastro.2017.03.015.

8. Danese, Silvio, and Claudio Fiocchi. 2011. “Ulcerative Colitis.” *The New England Journal of Medicine* 365 (18): 1713–25. https://doi.org/10.1056/NEJMra1102942.
9. Forero, Adriana, Snehal Ozarkar, Hongchuan Li, Chia Heng Lee, Emily A. Hemann, Marija S. Nadjsombati, Matthew R. Hendricks, et al. 2019. “Differential Activation of the Transcription Factor IRF1 Underlies the Distinct Immune Responses Elicited by Type I and Type III Interferons.” *Immunity* 51 (3): 451-464.e6. https://doi.org/10.1016/j.immuni.2019.07.007.
10. Günther, Claudia, Barbara Ruder, Iris Stolzer, Heidrun Dorner, Gui-Wei He, Mircea Teodor Chiriac, Konrad Aden, et al. 2019. “Interferon Lambda Promotes Paneth Cell Death Via STAT1 Signaling in Mice and Is Increased in Inflamed Ileal Tissues of Patients With Crohn’s Disease.” *Gastroenterology* 157 (5): 1310-1322.e13. https://doi.org/10.1053/j.gastro.2019.07.031.
11. Haber, Adam L., Moshe Biton, Noga Rogel, Rebecca H. Herbst, Karthik Shekhar, Christopher Smillie, Grace Burgin, et al. 2017. “A Single-Cell Survey of the Small Intestinal Epithelium.” *Nature* 551 (7680): 333–39. https://doi.org/10.1038/nature24489.
12. Haberman, Yael, Rebekah Karns, Phillip J. Dexheimer, Melanie Schirmer, Judith Somekh, Ingrid Jurickova, Tzipi Braun, et al. 2019. “Ulcerative Colitis Mucosal Transcriptomes Reveal Mitochondriopathy and Personalized Mechanisms Underlying Disease Severity and Treatment Response.” *Nature Communications* 10 (1): 38. https://doi.org/10.1038/s41467-018-07841-3.
13. Haberman, Yael, Timothy L. Tickle, Phillip J. Dexheimer, Mi-Ok Kim, Dora Tang, Rebekah Karns, Robert N. Baldassano, et al. 2014. “Pediatric Crohn Disease Patients Exhibit Specific Ileal Transcriptome and Microbiome Signature.” *The Journal of Clinical Investigation* 124 (8): 3617–33. https://doi.org/10.1172/JCI75436.
14. Henden, Andrea S., Motoko Koyama, Renee J. Robb, Adriana Forero, Rachel D. Kuns, Karshing Chang, Kathleen S. Ensbey, et al. 2021. “IFN-λ Therapy Prevents Severe Gastrointestinal Graft-versus-Host Disease.” *Blood* 138 (8): 722–37. https://doi.org/10.1182/blood.2020006375.

15. Hou, Junwei, Rongce Zhao, Weiya Xia, Chiung-Wen Chang, Yun You, Jung-Mao Hsu, Lei Nie, et al. 2020. “PD-L1-Mediated Gasdermin C Expression Switches Apoptosis to Pyroptosis in Cancer Cells and Facilitates Tumour Necrosis.” *Nature Cell Biology* 22 (10): 1264–75. https://doi.org/10.1038/s41556-020-0575-z.
16. Julien, Olivier, and James A. Wells. 2017. “Caspases and Their Substrates.” *Cell Death and Differentiation* 24 (8): 1380–89. https://doi.org/10.1038/cdd.2017.44.
17. Kim, Chang-Kyung, Vincent W. Yang, and Agnieszka B. Bialkowska. 2017. “The Role of Intestinal Stem Cells in Epithelial Regeneration Following Radiation-Induced Gut Injury.” *Current Stem Cell Reports* 3 (4): 320–32. https://doi.org/10.1007/s40778-017-0103-7.
18. Kotenko, Sergei V., Grant Gallagher, Vitaliy V. Baurin, Anita Lewis-Antes, Meiling Shen, Nital K. Shah, Jerome A. Langer, Faruk Sheikh, Harold Dickensheets, and Raymond P. Donnelly. 2003. “IFN-Lambdas Mediate Antiviral Protection through a Distinct Class II Cytokine Receptor Complex.” *Nature Immunology* 4 (1): 69–77. https://doi.org/10.1038/ni875.
19. Kovacs, Stephen B., and Edward A. Miao. 2017. “Gasdermins: Effectors of Pyroptosis.” *Trends in Cell Biology* 27 (9): 673–84. https://doi.org/10.1016/j.tcb.2017.05.005.
20. Kuriakose, Teneema, and Thirumala-Devi Kanneganti. 2018. “ZBP1: Innate Sensor Regulating Cell Death and Inflammation.” *Trends in Immunology* 39 (2): 123–34. https://doi.org/10.1016/j.it.2017.11.002.
21. Kuriakose, Teneema, Min Zheng, Geoffrey Neale, and Thirumala-Devi Kanneganti. 2018. “IRF1 Is a Transcriptional Regulator of ZBP1 Promoting NLRP3 Inflammasome Activation and Cell Death during Influenza Virus Infection.” *The Journal of Immunology* 200 (4): 1489–95. https://doi.org/10.4049/jimmunol.1701538.
22. Liberzon, Arthur, Chet Birger, Helga Thorvaldsdóttir, Mahmoud Ghandi, Jill P. Mesirov, and Pablo Tamayo. 2015. “The Molecular Signatures Database (MSigDB) Hallmark Gene Set Collection.” *Cell Systems* 1 (6): 417–25. https://doi.org/10.1016/j.cels.2015.12.004.

23. Major, Jack, Stefania Crotta, Miriam Llorian, Teresa M. McCabe, Hans Henrik Gad, Simon L. Priestnall, Rune Hartmann, and Andreas Wack. 2020. “Type I and III Interferons Disrupt Lung Epithelial Repair during Recovery from Viral Infection.” *Science* 369 (6504): 712–17. https://doi.org/10.1126/science.abc2061.
24. McElrath, Constance, Vanessa Espinosa, Jian-Da Lin, Jianya Peng, Raghavendra Sridhar, Orchi Dutta, Hsiang-Chi Tseng, et al. 2021. “Critical Role of Interferons in Gastrointestinal Injury Repair.” *Nature Communications* 12 (1): 2624. https://doi.org/10.1038/s41467-021-22928-0.
25. Meizlish, Matthew L., Ruth A. Franklin, Xu Zhou, and Ruslan Medzhitov. 2021. “Tissue Homeostasis and Inflammation.” *Annual Review of Immunology* 39 (April): 557–81. https://doi.org/10.1146/annurev-immunol-061020-053734.
26. Metcalfe, Ciara, Noelyn M. Kljavin, Ryan Ybarra, and Frederic J. de Sauvage. 2014. “Lgr5+ Stem Cells Are Indispensable for Radiation-Induced Intestinal Regeneration.” *Cell Stem Cell* 14 (2): 149–59. https://doi.org/10.1016/j.stem.2013.11.008.
27. Miyoshi, Hiroyuki, and Thaddeus S. Stappenbeck. 2013. “In Vitro Expansion and Genetic Modification of Gastrointestinal Stem Cells in Spheroid Culture.” *Nature Protocols* 8 (12): 2471–82. https://doi.org/10.1038/nprot.2013.153.
28. Muendlein, Hayley I., Wilson M. Connolly, Zoie Magri, Irina Smirnova, Vladimir Ilyukha, Avishekh Gautam, Alexei Degterev, and Alexander Poltorak. 2021. “ZBP1 Promotes LPS-Induced Cell Death and IL-1β Release via RHIM-Mediated Interactions with RIPK1.” *Nature Communications* 12 (1): 86. https://doi.org/10.1038/s41467-020-20357-z.
29. Newman, Aaron M., Chloé B. Steen, Chih Long Liu, Andrew J. Gentles, Aadel A. Chaudhuri, Florian Scherer, Michael S. Khodadoust, et al. 2019. “Determining Cell Type Abundance and Expression from Bulk Tissues with Digital Cytometry.” *Nature Biotechnology* 37 (7): 773–82. https://doi.org/10.1038/s41587-019-0114-2.
30. Ohara, Takahiro E., Marco Colonna, and Thaddeus S. Stappenbeck. 2022. “Adaptive Differentiation Promotes Intestinal Villus Recovery.” *Developmental Cell* 57 (2): 166-179.e6. https://doi.org/10.1016/j.devcel.2021.12.012.

31. Pineton de Chambrun, Guillaume, Laurent Peyrin-Biroulet, Marc Lémann, and Jean-Frédéric Colombel. 2010. “Clinical Implications of Mucosal Healing for the Management of IBD.” *Nature Reviews. Gastroenterology & Hepatology* 7 (1): 15–29. https://doi.org/10.1038/nrgastro.2009.203.
32. Place, David E, SangJoon Lee, and Thirumala-Devi Kanneganti. 2021. “PANoptosis in Microbial Infection.” *Current Opinion in Microbiology* 59 (February): 42–49. https://doi.org/10.1016/j.mib.2020.07.012.
33. Prokunina-Olsson, Ludmila, Brian Muchmore, Wei Tang, Ruth M. Pfeiffer, Heiyoung Park, Harold Dickensheets, Dianna Hergott, et al. 2013. “A Variant Upstream of IFNL3 (IL28B) Creating a New Interferon Gene IFNL4 Is Associated with Impaired Clearance of Hepatitis C Virus.” *Nature Genetics* 45 (2): 164–71. https://doi.org/10.1038/ng.2521.
34. Quirós, Miguel, and Asma Nusrat. 2019. “Contribution of Wound-Associated Cells and Mediators in Orchestrating Gastrointestinal Mucosal Wound Repair.” *Annual Review of Physiology* 81 (February): 189–209. https://doi.org/10.1146/annurev-physiol-020518-114504.
35. Roda, Giulia, Siew Chien Ng, Paulo Gustavo Kotze, Marjorie Argollo, Remo Panaccione, Antonino Spinelli, Arthur Kaser, Laurent Peyrin-Biroulet, and Silvio Danese. 2020. “Crohn’s Disease.” *Nature Reviews. Disease Primers* 6 (1): 22. https://doi.org/10.1038/s41572-020-0156-2.
36. Sato, Toshiro, Johan H. van Es, Hugo J. Snippert, Daniel E. Stange, Robert G. Vries, Maaike van den Born, Nick Barker, Noah F. Shroyer, Marc van de Wetering, and Hans Clevers. 2011. “Paneth Cells Constitute the Niche for Lgr5 Stem Cells in Intestinal Crypts.” *Nature* 469 (7330): 415–18. https://doi.org/10.1038/nature09637.
37. Sato, Toshiro, Daniel E. Stange, Marc Ferrante, Robert G. J. Vries, Johan H. Van Es, Stieneke Van den Brink, Winan J. Van Houdt, et al. 2011. “Long-Term Expansion of Epithelial Organoids from Human Colon, Adenoma, Adenocarcinoma, and Barrett’s Epithelium.” *Gastroenterology* 141 (5): 1762–72. https://doi.org/10.1053/j.gastro.2011.07.050.

38. Schmitt, Mark, Matthias Schewe, Andrea Sacchetti, Danny Feijtel, Wesley S. van de Geer, Miriam Teeuwssen, Hein F. Sleddens, et al. 2018. “Paneth Cells Respond to Inflammation and Contribute to Tissue Regeneration by Acquiring Stem-like Features through SCF/c-Kit Signaling.” *Cell Reports* 24 (9): 2312-2328.e7. https://doi.org/10.1016/j.celrep.2018.07.085.
39. Sheppard, Paul, Wayne Kindsvogel, Wenfeng Xu, Katherine Henderson, Stacy Schlutsmeyer, Theodore E. Whitmore, Rolf Kuestner, et al. 2003. “IL-28, IL-29 and Their Class II Cytokine Receptor IL-28R.” *Nature Immunology* 4 (1): 63–68. https://doi.org/10.1038/ni873.
40. Sposito, Benedetta, Achille Broggi, Laura Pandolfi, Stefania Crotta, Nicola Clementi, Roberto Ferrarese, Sofia Sisti, et al. 2021. “The Interferon Landscape along the Respiratory Tract Impacts the Severity of COVID-19.” *Cell* 184 (19): 4953-4968.e16. https://doi.org/10.1016/j.cell.2021.08.016.
41. Szczesny, Bartosz, Michela Marcatti, Akbar Ahmad, Mauro Montalbano, Attila Brunyánszki, Sofia-Iris Bibli, Andreas Papapetropoulos, and Csaba Szabo. 2018. “Mitochondrial DNA Damage and Subsequent Activation of Z-DNA Binding Protein 1 Links Oxidative Stress to Inflammation in Epithelial Cells.” *Scientific Reports* 8 (1): 914. https://doi.org/10.1038/s41598-018-19216-1.
42. Van Winkle, Jacob A, Stefan T Peterson, Elizabeth A Kennedy, Michael J Wheadon, Harshad Ingle, Chandni Desai, Rachel Rodgers, et al. 2022. “Homeostatic Interferon-Lambda Response to Bacterial Microbiota Stimulates Preemptive Antiviral Defense within Discrete Pockets of Intestinal Epithelium.” Edited by Andrew J MacPherson and Carla V Rothlin. *ELife* 11 (February): e74072. https://doi.org/10.7554/eLife.74072.
43. VanDussen, Kelli L., Naomi M. Sonnek, and Thaddeus S. Stappenbeck. 2019. “L-WRN Conditioned Medium for Gastrointestinal Epithelial Stem Cell Culture Shows Replicable Batch-to-Batch Activity Levels across Multiple Research Teams.” *Stem Cell Research* 37 (May): 101430. https://doi.org/10.1016/j.scr.2019.101430.
44. Walker, Forrest C., Pratyush R. Sridhar, and Megan T. Baldridge. 2021. “Differential Roles of Interferons in Innate Responses to

Mucosal Viral Infections." *Trends in Immunology* 42 (11): 1009–23. https://doi.org/10.1016/j.it.2021.09.003.

45. Wang, Yi, I. Ling Chiang, Takahiro E. Ohara, Satoru Fujii, Jiye Cheng, Brian D. Muegge, Aaron Ver Heul, et al. 2019. "Long-Term Culture Captures Injury-Repair Cycles of Colonic Stem Cells." *Cell* 179 (5): 1144-1159.e15. https://doi.org/10.1016/j.cell.2019.10.015.
46. Xi, Ranhui, Julia Montague, Xiaoli Lin, Chanyi Lu, Weiwei Lei, Keisuke Tanaka, Yali V Zhang, et al. 2021. "Up-Regulation of Gasdermin C in Mouse Small Intestine Is Associated with Lytic Cell Death in Enterocytes in Worm-Induced Type 2 Immunity." *Proceedings of the National Academy of Sciences of the United States of America* 118 (30): e2026307118. https://doi.org/10.1073/pnas.2026307118.
47. Yui, Shiro, Luca Azzolin, Martti Maimets, Marianne Terndrup Pedersen, Robert P. Fordham, Stine L. Hansen, Hjalte L. Larsen, et al. 2018. "YAP/TAZ-Dependent Reprogramming of Colonic Epithelium Links ECM Remodeling to Tissue Regeneration." *Cell Stem Cell* 22 (1): 35-49.e7. https://doi.org/10.1016/j.stem.2017.11.001.
48. Zhang, Jia-Yuan, Bo Zhou, Ru-Yue Sun, Yuan-Li Ai, Kang Cheng, Fu-Nan Li, Bao-Rui Wang, et al. 2021. "The Metabolite α-KG Induces GSDMC-Dependent Pyroptosis through Death Receptor 6-Activated Caspase-8." *Cell Research* 31 (9): 980–97. https://doi.org/10.1038/s41422-021-00506-9.

Chapter 5. Summary, Conclusions and Future Perspectives.

Summary.

In the past years, IFN-III have been labeled as the family of IFNs in charge of protecting mucosal barriers. They induce similar responses to IFN-I with the peculiarity of being less proinflammatory and of mediating a local and not systemic response (Broggi, Granucci, and Zanoni 2020; Lazear, Schoggins, and Diamond 2019). For this reason, IFN-III are considered promising alternatives to IFN-I as they hold the potential for similar therapeutic benefits, for example as antivirals, with limited side effects (Lazear, Nice, and Diamond 2015). However, in the course of my thesis, I have identified tissue-damaging effects of IFN-III during the restitution of respiratory and gastrointestinal epithelia that challenge their role as frontline defenders of barrier mucosae.

In Chapter 2 my colleagues and I uncovered that prolonged exposure to IFN-λ produced by lung dendritic cells downstream of TLR3 induces mouse morbidity. We found that IFN-λ inhibit epithelial repair following lung injury leading to increased susceptibility to secondary bacterial infections.

In Chapter 2 and more thoroughly in Chapter 3 we measured RNA and protein levels of specific members of type I and type III IFNs along the respiratory tract of COVID-19 patients. First, we noted that IFN-I/III expression levels in nasopharyngeal swabs correlate with viral load. Elderly patients, that have a higher risk of developing severe COVID-19, have a much lower correlation suggesting that their IFN responses are differently regulated. In the upper airways of patients with mild

pathology, we observed a strong IFN-λ1 and IFN-λ3 induction together with high expression of antiviral ISGs that likely restrict viral spread to the lower airways. IFN-I, and surprisingly IFN-λ2, characterized the upper and lower airways of severe COVID-19 patients and were associated with antiproliferative and proapoptotic gene signatures, revealing their possible contribution to immunopathology. Moreover, we confirmed that conventional dendritic cells, despite not being infection-permissive, contribute to the production of IFN-III via TLR3 sensing of factors released by infected lung epithelial cells, such as viral replication intermediates.

In Chapter 4 we found that IFN-III delay the restitution of gut epithelium in the colon after DSS-induced colitis and in the small intestine during the regenerative phase following radiation injury. Treatment of intestinal organoids with IFN-λ also inhibit their proliferation and survival. Our data suggest that IFN-III contribute to the formation of a novel protein complex that includes ZBP1 and GSDMC, which triggers the pyroptotic death of gut epithelial cells.

Conclusions.

A paradox remains unsolved: the dual nature of IFNs. The literature is polarized between the protective and detrimental functions of IFNs in all the pathological contexts that we assessed. The concept of host defense as a combination of resistance and tolerance can be extremely useful to explain some of these conflicting results. Upon viral infections host immune responses must trigger inhibition of virus replication, a resistance mechanism, and in parallel minimize tissue damage caused by the immune response itself, thus promoting tolerance (Schneider and Ayres 2008). Pathological outcomes can be caused by a failure in either of these responses. If disease severity (in a mouse model or a cohort of patients) is driven by a lack of resistance mechanisms leading to excessive viral load, blocking IFN-I or IFN-III signaling will likely be detrimental and their exogenous administration beneficial as they can increase host resistance by inducing an antiviral state. Importantly, this does not always apply. If defective resistance is due to autoantibodies against IFN-I or to inborn errors in IFNAR or IRF9 then IFN-I administration would not ameliorate disease but also not aggravate it (Bastard et al. 2020; Zhang et al. 2020). On the contrary, if disease severity is triggered by insufficient tolerance such as an excessive lung inflammation that is independent of viral load, the use of IFN therapy can be counterproductive as it potentiates resistance mechanisms in a setting where they are contributing to pathology (Russell and Clohisey Hendry 2022). Understanding if resistance or tolerance are drivers of disease is not trivial nor necessarily predictable. Resistance and tolerance can be driven by

similar players, they regulate each other and their relevance often varies throughout disease progression. IFNs represent obvious effectors of resistance to viral infections due to their induction of antiviral ISGs but they can also suppress tissue-damaging immune-mediated functions (Seo et al. 2011; Duerr et al. 2016; Broggi et al. 2017).

In conclusion, the multiple members of the IFN-I and IFN-III families exert opposite functions (also in terms of resistance and tolerance) according to the location and cell type that express, and/or respond to, them and to the stage of disease development. To maximize the clinical benefits of IFN-I and III, it is pivotal to identify the drivers of disease severity to define first of all if a patient is going to benefit from an IFN therapy and, if so, what are the optimal route and timing of intervention. For example, our work, together with several others, suggests that early or prophylactic administration of IFN-λ1 (or IFN-λ3) targeted to the nasal epithelium is a promising approach to treat SARS-CoV-2 infections as opposed to treatment of critically ill patients with systemic IFN-λ2 or any IFN-I that could contribute to immunopathology.

Future Perspectives.

The benefits of having a multitude of type I and III IFN subtypes that converge on a single receptor for each family and trigger similar gene responses have yet to be fully understood. Evolutionary analyses show that most of the members within each IFN family have evolved under strong selective constraints suggesting that they each play essential and nonredundant roles (Manry et al. 2011). Different members can be produced preferentially by distinct cell types and tissues upon recognition of different PAMPs (Hoffmann, Schneider, and Rice 2015). The kinetics of their expression and production can vary. Furthermore, each specific member binds the two subunits of its corresponding receptor with different affinities (Egli et al. 2014; Jaks et al. 2007). This affects the stability of the IFN-receptor complex, downstream signaling and ultimately the transcriptional (and possibly non-transcriptional) responses, qualitatively and in terms of duration (Hoffmann, Schneider, and Rice 2015). These differences confer distinct biological functions to each specific subtype, despite sharing signaling via the same receptor. A parallel and systematic analysis of each member of these families could explain some of the contradictory results that have been obtained by using mouse models that abolish the activity of an entire family of IFNs by knocking out their receptor. Finally, it can guide the selection of the best candidate within each IFN family for specific clinical needs.

References.

1. Bastard, Paul, Lindsey B. Rosen, Qian Zhang, Eleftherios Michailidis, Hans-Heinrich Hoffmann, Yu Zhang, Karim Dorgham, et al. 2020. “Autoantibodies against Type I IFNs in Patients with Life-Threatening COVID-19.” *Science (New York, N.Y.)* 370 (6515): eabd4585. https://doi.org/10.1126/science.abd4585.
2. Beer, Julius, Stefania Crotta, Angele Breithaupt, Annette Ohnemus, Jan Becker, Benedikt Sachs, Lisa Kern, et al. 2022. “Impaired Immune Response Drives Age-Dependent Severity of COVID-19.” *Journal of Experimental Medicine* 219 (12): e20220621. https://doi.org/10.1084/jem.20220621.
3. Broggi, Achille, Francesca Granucci, and Ivan Zanoni. 2020. “Type III Interferons: Balancing Tissue Tolerance and Resistance to Pathogen Invasion.” *Journal of Experimental Medicine* 217 (1): e20190295. https://doi.org/10.1084/jem.20190295.
4. Broggi, Achille, Yunhao Tan, Francesca Granucci, and Ivan Zanoni. 2017. “IFN-λ Suppresses Intestinal Inflammation by Non-Translational Regulation of Neutrophil Function.” *Nature Immunology* 18 (10): 1084–93. https://doi.org/10.1038/ni.3821.
5. Duerr, Claudia U., Connor D. A. McCarthy, Barbara C. Mindt, Manuel Rubio, Alexandre P. Meli, Julien Pothlichet, Megan M. Eva, et al. 2016. “Type I Interferon Restricts Type 2 Immunopathology through the Regulation of Group 2 Innate Lymphoid Cells.” *Nature Immunology* 17 (1): 65–75. https://doi.org/10.1038/ni.3308.
6. Egli, Adrian, Deanna M Santer, Daire O’Shea, D Lorne Tyrrell, and Michael Houghton. 2014. “The Impact of the Interferon-Lambda Family on the Innate and Adaptive Immune Response to Viral Infections.” *Emerging Microbes & Infections* 3 (1): 1–12. https://doi.org/10.1038/emi.2014.51.
7. Hoffmann, Hans-Heinrich, William M. Schneider, and Charles M. Rice. 2015. “Interferons and Viruses: An Evolutionary Arms Race of Molecular Interactions.” *Trends in Immunology* 36 (3): 124–38. https://doi.org/10.1016/j.it.2015.01.004.
8. Jaks, Eva, Martynas Gavutis, Gilles Uzé, Jacques Martal, and Jacob Piehler. 2007. “Differential Receptor Subunit Affinities of Type I Interferons Govern Differential Signal Activation.” *Journal*

of Molecular Biology 366 (2): 525–39. https://doi.org/10.1016/j.jmb.2006.11.053.

9. Lazear, Helen M., Timothy J. Nice, and Michael S. Diamond. 2015. "Interferon-λ: Immune Functions at Barrier Surfaces and Beyond." *Immunity* 43 (1): 15–28. https://doi.org/10.1016/j.immuni.2015.07.001.
10. Lazear, Helen M., John W. Schoggins, and Michael S. Diamond. 2019. "Shared and Distinct Functions of Type I and Type III Interferons." *Immunity* 50 (4): 907–23. https://doi.org/10.1016/j.immuni.2019.03.025.
11. Manry, Jérémy, Guillaume Laval, Etienne Patin, Simona Fornarino, Yuval Itan, Matteo Fumagalli, Manuela Sironi, et al. 2011. "Evolutionary Genetic Dissection of Human Interferons." *Journal of Experimental Medicine* 208 (13): 2747–59. https://doi.org/10.1084/jem.20111680.
12. Russell, C D, and S Clohisey Hendry. 2022. "Defining Resistance and Tolerance Traits in Covid-19: Towards a Stratified Medicine Approach." *QJM: An International Journal of Medicine* 115 (8): 513–19. https://doi.org/10.1093/qjmed/hcac143.
13. Schneider, David S., and Janelle S. Ayres. 2008. "Two Ways to Survive Infection: What Resistance and Tolerance Can Teach Us about Treating Infectious Diseases." *Nature Reviews. Immunology* 8 (11): 889–95. https://doi.org/10.1038/nri2432.
14. Seo, Sang-Uk, Hyung-Joon Kwon, Hyun-Jeong Ko, Young-Ho Byun, Baik Lin Seong, Satoshi Uematsu, Shizuo Akira, and Mi-Na Kweon. 2011. "Type I Interferon Signaling Regulates Ly6Chi Monocytes and Neutrophils during Acute Viral Pneumonia in Mice." *PLOS Pathogens* 7 (2): e1001304. https://doi.org/10.1371/journal.ppat.1001304.
15. Zhang, Qian, Paul Bastard, Zhiyong Liu, Jérémie Le Pen, Marcela Moncada-Velez, Jie Chen, Masato Ogishi, et al. 2020. "Inborn Errors of Type I IFN Immunity in Patients with Life-Threatening COVID-19." *Science (New York, N.Y.)* 370 (6515): eabd4570. https://doi.org/10.1126/science.abd4570.

Chapter 6. Publications.

1. Broggi, Achille, Sreya Ghosh, Benedetta Sposito, Roberto Spreafico, Fabio Balzarini, Antonino Lo Cascio, Nicola Clementi, et al. 2020. "Type III Interferons Disrupt the Lung Epithelial Barrier upon Viral Recognition." *Science* 369 (6504): 706–12. https://doi.org/10.1126/science.abc3545.
2. Sposito, Benedetta, Achille Broggi, Laura Pandolfi, Stefania Crotta, Nicola Clementi, Roberto Ferrarese, Sofia Sisti, et al. 2021. "The Interferon Landscape along the Respiratory Tract Impacts the Severity of COVID-19." *Cell* 184 (19): 4953-4968.e16. https://doi.org/10.1016/j.cell.2021.08.016.
3. Sposito, Benedetta, Julien Mambu, Katlynn Bugda Gwilt, Lionel Spinelli, Natalia Andreeva, Franck Galland, Philippe Naquet, et al. 2022. "Type III Interferons Induce Pyroptosis in Gut Epithelial Cells and Delay Tissue Restitution upon Acute Intestinal Injury." *BioRxiv*, March. https://doi.org/10.1101/2022.03.04.482997.